

1 A search for sparticles in zero lepton final states

2 Russell W. Smith

3 Submitted in partial fulfillment of the

4 requirements for the degree of

5 Doctor of Philosophy

6 in the Graduate School of Arts and Sciences

7 COLUMBIA UNIVERSITY

8 2016

9

© 2016

10

Russell W. Smith

11

All rights reserved

12

## ABSTRACT

13

A search for sparticles in zero lepton final states

14

Russell W. Smith

15 TODO : Here's where your abstract will eventually go. The above text is all in the  
16 center, but the abstract itself should be written as a regular paragraph on the page,  
17 and it should not have indentation. Just replace this text.



---

*Contents*

19	<b>Contents</b>	i
20	<b>1 Introduction</b>	1
21	<b>2 The Standard Model</b>	5
22	2.1 Overview	5
23	2.2 Field Content	5
24	2.3 Deficiencies of the Standard Model	15
25	<b>3 Supersymmetry</b>	21
26	3.1 Supersymmetric theories : from space to superspace	21
27	3.2 Minimally Supersymmetric Standard Model	24
28	3.3 Phenomenology	30
29	3.4 How SUSY solves the problems with the SM	32
30	3.5 Conclusions	34
31	<b>4 The Large Hadron Collider</b>	37
32	4.1 Basics of Accelerator Physics	37
33	4.2 Accelerator Complex	40
34	4.3 Large Hadron Collider	41
35	4.4 Dataset Delivered by the LHC	43
36	<b>5 The ATLAS detector</b>	49

37	5.1	Magnets	50
38	5.2	Inner Detector	52
39	5.3	Calorimetry	56
40	5.4	Muon Spectrometer	60
41	5.5	Trigger System	65
42	<b>6</b>	<b>Object Reconstruction</b>	<b>71</b>
43	6.1	Primitive Object Reconstruction	71
44	6.2	Physics Object Reconstruction and Quality Identification	77
45	<b>7</b>	<b>Recursive Jigsaw Reconstruction</b>	<b>103</b>
46	7.1	Razor variables	103
47	7.2	Recursive Jigsaw Reconstruction	108
48	7.3	Variables used in the search for zero lepton SUSY	114
49	<b>8</b>	<b>A search for supersymmetric particles in zero lepton final states with the Recursive Jigsaw Technique</b>	<b>121</b>
51	8.1	Simulation samples	121
52	8.2	Event selection	124
53	8.3	Background estimation	129
54	<b>9</b>	<b>Results</b>	<b>157</b>
55	9.1	Signal region distributions	157
56	9.2	Systematic Uncertainties	160
57	9.3	Limits and Model-dependent Exclusions	162
58	<b>Conclusion</b>		<b>169</b>
59	9.4	New Section	169
60	<b>Bibliography</b>		<b>171</b>

61	<b>Additional N-1 plots</b>	<b>185</b>
62	Compressed region N-1 plots	185



---

*Acknowledgements*



---

*Dedication*



*Introduction*

67 Particle physics is a remarkably successful field of scientific inquiry. The ability to  
 68 precisely predict the properties of a exceedingly wide range of physical phenomena,  
 69 such as the description of the cosmic microwave background [1, 2], the understanding  
 70 of the anomalous magnetic dipole moment of the electron [3, 4], and the measurement  
 71 of the number of weakly-interacting neutrino flavors [5] is truly amazing.

72 The theory that has allowed this range of predictions is the *Standard Model*  
 73 of particle physics (SM). The Standard Model combines the electroweak theory of  
 74 Glashow, Weinberg, and Salam [6–8] with the theory of the strong interactions, as  
 75 first envisioned by Gell-Mann and Zweig [9, 10]. This quantum field theory (QFT)  
 76 contains a number of particles, whose interactions describe phenomena up to the TeV  
 77 scale. These particles are manifestations of the fields of the Standard Model, after  
 78 application of the Higgs Mechanism. The particle content of the SM consists only of  
 79 six quarks, six leptons, four gauge bosons, and a scalar Higgs boson.

80 The Standard Model has some theoretical and experimental deficiencies. The SM  
 81 contains 26 free parameters<sup>1</sup>. We would like to understand these free parameters  
 82 in terms of a more fundamental theory.

83 The major theoretical concern of the Standard Model, as it pertains to this thesis,  
 84 is the *hierarchy problem* [11–15]. The light mass of the Higgs boson (125 GeV) should  
 85 be quadratically dependent on the scale of UV physics, due to the quantum corrections

---

<sup>1</sup>This is the Standard Model corrected to include neutrino masses. These parameters are the fermion masses (6 leptons, 6 quarks), CKM and PMNS mixing angles (8 angles, 2 CP-violating phases), W/Z/Higgs masses (3), the Higgs field expectation value, and the couplings of the strong, weak, and electromagnetic forces (3  $\alpha_{force}$  ).

86 from high-energy physics processes. The most perplexing experimental issue is the  
87 existence of *dark matter*, as demonstrated by galactic rotation curves [16–22]. This  
88 data has shown that there exists additional matter which has not yet been seen  
89 interacting with the particles of the Standard Model. There is no particle in the SM  
90 which can act as a candidate for dark matter.

91 Both of these major issues, as well as numerous others, can be solved by the  
92 introduction of *supersymmetry* (SUSY) [15, 23–35]. In supersymmetric theories, each  
93 SM particles has a so-called *superpartner*, or sparticle partner, differing from given SM  
94 particle by 1/2 in spin. These theories solve the hierarchy problem, since the quantum  
95 corrections induced from the superpartners exactly cancel those induced by the SM  
96 particles. In addition, these theories are usually constructed assuming *R*–parity,  
97 which can be thought of as the “charge” of supersymmetry, with SM particles having  
98  $R = 1$  and sparticles having  $R = -1$ . In collider experiments, since the incoming  
99 SM particles have total  $R = 1$ , the resulting sparticles are produced in pairs. This  
100 produces a rich phenomenology, which is characterized by significant hadronic activity  
101 and large missing transverse energy ( $E_T^{\text{miss}}$ ), which provide significant discrimination  
102 against SM backgrounds [36].

103 Despite the power of searches for supersymmetry where  $E_T^{\text{miss}}$  is a primary  
104 discriminating variable, there has been significant interest in the use of other variables  
105 to discriminate against SM backgrounds. These include searches employing variables  
106 such as  $\alpha_T$ ,  $M_{T,2}$ , and the razor variables ( $M_R, R^2$ ) [37–47]. In this thesis, we  
107 will present the first search for supersymmetry using the novel Recursive Jigsaw  
108 Reconstruction (RJR) technique. RJR can be considered the conceptual successor  
109 of the razor variables. We impose a particular final state “decay tree” on an events,  
110 which roughly corresponds to a simplified Feynmann diagram in decays containing  
111 weakly-interacting particles. We account for the missing degrees of freedom associated  
112 with weakly-interacting particles by a series of simplifying assumptions, which allow

113 us to calculate our variables of interest at each step in the decay tree. This allows  
114 an unprecedented understanding of the internal structure of the decay and additional  
115 variables to reject Standard Model backgrounds.

116 This thesis describes a search for the superpartners of the gluon and quarks, the  
117 gluino and squarks, in final states with zero leptons, with  $13.3 \text{ fb}^{-1}$  of data using  
118 the ATLAS detector. We organize the thesis as follows. The theoretical foundations  
119 of the Standard Model and supersymmetry are described in Chapters 2 and 3. The  
120 Large Hadron Collider and the ATLAS detector are presented in Chapters 4 and 5.  
121 The reconstruction of physics objects is presented in Chapter 6. Chapter 7 provides  
122 a detailed description of Recursive Jigsaw Reconstruction and a description of the  
123 variables used for the particular search presented in this thesis. Chapter 8 presents  
124 the details of the analysis, including details of the dataset, object reconstruction,  
125 and selections used. In Chapter 9, the final results are presented; since there is no  
126 evidence for a supersymmetric signal in the analysis, we present the final exclusion  
127 curves in simplified supersymmetric models.



*The Standard Model*130 **2.1 Overview**

131 The Standard Model (SM) is another name for a theory of the internal symmetry  
 132 group  $SU(3)_C \otimes SU(2)_L \otimes U(1)_Y$  and its associated set of parameters. The SM is the  
 133 culmination of years of work in both theoretical and experimental particle physics. In  
 134 this thesis, we take the view that theorists construct a model with the field content and  
 135 symmetries as inputs, and write down the most general Lagrangian consistent with  
 136 those symmetries. Assuming this model is compatible with nature (in particular, the  
 137 predictions of the model are consistent with previous experiments), experimentalists  
 138 are responsible for testing the parameters by measurements.

139 Additional theoretical background is in ?? . The philosophy and notations are  
 140 inspired by [48, 49].

141 **2.2 Field Content**

The Standard Model field content is

$$\begin{aligned} \text{Fermions} &: Q_L(3, 2)_{+1/3}, U_R(3, 1)_{+4/3}, D_R(3, 1)_{-2/3}, L_L(1, 2)_{-1}, E_R(1, 1)_{-2} \\ \text{Scalar (Higgs)} &: \phi(1, 2)_{+1} \\ \text{Vector Fields} &: G^\mu(8, 1)_0, W^\mu(1, 3)_0, B^\mu(1, 1)_0 \end{aligned} \tag{2.1}$$

142 where the  $(A, B)_Y$  notation represents the irreducible representation under  $SU(3)$   
 143 and  $SU(2)$ , with  $Y$  being the electroweak hypercharge. Each of these fermion fields

144 has an additional index, representing the three generation of fermions.

145 We observed that  $Q_L, U_R$ , and  $D_R$  are triplets under  $SU(3)_C$ ; these are the *quark*  
146 fields. The *color* group,  $SU(3)_C$  is mediated by the *gluon* field  $G^\mu(8, 1)_0$ , which has  
147 8 degrees of freedom. The fermion fields  $L_L(1, 2)_{-1}$  and  $E_R(1, 1)_{-2}$  are singlets under  
148  $SU(3)_C$ ; we call them the *lepton* fields.

149 Next, we note the “left-handed” (“right-handed”) fermion fields, denoted by  $L(R)$   
150 subscript, The left-handed fields form doublets under  $SU(2)_L$ . These are mediated  
151 by the three degrees of freedom of the “W” fields  $W^\mu(1, 3)_0$ . These fields only act  
152 on the left-handed particles of the Standard Model. This is the reflection of the  
153 “chirality” of the Standard Model The left-handed and right-handed particles are  
154 treated differently by the electroweak forces. The right-handed fields,  $U_R, D_R$ , and  
155  $E_R$ , are singlets under  $SU(2)_L$ .

156 The  $U(1)_Y$  symmetry is associated to the  $B^\mu(1, 1)_0$  boson with one degree of  
157 freedom. The charge  $Y$  is known as the electroweak hypercharge.

158 To better understand the phenomenology of the Standard Model, let us investigate  
159 each of the *sectors* of the Standard Model separately.

## 160 Electroweak sector

The electroweak sector refers to the  $SU(2)_L \otimes U(1)_Y$  portion of the Standard Model gauge group. Following our philosophy of writing all gauge-invariant and renormalizable terms, the electroweak Lagrangian can be written as

$$\mathcal{L} = W_a^{\mu\nu} W_{\mu\nu}^a + B^{\mu\nu} B_{\mu\nu} + (D^\mu \phi)^\dagger D_\mu \phi - \mu^2 \phi^\dagger \phi - \lambda (\phi^\dagger \phi)^2. \quad (2.2)$$

where  $W_a^{\mu\nu}$  are the three ( $a = 1, 2, 3$ ) gauge bosons associated to the  $SU(2)_L$  gauge group,  $B^{\mu\nu}$  is the one gauge boson of the  $U(1)_Y$  gauge group, and  $\phi$  is the complex Higgs multiplet. The covariant derivative  $D^\mu$  is given by

$$D^\mu = \partial^\mu + \frac{ig}{2} W_a^\mu \sigma_a + \frac{ig'}{2} B^\mu \quad (2.3)$$

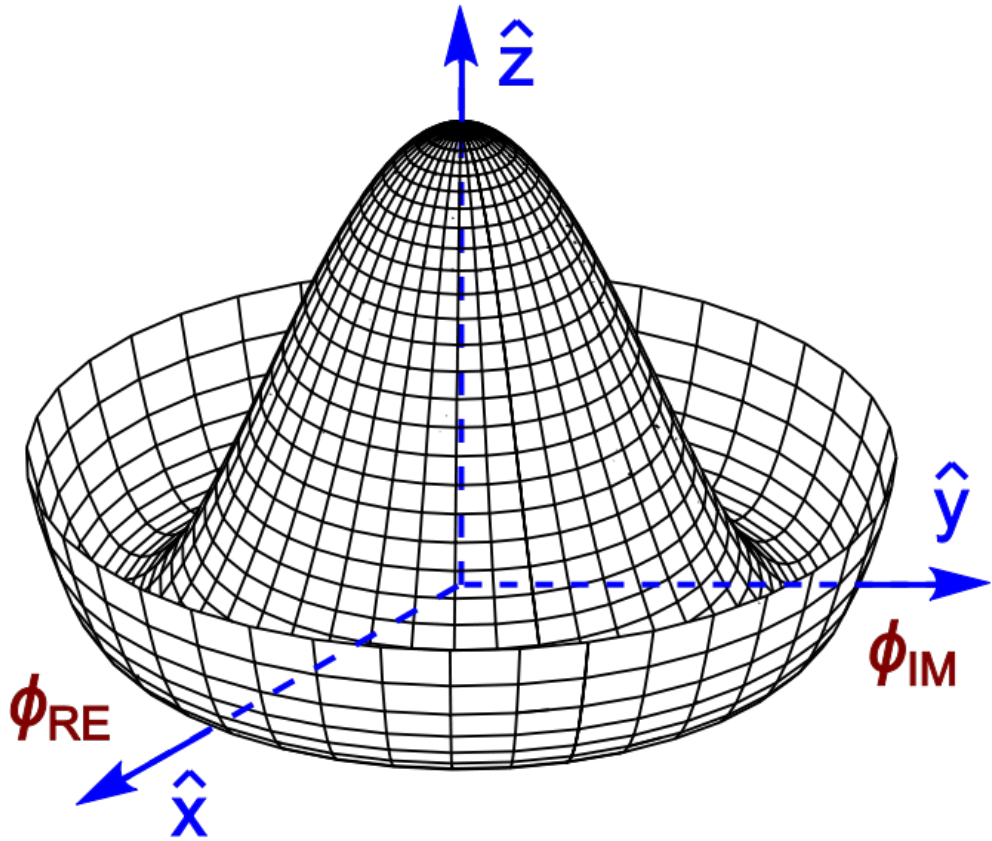


Figure 2.1: Sombrero potential

where  $i\sigma_a$  are the Pauli matrices times the imaginary constant, which are the generators for  $SU(2)_L$ , and  $g$  and  $g'$  are the  $SU(2)_L$  and  $U(1)_Y$  coupling constants, respectively. The field strength tensors  $W_a^{\mu\nu}$  and  $B^{\mu\nu}$  are given by the commutator of the covariant derivative associated to each field

$$B^{\mu\nu} = \partial^\mu B^\nu - \partial^\nu B^\mu \quad (2.4)$$

$$W_a^{\mu\nu} = \partial^\mu W_a^\nu - \partial^\nu W_a^\mu - g\epsilon_{abc}W_a^\mu W_b^\nu, \quad i = 1, 2, 3$$

161

162     The terms in the Lagrangian Eq. (2.2) proportional to  $\mu^2$  and  $\lambda$  make up the  
 163     “Higgs potential” [50]. As normal (see Appendix ??), we restrict  $\lambda > 0$  to guarantee  
 164     our potential is bounded from below, and we also require  $\mu^2 < 0$ , which gives us the  
 165     standard “sombrero” potential shown in Fig. 2.1.

This potential has infinitely many minima at  $\langle \phi \rangle = \sqrt{2m/\lambda}$ . The ground state is *spontaneously* broken by the choice of ground state, which induces a vacuum expectation value (VEV). Without loss of generality, we can choose the Higgs field  $\phi$  to point in the real direction, and write the Higgs field  $\phi$  in the following form :

$$\phi = \frac{1}{\sqrt{2}} \exp\left(\frac{i}{v} \sigma_a \theta_a\right) \begin{pmatrix} 0 \\ v + h(x) \end{pmatrix}. \quad (2.5)$$

We choose a gauge to rotate away the dependence on  $\theta_a$ , such that we can write simply

$$\phi = \frac{1}{\sqrt{2}} \begin{pmatrix} 0 \\ v + h(x) \end{pmatrix}. \quad (2.6)$$

Now, we can see how the masses of the vector bosons are generated from the application of the Higgs mechanism. We plug Eq. Eq. (2.6) back into the electroweak Lagrangian, and only showing the relevant mass terms in the vacuum state where  $h(x) = 0$  see that (dropping the Lorentz indices) :

$$\begin{aligned} \mathcal{L}_M &= \frac{1}{8} \left| \begin{pmatrix} gW_3 + g'B & g(W_1 - iW_2) \\ g(W_1 + iW_2) & -gW_3 + g'B \end{pmatrix} \begin{pmatrix} 0 \\ v \end{pmatrix} \right|^2 \\ &= \frac{g^2 v^2}{8} \left[ W_1^2 + W_2^2 + \left( \frac{g'}{g} B - W_3 \right)^2 \right] \end{aligned} \quad (2.7)$$

Defining the *Weinberg* angle  $\tan(\theta_W) = g'/g$  and the following *physical* fields :

$$W^\pm = \frac{1}{\sqrt{2}} (W_1 \mp iW_2) \quad (2.8)$$

$$Z^0 = \cos \theta_W W_3 - \sin \theta_W B$$

$$A^0 = \sin \theta_W W_3 + \cos \theta_W B$$

we can write the piece of the Lagrangian associated to the vector boson masses as

$$\mathcal{L}_{MV} = \frac{1}{4} g^2 v^2 W^+ W^- + \frac{1}{8} (g^2 + g'^2) v^2 Z^0 Z^0. \quad (2.9)$$

and we have the following values of the masses for the vector bosons :

$$\begin{aligned} m_W^2 &= \frac{1}{4}v^2g^2 \\ m_Z^2 &= \frac{1}{4}v^2(g^2 + g'^2) \\ m_A^2 &= 0 \end{aligned} \tag{2.10}$$

We thus see how the Higgs mechanism gives rise to the masses of the  $W^\pm$  and  $Z$  boson in the Standard Model. As expected, the mass of the photon is zero. The  $SU(2)_L \otimes U(1)_Y$  symmetry of the initially massless  $W_{1,2,3}$  and  $B$  fields is broken to the  $U(1)_{EM}$ . Of the four degrees of freedom in the complex Higgs doublet, three are “eaten” when we give mass to the  $W^\pm$  and  $Z_0$ , while the other degree of freedom is the Higgs particle, as discovered in 2012 by the ATLAS and CMS collaborations [51, 52].

### 173 Quantum Chromodynamics

Quantum chromodynamics (or the theory of the *strong* force) characterizes the behavior of *colored* particles, collectively known as *partons*. The partons of the Standard Model are the (fermionic) quarks, and the (bosonic) gluons. The strong force is governed by  $SU(3)_C$ , an unbroken symmetry in the Standard Model, which implies the gluon remains massless. Defining the covariant derivative for QCD as

$$D^\mu = \partial^\mu + ig_s G_a^\mu L_a, a = 1, \dots, 8 \tag{2.11}$$

where  $L_a$  are the generators of  $SU(3)_C$ , and  $g_s$  is the coupling constant of the strong force. The QCD Lagrangian then is given by

$$\mathcal{L}_{\text{QCD}} = i\bar{\psi}_f D_\mu \gamma^\mu \psi_f - \frac{1}{4} G_{a,\mu\nu} G_a^{\mu\nu} \tag{2.12}$$

where the summation over  $f$  is for quarks *families*, and  $G_a^{\mu\nu}$  is the gluon field strength tensor, given by

$$G_a^{\mu\nu} = \partial^\mu G_a^\nu - \partial^\nu G_a^\mu - g_s f^{abc} G_b^\mu G_c^\nu, a, b, c = 1, \dots, 8 \tag{2.13}$$

174 where  $f^{abc}$  are the structure constants of  $SU(3)_C$ , which are analogous to  $\epsilon_{abc}$  for  
175  $SU(2)_L$ . The kinetic term for the quarks is contained in the standard  $\partial_\mu$  term, while  
176 the field strength term contains the interactions between the quarks and gluons, as  
177 well as the gluon self-interactions.

178 Written down in this simple form, the QCD Lagrangian does not seem much  
179 different from the QED Lagrangian, with the proper adjustments for the different  
180 group structures. The gluon is massless, like the photon, so one could naïvely expect  
181 an infinite range force, and it pays to understand why this is not the case. The  
182 reason for this fundamental difference is the gluon self-interactions arising in the  
183 field strength tensor term of the Lagrangian. This leads to the phenomena of *color*  
184 *confinement*, which describes how one only observes color-neutral particles alone in  
185 nature. In contrast to the electromagnetic force, particles which interact via the  
186 strong force experience a *greater* force as the distance between the particles increases.  
187 At long distances, the potential is given by  $V(r) = -kr$ . At some point, it is more  
188 energetically favorable to create additional partons out of the vacuum than continue  
189 pulling apart the existing partons, and the colored particles undergo *fragmentation*.  
190 This leads to *hadronization*. Bare quarks and gluons are actually observed as sprays  
191 of hadrons (primarily kaons and pions). These sprays are known as *jets*, which are  
192 what are observed by experiments.

193 It is important to recognize the importance of understanding these QCD inter-  
194 actions in high-energy hadron colliders such as the LHC. Since protons are hadrons,  
195 proton-proton collisions such as those produced by the LHC are primarily governed  
196 by the processes of QCD. In particular, by far the most frequent process observed in  
197 LHC experiments is dijet production from gluon-gluon interactions, as can be seen  
198 (Fig. 2.2). These gluons that interact are part of the *sea* particles inside the proton; the  
199 simple  $p = uud$  model does not apply. The main *valence*  $uud$  quarks are constantly  
200 interacting via gluons, which can themselves radiate gluons or split into quarks, and

## Standard Model Production Cross Section Measurements

Status: August 2016

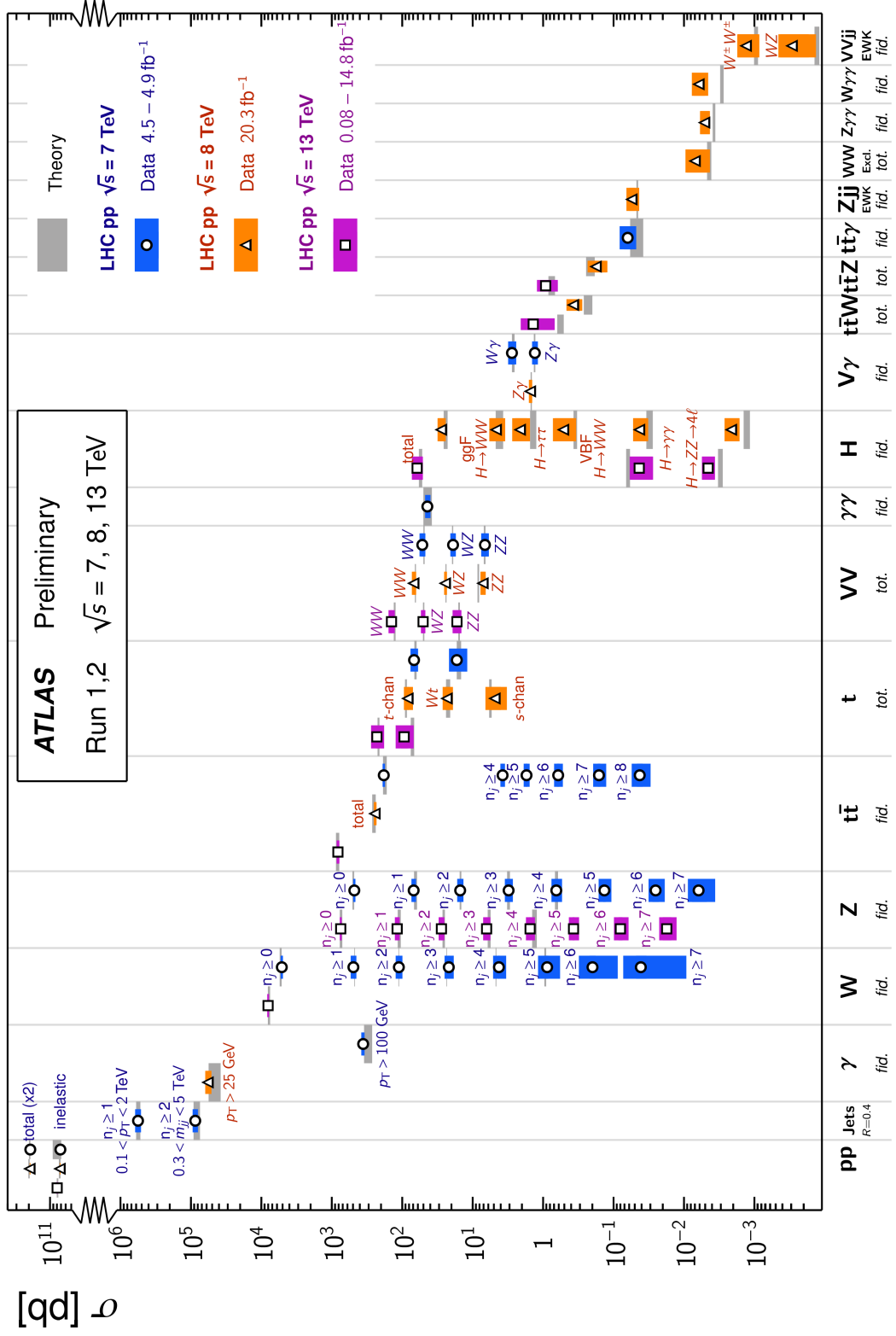


Figure 2.2: Cross-sections of various Standard Model processes

so on. A more useful understanding is given by the colloquially-known *bag* model [53, 54], where the proton is seen as a “bag” of (in principle) infinitely many partons, each with energy  $E < \sqrt{s} = 6.5$  TeV. One then collides this (proton) bag with another, and views the products of this very complicated collision, where calculations include many loops in nonperturbative QCD calculations.

Fortunately, we are generally saved by the QCD factorization theorems [55]. This allows one to understand the hard (i.e. short distance or high energy)  $2 \rightarrow 2$  parton process using the tools of perturbative QCD, while making series of approximations known as a *parton shower* model to understand the additional corrections from nonperturbative QCD. We will discuss the reconstruction of jets by experiments in Ch. 6.

## Fermions

We will now look more closely at the fermions in the Standard Model [56].

As noted earlier in Sec. 2.2, the fermions of the Standard Model can be first distinguished between those that interact via the strong force (quarks) and those which do not (leptons).

There are six leptons in the Standard Model, which can be placed into three *generations*.

$$\begin{pmatrix} e \\ \nu_e \end{pmatrix}, \begin{pmatrix} \mu \\ \nu_\mu \end{pmatrix}, \begin{pmatrix} \tau \\ \nu_\tau \end{pmatrix} \quad (2.14)$$

There is the electron ( $e$ ), muon ( $\mu$ ), and tau ( $\tau$ ), each of which has an associated neutrino ( $\nu_e, \nu_\mu, \nu_\tau$ ). Each of the so-called charged (“electron-like”) leptons has electromagnetic charge  $-1$ , while the neutrinos all have  $q_{EM} = 0$ .

Often in an experimental context, lepton is used to denote the stable electron and metastable muon, due to their striking experimental signatures. Taus are often treated separately, due to their much shorter lifetime of  $\tau_\tau \sim 10^{-13}s$ . These decay

223 through hadrons or the other leptons, so often physics analyses at the LHC treat  
224 them as jets or leptons, as will be done in this thesis.

225 As the neutrinos are electrically neutral, nearly massless, and only interact via the  
226 weak force, it is quite difficult to observe them directly. Since LHC experiments rely  
227 overwhelmingly on electromagnetic interactions to observe particles, the presence of  
228 neutrinos is not observed directly. Neutrinos are instead observed by the conservation  
229 of four-momentum in the plane transverse to the proton-proton collisions, known as  
230 *missing transverse energy*.

There are six quarks in the Standard Model : up, down, charm, strange, top, and bottom. Quarks are similar organized into three generations :

$$\begin{pmatrix} u \\ d \end{pmatrix}, \begin{pmatrix} c \\ s \end{pmatrix}, \begin{pmatrix} t \\ b \end{pmatrix} \quad (2.15)$$

231 where we speak of “up-like” quarks and “down-like” quarks.

232 Each up-like quark has charge  $q_{up} = 2/3$ , while the down-like quarks have  $q_{down} =$   
233  $-1/3$ . At the high energies of the LHC, one often makes the distinction between  
234 the light quarks ( $u, d, c, s$ ), the bottom quark, and top quark. In general, due to  
235 the hadronization process described above, the light quarks, with masses  $m_q < \sim$   
236 1.5 GeV are indistinguishable by LHC experiments. Their hadronic decay products  
237 generally have long lifetimes and they are reconstructed as jets.<sup>1</sup>. The bottom quark  
238 hadronizes primarily through the  $B$ -mesons, which generally travels a short distance  
239 before decaying to other hadrons. This allows one to distinguish decays via  $b$ -quarks  
240 from other jets. This procedure is known as *b-tagging* and will be discussed more in  
241 Ch.Ch. 5.

242 Due to its large mass, the top quark decays before it can hadronize. There are  
243 no bound states associated to the top quark. The top is of particular interest at

---

<sup>1</sup>In some contexts, charm quarks are also treated as a separate category, although it is quite difficult to distinguish charm quarks from the other light quarks at high energy colliders.

## Standard Model Interactions (Forces Mediated by Gauge Bosons)

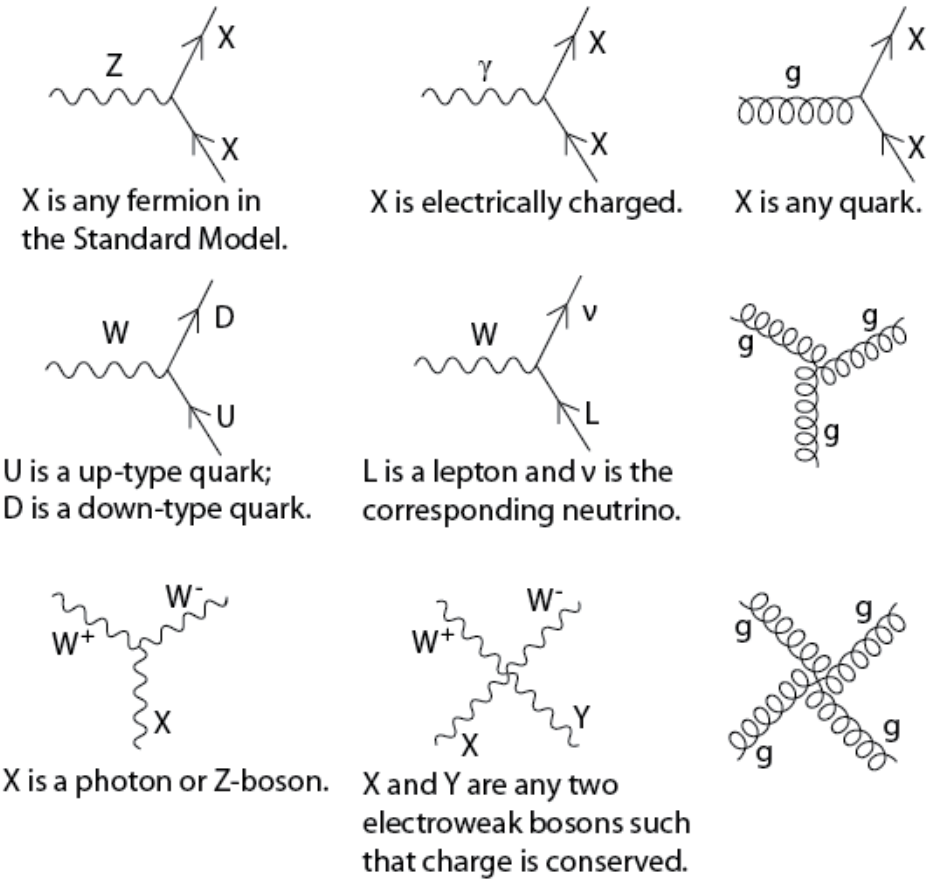


Figure 2.3: The interactions of the Standard Model

- 244 the LHC; it has a striking signature through its most common decay mode  $t \rightarrow Wb$ .  
 245 Decays via tops, especially  $t\bar{t}$  are frequently an important signal decay mode, or an  
 246 important background process.

### 247 **Interactions in the Standard Model**

- 248 We briefly overview the entirety of the fundamental interactions of the Standard  
 249 Model. These can also be found in Fig. 2.3.  
 250 The electromagnetic force, mediated by the photon, interacts with via a three-

251 point coupling all charged particles in the Standard Model. The photon thus interacts  
252 with all the quarks, the charged leptons, and the charged  $W^\pm$  bosons.

253 The weak force is mediated by three particles : the  $W^\pm$  and the  $Z^0$ . The  $Z^0$  can  
254 interacts with all fermions via a three-point coupling. A real  $Z_0$  can thus decay to  
255 a fermion-antifermion pair of all SM fermions except the top quark, due to its large  
256 mass. The  $W^\pm$  has two important three-point interactions with fermions. First, the  
257  $W^\pm$  can interact with an up-like quark and a down-like quark; an important example  
258 in LHC experiments is  $t \rightarrow Wb$  The coupling constants for these interactions are  
259 encoded in the unitary matrix known as the Cabibbo–Kobayashi–Maskawa (CKM)  
260 matrix [57, 58], and are generally known as flavor-changing interactions. Secondly,  
261 the  $W^\pm$  interacts with a charged lepton and its corresponding neutrino. In this case,  
262 the unitary matrix that corresponds to CKM matrix for quarks is the identity matrix,  
263 which forbids (fundamental) vertices such as  $\mu \rightarrow We$ . For leptons, instead this is  
264 a two-step process :  $\mu \rightarrow \nu_m u W \rightarrow \nu_m u \bar{\nu}_e e$ . Finally, there are the self-interactions  
265 of the weak gauge bosons. There is a three-point and four-point interaction. All  
266 combinations are allowed which conserve electric charge.

267 The strong force is mediated by the gluon, which as discussed above also carries  
268 the strong color charge. There is the fundamental three-point interaction, where a  
269 quark radiates a gluon. Additionally, there are the three-point and four-point gluon-  
270 only interactions.

## 271 2.3 Deficiencies of the Standard Model

272 The Standard Model has been enormously successful. This relatively simple theory is  
273 capable of explaining a very wide range of phenomenom, which ultimately break down  
274 to combinations of nine diagrams shown in Fig. 2.3 at tree level. Unfortunately, there  
275 are some unexplained problems with the Standard Model. We cannot go through all

$m_e$	Electron mass	511 keV
$m_\mu$	Muon mass	105.7 MeV
$m_\tau$	Tau mass	1.78 GeV
$m_u$	Up quark mass	1.9 MeV ( $m_{\bar{MS}} = 2\text{GeV}$ )
$m_d$	Down quark mass	4.4 MeV ( $m_{\bar{MS}} = 2\text{GeV}$ )
$m_s$	Strange quark mass	87 MeV ( $m_{\bar{MS}} = 2\text{GeV}$ )
$m_c$	Charm quark mass	1.32 GeV ( $m_{\bar{MS}} = m_c$ )
$m_b$	Bottom quark mass	4.24 GeV ( $m_{\bar{MS}} = m_b$ )
$m_t$	Top quark mass	172.7 GeV (on-shell renormalization)
$\theta_{12}$ CKM	12-mixing angle	13.1°
$\theta_{23}$ CKM	23-mixing angle	2.4°
$\theta_{13}$ CKM	13-mixing angle	0.2°
$\delta$ CKM	CP-violating Phase	0.995
$g'$	U(1) gauge coupling	0.357 ( $m_{\bar{MS}} = m_Z$ )
$g$	SU(2) gauge coupling	0.652 ( $m_{\bar{MS}} = m_Z$ )
$g_s$	SU(3) gauge coupling	1.221 ( $m_{\bar{MS}} = m_Z$ )
$\theta_{QCD}$	QCD vacuum angle	~0
VEV	Higgs vacuum expectation value	246 GeV
$m_H$	Higgs mass	125 GeV

Table 2.1: Parameters of the Standard Model. For values dependent on the renormalization scheme, we use a combination of the on-shell normalization scheme [59–62] and modified minimal subtraction scheme with  $m_{\bar{MS}}$  as indicated in the table [63]

276 of the potential issues in this thesis, but we will motivate the primary issues which  
 277 naturally lead one to *supersymmetry*, as we will see in Ch. 3.

The Standard Model has many free parameters, shown in Tab. 2.1. In general, we prefer models with less free parameters. A great example of this fact, and the primary experimental evidence for EWSB, is the relationship between the couplings of the weak force and the masses of the gauge bosons of the weak force :

$$\rho \equiv \frac{m_W^2}{m_Z^2 \cos^2 \theta_W} \stackrel{?}{=} 1 \quad (2.16)$$

278 where ? indicates that this is a testable prediction of the Standard Model (in  
 279 particular, that the gauge bosons gain mass through EWSB). This relationship has  
 280 been measured within experimental and theoretical predictions. We would like to  
 281 produce additional such relationships, which would exist if the Standard Model is a

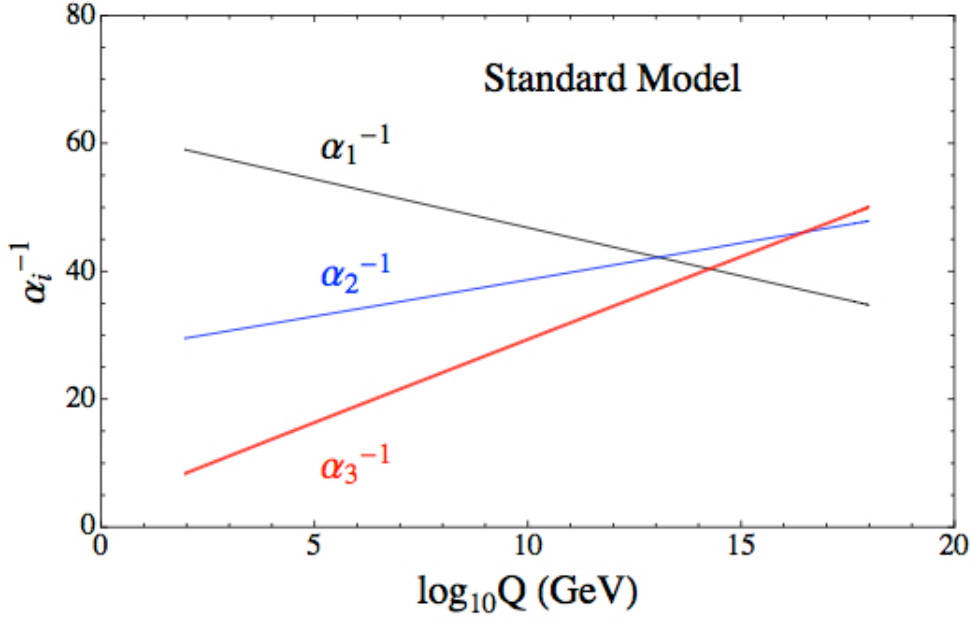


Figure 2.4: The running of Standard Model gauge couplings. The Standard Model couplings do not unify at high energies, which indicates it cannot completely describe nature through the Planck scale.

282 low-energy approximation of some other theory.

283 An additional issue is the lack of *gauge coupling unification*. The couplings of  
 284 any quantum field theory “run” as a function of the distance scales (or inversely,  
 285 energy scales) of the theory. The idea is closely related to the unification of the  
 286 electromagnetic and weak forces at the so-called *electroweak scale* of  $O(100 \text{ GeV})$ .  
 287 One would hope this behavior was repeated between the electroweak forces and the  
 288 strong force at some suitable energy scale. The Standard Model does not exhibit this  
 289 behavior, as we can see in Fig. 2.4.

But, the most significant problem with the Standard Model is the *hierarchy problem*. In its most straightforward incarnation, the Higgs scalar field is subject to quantum corrections through loop diagrams, as shown in Fig. 2.5. For demonstration, we use the contributions from the top quark, since the top quark has the largest Higgs Yukawa coupling due to its large mass. In general, we should expect these corrections to quadratically depend on the scale of the ultraviolet physics,  $\Lambda$ . Briefly assume

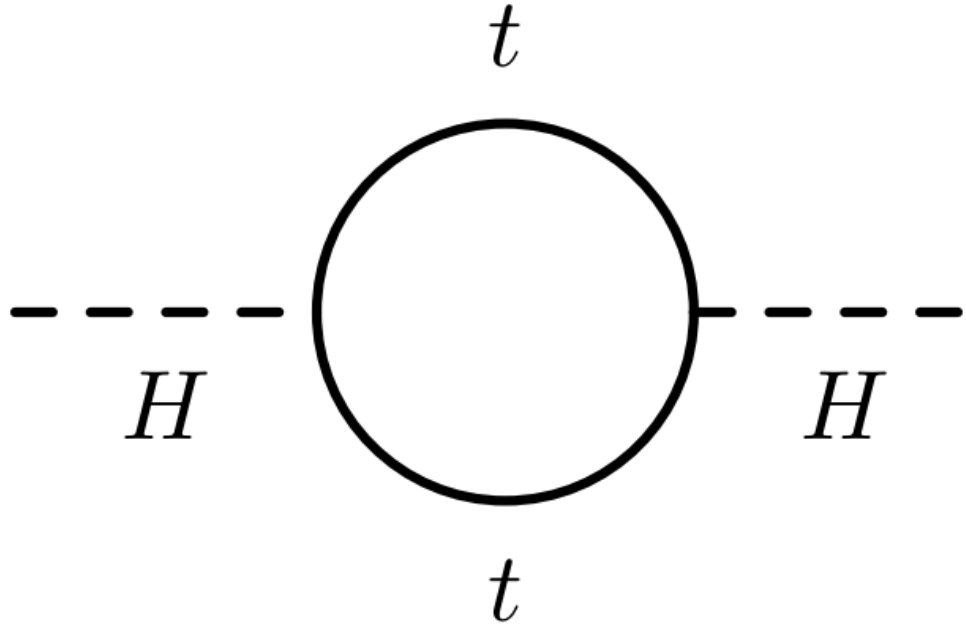


Figure 2.5: The dominant quantum loop correction to the Higgs mass in the Standard Model.

there is no new physics before the Planck scale of gravity,  $\Lambda_{\text{Planck}} = 10^{19}$  GeV. In this case, we expect the corrections to the Higgs mass to be

$$\delta m_H^2 \approx \left( \frac{m_t}{8\pi^2 \langle \phi \rangle_{VEV}} \right)^2 \Lambda_{\text{Planck}}^2. \quad (2.17)$$

290 To achieve the miraculous cancellation required to get the observed Higgs mass of  
 291 125 GeV, one needs to then set the bare Higgs mass  $m_0$ , our input to the Standard  
 292 Model Lagrangian, itself to a *precise* value  $\sim 10^{19}$  GeV. This extraordinary level of  
 293 parameter finetuning is quite undesirable, and within the framework of the Standard  
 294 Model alone, there is little that can be done to alleviate this issue.

295 An additional concern, of a different nature, is the lack of a *dark matter* candidate  
 296 in the Standard Model. Dark matter was discovered by observing galactic rotation  
 297 curves, which showed that much of the matter that interacts gravitationally is invisible  
 298 to our (electromagnetic) telescopes [16–22]. The postulation of the existence of dark  
 299 matter, which interacts at least through gravity, allows one to understand these galactic

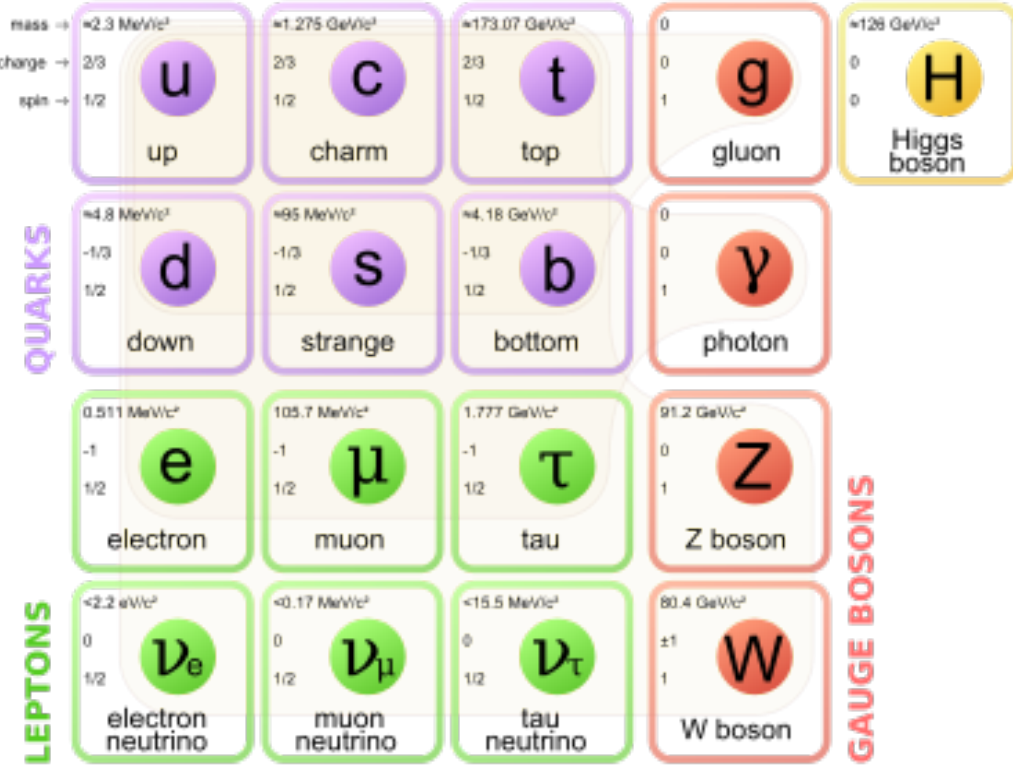


Figure 2.6: Particles of the Standard Model

300 rotation curves. Unfortunately, no particle in the Standard Model could possibly be  
 301 the dark matter particle. The only candidate truly worth another look is the neutrino,  
 302 but it has been shown that the neutrino content of the universe is simply too small  
 303 to explain the galactic rotation curves [22, 64]. The experimental evidence from  
 304 the galactic rotations curves thus show there *must* be additional physics beyond the  
 305 Standard Model, which is yet to be understood.

306 In the next chapter, we will see how these problems can be alleviated by the theory  
 307 of supersymmetry.



*Supersymmetry*

310 This chapter will introduce supersymmetry (SUSY) [15, 23–35]. We will begin  
 311 by introducing the concept of a *superspace*, and discuss some general ingredients of  
 312 supersymmetric theories. This will include a discussion of how the problems with the  
 313 Standard Model described in Ch. 2 are naturally fixed by these theories.

314 The next step is to discuss the particle content of the *Minimally Supersymmetric*  
 315 *Standard Model* (MSSM). As its name implies, this theory contains the minimal  
 316 additional particle content to make Standard Model supersymmetric. We then discuss  
 317 the important phenomenological consequences of this theory, especially as it would  
 318 be observed in experiments at the LHC.

319 **3.1 Supersymmetric theories : from space to  
 320 superspace**

321 **Coleman-Mandula “no-go” theorem**

322 We begin the theoretical motivation for supersymmetry by citing the “no-go” theorem  
 323 of Coleman and Mandula [65]. This theorem forbids *spin-charge unification*. It  
 324 states that all quantum field theories which contain nontrivial interactions must be  
 325 a direct product of the Poincaré group of Lorentz symmetries, the internal product  
 326 of gauge symmetries, and the discrete symmetries of parity, charge conjugation,  
 327 and time reversal. The assumptions which go into building the Coleman-Mandula

theorem are quite restrictive, but there is solution, which has become known as *supersymmetry* [26, 66]. In particular, we must introduce a *spinorial* group generator  $Q$ . Alternatively, and equivalently, this can be viewed as the addition of anti-commuting coordinates. Space plus these new anti-commuting coordinates is then called *superspace* [67]. We will not investigate this view in detail, but it is also a quite intuitive and beautiful way to construct supersymmetry [15].

### 334 Supersymmetry transformations

A *supersymmetric* transformation  $Q$  transforms a bosonic state into a fermionic state, and vice versa :

$$Q |\text{Fermion}\rangle = |\text{Boson}\rangle \quad (3.1)$$

$$Q |\text{Boson}\rangle = |\text{Fermion}\rangle \quad (3.2)$$

To ensure this relation holds,  $Q$  must be an anticommuting spinor. Additionally, since spinors are inherently complex,  $Q^\dagger$  must also be a generator of the supersymmetry transformation. Since  $Q$  and  $Q^\dagger$  are spinor objects (with  $s = 1/2$ ), we can see that supersymmetry must be a spacetime symmetry. The Haag-Lopuszanski-Sohnius extension [66] of the Coleman-Mandula theorem [65] is quite restrictive about the forms of such a symmetry. Here, we simply write the (anti-) commutation relations [15] :

$$Q_\alpha, Q_{\dot{\alpha}}^\dagger = -2\sigma_{\alpha\dot{\alpha}\mu} P_\mu \quad (3.3)$$

$$Q_\alpha, Q_{\dot{\beta}} = Q_{\dot{\alpha}}^\dagger, Q_{\dot{\beta}}^\dagger = 0 \quad (3.4)$$

$$[P^\mu, Q_\alpha] = [P^\mu, Q_{\dot{\alpha}}^\dagger] = 0 \quad (3.5)$$

### 335 Supermultiplets

In a supersymmetric theory, we organize single-particle states into irreducible representations of the supersymmetric algebra which are known as *supermultiplets*.

338 Each supermultiplet contains a fermion state  $|F\rangle$  and a boson state  $|B\rangle$ . These two  
339 states are known as *superpartners*. These are related by some combination of  
340  $Q$  and  $Q^\dagger$ , up to a spacetime transformation.  $Q$  and  $Q^\dagger$  commute with the mass-  
341 squared operator  $-P^2$  and the operators corresponding to the gauge transformations  
342 [15]: in particular, the gauge interactions of the Standard Model. In an unbroken  
343 supersymmetric theory, this means the states  $|F\rangle$  and  $|B\rangle$  have exactly the same mass,  
344 electromagnetic charge, electroweak isospin, and color charges. One can also prove  
345 [15] that each supermultiplet contains the exact same number of bosonic ( $n_B$ ) and  
346 fermion ( $n_F$ ) degrees of freedom. We now explore the possible types of supermultiples  
347 one can find in a renormalizable supersymmetric theory.

348 Since each supermultiplet must contain a fermion state, the simplest type of  
349 supermultiplet contains a single Weyl fermion state ( $n_F = 2$ ) which is paired with  
350  $n_B = 2$  scalar bosonic degrees of freedom. This is most conveniently constructed  
351 as single complex scalar field. We call this construction a *scalar supermultiplet* or  
352 *chiral supermultiplet*. The second name is indicative, as only chiral supermultiplets  
353 can contain fermions whose right-handed and left-handed components transform  
354 differently under the gauge interactions (as of course happens in the Standard Model).

355 The second type of supermultiplet we construct is known as a *gauge supermul-*  
356 *tiplet*. We take a spin-1 gauge boson (which must be massless due to the gauge  
357 symmetry, so  $n_B = 2$ ) and pair this with a single massless Weyl spinor<sup>1</sup>. The gauge  
358 bosons transform as the adjoint representation of their respective gauge groups  
359 Their fermionic partners, which are known as gauginos, must also. In particular,  
360 the left-handed and right-handed components of the gaugino fermions have the same  
361 gauge transformation properties.

362 Excluding gravity, this is the entire list of supermultiplets which can participate  
363 in renormalizable interactions in what is known as  $N = 1$  supersymmetry. This

---

<sup>1</sup>Choosing an  $s = 3/2$  massless fermion leads to nonrenormalizable interactions.

means there is only one copy of the supersymmetry generators  $Q$  and  $Q^\dagger$ . This is essentially the only “easy” phenomenological choice, since it is the only option in four dimensions which allows for the chiral fermions and parity violations to be built into the Standard Model. We will not look further into  $N > 1$  supersymmetry in this thesis.

The primary goal, after understanding the possible structures of the multiplets above, is to fit the Standard Model particles into a multiplet, and therefore make predictions about their supersymmetric partners. We explore this in the next section.

## 3.2 Minimally Supersymmetric Standard Model

To construct what is known as the MSSM [15, 68–71], we need a few ingredients and assumptions. First, we match the Standard Model particles with their corresponding superpartners of the MSSM. We will also introduce the naming of the superpartners (also known as *sparticles*). We discuss a very common additional restraint imposed on the MSSM, known as  $R$ –parity. We also discuss the concept of soft supersymmetry breaking and how it manifests itself in the MSSM.

### Chiral supermultiplets

The first thing we deduce is directly from Sec. 3.1. The bosonic superpartners associated to the quarks and leptons *must* be spin 0, since the quarks and leptons must be arranged in a chiral supermultiplet. This is essential, since the chiral supermultiplet is the only one which can distinguish between the left-handed and right-handed components of the Standard Model particles. The superpartners of the quarks and leptons are known as *squarks* and *sleptons*, or *sfermions* in aggregate. (for “scalar quarks”, “scalar leptons”, and “scalar fermion”). The “s-” prefix can also be added to the individual quarks i.e. *selectron*, *sneutrino*, and *stop*. The notation

388 is to add a  $\sim$  over the corresponding Standard Model particle i.e.  $\tilde{e}$ , the selectron is  
 389 the superpartner of the electron. The two-component Weyl spinors of the Standard  
 390 Model must each have their own (complex scalar) partner i.e.  $e_L, e_R$  have two distinct  
 391 partners :  $\tilde{e}_L, \tilde{e}_R$ . As noted above, the gauge interactions of any of the sfermions are  
 392 identical to those of their Standard Model partners.

Due to the scalar nature of the Higgs, it must obviously lie in a chiral supermultiplet. To avoid gauge anomalies and ensure the correct Yukawa couplings to the quarks and leptons [15], we must add additional Higgs bosons to any supersymmetric theory. In the MSSM, we have two chiral supermultiplets. The SM (SUSY) parts of the multiplets are denoted  $H_u(\tilde{H}_u)$  and  $H_d(\tilde{H}_d)$ . Writing out  $H_u$  and  $H_d$  explicitly:

$$H_u = \begin{pmatrix} H_u^+ \\ H_u^0 \end{pmatrix} \quad (3.6)$$

$$H_d = \begin{pmatrix} H_d^0 \\ H_d^- \end{pmatrix} \quad (3.7)$$

393 we see that  $H_u$  looks very similar to the SM Higgs with  $Y = 1$ , and  $H_d$  is symmetric  
 394 with  $+ \rightarrow -$  and  $Y = -1$ . The SM Higgs boson,  $h_0$ , is a linear superposition of the  
 395 neutral components of these two doublets. The SUSY parts of the Higgs multiplets,  
 396  $\tilde{H}_u$  and  $\tilde{H}_d$ , are each left-handed Weyl spinors. For generic spin-1/2 sparticles, we  
 397 add the “-ino” suffix. We then call the partners of the two Higgs collectively the  
 398 *Higgsinos*.

### 399 Gauge supermultiplets

400 The superpartners of the gauge bosons must all be in gauge supermultiplets since  
 401 they contain a spin-1 particle. Collectively, we refer to the superpartners of the  
 402 gauge bosons as the gauginos.

403 The first gauge supermultiplet contains the gluon, and its superpartner, which is  
 404 known as the *gluino*, denoted  $\tilde{g}$ . The gluon is of course the SM mediator of  $SU(3)_C$

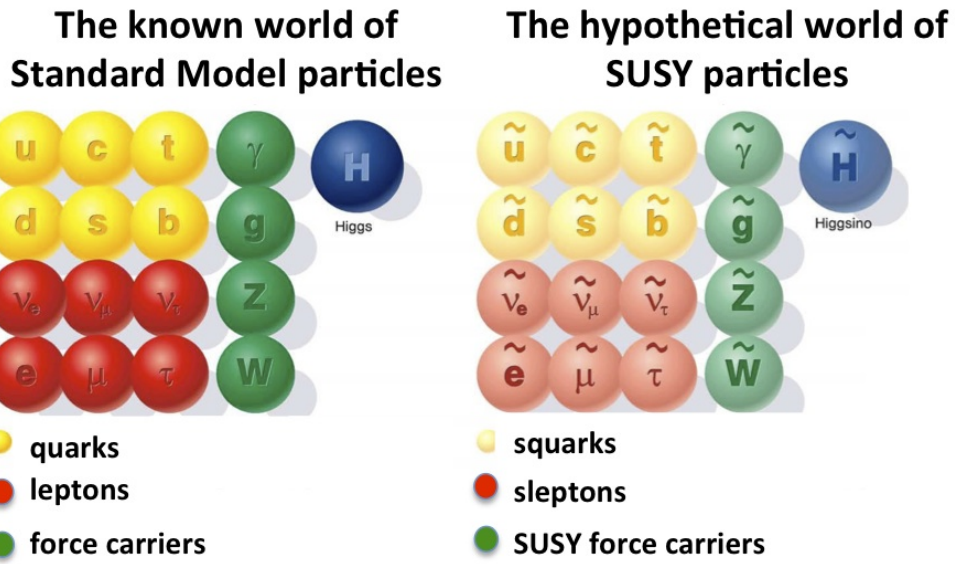


Figure 3.1: Particles of the MSSM

405 The gluino is also a colored particle, subject to  $SU(3)_C$ . From the SM before EWSB,  
 406 we have the four gauge bosons of the electroweak symmetry group  $SU(2)_L \otimes U(1)_Y$  :  
 407  $W^{1,2,3}$  and  $B^0$ . The superpartners of these particles are thus the *winos*  $\tilde{W}^{1,2,3}$  and  
 408 *bino*  $\tilde{B}^0$ , where each is placed in another gauge supermultiplet with its corresponding  
 409 SM particle. After EWSB, without breaking supersymmetry, we would also have the  
 410 zino  $\tilde{Z}^0$  and photino  $\tilde{\gamma}$ .

411 The entire particle content of the MSSM can be seen in Fig. 3.1.

412 At this point, it's important to take a step back. Where are these particles?  
 413 As stated above, supersymmetric theories require that the masses and all quantum  
 414 numbers of the SM particle and its corresponding sparticle are the same. Of course,  
 415 we have not observed a selectron, squark, or wino. The answer, as it often is, is that  
 416 supersymmetry is *broken* by the vacuum state of nature [15].



Figure 3.2: This Feynmann diagram shows how proton decay is induced in the MSSM, if one does not impose  $R$ -parity.

### 417 **$R$ -parity**

This section is a quick aside to the general story.  $R$  – parity refers to an additional discrete symmetry which is often imposed on supersymmetric models. For a given particle state, we define

$$418 \quad R = (-1)^{3(B-L)+2s} \quad (3.8)$$

418 where  $B, L$  is the baryon (lepton) number and  $s$  is the spin. The imposition of  
 419 this symmetry forbids certain terms from the MSSM Lagrangian that would violate  
 420 baryon and/or lepton number. This is required in order to prevent proton decay, as  
 421 shown in Fig. 3.2<sup>2</sup>. .

422 In supersymmetric models, this is a  $\mathbb{Z}_2$  symmetry, where SM particles have  $R = 1$   
 423 and sparticles have  $R = -1$ . We will take  $R$  – parity as part of the definition of  
 424 the MSSM. We will discuss later the *drastic* consequences of this symmetry on SUSY  
 425 phenomenology

### 426 **Soft supersymmetry breaking**

The fundamental idea of *soft* supersymmetry breaking [15, 34, 35, 72, 73] is that we would like to break supersymmetry without reintroducing the quadratic divergences

---

<sup>2</sup>Proton decay can actually be prevented by allowing only one of the four potential R-parity violating terms to survive.

we discussed at the end of Chapter Ch. 2. We write the Lagrangian in a form :

$$\mathcal{L}_{\text{MSSM}} = \mathcal{L}_{\text{SUSY}} + \mathcal{L}_{\text{soft}} \quad (3.9)$$

427 In this sense, the symmetry breaking is “soft”, since we have separated out the  
 428 completely symmetric terms from those soft terms which will not allow the quadratic  
 429 divergences to the Higgs mass.

430 The explicitly allowed terms in the soft-breaking Lagrangian are [35]:

431 • Mass terms for the scalar components of the chiral supermultipletss

432 • Mass terms for the Weyl spinor components of the gauge supermultipletss

433 • Trilinear couplings of scalar components of chiral supermultiplets

In particular, using the field content described above for the MSSM, the softly-broken portion of the MSSM Lagrangian can be written

$$\mathcal{L}_{\text{soft}} = -\frac{1}{2} \left( M_3 \tilde{g} \tilde{g} + M_2 \tilde{W} \tilde{W} + M_1 \tilde{B} \tilde{B} + c.c. \right) \quad (3.10)$$

$$- \left( \tilde{u} a_u \tilde{Q} H_u - \tilde{d} a_d \tilde{Q} H_d - \tilde{e} a_e \tilde{L} H_d + c.c. \right) \quad (3.11)$$

$$- \tilde{Q}^\dagger m_Q^2 \tilde{Q} - \tilde{L}^\dagger m_L^2 \tilde{L} - \tilde{u} m_u^2 \tilde{u}^\dagger - \tilde{d} m_d^2 \tilde{d}^\dagger - \tilde{e} m_e^2 \tilde{e}^\dagger \quad (3.12)$$

$$- m_{H_u}^2 H_u^* H_u - m_{H_d}^2 H_d^* H_d - (b H_u H_d + cc). \quad (3.13)$$

434 where we have introduced the following notations :

435 1.  $M_3, M_2, M_1$  are the gluino, wino, and bino masses.

436 2.  $a_u, a_d, a_e$  are complex  $3 \times 3$  matrices in family space.

437 3.  $m_Q^2, m_u^2, m_d^2, m_L^2, m_e^2$  are hermitian  $3 \times 3$  matrices in family space.

438 4.  $m_{H_u}^2, m_{H_d}^2, b$  are the SUSY-breaking contributions to the Higgs potential.

439 We have written matrix terms without any sort of additional notational decoration  
 440 to indicate their matrix nature, and we now show why. The first term Item 1 is the  
 441 set of mass terms for the gluino, wino, and bino. The second term Item 2, containing  
 442  $a_u, a_d, a_e$ , has strong constraints from experiments [74, 75]. We will assume that  
 443 each  $a_i, i = u, d, e$  is proportional to the Yukawa coupling matrix :  $a_i = A_{i0}y_i$ . The  
 444 third term Item 3 can be similarly constrained by experiments [68, 75–82]. We will  
 445 assume the elements of the fourth term Item 4 contributing to the Higgs potential as  
 446 well as all of the Item 1 terms must be real, which limits the possible CP-violating  
 447 interactions to those of the Standard Model. We thus only consider flavor-blind,  
 448 CP-conserving interactions within the MSSM.

The important mixing for mass and gauge interaction eigenstates in the MSSM occurs within electroweak sector, in a process akin to EWSB in the Standard Model. The neutral portions of the Higgsinos doublets and the neutral gauginos ( $\tilde{H}_u^0, \tilde{H}_d^0, \tilde{B}^0, \tilde{W}^0$ ) of the gauge interaction basis mix to form what are known as the *neutralinos* of mass basis :

$$M_{\tilde{\chi}} = \begin{pmatrix} M_1 & 0 & -c_\beta s_W m_Z & s_\beta s_W m_Z \\ 0 & M_2 & c_\beta c_W m_Z & -s_\beta c_W m_Z \\ -c_\beta s_W m_Z & c_\beta c_W m_Z & 0 & -\mu \\ s_\beta s_W m_Z & -s_\beta c_W m_Z & -\mu & 0 \end{pmatrix} \quad (3.14)$$

449 where  $s(c)$  are the sine and cosine of angles related to EWSB, which introduced  
 450 masses to the gauginos and higgsinos. Diagonalization of this matrix gives the four  
 451 neutralino mass states, listed without loss of generality in order of increasing mass :  
 452  $\tilde{\chi}_{1,2,3,4}^0$ .

453 The neutralinos, especially the lightest neutralino  $\tilde{\chi}_1^0$ , are important ingredients  
 454 in SUSY phenomenology.

455 The same process can be done for the electrically charged gauginos with  
 456 the charged portions of the Higgsino doublets along with the charged winos

457  $(\tilde{H}_u^+, \tilde{H}_d^+, \tilde{W}^+, \tilde{W}^-)$ . This leads to the *charginos*, again in order of increasing mass :  
458  $\tilde{\chi}_{1,2}^\pm$ .

459 

### 3.3 Phenomenology

460 We are finally at the point where we can discuss the phenomenology of the MSSM,  
461 in particular as it manifests itself at the energy scales of the LHC.

462 As noted above in Sec. 3.2, the assumption of  $R$ -parity has important conse-  
463 quences for MSSM phenomenology. The SM particles have  $R = 1$ , while the sparticles  
464 all have  $R = -1$ . Simply, this is the “charge” of supersymmetry. Since the particles  
465 of LHC collisions ( $pp$ ) have total incoming  $R = 1$ , we must expect that all sparticles  
466 will be produced in *pairs*. An additional consequence of this symmetry is the fact  
467 that the lightest supersymmetric particle (LSP) is *stable*. Off each branch of the  
468 Feynmann diagram shown in Fig. 3.3, we have  $R = -1$ , and this can only decay to  
469 another sparticle and a SM particle. Once we reach the lightest sparticle in the decay,  
470 it is absolutely stable. This leads to the common signature  $E_T^{\text{miss}}$  for a generic SUSY  
471 signal.

472 For this thesis, we will be presenting an inclusive search for squarks and gluinos  
473 with zero leptons in the final state. This is a very interesting decay channel, due to  
474 the high cross-sections of  $\tilde{g}\tilde{g}$  and  $\tilde{q}\tilde{q}$  decays, as can be seen in Sec. 3.3 [83].

475 This is a direct consequence of the fact that these are the colored particles of the  
476 MSSM. Since the sparticles interact with the gauge groups of the SM in the same way  
477 as their SM partners, the colored sparticles, the squarks and gluinos, are produced  
478 and decay as governed by the color group  $SU(3)_C$  with the strong coupling  $g_S$ . Gluino  
479 pair production is particularly copious, due to color factor corresponding to the color  
480 octet of  $SU(3)_C$ .

481 In the case of squark pair production, the most common decay mode of the squark

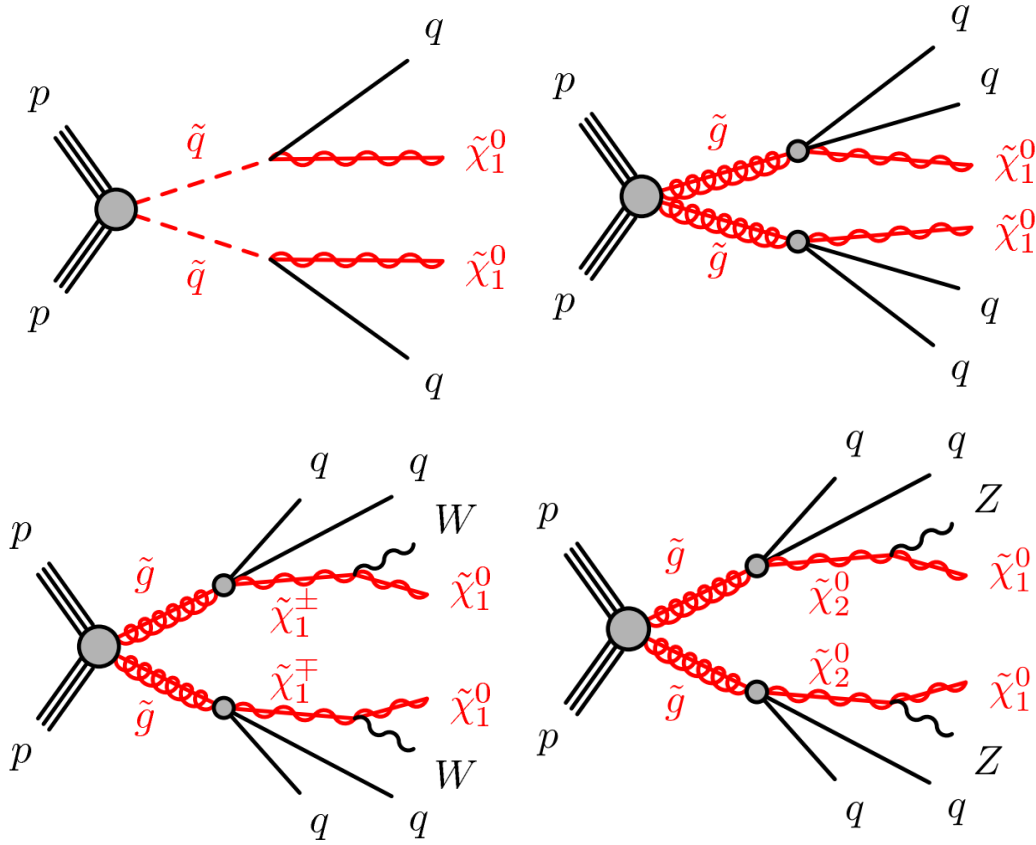


Figure 3.3: SUSY signals considered in this thesis

in the MSSM is a decay directly to the LSP plus a single SM quark [15]. This means the basic search strategy for squark pair production is two jets from the final state quarks, plus missing transverse energy from the LSPs.

For gluino pair production, the most common decay is  $\tilde{g} \rightarrow g\tilde{q}$ , due to the large  $g_S$  coupling. The squark then decays as listed above. In this case, we generically search for four jets and missing transverse energy from the LSPs.

In the context of experimental searches for SUSY, we often consider *simplified models*. These models make certain assumptions which allow easy comparisons of results by theorists and experimentalists. In the context of this thesis, the simplified models will make assumptions about the branching ratios described in the preceding paragraphs. In particular, we will often choose a model where the decay of interest occurs with 100% branching ratio. This is entirely for ease of interpretation, but it is

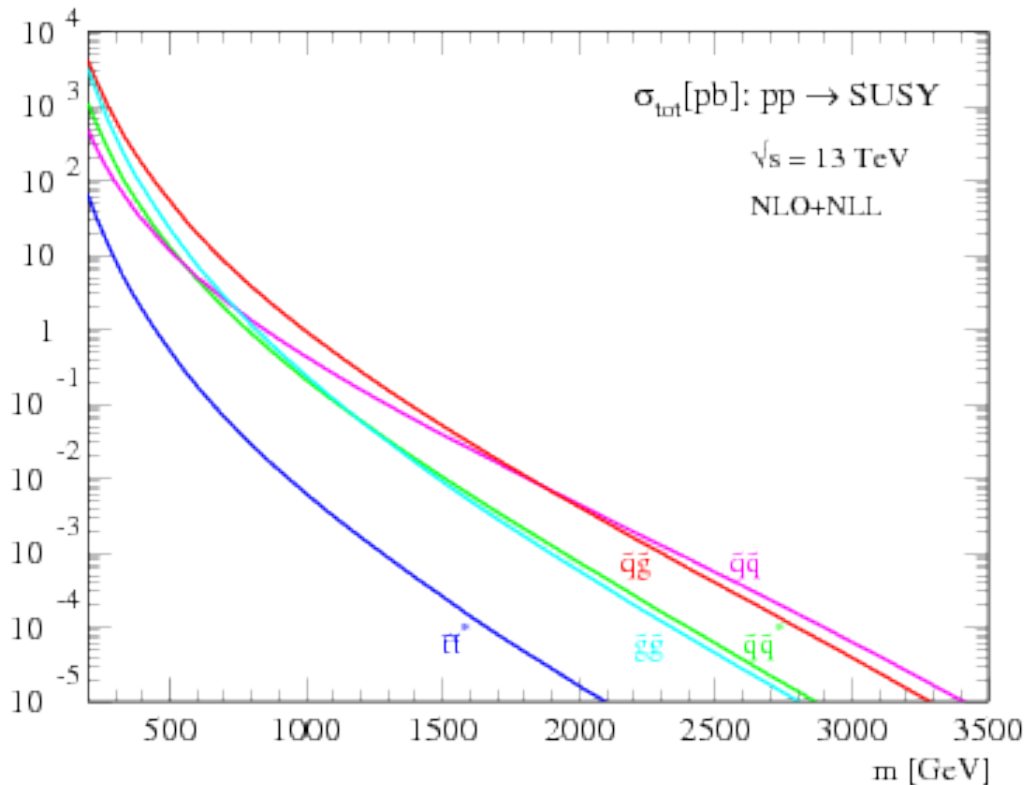


Figure 3.4: SUSY production cross-sections as a function of sparticle mass at  $\sqrt{s} = 13$  TeV.

494 important to recognize that these are more a useful comparison tool, especially with  
 495 for setting limits, than a strict statement about the potential masses of sought-after  
 496 beyond the Standard Model particle.

## 497 3.4 How SUSY solves the problems with the SM

498 We now return to the issues with the Standard Model as described in Ch. 2 to see  
 499 how these issues are solved by supersymmetry.

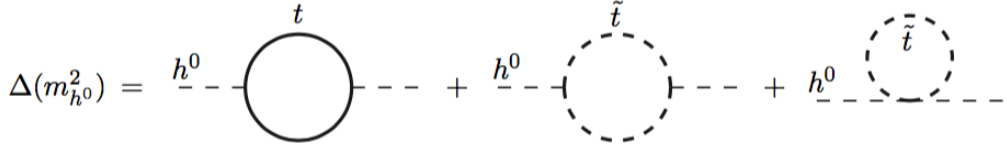


Figure 3.5: Loop diagrams correct the Higgs mass in the MSSM

## 500 Quadratic divergences to the Higgs mass

The quadratic divergences induced by the loop corrections to the Higgs mass, for example from the top Yukawa coupling, goes as

$$\delta m_H^2 \approx \left( \frac{m_t}{8\pi^2 \langle \phi \rangle_{VEV}} \right)^2 \Lambda_{Planck}^2. \quad (3.15)$$

501 The miraculous thing about SUSY is each of these terms *automatically* comes with  
 502 a term which exactly cancels this contribution [15]. The fermions and bosons  
 503 have opposite signs in this loop diagram to all orders in perturbation theory, which  
 504 completely solves the hierarchy problem. This is the strongest motived reason for  
 505 supersymmetry.

## 506 Gauge coupling unification

507 An additional motivation for supersymmetry is seen by the gauge coupling unification  
 508 high scales. In the Standard Model, as we saw the gauge couplings fail to unify at  
 509 high energies. In the MSSM and many other forms of supersymmetry, the gauge  
 510 couplings unify at high energy, as can be seen in Fig. 3.6. This provides additional  
 511 aesthetic motivation for supersymmetric theories.

## 512 Dark matter

513 As we discussed previously, the lack of any dark matter candidate in the Standard  
 514 Model naturally leads to beyond the Standard Model theories. In the Standard Model,  
 515 there is a natural dark matter candidate in the lightest supersymmetric particle [15]

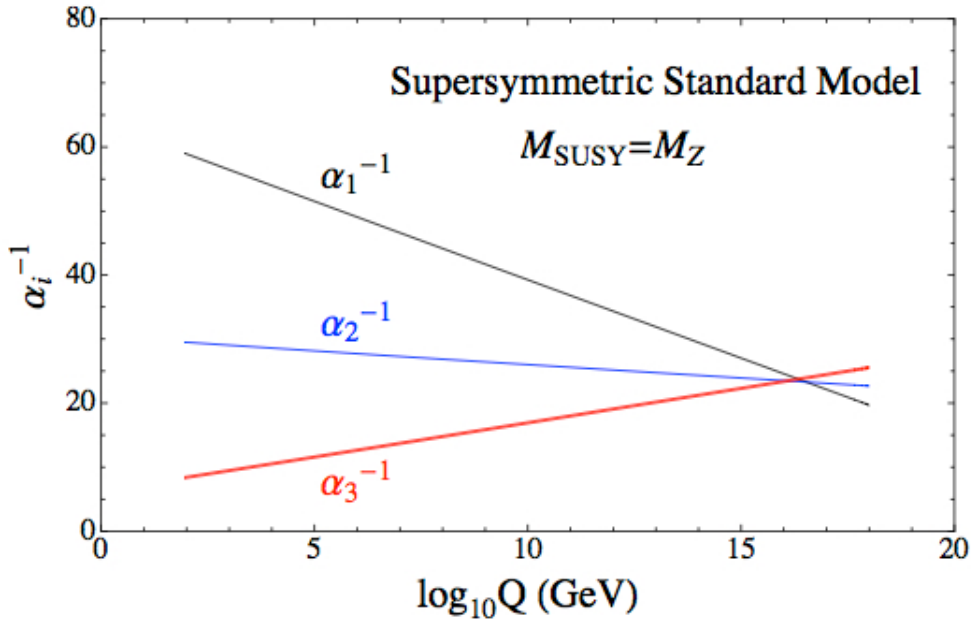


Figure 3.6: The running of Standard Model gauge couplings: compare to Fig. 2.4. The MSSM gauge couplings nearly intersect at high energies.

516 The LSP would in dark matter experiments be called a *weakly-interacting massive*  
 517 *particle* (WIMP), which is a type of cold dark matter [22, 84]. These WIMPS would  
 518 only interact through the weak force and gravity, which is exactly as a model like  
 519 the MSSM predicts for the neutralino. In Fig. 3.7, we can see the current WIMP  
 520 exclusions for a given mass. The range of allowed masses which have not been  
 521 excluded for LSPs and WIMPs have significant overlap. This provides additional  
 522 motivation outside of the context of theoretical details.

### 523 3.5 Conclusions

524 Supersymmetry is the most well-motivated theory for physics beyond the Standard  
 525 Model. It provides a solution to the hierarchy problem, leads to gauge coupling  
 526 unification, and provides a dark matter candidate consistent with galactic rotation  
 527 curves. As noted in this chapter, due to the LSPs in the final state, most SUSY



Figure 3.7: WIMP exclusions from direct dark matter detection experiments.

528 searches require a significant amount of missing transverse energy in combination  
 529 with jets of high transverse momentum. However, there is some opportunity to do  
 530 better than this, especially in final states where one has two weakly-interacting LSPs  
 531 on opposite sides of some potentially complicated decay tree. We will see how this is  
 532 done in Ch. 7.



*The Large Hadron Collider*

535 The Large Hadron Collider (LHC) produces high-energy protons which collide at the  
 536 center of multiple large experiments at CERN on the outskirts of Geneva, Switzerland  
 537 [85]. The LHC produces the highest energy collisions in the world, with a design  
 538 center-of-mass energy of  $\sqrt{s} = 14$  TeV, which allows the experiments to investigate  
 539 physics at higher energies than previous colliders. This chapter will summarize the  
 540 basics of accelerator physics, especially with regards to discovering physics beyond  
 541 the Standard Model. We will describe the CERN accelerator complex and the LHC.

542 **4.1 Basics of Accelerator Physics**

543 This section follows closely the presentation of [86].

Simple particle accelerators simply rely on the acceleration of charged particles in a static electric field. Given a field of strength  $E$ , charge  $q$ , and mass  $m$ , this is simply

$$a = \frac{qE}{m}. \quad (4.1)$$

544 For a given particle with a given mass and charge, this is limited by the static electric  
 545 field which can be produced, which in turn is limited by electrical breakdown at high  
 546 voltages.

547 There are two complementary solutions to this issue. First, we use the *radio*  
 548 *frequency acceleration* technique. We call the devices used for this *RF cavities*. The  
 549 cavities produce a time-varied electric field, which oscillate such that the charged

550 particles passing through it are accelerated towards the design energy of the RF  
 551 cavity. This oscillation forces the particles into *bunches*, since particles which are  
 552 slightly off the central energy induced by the RF cavity are accelerated towards the  
 553 design energy.

Second, one bends the particles in a magnetic field, which allows them to pass through the same RF cavity over and over. This second process is often limited by *synchrotron radiation*, which describes the radiation produced when a charged particle is accelerated. The power radiated is

$$P \sim \frac{1}{r^2} \left( E/m \right)^4 \quad (4.2)$$

554 where  $r$  is the radius of curvature and  $E, m$  is the energy (mass) of the charged  
 555 particle. Given an energy which can be produced by a given set of RF cavities (which  
 556 is *not* limited by the mass of the particle), one then has two options to increase the  
 557 actual collision energy : increase the radius of curvature or use a heavier particle.  
 558 Practically speaking, the easiest options for particles in a collider are protons and  
 559 electrons, since they are copiously produced in nature and do not decay<sup>1</sup>. Given the  
 560 dependence on mass, we can see why protons are used to reach the highest energies.  
 561 The tradeoff for this is that protons are not point particles, and we thus we don't  
 562 know the exact incoming four-vectors of the protons. This is a reflection of the “bag  
 563 model” discussed in Ch. 2, where each proton is actually a bag of incoming quarks  
 564 and gluons, which individually contribute to the total proton energy.

The particle *beam* refers to the bunches combined. An important property of a beam of a particular energy  $E$ , moving in uniform magnetic field  $B$ , containing particles of momentum  $p$  is the *beam rigidity* :

$$R \equiv rB = p/c. \quad (4.3)$$

---

<sup>1</sup>Muon colliders are a potential future option at high energies, since the relativistic  $\gamma$  factor gives them a relatively long lifetime in the lab frame.

565 The linear relation between  $r$  and  $p$ , or alternatively  $B$  and  $p$  have important  
 566 consequences for LHC physics. For hadron colliders, this is the limiting factor on  
 567 going to higher energy scales; one needs a proportionally larger magnetic field to  
 568 keep the beam accelerating in a circle.

569 Besides the rigidity of the beam, the most important quantities to characterize  
 570 a beam are known as the (normalized) *emittance*  $\epsilon_N$  and the *betatron function*  $\beta$ .  
 571 These quantities determine the transverse size  $\sigma$  of a relativistic beam  $v \leq c$  beam :  
 572  $\sigma^2 = \beta^* \epsilon_N / \gamma_{\text{rel}}$ , where  $\beta^*$  is the value of the betatron function at the collision point  
 573 and  $\gamma_{\text{rel}}$  is the Lorentz factor.

These quantities determine the *instantaneous luminosity*  $L$  of a collider, which combined with the cross-section  $\sigma$  of a particular physics process, give the rate of the physics process :

$$R = L\sigma. \quad (4.4)$$

The instantaneous luminosity  $L$  is given by :

$$L = \frac{f_{\text{rev}} N_b^2 F}{4\pi\sigma^2} = \frac{f_{\text{rev}} n N_b^2 \gamma_{\text{rel}} F}{4\pi\beta^* \epsilon_N}. \quad (4.5)$$

574 Here we have introduced the frequency of revolutions  $f_{\text{rev}}$ , the number of bunches  $n$ ,  
 575 the number of protons per bunch  $N_b^2$ , and a geometric factor  $F$  related to the crossing  
 576 angle of the beams.

The *integrated luminosity*  $\int L dt$  gives the total number of a particular physics process  $P$ , with cross-section  $\sigma_P$ .

$$N_P = \sigma_P \int L dt. \quad (4.6)$$

577 Due to this simple relation, one can also quantify the “amount of data delivered” by  
 578 a collider simply by  $\int L dt$ .



Figure 4.1: The CERN accelerator complex. Copyright CERN.

## 4.2 Accelerator Complex

The Large Hadron Collider is the last accelerator in a chain of accelerators which together form the CERN accelerator complex, shown in Fig. 4.1. The protons begin their journey to annihilation in a hydrogen source, where they are subsequently ionized. The first acceleration occurs in the Linac 2, a linear accelerator composed of RF cavities. The protons leave the Linac 2 at an energy of 50 MeV and enter the Proton Synchrotron Booster (PSB). The PSB contains four superimposed rings, which accelerate the protons to 1.4 GeV. The protons are then injected into the Proton Synchrotron (PS). This synchrotron increases the energy up to 25 GeV. After leaving the PS, the protons enter the Super Proton Synchrotron (SPS). This is the last step before entering the LHC ring, and the protons are accelerated to 450 GeV. From the SPS, the protons are injected into the beam pipes of the LHC. The process

591 to fill the LHC rings with proton bunches from start to finish typically takes about  
592 four minutes.

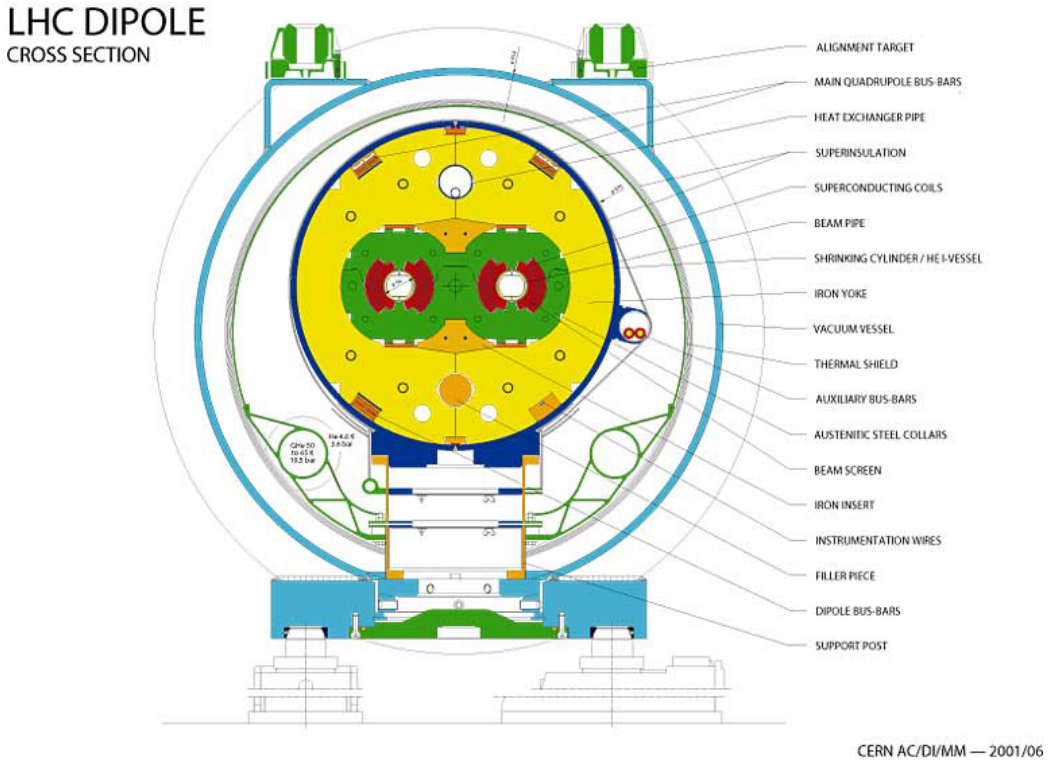
593 **4.3 Large Hadron Collider**

The Large Hadron Collider is the final step in the CERN accelerator complex, and produces the collisions analyzed in this thesis. From the point of view of experimentalists on the general-purpose ATLAS and CMS experiments, the main goal of the LHC is to deliver collisions at the highest possible energy, with the highest possible instantaneous luminosity. The LHC was installed in the existing 27 km tunnel used by the Large Electron Positron (LEP) collider [87]. This allowed the existing accelerator complex at CERN, described in the previous section, to be used as the injection system to prepare the protons up to 450 GeV. Many aspects of the LHC design were decided by this very constraint, and specified the options allowed to increase the energy or luminosity. In particular, the radius of the tunnel was already specified. From Eq.Eq. (4.3), this implies the momentum (or energy) of the beam is entirely determined by the magnetic field. Given the 27 km circumference of the LEP tunnel, one can calculate the required magnetic field to reach the 7 TeV per proton design energy of the LHC :

$$r = C/2\pi = 4.3 \text{ km} \quad (4.7)$$

$$\rightarrow B = \frac{p}{rc} = 5 \text{ T} \quad (4.8)$$

594 In fact, the LHC consists of eight 528 m straight portions consisting of RF cavities,  
595 used to accelerate the particles, and 8 circular portions which bend the protons  
596 around the LHC ring. These circular portions actually have a slightly smaller radius  
597 of curvature  $r = 2804$  m, and require  $B = 8.33$  T. To produce this large field,  
598 superconducting magnets are used.



CERN AC/DI/MM — 2001/06

Figure 4.2: Schematic of an LHC dipole magnet. Copyright CERN.

## 599    Magnets

600 There are many magnets used by the LHC machine, but the most important are  
 601 the 1232 dipole magnets. A schematic is shown in Fig. Fig. 4.2 and a photograph is  
 602 present in Fig. 4.3.

603       The magnets are made of Niobium and Titanium. The maximum field strength is  
 604 10 T when cooled to 1.9 Kelvin. The magnets are cooled by superfluid helium, which  
 605 is supplied by a large cryogenic system. Due to heating between the eight helium  
 606 refrigerators and the beampipe, the helium is cooled in the refrigerators to 1.8 K.

607       A failure in the cooling system can cause what is known as a *quench*. If the  
 608 temperature goes above the critical superconducting temperature, the metal loses its  
 609 superconducting properties, which leads to a large resistance in the metal. This leads  
 610 to rapid temperature increases, and can cause extensive damages if not controlled.

611       The dipole magnets are 16.5 meters long with a diameter of 0.57 meters. There

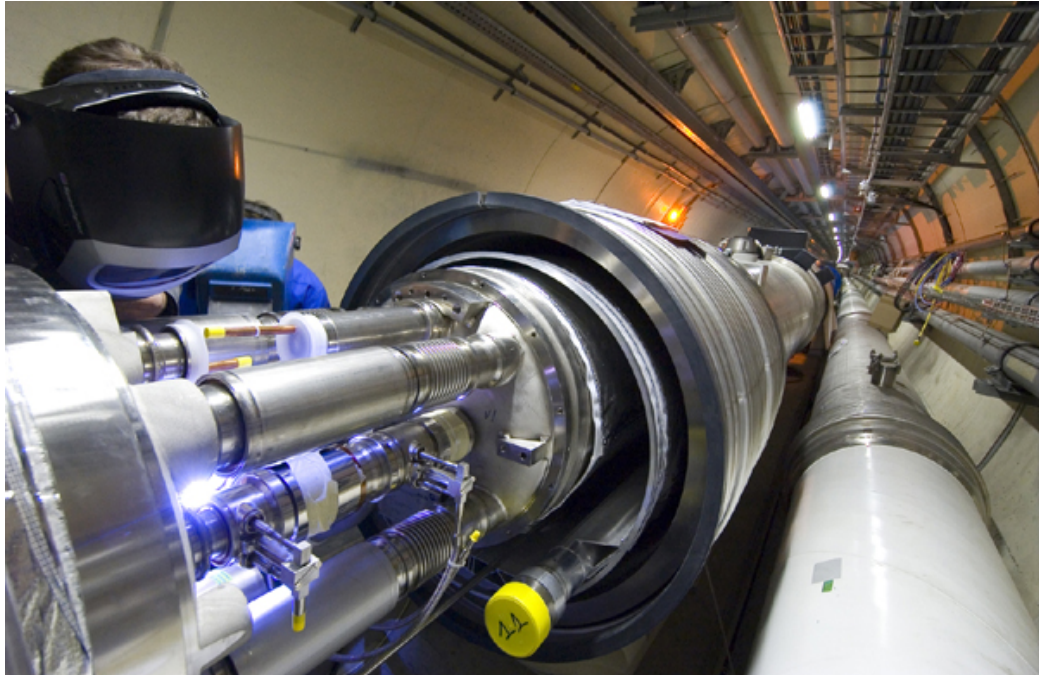


Figure 4.3: Photograph of a technician connecting an LHC dipole magnet. Copyright CERN.

612 are two individual beam pipes inside each magnet, which allows the dipoles to house  
613 the beams travelling in both directions around the LHC ring. They curve slightly,  
614 at an angle of 5.1 mrad, which carefully matches the curvature of the ring. The  
615 beampipes inside of the magnets are held in high vacuum to avoid stray interactions  
616 with the beam.

## 617 4.4 Dataset Delivered by the LHC

618 In this thesis, we analyze the data delivered by the LHC to ATLAS in the 2015 and  
619 2016 datasets. The beam parameters relevant to this dataset are available in Tab. 4.1.  
620

621 The peak instantaneous luminosity delivered in 2015 (2016) was  $L =$   
622  $5.2(11) \text{ cm}^{-2}\text{s}^{-1} \times 10^{33}$ . One can note that the instantaneous luminosity delivered in  
623 the 2016 dataset exceeds the design luminosity of the LHC. The total integrated

Parameter	Injection	Extraction
Energy (GeV)	450	7000
Rigidity (T-m)	3.8	23353
Bunch spacing (ns)	25	25
Design Luminosity ( $\text{cm}^{-2}\text{s}^{-1} \times 10^3$ )	-	1.0
Bunches per proton beam	2808	2808
Protons per bunch	1.15 e11	1.15 e11
Beam lifetime (hr)	-	10
Normalized Emittance $\epsilon_N$ (mm $\mu\text{rad}$ )	3.3	3.75
Betatron function at collision point $\beta^*$ (cm)	-	55

Table 4.1: Beam parameters of the Large Hadron Collider.

624 luminosity delivered was  $13.3 \text{ fb}^{-1}$ . In Fig. 4.4, we display the integrated luminosity  
 625 per day for 2015 and 2016.

## 626 Pileup

627 *Pileup* is the term for the additional proton-proton interactions which occur during  
 628 each bunch crossing of the LHC. At the beginning of the LHC physics program, there  
 629 had not been a collider which averaged more than a single interaction per bunch  
 630 crossing. In the LHC, each bunch crossing (or *event*) generally contains multiple  
 631 proton-proton interactions. An simulated event with many *vertices* can be seen in  
 632 Fig. 4.5. The so-called *primary vertex* (or *hard scatter vertex*) refers to the vertex  
 633 which has the highest  $\Sigma p_T^2$  The summation occurs over the *tracks* in the detector,  
 634 which we will describe later [ATL-INDET-PUB-2009-001]. We then distinguish  
 635 between *in-time* pileup and *out-of-time* pileup. In-time pileup refers to the additional  
 636 proton-proton interactions which occur in the event. Out-of-time pileup refers to  
 637 effects related to proton-proton interactions previous bunch crossings.

638 We quantify in-time pileup by the number of “primary”<sup>2</sup> vertices in a particular  
 639 event. To quantify the out-of-time pileup, we use the average number of interactions

---

<sup>2</sup>The primary vertex is as defined above, but we unfortunately use the same name here.

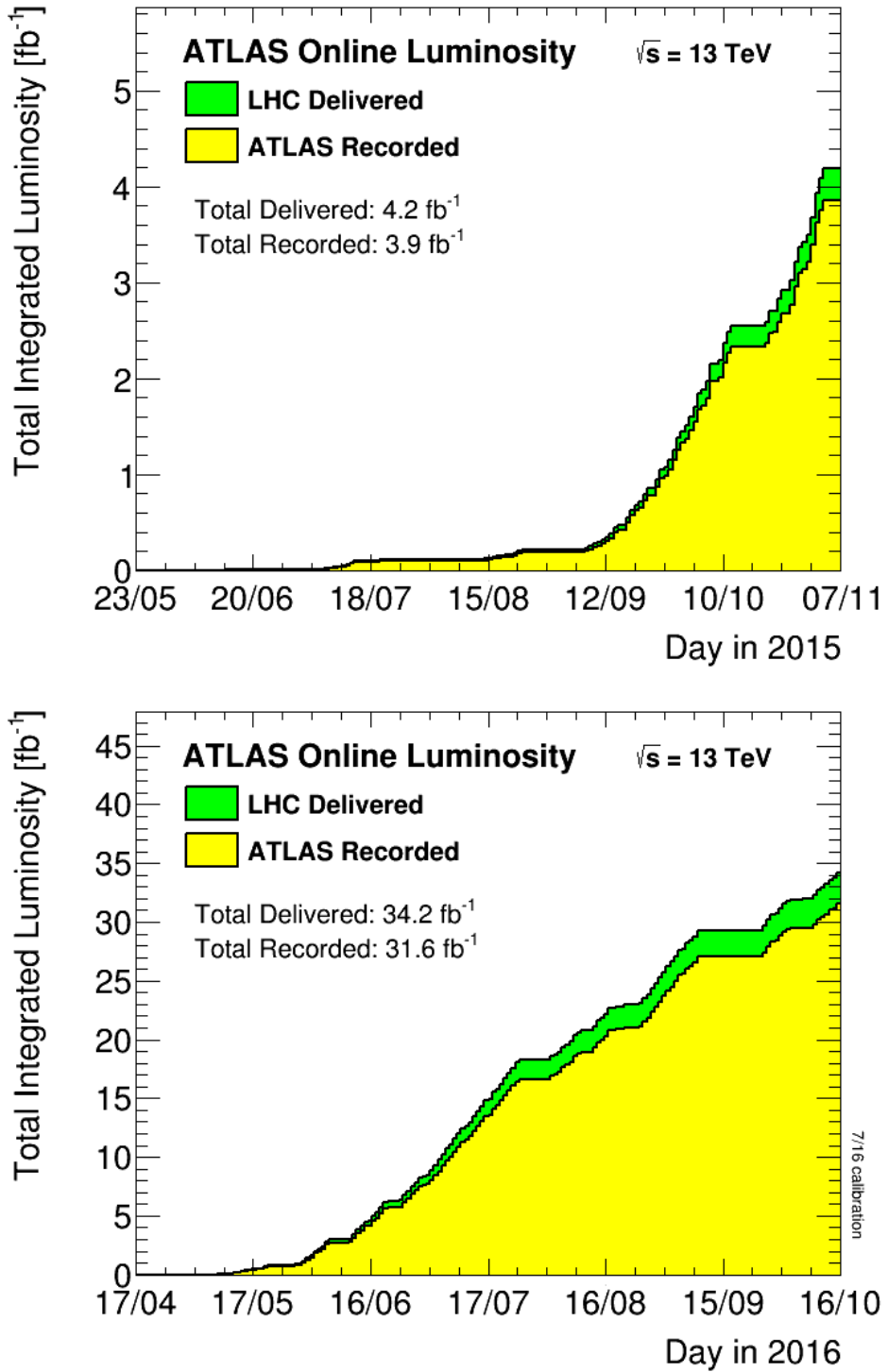


Figure 4.4: Integrated Luminosity delivered by the LHC and collected by ATLAS in the 2015 and 2016 datasets.

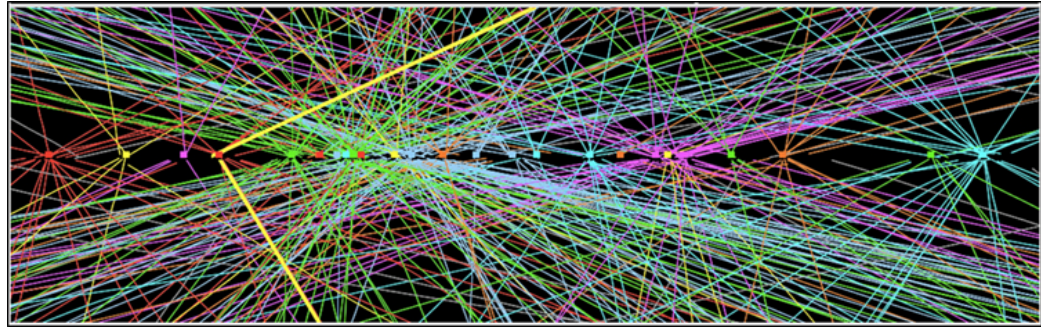


Figure 4.5: Simulated event with many pileup vertices.

640 per bunch crossing  $\langle \mu \rangle$ . In Fig. 4.6, we show the distribution of  $\mu$  for the dataset  
641 used in this thesis.



Figure 4.6: Mean number of interactions per bunch crossing in the 2015 and 2016 datasets.



*The ATLAS detector*

644 The dataset analyzed in this thesis was taken by the ATLAS detector [88], which  
 645 is located at the “Point 1” cavern of the LHC, just across the street from the main  
 646 CERN campus. The much-maligned acronym stands for *A Toroidal LHC ApparatuS*.  
 647 ATLAS is a massive cylindrical detector, with a radius of 12.5 m and a length of  
 648 44 m, with nearly hermitic coverage around the collision point. Each of the many  
 649 subdetectors plays a role in measuring the energy, momentum, and type of the particles  
 650 produced in collisions delivered by the LHC. These subdetectors are immersed in  
 651 a hybrid solenoid-toroid magnet system which allows for precise measurements of  
 652 particle momenta. The central solenoid magnet contains a magnetic field of 2 T. A  
 653 schematic of the detector is shown in Fig. 5.1.

654 The *inner detector* (ID) lies closest to the collision point, and contains three  
 655 separate subdetectors. It provides pseudorapidity<sup>1</sup> coverage of  $|\eta| < 2.5$  for charged  
 656 particles. The tracks reconstructed from the inner detector hits are used to  
 657 reconstruct the primary vertices and to determine the momemta of charged particles.  
 658 The ATLAS *calorimeter* consists of two subdetectors, known as the *electromagnetic*  
 659 and *hadronic* calorimeters. These detectors stop particles and measure their energy

---

<sup>1</sup>ATLAS uses a right-handed Cartesian coordinate system. The origin is defined by the nominal beam interaction point. The positive- $z$  direction is defined by the incoming beam travelling counterclockwise around the LHC. The positive- $x$  direction points towards the center of the LHC ring from the origin, and the positive- $y$  direction points upwards towards the sky. For particles of transverse (in the  $x - y$  plane) momentum  $p_T = \sqrt{p_x^2 + p_y^2}$  and energy  $E$ , it is generally most convenient fully describe this particle’s kinematics as measured by the detector in the  $(p_T, \phi, \eta, E)$  basis. The angle  $\phi = \arctan(p_y/p_x)$  is the standard azimuthal angle, and  $\eta = \ln \tan(\theta/2)$  is known as the pseudorapidity, and defined based on the standard polar angle  $\theta = \arccos(p_z/p_T)$ . For locations of detector elements, both  $(r, \phi, \eta)$  and  $(z, \phi, \eta)$  can be useful.



Figure 5.1: The ATLAS detector. Copyright CERN.

660 deposition. The calorimeters provide coverage out to pseudorapidity of  $|\eta| < 4.9$ . The  
 661 muon spectrometer is aptly named, as it measures muons, which are the only particles  
 662 which generally reach the outer portions of the detector. In this region, we have the  
 663 large tracking systems of the muon spectrometer, which provide precise measurements  
 664 of muon momenta. The muon spectrometer has pseudorapidity coverage of  $|\eta| < 2.7$ .

## 665 5.1 Magnets

666 ATLAS contains multiple magnetic systems. Primarily, we are concerned with the  
 667 solenoid, used by the inner detector, and the toroids located outside of the ATLAS  
 668 calorimeter. A schematic is shown in Fig. 5.2. These magnetic fields are used to bend  
 669 charged particles, which subsequently allows one to measure their momentum.

670 The ATLAS central solenoid is a 2.3 m diameter, 5.3 m long solenoid at the center  
 671 of the ATLAS detector. It produces a uniform magnetic field of 2 T. An important  
 672 design constraint for the central solenoid was the decision to place it in between

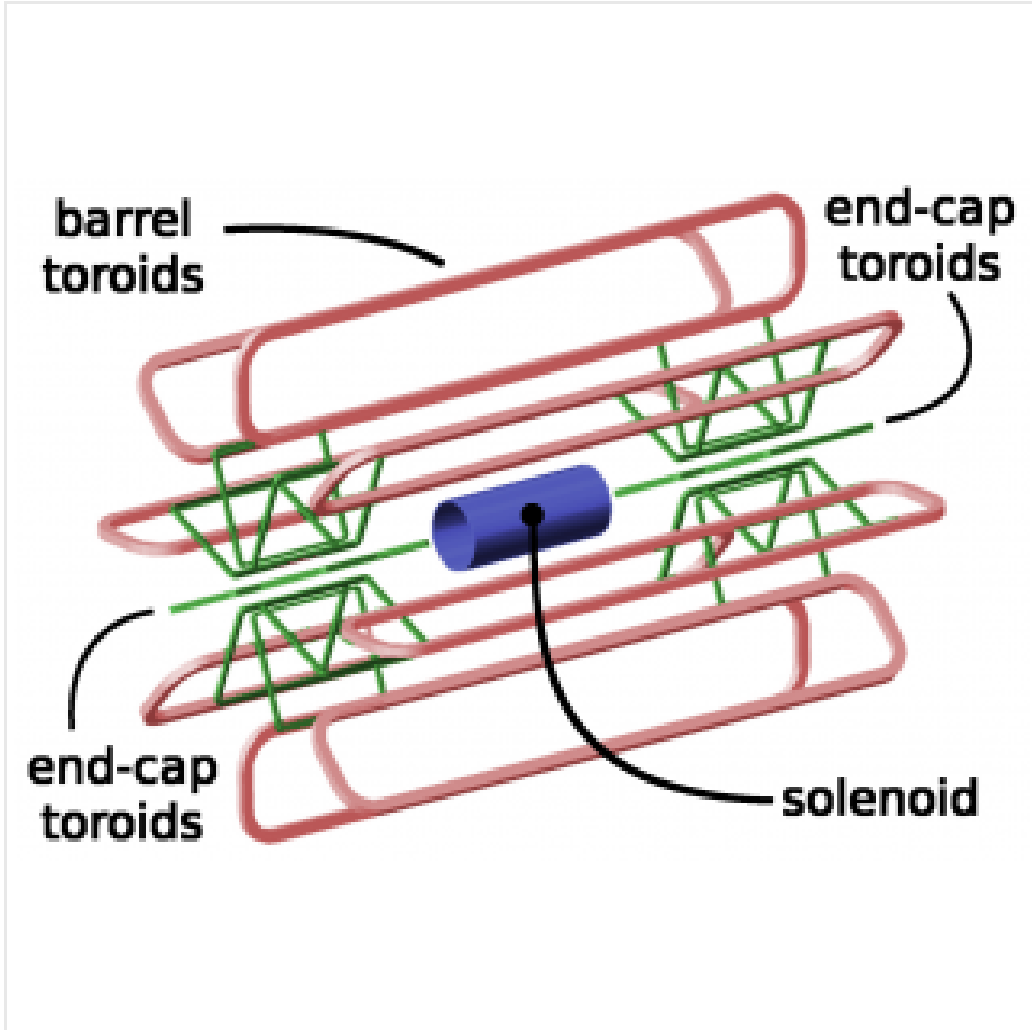


Figure 5.2: The ATLAS magnet system. Copyright CERN.

673 the inner detector and the calorimeters. To avoid excessive energy deposition which  
674 could affect calorimeter measurements, the central solenoid must be as transparent  
675 as possible<sup>2</sup>.

676 The toroid system consists of eight air-core superconducting barrel loops, which  
677 give ATLAS its distinctive shape. There are also two endcap air-core magnets. These  
678 produce a magnetic field in a region of approximately 26 m in length and 10 m of  
679 radius. The magnetic field in this region is non-uniform.

---

<sup>2</sup>This is also one of the biggest functional differences between ATLAS and CMS In CMS, the solenoid is outside of the calorimeters.



Figure 5.3: The ATLAS inner detector. Copyright CERN.

## 680 5.2 Inner Detector

681 The ATLAS inner detector consists of three separate tracking detectors, which are  
 682 known as, in order of increasing distance from the interaction point, the Pixel  
 683 Detector, Semiconductor Tracker (SCT), and the Transition Radiation Tracker  
 684 (TRT). When charged particles pass through these tracking layers, they produce  
 685 *hits*, which using the known 2 T magnetic field, allows the reconstruction of *tracks*.  
 686 Tracks are used as inputs for reconstruction of many higher-level physics objects,  
 687 such as electrons, muons, photons, and  $E_T^{\text{miss}}$ . Accurate track reconstruction is thus  
 688 crucial for precise measurements of charged particles.

### 689 Pixel Detector

690 The ATLAS pixel detector consists four layers of silicon “pixels” [89]. This refers  
 691 to the segmentation of the active medium into pixels, which provide precise 3D hit  
 692 locations. The layers are known as the “Insertable” B-Layer (IBL), the B-Layer (or

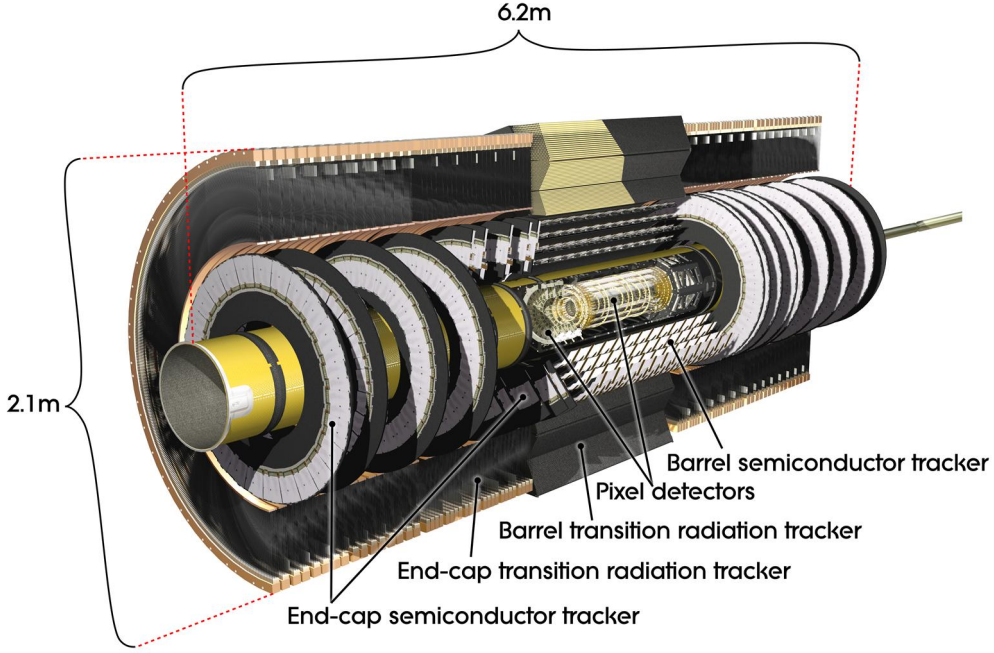


Figure 5.4: The ATLAS pixel detector. Copyright CERN.

693 Layer-0), Layer-1, and Layer-2, in order of increasing distance from the interaction  
 694 point. These layers are close to the interaction point, and therefore experience  
 695 significant radiation exposure.

696 Layer-1, Layer-2, and Layer-3 were installed with the initial construction of  
 697 ATLAS. They contain front-end integrated electronics (FEI3s) bump-bonded to 1744  
 698 silicon modules. Each module is  $250 \mu\text{m}$  in thickness and contains 47232 pixels.  
 699 These pixels have planar sizes of  $50 \times 400 \mu\text{m}^2$  or  $50 \times 600 \mu\text{m}^2$ , to provide highly  
 700 accurate location information. The FEI3s are mounted on long rectangular structures  
 701 known as staves, which encircle the beam pipe. A small tilt to each stave allows full  
 702 coverage in  $\phi$ . These layers are at radii of 50.5 mm, 88.5 mm, and 122.5 mm from  
 703 the interaction point.

704 The IBL was added to ATLAS after Run1 in 2012 at a radius of 33 mm from the  
 705 interaction point [90]. The IBL was required to preserve the integrity of the pixel  
 706 detector as radiation damage leads to inoperative pixels in the other layers. The IBL

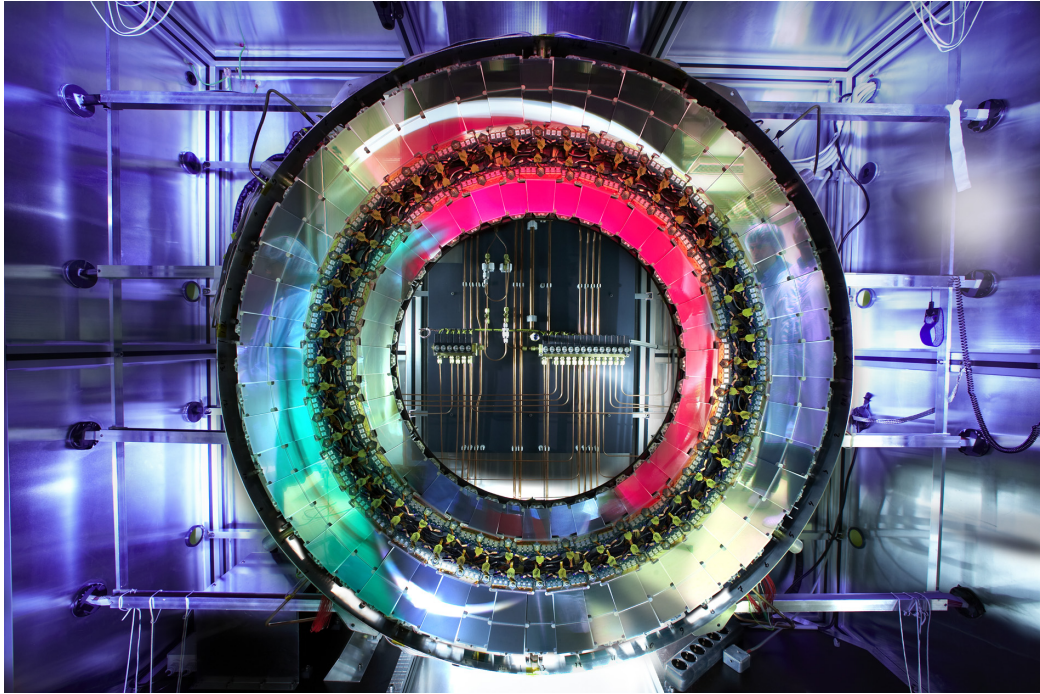


Figure 5.5: A ring of the Semiconductor Tracker. Copyright CERN.

707 consists of 448 FEI4 chips, arranged onto 14 staves. Each FEI4 has 26880 pixels, of  
708 planar size  $50 \times 250 \mu\text{m}$ . This smaller granularity was required due to the smaller  
709 distance to the interaction point.

710 In total, a charged particle passing through the inner detector would expect to  
711 leave four hits in the pixel detector.

## 712 Semiconductor Tracker

713 The SCT is a silicon strip detector directly beyond Layer-2 of the pixel detector [91].  
714 The dual-sensors of the SCT contain  $2 \times 768$  individual strips. Each strip has area  
715  $6.4 \text{ cm}^2$ . The SCT dual-sensor is double-layered, at a relative angle of 40 mrad.  
716 Together, these layers provide the necessary 3D information for track reconstruction.  
717 There are four of these double-layers, at radii of 284 mm, 355 mm, 427 mm, and 498  
718 mm. These double-layers provide hits comparable to those of the pixel detector. The  
719 SCT provides an four additional hits to reconstruct tracks for each charged particle.

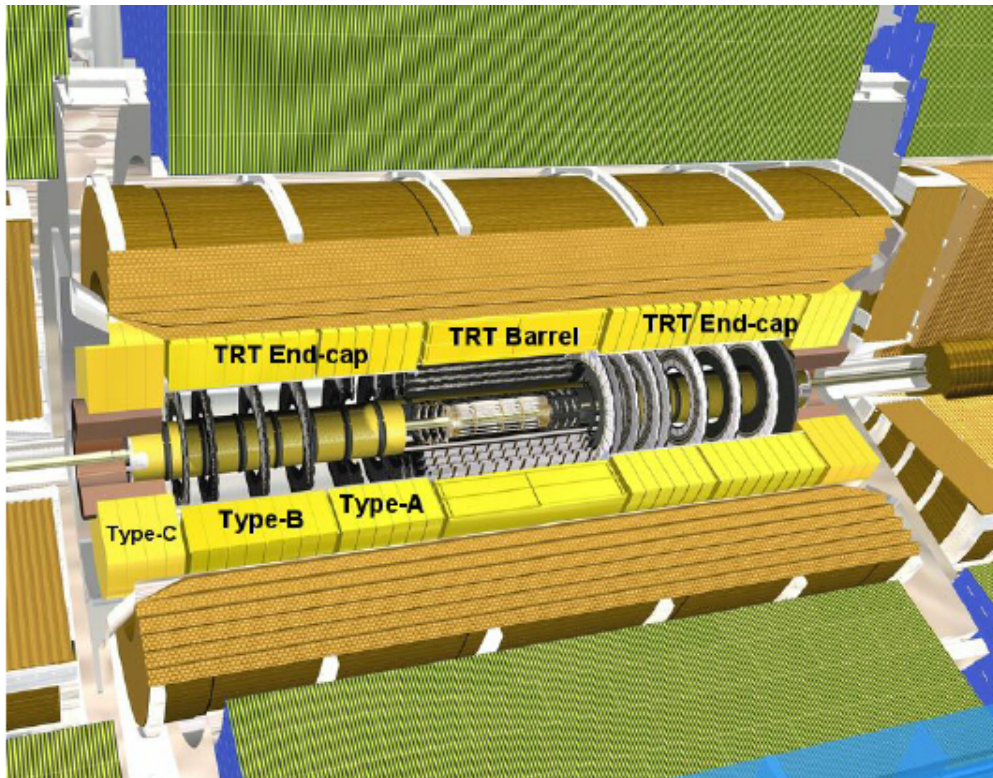


Figure 5.6: A schematic of the Transition Radiation Tracker. Copyright CERN.

## 720 Transition Radiation Tracker

721 The Transition Radiation Tracker is the next detector radially outward from the SCT.  
722 It contains straw drift tubes. Each tube contains a tungsten gold-plated wire of  $32 \mu\text{m}$   
723 diameter held under high voltage (-1530 V) with the edge of the Kapton-aluminum  
724 tube. They are filled with a gas mixture of primarily xenon that is ionized when  
725 a charged particle passes through the tube. The ions are collected by the “drift”  
726 due to the voltage inside the tubes, which is read out by the electronics. Due to  
727 the dielectric difference between the gas and tubes, transition radiation is induced.  
728 This is important for distinguishing electrons from their predominant background of  
729 minimum ionizing particles. Generally, electrons have a much larger Lorentz factor  
730 than minimum ionizing particles, which leads to additional transition radiation. This  
731 is used to discriminate electrons from background in electron reconstruction.

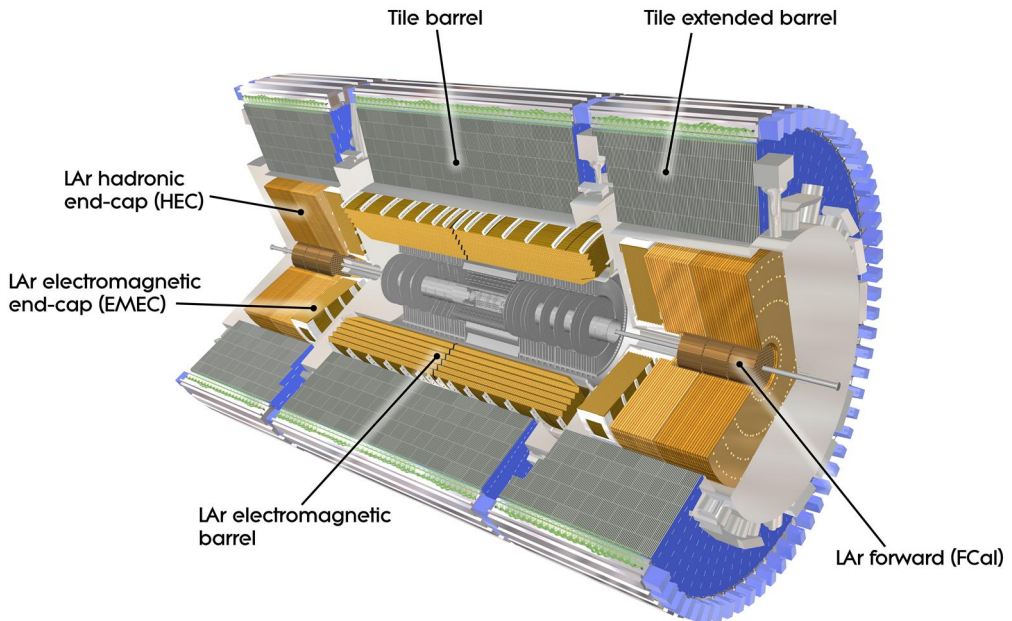


Figure 5.7: The ATLAS calorimeter. Copyright CERN.

### <sup>732</sup> 5.3 Calorimetry

<sup>733</sup> The calorimetry of the ATLAS detector also includes multiple subdetectors which  
<sup>734</sup> allow precise measurements of the electrons, photons, and hadrons produced in  
<sup>735</sup> collisions delivered by the LHC. Calorimeters work by stopping particles in their  
<sup>736</sup> material and measuring the energy deposition. This energy is deposited as a  
<sup>737</sup> cascade of particles induce from interactions with the detector material known as  
<sup>738</sup> *showers*. ATLAS uses *sampling* calorimeters, alternating a dense absorbing material  
<sup>739</sup> to induce showers with an active layer to measure energy depositions by the induced  
<sup>740</sup> showers. Since some energy is deposited into the absorption layers as well, the energy  
<sup>741</sup> depositions must be properly calibrated for the detector.

<sup>742</sup> Electromagnetic objects (electrons and photons) and hadrons have different  
<sup>743</sup> interaction properties. We use different types of calorimeters to accurately measure  
<sup>744</sup> these classes of objects, which we call *electromagnetic* and *hadronic* calorimeters.  
<sup>745</sup> ATLAS contains multiple separate calorimeters : the liquid argon (LAr) electro-

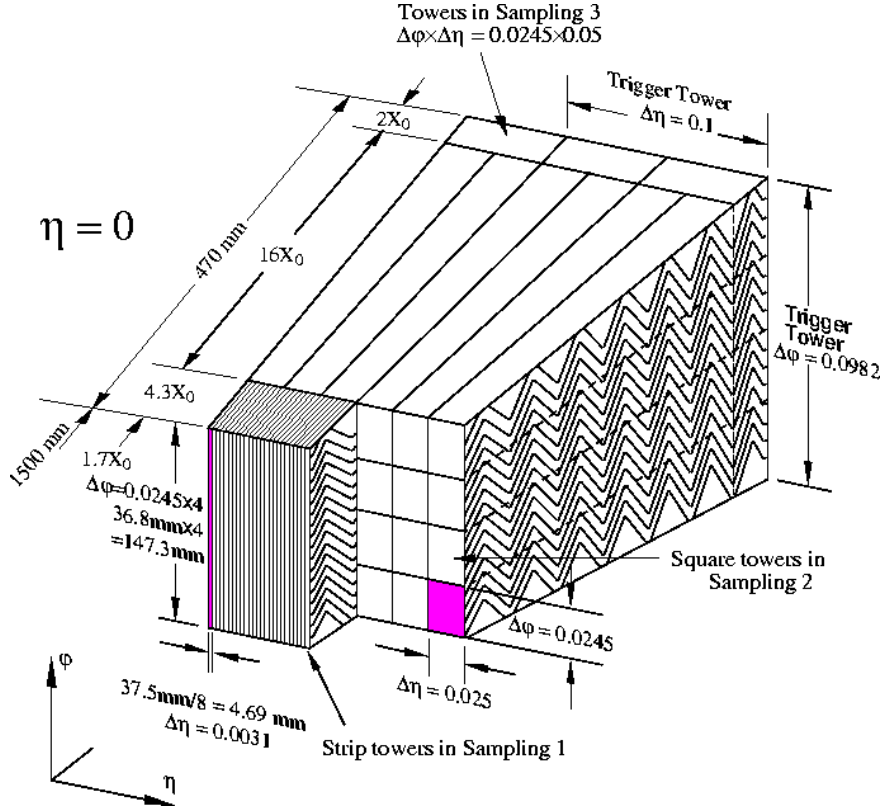


Figure 5.8: A schematic of a subsection of the barrel LAr electromagnetic calorimeter.  
Copyright CERN.

746 magnetic barrel calorimeter, the Tile barrel hadronic calorimeter, the LAr endcap  
 747 electromagnetic calorimeter, the LAr endcap hadronic calorimeter, and the LAr  
 748 Forward Calorimeter (FCal). Combined, these provide full coverage in  $\phi$  up to  
 749  $|\eta| < 4.9$ . They are shown in Fig. 5.7.

## 750 Electromagnetic Calorimeters

751 The electromagnetic calorimeters of the ATLAS detector consist of the barrel and  
 752 endcap LAr calorimeters. These are arranged into an “accordion” shape, shown  
 753 in Fig. 5.8, which allows full coverage in  $\phi$  and significant coverage in  $\eta$  while  
 754 still allowing support structures for detector operation. The accordion is made of  
 755 layers with liquid argon (active detection material) and lead (absorber) to induce  
 756 electromagnetic showers. The LAr EM calorimeters are each more than 20 radiation

757 lengths deep, which provides the high stopping power necessary to properly measure  
758 the electromagnetic showers.

759 The barrel component of the LAr EM calorimeter extends from the center of the  
760 detector out to  $|\eta| < 1.475$ . The calorimeter has a presampler, which measures the  
761 energy of any EM shower induced before the calorimeter. This has segmentation of  
762  $\Delta\eta = 0.025, \Delta\phi = .01$ . There are three “standard” layers in the barrel, which have  
763 decreasing segmentation into calorimeter *cells* as one travels radially outward from  
764 the interaction point. The first layer has segmentation of  $\Delta\eta = 0.003, \Delta\phi = .1,$   
765 and is quite thin with a depth of 4 radiation lengths. It provides precise  $\eta$  and  
766  $\phi$  measurements for incoming EM objects. The second layer is the deepest at 16  
767 radiation lengths, with a segmentation of  $\Delta\eta = 0.025, \Delta\phi = 0.025$ . It is primarily  
768 responsible for stopping the incoming EM particles, which dictates its large relative  
769 thickness, and measures most of the energy of the incoming particles. The third layer  
770 is only 2 radiation lengths deep, with a rough segmentation of  $\Delta\eta = 0.05, \Delta\phi = .025$ .  
771 The deposition in this layer is primarily used to distinguish hadrons interacting  
772 electromagnetically and entering the hadronic calorimeter from the strictly EM  
773 objects which are stopped in the second layer.

774 The barrel EM calorimeter has a similar overall structure, but extends from  $1.4 <$   
775  $|\eta| < 3.2$ . The  $\eta$  segmentation is smaller in the endcap than the barrel, while the  
776  $\phi$  segmentation is the same. In total, the EM calorimeters contain about 190000  
777 individual calorimeter cells.

## 778 Hadronic Calorimeters

779 The hadronic calorimetry of ATLAS sits directly outside the EM calorimetry. It  
780 contains three subdetectors : the barrel Tile calorimeter, the endcap LAr calorimeter,  
781 and the Forward LAr Calorimeter. Similar to the EM calorimeters, these are  
782 sampling calorimeters that alternate steel (dense material) with an active layer



Figure 5.9: A schematic of Tile hadronic calorimeter. Copyright CERN.

783 (plastic scintillator).

784 The barrel Tile calorimeter extends out to  $|\eta| < 1.7$ . It has three layers, which  
 785 combined give about 10 interaction lengths to provide excellent stopping power for  
 786 hadrons. This is critical to avoid excess *punchthrough* to the muon spectrometer  
 787 beyond the hadronic calorimeters. The first layer has a depth of 1.5 interaction  
 788 lengths. The second layer is again the thickest at a depth of 4.1 interaction lengths.  
 789 Most of the energy of incoming particles is deposited in the second layer. Both  
 790 the first and second layer have segmentation of  $\Delta\eta = 0.1, \Delta\phi = 0.1$ . Generally,  
 791 one does not need as fine granularity in the hadronic calorimeter, since the energy  
 792 depositions in the hadronic calorimeters will be summed into the composite objects as  
 793 jets. The third layer has a thickness of 1.8 interaction lengths, with a segmentation of  
 794  $\Delta\eta = 0.2, \Delta\phi = 0.1$ . The use of multiple layers gives information about the induced  
 795 hadronic shower as it propagates through the detector material.

796 The endcap LAr hadronic calorimeter is a sampling calorimeter which covers the

797 region  $1.5 < |\eta| < 3.2$ . Liquid argon is the active material and it uses a copper  
798 absorber. Unlike the other sampling calorimeters in ATLAS, it does not use the  
799 accordion shape. Instead, it is a flat detector perpendicular to the interaction point.  
800 The segmentation varies with  $\eta$ , ranging from cells of size  $\Delta\eta = 0.1, \Delta\phi = 0.1$  in the  
801 center region to  $\Delta\eta = 0.2, \Delta\phi = 0.2$  in the forward region.

802 The forward LAr calorimeter is the last subdetector of the ATLAS calorimetry.  
803 Of those subdetectors which are used for standard reconstruction techniques, the  
804 FCal sits at the most extreme values of  $3.1 < |\eta| < 4.9$ . The FCal itself is made of  
805 three subdetectors: the electromagnetic FCal1 and hadronic FCal2 and FCal3. The  
806 absorber in FCal1 is copper, with a liquid argon active medium. FCal2 and FCal3  
807 also use a liquid argon active medium, with a tungsten absorber.

## 808 5.4 Muon Spectrometer

809 The muon spectrometer sits outside the hadronic calorimetry, with pseudorapidity  
810 coverage out to  $|\eta| < 2.7$ . The MS is a huge detector, with some detector elements  
811 existing as far as 11 m in radius from the interaction point. This system is used  
812 almost exclusively to measure the momenta of muons. These systems provide a  
813 rough measurement, which is used in triggering (described in Sec. 5.5), and a precise  
814 measurement to be used in offline event reconstruction. The MS produces tracks in a  
815 similar way to the ID. The hits in each subdetector are recorded and then tracks are  
816 produced from these hits. Muon spectrometer tracks are largely independent of the  
817 ID tracks due to the independent solenoidal and toroidal magnet systems used in the  
818 ID and MS respectively. The MS consists of four separate subdetectors: the barrel  
819 region is covered by the Resistive Plate Chambers (RPCs) and Monitored Drift Tubes  
820 (MDTs) while the endcaps are covered by MDTs, Thin Gap Chambers (TGCs), and  
821 Cathode Strip Chambers (CSCs).

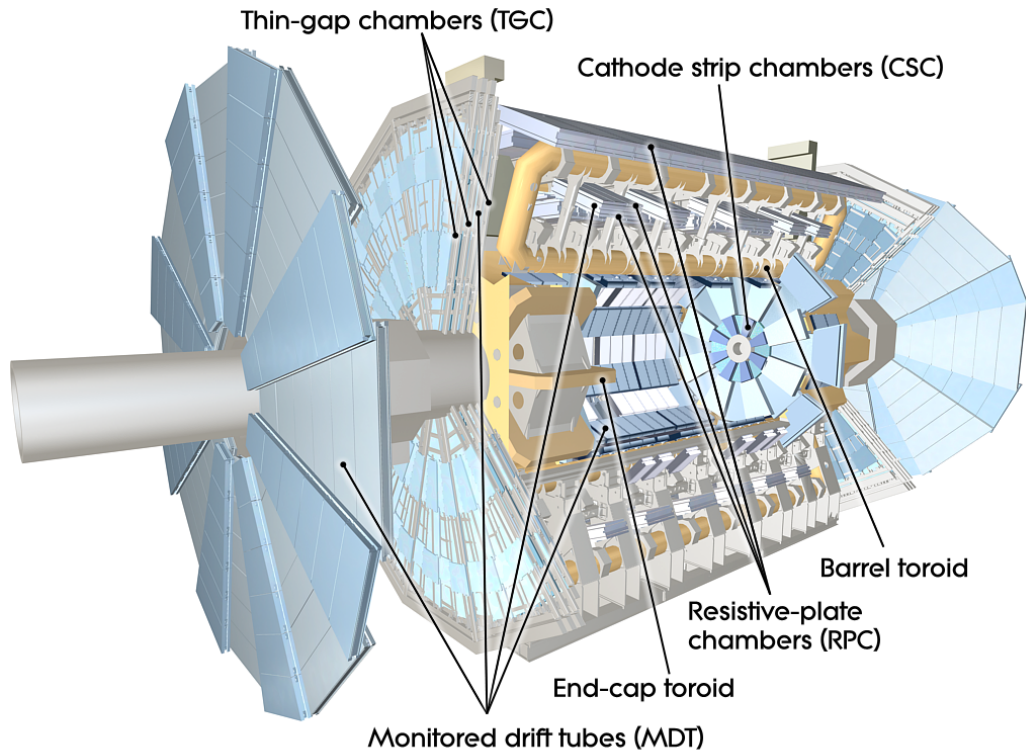


Figure 5.10: The ATLAS muon spectrometer. Copyright CERN.

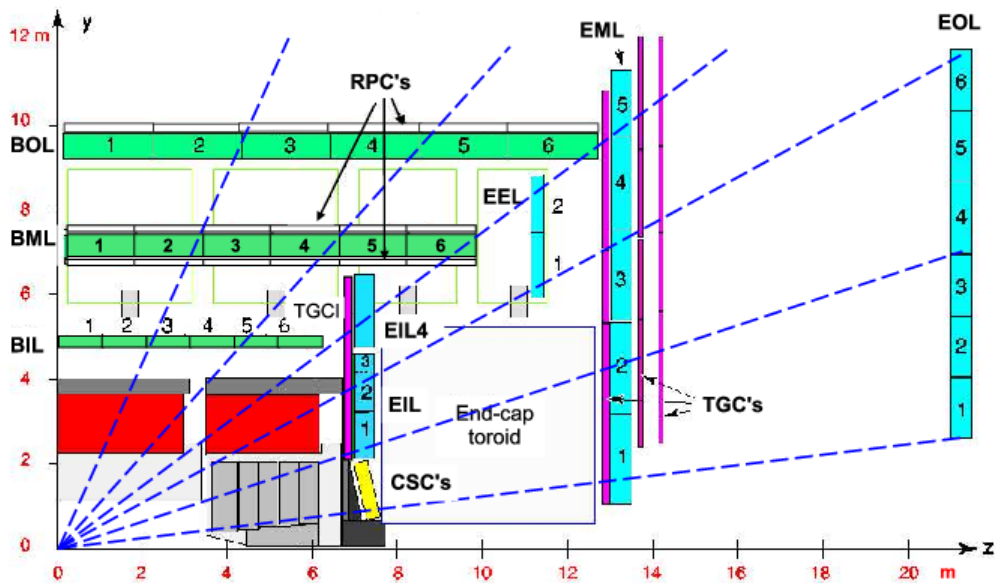


Figure 5.11: A schematic in  $z/\eta$  showing the location of the subdetectors of the muon spectrometer. Copyright CERN.

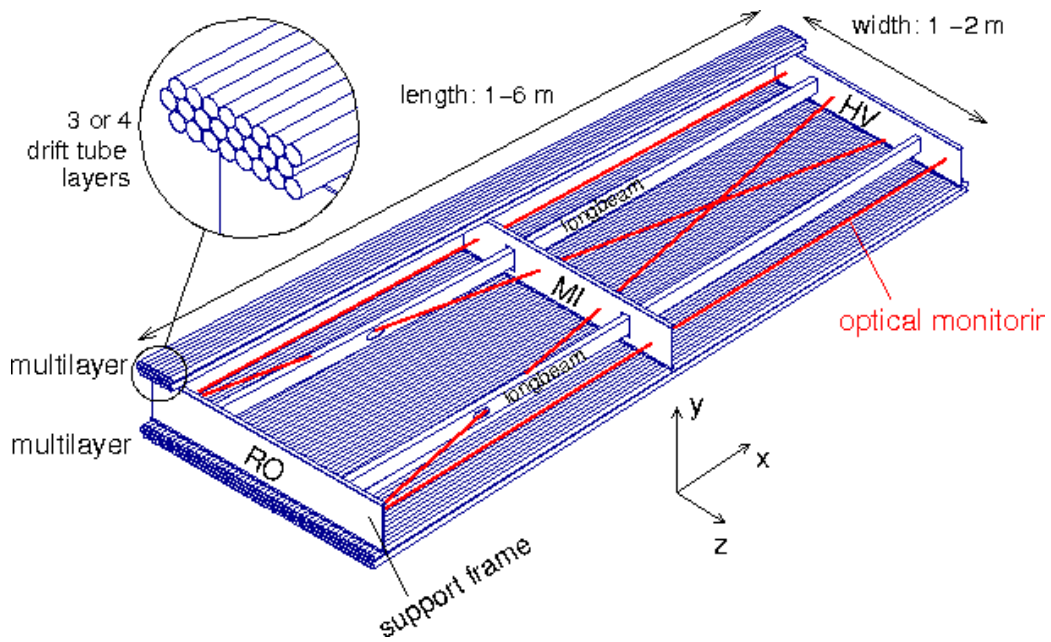


Figure 5.12: Schematic of a Muon Drift Tube chamber. Copyright CERN.

## 822 Monitored Drift Tubes

823 The MDT system is the largest individual subdetector of the MS. MDTs provide  
824 precision measurements of muon momenta as well as fast measurements used for  
825 triggering. There are 1088 MDT chambers providing coverage out to pseudorapidity

826  $|\eta| < 2.7$ . Each consists of an aluminum tube containing an argon-CO<sub>2</sub> gas mixture.  
827 In the center of each tube there 50  $\mu\text{m}$  diameter tungsten-rhenium wire at a voltage of  
828 3080 V. A muon entering the tube will induce ionization in the gas, which will “drift”  
829 towards the wire due to the voltage. One measures this ionization as a current in the  
830 wire. The current comes with a time measurement related to how long it takes the  
831 ionization to drift to the wire.

832 These tubes are layered in a pattern shown in Fig. 5.12. Combining the  
833 measurements from the tubes in each layer gives good position resolution. The  
834 system consists of three subsystems of these layers, at 5 m, 7 m, and 9 m from the  
835 interaction point. The innermost layer is directly outside the hadronic calorimeter.  
836 The combination of these three measurements gives precise momenta measurements  
837 for muons.

## 838 Resistive Plate Chambers

839 The RPC system is alternated with the MDT system in the barrel. The first two layers  
840 of RPC detectors surround the second MDT layer while the third is outside the final  
841 MDT layer. The RPC system covers pseudorapidity  $|\eta| < 1.05$ . Each RPC consists  
842 of two parallel plates at a distance of 2 mm surrounding a C<sub>2</sub>H<sub>2</sub>F<sub>4</sub> mixture. The  
843 electric field between these plates is 4.9k kV/mm. Just as in the MDTs, an incoming  
844 muon ionizes the gas, and the deposited ionization is collected by the detector (in this  
845 case on the plates). It is quite fast, but with a relatively poor spatial resolution of  
846 1 cm. Still, it can provide reasonable  $\phi$  resolution due to its large distance from the  
847 interaction point. This is most useful in triggering, where the timing requirements  
848 are quite severe. The RPCs also complement the MDTs by providing a measurement  
849 of the non-bending coordinate.



Figure 5.13: Photo of the installation of Cathode Strip Chambers and Monitored Drift Tubes. Copyright CERN.

## 850    **Cathode Strip Chambers**

851    The CSCs are used in place of MDTs in the first layer of the endcaps. This region,  
852    at  $2.0 < |\eta| < 2.7$ , has higher particle multiplicity at close distance to the interaction  
853    point from low-energy photons and neutrons. The MDTs are not equip to deal with  
854    the high particle rate in this region, so the CSCs were designed to deal with this  
855    deficiency.

856    Each CSC consists multiwire proportional chambers, oriented radially outward  
857    from the interaction point. These chambers overlap partially in  $\phi$ . The wires contain  
858    a gas mixture of argon and CO<sub>2</sub>, which is ionized when muons enter. The detectors  
859    operate with a voltage of 1900 V, with much lower drift times than the MDTs. They  
860    provide less hits than MDTs, but their lower drift times lower uptime and reduce the  
861    amount of detector overload.

862    The CSCs are arranged into four planes on the wheels of the muon spectrometer,  
863    as seen in Fig. Fig. 5.13. There are 32 CSCs in total, with 16 on each side of the  
864    detector in  $\eta$ .

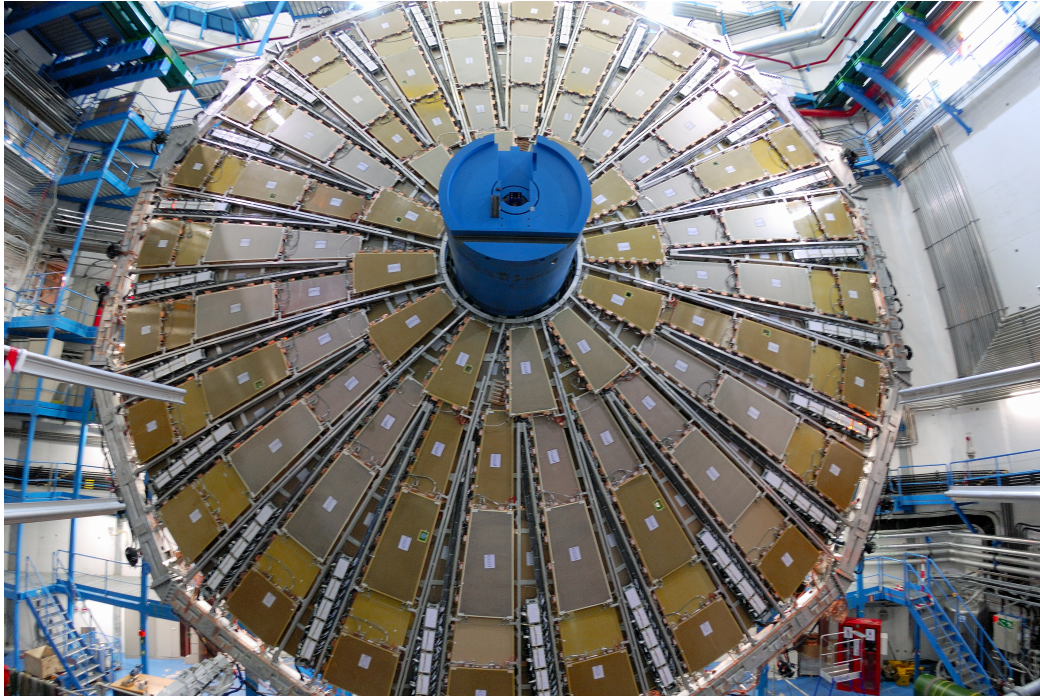


Figure 5.14: Photo of a muon Big Wheel, consisting of Thin Gap Chambers.  
Copyright CERN.

### 865    **Thin Gap Chambers**

866    The TGCs serve the purpose of the RPCs in the endcap at pseudorapidity of  $1.05 <$   
867     $|\eta| < 2.4$ , by providing fast measurements used for triggering. They are multiwire  
868    proportional chambers similar to the CSCs. The fast readouts necessary for triggering  
869    are provided by a high electric field and a small wire-to-wire distance of 1.8 mm.  
870    These detectors provide both  $\eta$  and  $\phi$  information, allowing the trigger to use as  
871    much information as possible when selecting events.

## 872    **5.5 Trigger System**

873    The data rate delivered by the LHC is staggering [92]. In the 2016 dataset, the  
874    collision rate was 40 MHz, meaning a *bunch spacing* of 25 ns. In each of the event,  
875    there are many proton-proton collisions. Most of the collisions are uninteresting,  
876    such as elastic scattering of protons, or even inelastic scattering leading to low-energy

877 dijet events. These low-energy events have have been studied in detail in previous  
878 experiments.

879 Even if one is genuinely interested in these events, it's *impossible* to save all of  
880 the information available in each event. If all events were written "to tape" (as the  
881 jargon goes), ATLAS would store terabytes of data per second. We are limited to only  
882 about 1000 Hz readout by computing processing time and storage space. We thus  
883 implement a *trigger* which provides fast inspection of events to drastically reduce  
884 the data rate from the 40 MHz provided by the LHC to the 1000 Hz we can write to  
885 tape for further analysis.

886 The ATLAS trigger system consists of a two-level trigger, known as the Level-  
887 1 trigger (L1 trigger) and the High-Level Trigger (HLT)<sup>3</sup>. Trigger selections are  
888 organized into *trigger chains*, where events passing a particular L1 trigger are passed  
889 to a corresponding HLT trigger. For example, one would require a particular high- $p_T$   
890 muon at L1, with additional quality requirements at HLT. One can also use HLT  
891 triggers as prerequisites for each other, as is done in some triggers requiring both jets  
892 and  $E_T^{\text{miss}}$ .

## 893 **Level-1 Trigger**

894 The L1 trigger is hardware-based, and provides the very fast rejection needed to  
895 quickly select events of interest. The L1 trigger uses only what is known as *prompt*  
896 data to quickly identify interesting events. Only the calorimeters and the triggering  
897 detectors (RPCs and TGCs) of the MS are fast enough to be considered at L1,  
898 since the tracking reconstruction algorithms used by the ID and the more precise  
899 MS detectors are very slow. This allows quick identification of events with the

---

<sup>3</sup>In Run1, ATLAS ran with a three-level trigger system. The L1 was essentially as today. The HLT consisted of two separate systems known as the L2 trigger and the Event Filter (EF). This was changed to the simpler system used today during the shutdown between Run1 and Run2.

900 most interesting physical objects: large missing transverse momentum and high- $p_T$   
901 electrons, muons, and jets.

902 L1 trigger processing is done locally. This means that events are selected without  
903 considering the entire available event. Energy deposits over some threshold are  
904 reconstructed as *regions of interest* (RoIs). These RoIs are then compared using  
905 pattern recognition hardware to “expected” patterns for the given RoIs. Events with  
906 RoIs matching these expected patterns are then handed to the HLT through the  
907 Central Trigger Processor. This step lowers the data rate down to about 75 kHz.

908 **High-Level Trigger**

909 After passing the L1 trigger, events are passed to the HLT, which takes the incoming  
910 data rate from  $\sim$ 75 kHz down to the  $\sim$ 1 kHz that can be written to tape. The HLT  
911 performs much like a simplified offline reconstruction, using many common quality  
912 and analysis cuts to eliminate uninteresting events. This is done by using computing  
913 farms located close to the detector, which process events in parallel. Individually,  
914 each event which enters the computing farms takes about 4 seconds to reconstruct.  
915 However, some events take significantly longer to reconstruct, which necessitates  
916 careful monitoring of the HLT to ensure smooth operation.

917 HLT triggers are targeted to a particular physics process, such as a  $E_T^{\text{miss}}$  trigger,  
918 single muon trigger, or multijet trigger. The collection of all triggers is known as  
919 the trigger *menu*. Since many low-energy particles are produced in collisions, it is  
920 necessary to set a *trigger threshold* on the object of interest. Due to the changing  
921 luminosity conditions of the LHC, these thresholds change constantly. The most  
922 common strategy is to increase the trigger thresholds with increasing instantaneous  
923 luminosity. This allows an approximately constant number of events to be written  
924 for further analysis. Triggers which have rates higher than those designated by the  
925 menu are *prescaled*. A prescaled trigger only records every  $n$ th event which passes

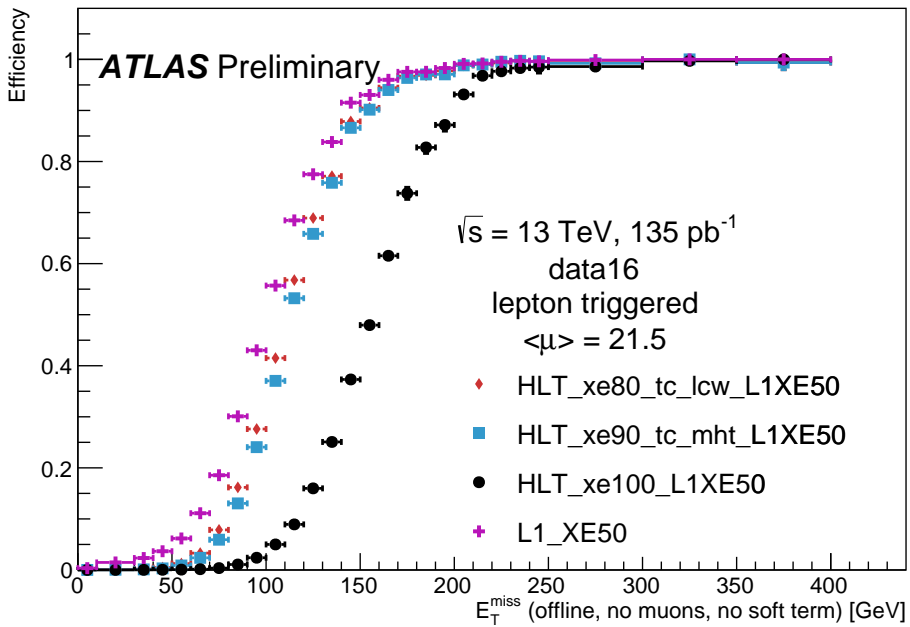


Figure 5.15: Turn-on curves for the  $E_T^{\text{miss}}$  triggers used in this thesis.

the trigger requirements, where  $n$  is the prescale value. Inne wishes to investigate all data events passing some set of analysis cuts, so often one uses the “lowest threshold unprescaled trigger”. *Turn-on curves* allow one to select the needed offline analysis cut to ensure the trigger is fully efficient. An example turn-on curve for the  $E_T^{\text{miss}}$  triggers used in the signal region of this analysis is shown in Fig. 5.15.

The full set of the lowest threshold unprescaled triggers considered here can be found in Tab. 5.1. These are the lowest unprescaled triggers associated to the SUSY signal models and Standard Model backgrounds considered in this thesis. More information can be found in [92].

Physics Object	Trigger	$p_T$ Threshold (GeV)	Level-1 Seed	Requirements	Rate (Hz)
<b>2015 Data</b>					
$E_T^{\text{miss}}$	HLT_xe70	70	L1_XE50	-	60
Muon	HLT_mu24_loose	24	L1_MU15	isolated, loose	130
Muon	HLT_mu50	50	L1_MU15	-	30
Electron	HLT_e24_lhmedium_iloose	24	L1_EM20VH	medium OR isolated, loose	140
Electron	HLT_e60_lhmedium	60	L1_EM20VH	medium	10
Electron	HLT_e120_lhloose	120	L1_EM20VH	loose	<10
Photon	HLT_g120_loose	120	L1_EM20VH	loose	20
<b>2016 Data</b>					
$E_T^{\text{miss}}$	HLT_xe100_mht_L1XE50	100	L1_XE50	-	180
Muon	HLT_mu24_ivarmedium	24	L1_MU20	medium	120
Muon	HLT_mu50	50	L1_MU20	-	40
Electron	HLT_e24_lhtight_nod0	24	L1_EM22VHI	tight with no $d_0$ OR loose	110
Electron	HLT_e60_lhmedium_nod0	60	L1_EM22VHI	medium with no $d_0$	10
Electron	HLT_e140_lhloose_nod0	140	L1_EM22VHI	loose with no $d_0$	<10
Photon	HLT_g140_loose	140	L1_EM22VHI	loose	20

Table 5.1: High-Level Triggers used in this thesis. Descriptions of loose, medium, tight, and isolated can be found in [92]. The  $d_0$  cut refers to a quality cut on the vertex position, which was removed from many triggers in 2016 to increase sensitivity to displaced vertex signals. For most triggers, the increased thresholds in 2016 compared to 2016 were designed to keep the rate approximately equal.



## *Object Reconstruction*

937 This chapter describes the reconstruction algorithms used within ATLAS. We will  
938 make the distinction between the “primitive” objects which are reconstructed from  
939 the detector signals from the “composite” physics objects we use in measurements  
940 and searches for new physics.

### **941 6.1 Primitive Object Reconstruction**

942 The primitive objects reconstructed by ATLAS are *tracks* and (calorimeter) *clusters*.  
943 These are reconstructed directly from tracking hits and calorimeter energy deposits  
944 into cells. Tracks can be further divided into inner detector and muon spectrom-  
945 eter tracks. Calorimeter clusters can be divided into sliding-window clusters and  
946 topological clusters (topoclusters).

#### **947 Inner Detector Tracks**

948 Inner detector tracks are reconstructed from hits in the inner detector [93, 94] These  
949 hits indicate that a charged particle has passed through the detector material. Due  
950 to the 2 T solenoid in the inner detector, the hits associated with any individual  
951 particle will be curved. The amount of curvature determines the momentum of the  
952 particle. In any given event, there are upwards of  $10^4$  hits, making it impossible to do  
953 any sort of combinatorics to reconstruct tracks. There are two algorithms used by  
954 ATLAS track reconstruction, known as *inside-out* and *outside-in*.

955       ATLAS first employs the inside-out algorithm. One assumes the track begins  
956 at the interaction point. Moving out from the interaction point, one creates track  
957 seeds. Track seeds are proto-tracks constructed from three hits. These hits can be  
958 distributed as three pixel hits, two pixel hits and one SCT hit, or three SCT hits.  
959 One extrapolates the track and uses a combinatorial Kalman filter [93], which adds  
960 the rest of the pixel and SCT hits to the seeds. This is done seed by seed, so it  
961 avoids the combinatorial complexity involved with checking all hits with all seeds.  
962 At this point, the algorithm applies an additional filter to avoid ambiguities from  
963 nearby tracks. The TRT hits are added to the seeds using the same method. After  
964 this procedure, all hits are associated to a track.

965       The next step is to determine the correct kinematics of the track. This is  
966 done by applying a fitting algorithm which outputs the best-fit track parameters  
967 by minimizing the track distance from hits, weighted by each hit's resolution. These  
968 parameters are  $(d_0, z_0, \eta, \phi, q/p)$  where  $d_0$  ( $z_0$ ) is the transverse (longitudinal) impact  
969 parameter and  $q/p$  is the charge over the track momenta. This set of parameters  
970 uniquely defines the measurement of the trajectory of the charged particle associated  
971 to the track. An illustration of a track with these parameters is shown in Fig. 6.1.

972       The other track reconstruction algorithm is the outside-in algorithm. As the  
973 name implies, we start from the outside of the inner detector, in the TRT, and  
974 extend the tracks in toward the interaction point. One begins by seeding from  
975 TRT hits, and extending the track back towards the center of the detector. The  
976 same fitting procedure is used as in the inside-out algorithm to find the optimal  
977 track parameters. This algorithm is particularly important for finding tracks which  
978 originate from interactions with the detector material, especially the SCT. For tracks  
979 from primary vertices, this often finds the same tracks as the inside-out algorithm,  
980 providing an important check on the consistency of the tracking procedure.

981       In the high luminosity environment of the LHC, even the tracks reconstructed

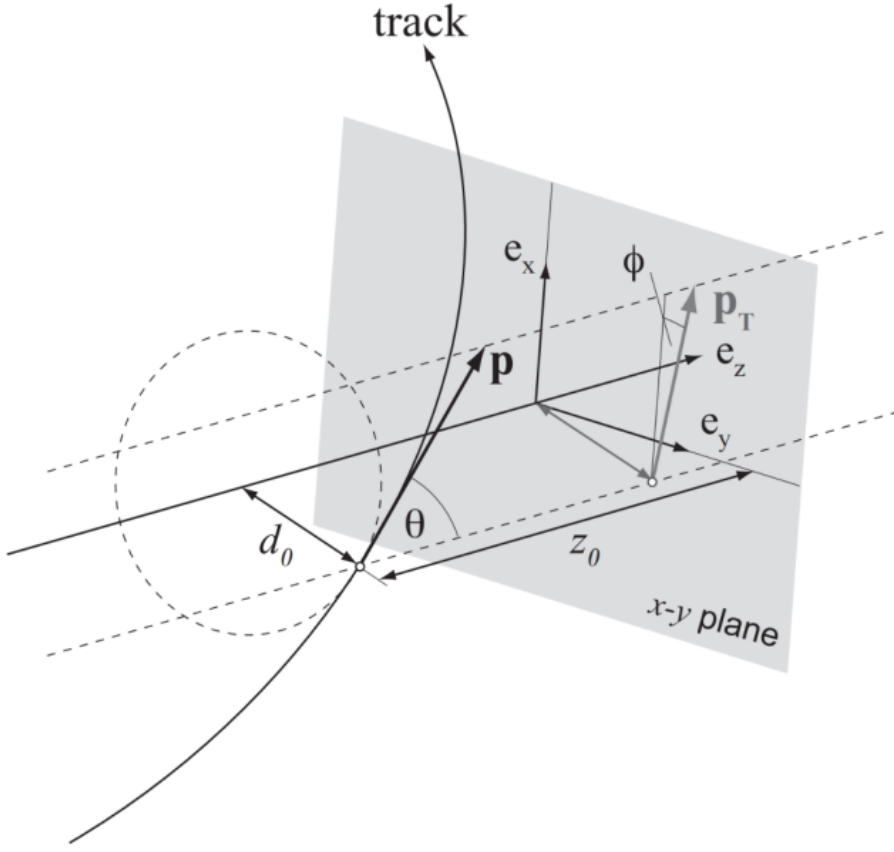
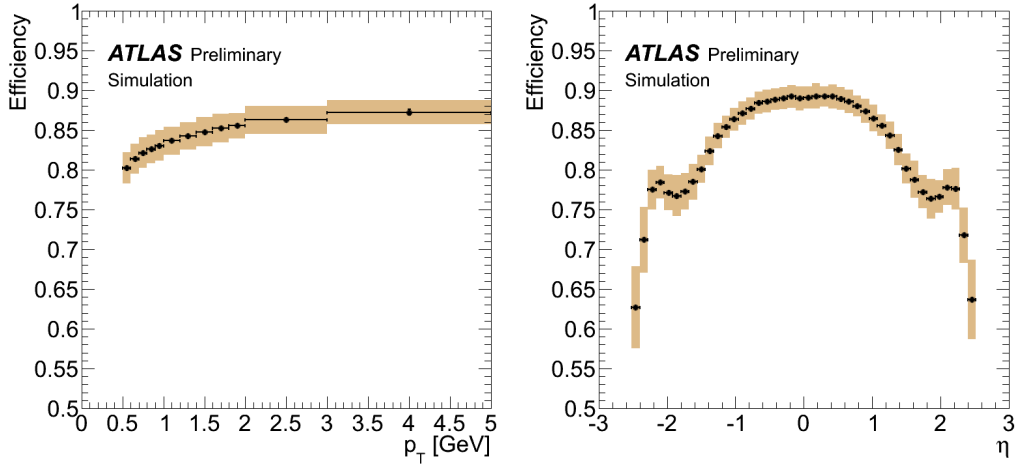


Figure 6.1: The parameters associated to a track.

from precision detectors such as those of ATLAS inner detector can sometimes lead to fake tracks from simple combinatoric chance. Several quality checks are imposed after track fitting which reduce this background. Seven silicon (pixel + SCT) hits are required for all tracks. No more than two *holes* are allowed in the pixel detector. Holes are expected measurements from the track that are missing in the pixel detector. Finally, tracks with poor fit quality, as measured by  $\chi^2/ndf$ , are also rejected. Due to the high quality of the silicon measurements in the pixel detector and SCT, these requirements give good track reconstruction efficiency, as seen in Fig. 6.2 for simulated events [95].



(a) Track reconstruction as a function of  $p_T$ . (b) Track reconstruction as a function of  $\eta$ .

Figure 6.2: Track reconstruction efficiency as a function of track  $p_T$  and  $\eta$ . The efficiency is defined as the number of reconstructed tracks divided by the number of generate charged particles.

## 991 Sliding-window clusters

992 The sliding-window algorithm is a way to combine calorimeter cells into composite  
 993 objects (clusters) to be used as inputs for other algorithms [96]. Sliding-window  
 994 clusters are the primary inputs to electron and photon reconstruction, as described  
 995 below. The electromagnetic calorimeter has high granularity, with a cell size of  
 996  $(\eta, \phi) = (.025, .025)$  in the coarsest second layer throughout most of the calorimeter.  
 997 The “window” consists of 3 by 5 cells in the  $(\eta, \phi)$  space. All layers are added on  
 998 this same 2D space. One translates this window over the space and seeds a cluster  
 999 whenever the energy sum of the cells is maximized. If the seed energy is greater  
 1000 than 2.5 GeV, this seed is called a sliding-window cluster. This choice was motivated  
 1001 to optimize the reconstruction efficiency of proto-electrons and proto-photons while  
 1002 rejecting fakes from electronic noise and additional particles from pileup vertices.

1003 **Topological clusters**

1004 Topoclusters are the output of the algorithm used within ATLAS to combine  
1005 hadronic and electromagnetic calorimeter cells in a way which extracts signal from  
1006 a background of significant electronic noise [97]. They are the primary input to the  
1007 algorithms which reconstruct jets.

1008 Topological clusters are reconstructed from calorimeter cells in the following way.  
1009 First, one maps all cells onto a single  $\eta - \phi$  plane so one can speak of *neighboring*  
1010 cells. Two cells are considered neighboring if they are in the same layer and directly  
1011 adjacent, or if they are in adjacent layers and overlap in  $\eta - \phi$  space. The *significance*  
1012  $\xi_{\text{cell}}$  of a cell during a given event is

$$\xi_{\text{cell}} = \frac{E_{\text{cell}}}{\sigma_{\text{noise},\text{cell}}} \quad (6.1)$$

1013 where  $\sigma_{\text{noise},\text{cell}}$  is measured for each cell in ATLAS and  $E_{\text{cell}}$  measures the current  
1014 energy level of the cell. One thinks of this as the measurement of the energy *over*  
1015 *threshold* for the cell.

1016 Topocluster *seeds* are defined as calorimeter cells which have a significance  $\xi_{\text{cell}} >$   
1017 4. These are the inputs to the algorithm. One iteratively tests all cells adjacent  
1018 to these seeds for  $\xi_{\text{cell}} > 2$ . Each cells passing this selection is then added to the  
1019 topocluster, and the procedure is repeated. When the algorithm reaches the point  
1020 where there are no additional adjacent cells with  $\xi_{\text{cell}} > 2$ , every positive-energy cell  
1021 adjacent to the current proto-cluster is added. The collection of summed cells is a  
1022 topocluster. An example of this procedure for a simulation dijet event is shown in  
1023 Fig. 6.3.

1024 There are two calibrations used for clusters [98]. These are known as the  
1025 electromagnetic (EM) scale [99] and the local cluster weighting (LCW) scale [97].  
1026 The EM scale is the energy read directly out of the calorimeters as described. This  
1027 scale is appropriate for electromagnetic processes. The LCW scale applies additional

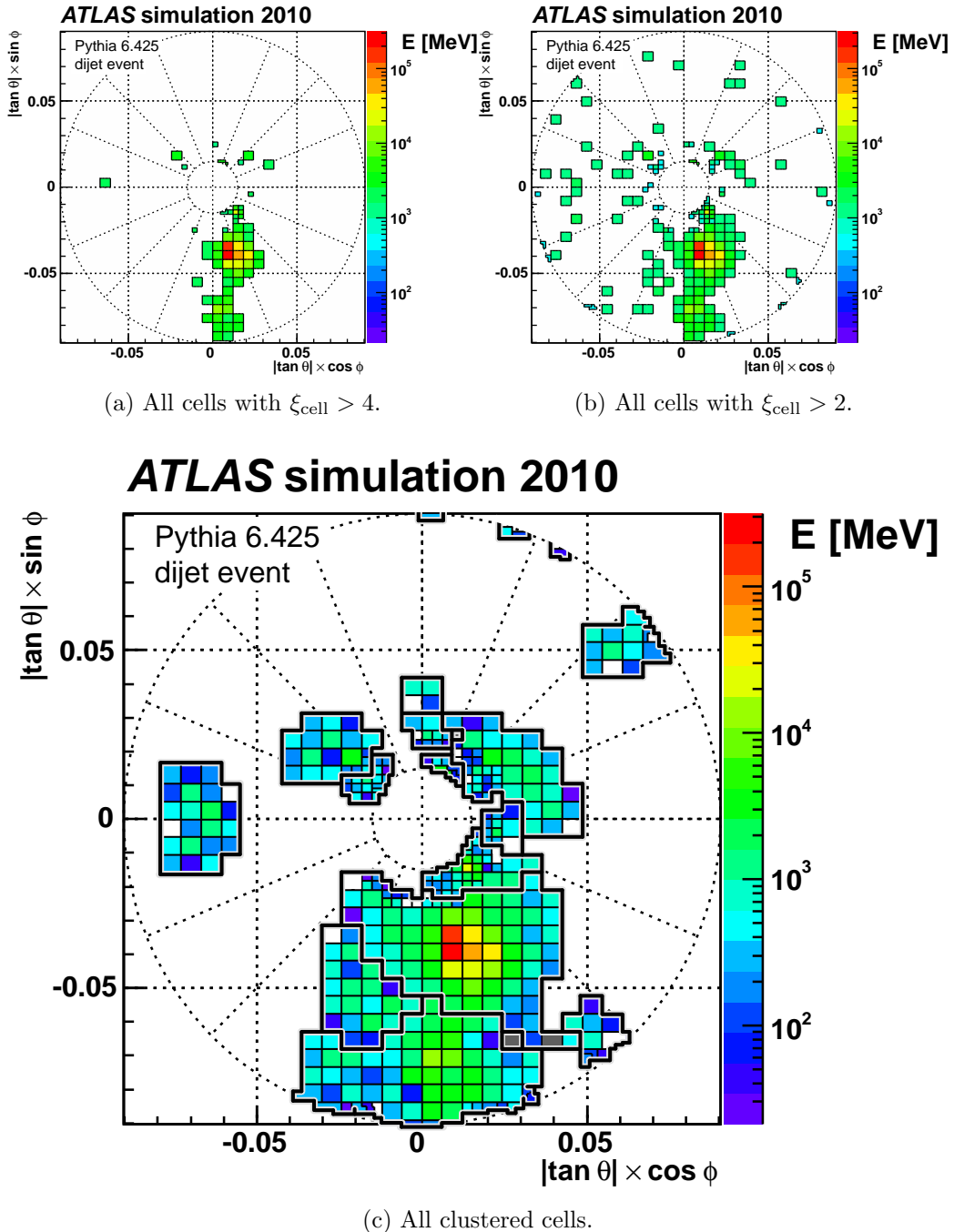


Figure 6.3: Example of topoclustering on a simulated dijet event.

1028 scaling to the clusters based on the shower development. The cluster energy can be  
1029 corrected for calorimeter noncompensation and the differences in the hadronic and  
1030 electromagnetic calorimeters’ responses. This scale provides additional corrections  
1031 that improve the accuracy of hadronic energy measurements. This thesis only uses  
1032 the EM scale corrections. LCW scaling requires additional measurements that only  
1033 became available with additional data. Due to the jet calibration procedure that  
1034 we will describe below, it is also a relatively complicated procedure to rederive the  
1035 “correct” jet energy.

## 1036 Muon Spectrometer Tracks

1037 Muon spectrometer tracks are fit using the same algorithms as the ID tracks, but  
1038 different subdetectors. The tracks are seeded by hits in the MDTs or CSCs. After  
1039 seeding in the MDTs and CSCs, the hits from all subsystems are refit as the final  
1040 MS track. These tracks are used as inputs to the muon reconstruction, as we will see  
1041 below.

## 1042 6.2 Physics Object Reconstruction and Quality

### 1043 Identification

1044 There are essentially six objects used in ATLAS searches for new physics: electrons,  
1045 photons, muons,  $\tau$ -jets, jets, and  $E_T^{\text{miss}}$ . The reconstruction of these objects is  
1046 described here. In this thesis,  $\tau$  lepton jets are not treated differently from other  
1047 hadronic jets, and we will not consider their reconstruction algorithms. A very  
1048 convenient summary plot is shown in Fig. 6.4.

1049 One often wishes to understand “how certain” we are that a particular object  
1050 is truly the underlying physics object. In ATLAS, we often generically consider, in

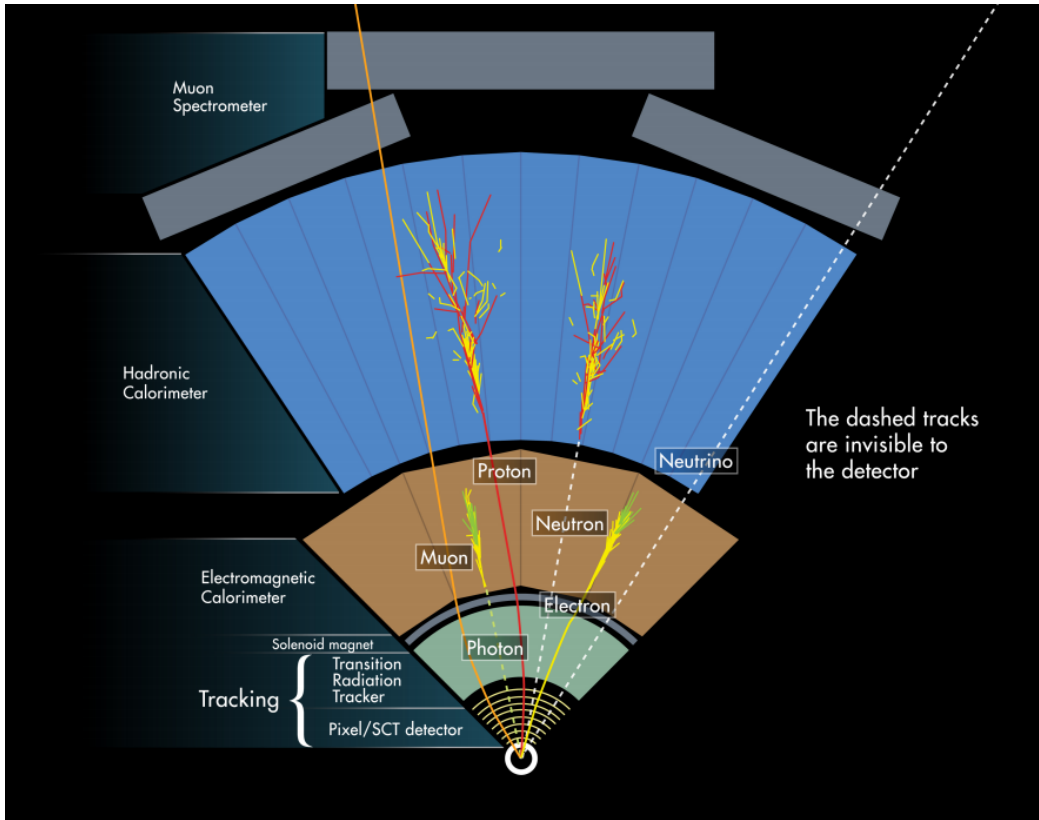


Figure 6.4: The interactions of particles with the ATLAS detector. Solid lines indicate the particle is interacting with the detector, while dashed lines are shown where the particle does not interact.

1051 order, *very loose*, *loose*, *medium*, and *tight* objects<sup>1</sup>. These are ordered in terms of  
 1052 decreasing object efficiency, or equivalently, decreasing numbers of fake objects. We  
 1053 will also describe briefly the classification of objects into these categories.

1054 In this thesis, since we present a search for new physics in a zero lepton final state,  
 1055 we will provide additional details about jet and  $E_T^{\text{miss}}$  reconstruction.

---

<sup>1</sup> These are not all used for all objects, but it's conceptually useful to think of these different categories.

1056 **Electrons and Photons**

1057 **Reconstruction**

1058 The reconstruction of electrons and photons (often for brevity called “electromagnetic  
1059 objects”) is very similar [96, 100, 101]. This is because the reconstruction begins  
1060 with the energy deposit in the calorimeter in the form of an electromagnetic shower.  
1061 For any incoming  $e/\gamma$ , many more electrons and photons are produced in the shower.  
1062 The measurement in the calorimeter is similar for these two objects.

1063 One begins the reconstruction of electromagnetic objects from the sliding-window  
1064 clusters reconstructed from the EM calorimeter. These  $E > 2.5$  GeV clusters the  
1065 the primary seed for electrons and photons. One then looks for all ID tracks within  
1066  $\Delta R < 0.3$ , where  $\Delta R = \sqrt{\Delta\eta^2 + \Delta\phi^2}$ . We “match” the track and cluster if they are  
1067 within  $\Delta\phi < 0.2$  in the direction of track curvature, or  $\Delta\phi < 0.05$  in the direction  
1068 opposite the track curvature. Those track-cluster seeds with tracks pointing to the  
1069 primary vertex are reconstructed as electrons.

1070 For photons, we have two options to consider, known as *converted* and *unconverted*  
1071 photons. Due to the high energy of the LHC collisions, typical photons have energy  
1072  $>\sim 1$  GeV. At this scale, photons interact almost exclusively via pair-production  
1073 in the presence of the detector material, as shown in Fig. 6.5 [56]. If the track-  
1074 cluster seed has a track which does not point at the primary vertex, we reconstruct  
1075 this object as a converted photon. This happens since the photon travels a distance  
1076 before decay into two electrons, and see the tracks coming from this secondary vertex.  
1077 Those clusters which do not have any associated tracks are then reconstruced as an  
1078 unconverted photon.

1079 The final step in electromagnetic object reconstruction is the final energy value.  
1080 This process is different between electrons and photons due to their differing  
1081 signatures in the EM calorimeter. In the barrel, electrons energies are assigned as

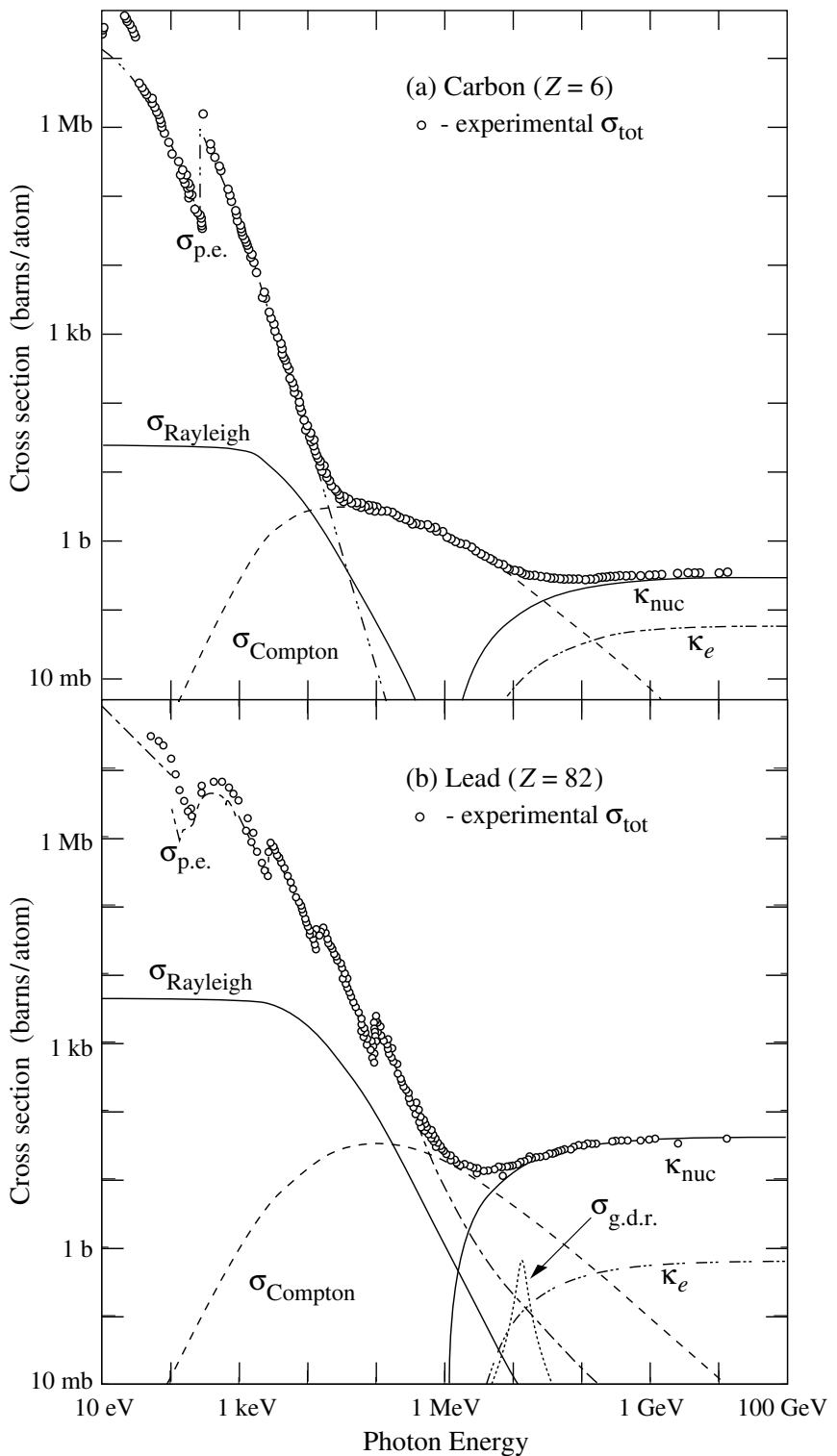


Figure 6.5: Photon total cross sections as a function of energy in carbon and lead, showing the contributions of different processes [56].

1082 the sum of the 3 clusters in  $\eta$  and 7 clusters in  $\phi$  to account for the electron curving  
1083 in the  $\phi$  direction. Barrel photons are assigned the energy sum of (3, 5) clusters in  
1084 ( $\eta, \phi$ ) space. In the endcap, the effect of the magnetic field on the electrons is smaller,  
1085 and there is a coarser granularity. Both objects sum the (5, 5) clusters for their final  
1086 energy value.

## 1087 Quality Identification

1088 Electrons have a number of important backgrounds which can give fakes. Fake  
1089 electrons come primarily from secondary vertices in hadron decays or misidentified  
1090 hadronic jets. To reduce these backgrounds, quality requirements are imposed on  
1091 electron candidates. Loose electrons have requirements imposed on the shower  
1092 shapes in the electromagnetic calorimeter and on the quality of the associated ID  
1093 track. There is also a requirement that there is a small energy deposition in the  
1094 hadronic calorimeter behind the electron, to avoid jets being misidentified as electrons  
1095 (low hadronic leakage). Medium and tight electrons have increasingly stronger  
1096 requirements on these variables, and additional requirements on the isolation (as  
1097 measured by  $\Delta R$ ) and matching of the ID track momentum and the calorimeter  
1098 energy deposit.

1099 Photons are relatively straightforward to measure, since there are few background  
1100 processes [102]. The primary is pion decays to two photons, which can cause a jet  
1101 to be misidentified as photon. Loose photons have requirements on the shower shape  
1102 and hadronic leakage. Tight photons have tighter shower shape cuts, especially on  
1103 the high granularity first layer of the EM calorimeter. The efficiency for unconverted  
1104 tight photons as a function of  $p_T$  is shown in

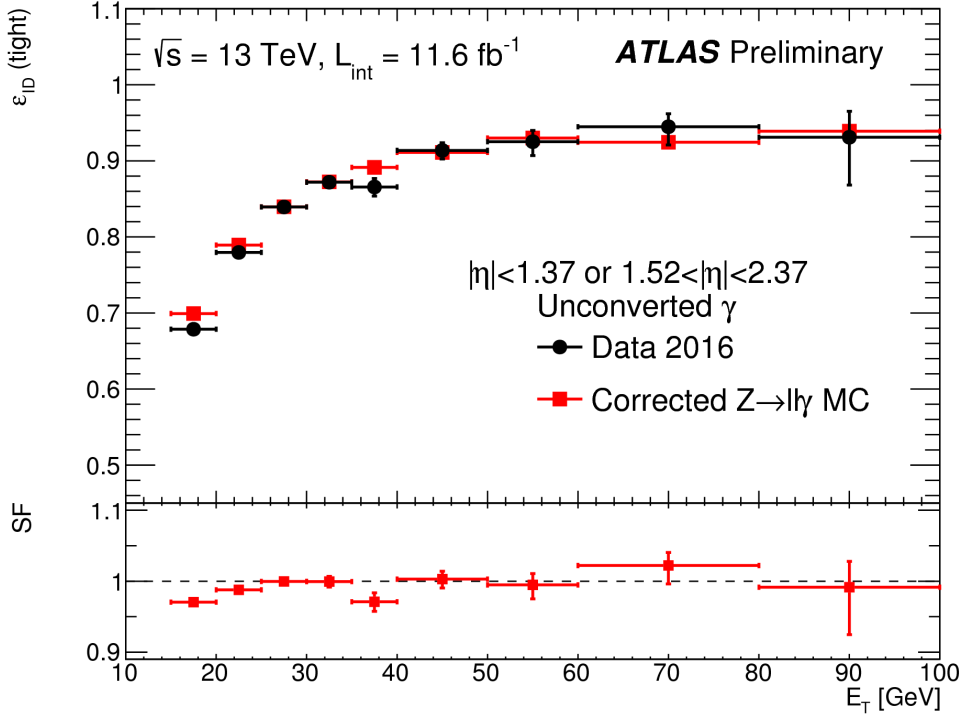


Figure 6.6: Unconverted photon efficiency as measured in [102].

## 1105 Muons

### 1106 Reconstruction

1107 Muons are reconstructed using measurements from all levels of the ATLAS detec-  
 1108 tor [103]. They leave a ID track, a small, characteristic deposition in the EM calorime-  
 1109 ter, and then a track in the muon spectrometer. The primary reconstruction technique  
 1110 produces a so-called *combined* muon. “Combined” means using a combination of the  
 1111 ID and MS tracks to produce the final reconstructed muon kinematics. This is done  
 1112 by refitting the hits associated to both tracks, and using this refit track for the muon  
 1113 kinematics.

### 1114 Quality Identification

Several additional criteria are used to assure muon measurements are free of significant background contributions, especially from pion and kaon decays to muons.

Muons produced via these decay processes are often characterized by a “kink”. Candidate muons with a poor fit quality, characterized by  $\chi^2/\text{n.d.f.}$ , are thus rejected. Additionally, the absolute difference in momentum measurements between the ID and MS provide another handle, since the other decay products from hadron decays carry away some amount of the initial hadron momentum. This is measured by

$$\rho' = \frac{|p_T^{\text{ID}} - p_T^{\text{MS}}|}{p_T^{\text{Combined}}}. \quad (6.2)$$

Additionally, there is a requirement on the  $q/p$  significance, defined as

$$S_{q/p} = \frac{|(q/p)^{\text{ID}} - (q/p)^{\text{MS}}|}{\sqrt{\sigma_{\text{ID}}^2 + \sigma_{\text{MS}}^2}}. \quad (6.3)$$

1115 The  $\sigma_{\text{ID,MS}}$  in the denominator of Eq. Eq. (6.3) are the uncertainties on the corre-  
 1116 sponding quantity from the numerator. Finally, cuts are placed on the number of  
 1117 hits in the various detector elements.

1118 Subsequently tighter cuts on these variables allow one to define the different muon  
 1119 identification criteria. Loose muons have the highest reconstruction efficiency, but  
 1120 the highest number of fake muons, since there are no requirements on the number  
 1121 of subdetector hits and the loosest requirements on the suite of quality variables.  
 1122 Medium muons consist of Loose muons with tighter cuts on the quality variables.  
 1123 They also require more than three MDT hits in at least two MDT layers. These are  
 1124 the default used by ATLAS analyses. Tight muons have stronger cuts than those of  
 1125 the medium selection, and reducing the reconstruction efficiency. The reconstruction  
 1126 efficiency as a function of  $p_T$  can be seen for Medium muons in Fig. 6.7.

## 1127 Jets

1128 Jets are composite objects corresponding to many physical particles [56, 104, 105]  
 1129 This is a striking difference from the earlier particles. Fortunately, we normally (and  
 1130 in this thesis) only need information about the original particle produced in the

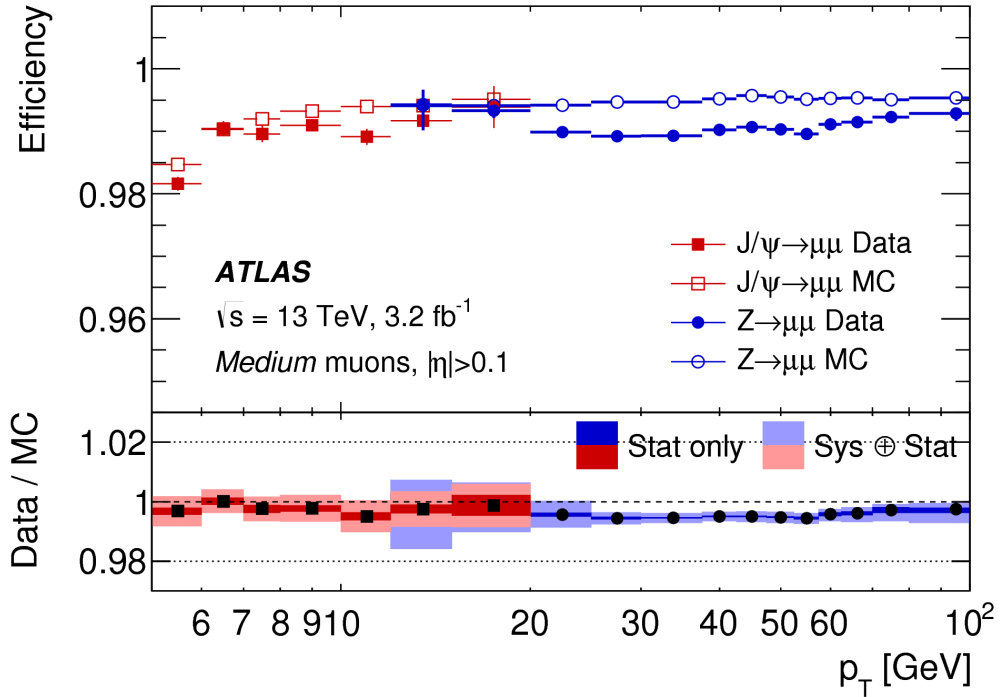


Figure 6.7: Medium muon efficiency as measured in [103].

1131 primary collision. In the SM, this corresponds to quarks and gluons. Due to the  
 1132 hadronization process, free quarks and gluons spontaneously hadronize and produce  
 1133 a hadronic shower, which we call a jet. These showers can be measured by the EM  
 1134 and hadronic calorimeters, and the charged portions can be measured in the ID. The  
 1135 first step is to combine these measurements into a composite object representing the  
 1136 underlying physical parton. This is done via jet algorithms.

## 1137 Jet Algorithms

1138 It might seem straightforward to combine the underlying physical particles into a  
 1139 jet. There are three important characteristics required for any jet reconstruction  
 1140 algorithm to be used by ATLAS.

- 1141 • Collinear safety - if any particle with four-vector  $p$  is replaced by two particles  
 1142 of  $p_1, p_2$  with  $p = p_1 + p_2$ , the subsequent jet should not change

1143     • Radiative (infrared) safety - if any particle with four-vector  $p$  radiates a particle  
1144       of energy  $\alpha \rightarrow 0$ , the subsequent jet should not change

1145     • Fast - the jet algorithm should be “fast enough” to be useable by ATLAS  
1146       computing resources

1147 The first two requirements can be seen in terms of requirements on soft gluon emission.  
1148 Since partons emit arbitrarily soft gluons freely, one should expect the algorithms  
1149 to not be affected by this emission. The final requirement is of course a practical  
1150 limitation.

The algorithms in use by ATLAS (and CMS) which satisfies these requirements are collectively known as the  $k_T$  algorithms [106–108]. These algorithms iteratively combine the “closest” objects, defined using the following distance measures :

$$d_{ij} = \min(k_{T,i}^{2p}, k_{T,j}^{2p}) \frac{\Delta_{ij}^2}{R^2} \quad (6.4)$$
$$d_{iB} = k_{Ti}^{2p}$$

1151 In Eq.Eq. (6.4),  $k_{T,i}$  is the transverse momentum of  $i$ -th jet *constituent* and  $\Delta_{ij}$  is  
1152 the angular distance  $\Delta R$  between the constituents. Both  $R$  and  $p$  are adjustable  
1153 parameters:  $R$  is known as the (jet) *cone size* and  $p$  regulates the power of the energy  
1154 versus the geometrical scales. The algorithm sequence, for a given set of objects  $i$   
1155 with four-vector  $k$  :

1156 1. Find the minimum distance in the set of all  $d_{ij}$  and  $d_{iB}$ .

1157 2. If the distance is one of the  $d_{ij}$ , combine the input pair of object  $i, j$  and return  
1158 to (1). If the distance is one of the  $d_{iB}$ , remove the object from the list, call it  
1159 a jet, and return to (1).

1160 This process ends when all objects  $i$  have been added to a jet.

1161 Any choice of  $(p, R)$  has requirements of collinear and radiative safety. In essence,  
1162 the choice is then to optimize based on speed and the potential for new physics

1163 discoveries. In ATLAS, we make the choice of  $p = -1$  which is also known as the  
1164 *anti- $k_T$*  algorithm. The choice of  $R = 0.4$  is used for the distance parameter of the  
1165 jets.

1166 The primary “nice” quality of this algorithm can be seen with the following  
1167 example. Consider three inputs to an anti- $k_T$  algorithm, all with  $\eta = 0$  :

- 1168 • Object 1 :  $(p_T, \phi) = (30 \text{ GeV}, 0)$
- 1169 • Object 2 :  $(p_T, \phi) = (20 \text{ GeV}, -0.2)$
- 1170 • Object 3 :  $(p_T, \phi) = (10 \text{ GeV}, 0.2)$
- 1171 • Object 4 :  $(p_T, \phi) = (1 \text{ GeV}, 0.5)$

1172 In the case shown, it seems natural to first combine the “bigger” objects 1 and 2.  
1173 These then pick up the extra small object 3, and object 4 is not included in the jet.  
1174 This is what is done by the anti- $k_T$  algorithm. The (normal)  $k_T$  algorithm with  $p = 1$   
1175 instead combines the smallest objects, 3 and 4, first. Object 1 and 2 combine to form  
1176 their own jet, instead of these jets picking up object 3. This behavior is not ideal due  
1177 to effects from pileup, as we will see in the next section.

## 1178 Jet Reconstruction

1179 In ATLAS, jets are reconstructed using multiple different objects as inputs, including  
1180 tracks, “truth” objects, calorimeter clusters, and *particle flow objects* (PFOs).  
1181 For physics analyses, ATLAS primarily uses jets reconstructed from calorimeter  
1182 clusters, but we will describe the others here, as they are often used for systematic  
1183 uncertainties.

1184 Calorimeter jets are reconstructed using topoclusters with the anti- $k_T$  algorithm  
1185 with  $R = 0.4$ . The jet reconstruction algorithm is run on the collection of all  
1186 topoclusters reconstructed as in Sec. 6.1. Both EM and LCW scale clusters are

1187 used in the ATLAS reconstruction software and produce two sets of jets for analysis.  
1188 As stated above, this thesis presents an analysis using jets reconstructed using EM  
1189 scale clusters, which we refer to as *EM jets*.

1190 Tracks can be used as inputs to jet reconstruction algorithms. Jets reconstructed  
1191 from tracks are known as *track jets*. Since the ID tracks do not measure neutral  
1192 objects, these jets underestimate the true jet energy. However, these are still useful  
1193 for checks and derivations of systematic uncertainties.

1194 *Truth* jets are reconstructed from *truth* particles. In this case, truth is jargon  
1195 for simulation. In simulation, the actual simulated particles are available and used  
1196 as inputs to the jet reconstruction algorithms. Similarly to track jets, these are not  
1197 useful in and of themselves, but are used in conjunction with studies of reconstructed  
1198 jets.

1199 The last object used as inputs to jet reconstruction algorithms are *particle flow*  
1200 *objects* (PFOs). These are used extensively as the primary input to jet particle  
1201 reconstruction algorithms by the CMS collaboration [109]. Particle flow objects are  
1202 reconstructed by associating tracks and clusters through a combination of angular  
1203 distance measures and detector response measurements to create a composite object  
1204 which contains information from both the ID and the calorimeters. For calorimeter  
1205 clusters which do not have any associated ID track, the cluster is simply the PFO.  
1206 The natural association between tracks and clusters provides easy pileup subtraction  
1207 since tracks are easily associated to the primary vertex. As pileup has increased, the  
1208 utility of using PFOs as inputs to jet reconstruction has increased as well.

## 1209 Jet Calibration

1210 Jets as described in the last section are still *uncalibrated*. Even correcting the cluster  
1211 energies using the LCW does not fully correct the jet energy, due to particles losing  
1212 energy in the calorimeters. This is corrected using the *jet energy scale* (JES). The

1213 JES is a series of calibrations which on average restore the correct truth jet energy  
1214 for a given reconstructed jet. The steps to derive the JES are described in Fig. 6.8  
1215 and described here.

1216 The first step is the origin correction. This adjusts the jet to point at the  
1217 primary vertex. Next, is the jet-area based pileup correction. This step subtracts  
1218 the “average” pileup as measured by the energy density  $\rho$  outside of the jets and  
1219 assumes this is a good approximation for the pileup inside the jet. One removes  
1220 energy  $\Delta E = \rho \times A_{\text{jet}}$  in this step. The residual pileup correction applies a final offset  
1221 correction by parametrizing the change in jet energy as a function of the number of  
1222 primary vertices  $N_{\text{PV}}$  and the average number of interactions  $\mu$ . More details can be  
1223 found in [105].

1224 The next step is the most important single correction, known as the AbsoluteE-  
1225 taJES. Due to the use of noncompensation and sampling calorimeters in ATLAS,  
1226 the measured energy of a jet is a fraction of the true energy of the outgoing parton.  
1227 Additionally, due to the use of different technologies and calorimeters throughout the  
1228 detector, there are directional biases induced by these effects. The correction bins a  
1229 multiplicative factor in  $p_{\text{T}}$  and  $\eta$  which scales the reconstructed jets to corresponding  
1230 truth jet  $p_{\text{T}}$ . This step does not entirely correct the jets, since it is entirely a  
1231 simulation-based approach.

1232 The final steps are known as the global sequential calibration (GSC) and the  
1233 residual in-situ calibration. The GSC uses information about the jet showering shape  
1234 to apply additional corrections based on the expected shape of gluon or quark jets.  
1235 The final step is the residual in-situ calibration, which is only applied to data. This  
1236 step uses well-measured objects recoiling off a jet to provide a final correction to the  
1237 jets in data. In the low  $p_{\text{T}}$  region ( $20 \text{ GeV} \lesssim p_{T,\text{jet}} \lesssim 200 \text{ GeV}$ ),  $Z \rightarrow ll$  events are  
1238 used as a reference object. In the  $p_{\text{T}}$  region ( $100 \text{ GeV} \lesssim p_{T,\text{jet}} \lesssim 600 \text{ GeV}$ ), the reference  
1239 object is a photon, while in the high  $p_{\text{T}}$  region ( $p_{T,\text{jet}} \gtrsim 200 \text{ GeV}$ ), the high  $p_{\text{T}}$  jet is

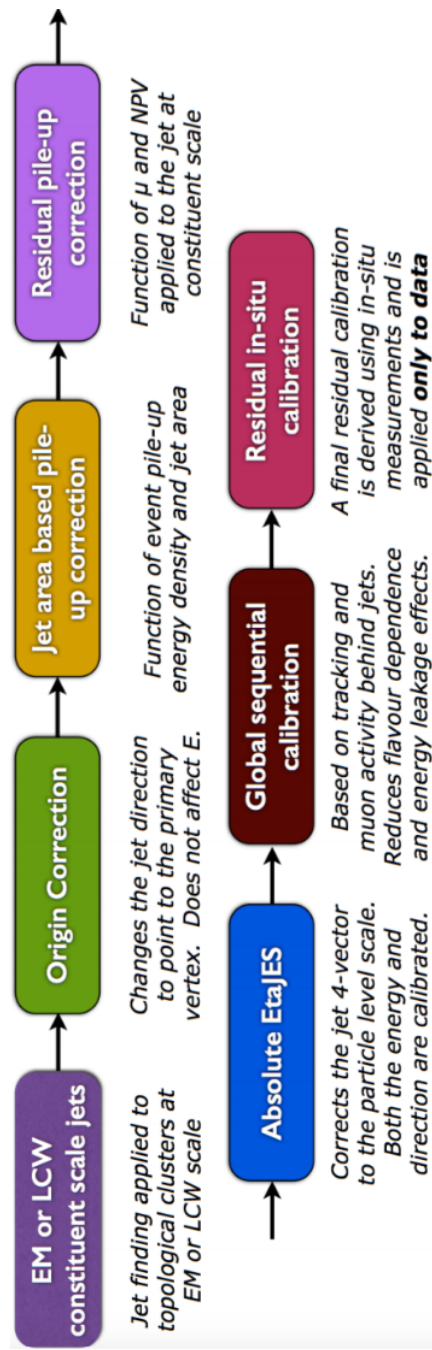


Figure 6.8: The steps used by ATLAS to calibrate jets

1240 compared to multiple smaller  $p_T$  jets. The reference object is the group of multijets.  
 1241 After the application of the residual in-situ calibration, the data and MC scales are  
 1242 identical up to corresponding uncertainties. The combined JES uncertainty as a  
 1243 function of  $p_T$  is shown in Fig. 6.9.

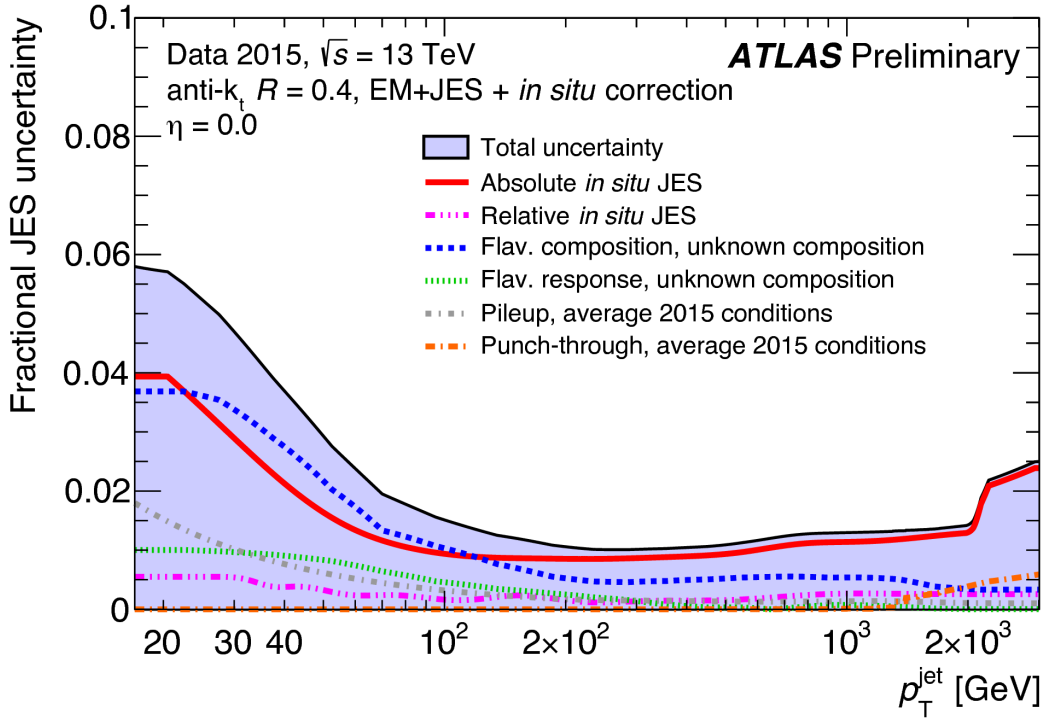


Figure 6.9: Combined jet energy scale uncertainty as a function of  $p_T$  at  $\eta = 0$ .

## 1244 Jet Vertex Tagger

1245 The *jet vertex tagger* (JVT) technique is used to separate pileup jets from those  
 1246 associated to the hard primary vertex [110]. The technique for doing so first involves  
 1247 *ghost association* [111]. Ghost association runs the anti- $k_T$  jet clustering algorithm  
 1248 on a combined collection of the topoclusters and tracks. The tracks *only* momenta  
 1249 are set to zero<sup>2</sup>, with only the directional information included. As discussed above,  
 1250 the anti- $k_T$  algorithm is “big to small”; tracks are associated to the “biggest” jet  
 1251 near them in  $(\eta, \phi)$ . This method uniquely associates each track to a jet, without  
 1252 changing the final jet kinematics.

1253 The JVT technique uses a combination of track variables to determine the  
 1254 likelihood that the jet originated at the primary vertex. For jets which have associated  
 1255 tracks from ghost association, this value ranges from 0 (likely pileup jet) to 1 (likely

---

<sup>2</sup>Not exactly zero, since zero momentum tracks wouldn’t have a well-defined  $(\eta, \phi)$  coordinate, but set to a value obeying  $p_{T,track} << 400$  MeV =  $p_{track,min}$ . This is the minimum momentum for a track to reach the ATLAS inner detector.

1256 hard scatter jet). Jets without associated tracks are assigned  $\text{JVT} = -.1$ . The  
1257 working point of  $\text{JVT} > .59$  is used for jets in this thesis.

1258 **B-jets**

1259 Jets originating from bottom quarks (b-jets) can be *tagged* by the ATLAS detec-  
1260 tor [112, 113]. B-hadrons, which have a comparatively long lifetime compared  
1261 to hadrons consisting of lighter quarks, can travel a macroscopic distance inside  
1262 the ATLAS detector. The high-precision tracking detectors identify the secondary  
1263 vertices from these decays and the jet matched to that vertex is called a *b-jet*. The  
1264 MV2c10 algorithm [112, 113], based on boosted decision trees, identifies these jets  
1265 using a combination of variables sensitive to the difference between light-quark and  
1266 b-quark jets. The efficiency of this tagger is 77%, with a rejection factor of 134 for  
1267 light-quarks and 6 for charm jets.

1268 **Missing Transverse Momentum**

1269 Missing transverse momentum  $E_{\text{T}}^{\text{miss}}$  [114] is a key observable in searches for new  
1270 physics, especially in SUSY searches [115, 116]. However,  $E_{\text{T}}^{\text{miss}}$  is not a uniquely  
1271 defined object when considered from the detector perspective (as compared to the  
1272 Feynammn diagram), and it is useful to understand the choices that affect the  
1273 performance of this observable in searches for new physics.

1274  **$E_{\text{T}}^{\text{miss}}$  Definitions**

*Hard* objects refers to all physical objects as defined in the previous sections. The  
 $E_{\text{T}}^{\text{miss}}$  reconstruction procedure uses these hard objects and the *soft term* to provide  
a value and direction of the missing transverse momentum. The  $E_{x(y)}^{\text{miss}}$  components

are calculated as:

$$E_{x(y)}^{\text{miss}} = E_{x(y)}^{\text{miss, } e} + E_{x(y)}^{\text{miss, } \gamma} + E_{x(y)}^{\text{miss, jets}} + E_{x(y)}^{\text{miss, } \mu} + E_{x(y)}^{\text{miss, soft}}, \quad (6.5)$$

1275 where each value  $E_{x(y)}^{\text{miss, } i}$  is the negative vectorial sum of the calibrated objects defined  
1276 in the previous sections.

1277 For purposes of  $E_T^{\text{miss}}$  reconstruction, we must assign an *overlap removal* ordering.  
1278 This is to avoid double counting of the underlying primitive objects (clusters and  
1279 tracks) which are inputs to the reconstruction of the physics objects. We resolve this  
1280 in the following order : electrons, photons , jets and muons. This is motivated by the  
1281 performance of the reconstruction of these objects in the calorimeters.

1282 The soft term  $E_{x(y)}^{\text{miss, soft}}$  contains all of the primitive objects which are not  
1283 associated to any of the reconstructed physics objects. we need to choose which  
1284 primitive object to use. The primary choices which have been used within ATLAS  
1285 are the *calorimeter-based soft term* (CST) and the *track-based soft term* (TST) [114].  
1286 Based on the soft term choice, we then call  $E_T^{\text{miss}}$  built with a CST (TST) soft term  
1287 simply CST (TST)  $E_T^{\text{miss}}$ . An additional option, which will be important as pileup  
1288 continues to increase, is particle flow  $E_T^{\text{miss}}$  (PFlow  $E_T^{\text{miss}}$ ).

1289 The CST  $E_T^{\text{miss}}$  was used for much of the early ATLAS data-taking. CST  $E_T^{\text{miss}}$   
1290 is built from the calibrated hard objects, combined with the calorimeter clusters  
1291 which are *not* assigned to any of those hard objects. In the absence of pileup, it  
1292 provides the best answer for the “true”  $E_T^{\text{miss}}$  in a given event, due to the impressive  
1293 hermiticity of the calorimeters. Unfortunately, the calorimeters do not know from  
1294 where their energy deposition came, and thus CST is susceptible to drastically reduced  
1295 performance with increasing pileup.

1296 TST  $E_T^{\text{miss}}$  is the standard for ATLAS searches as currently performed by ATLAS.  
1297 TST  $E_T^{\text{miss}}$  is reconstructed using the calibrated hard objects and a soft term from  
1298 the tracks which are not assigned to any of those hard objects. In particular, due  
1299 to the track-vertex association efficiency, one chooses tracks which only come from

1300 the primary vertex. This reduces the pileup contributions to the  $E_T^{\text{miss}}$  measurement.  
1301 However, since the ID tracking system is unable to detect neutral objects, the TST  
1302  $E_T^{\text{miss}}$  is “wrong”. In most searches for new physics, the soft  $E_T^{\text{miss}}$  is generally a small  
1303 fraction of the total  $E_T^{\text{miss}}$ , and thus this bias is not particularly hurtful.

1304 PFlow  $E_T^{\text{miss}}$  uses the PFOs described above to build the  $E_T^{\text{miss}}$ . The PFOs which  
1305 are assigned to hard objects are calibrated, and the PFOs which are not assigned  
1306 to any hard object are added to the soft term. In this context, it is convenient to  
1307 distinguish between “charged” and “neutral” PFOs. Charged PFOs can be seen as  
1308 a topocluster which has an associated track, while neutral PFOs do not. A charged  
1309 PFO is essentially a topocluster which is matched with the primary vertex. The  
1310 neutral PFOs have the same status as the original topoclusters. Thus a “full” PFlow  
1311  $E_T^{\text{miss}}$  should have performance somewhere between TST  $E_T^{\text{miss}}$  and CST  $E_T^{\text{miss}}$ <sup>3</sup>. A  
1312 *charged* PFlow  $E_T^{\text{miss}}$  should be the same as TST.

### 1313 Measuring $E_T^{\text{miss}}$ Performance : event selection

1314 The question is now straightforward: how do we compare these different algorithms?  
1315 We compare these algorithms in  $Z \rightarrow \ell\ell + \text{jets}$  and  $W \rightarrow \ell\nu + \text{jets}$  events. Due to  
1316 the presence of leptons, these events are well-measured “standard candles”. Here  
1317 we present the results in early 2015 data with  $Z \rightarrow \mu\mu$  and  $W \rightarrow e\nu$  events, as  
1318 shown in [117, 118]. This result was important to assure the integrity of the  $E_T^{\text{miss}}$   
1319 measurements at the higher energy and pileup environment of Run-2.

1320 The  $Z \rightarrow \ell\ell$  selection is used to measure the intrinsic  $E_T^{\text{miss}}$  resolution of the  
1321 detector. Neutrinos only occur in these events from heavy-flavor decays inside of jets,  
1322 and thus  $Z \rightarrow \ell\ell$  events have very low  $E_T^{\text{miss}}$ . This provides an ideal event topology  
1323 to understand the modelling of  $E_T^{\text{miss}}$  mismeasurement. Candidate  $Z \rightarrow \mu\mu$  events  
1324 are first required to pass a muon or electron trigger, as described in Tab. 5.1. Offline,

---

<sup>3</sup>Naively, due to approximate isospin symmetry, about 2/3 of the hadrons will be charged and 1/3 will be neutral.

1325 the selection of  $Z \rightarrow \mu\mu$  events requires exactly two medium muons. The muons are  
 1326 required to have opposite charge and  $p_T > 25$  GeV, and mass of the dimuon system  
 1327 is required to be consistent with the  $Z$  mass  $|m_l - m_Z| < 25$  GeV.

$W \rightarrow \ell\nu$  events are an important topology to evaluate the  $E_T^{\text{miss}}$  modelling in events with real  $E_T^{\text{miss}}$ . This  $E_T^{\text{miss}}$  is from the neutrino, which is not detected. The  $E_T^{\text{miss}}$  in these events has a characteristic distribution with a peak at  $\frac{1}{2}m_W$ . The selection of  $W \rightarrow e\nu$  events begins with the selection of exactly one electron of medium quality. A selection on TST  $E_T^{\text{miss}} > 25$  GeV drastically reduces the background from multijet events where the jet fakes an electron. The transverse mass is used to select the  $W \rightarrow e\nu$  events :

$$m_T = \sqrt{2p_T^\ell E_T^{\text{miss}}(1 - \cos \Delta\phi)}, \quad (6.6)$$

1328 where  $\Delta\phi$  is the difference in the  $\phi$  between the  $E_T^{\text{miss}}$  and the electron.  $m_T$  is required  
 1329 to be greater than 50 GeV.

1330 There are two main ingredients to investigate : the  $E_T^{\text{miss}}$  resolution and the  $E_T^{\text{miss}}$   
 1331 scale.

### 1332 Measuring $E_T^{\text{miss}}$ Performance in early 2015 data : metrics

1333 To compare these algorithms we use the  $E_T^{\text{miss}}$  resolution,  $E_T^{\text{miss}}$  scale, and linearity.  
 1334 Representative distributions of TST  $E_x^{\text{miss}}$ ,  $E_y^{\text{miss}}$ , and  $E_T^{\text{miss}}$  from early 2015 datataking are shown in Fig. 6.10.

The  $E_T^{\text{miss}}$  resolution is an important variable due to the fact that the bulk of the distributions associated to  $E_{x(y)}^{\text{miss}}$  are Gaussian distributed [Aad2012]. However, to properly measure the tails of this distribution, especially when considering non-calorimeter based soft terms, it is important to use the root-mean square as the proper measure of the resolution. This is strictly larger than resolution as measured using a fit to a Gaussian, due to the long tails from i.e. track mismeasurements. The resolution is measured with respect to two separate variables :  $\sum E_T$  and  $N_{\text{PV}}$ .  $\sum E_T$

is an important measure of the “total event activity”. It is defined as

$$\sum E_T = \sum p_T^e + \sum p_T^\gamma + \sum p_T^\tau + \sum p_T^{\text{jets}} + \sum p_T^\mu + \sum p_T^{\text{soft}}. \quad (6.7)$$

1336 The measurement as a function of  $N_{\text{PV}}$  is useful to understand the degradation of  
 1337  $E_T^{\text{miss}}$  performance with increasing pileup. Fig. 6.11 shows the TST  $E_T^{\text{miss}}$  resolution  
 1338 in the early 2015 data compared with simulation. The degradation of the TST  $E_T^{\text{miss}}$   
 1339 performance is shown as a function of pileup  $N_{\text{PV}}$  and total event activity  $\sum E_T$ . We  
 1340 see that the degradation is significant as a function of these variables, but simulation  
 1341 describes the data well.

Another important performance metric is the  $E_T^{\text{miss}}$  scale. This indicates how well we measure the magnitude of the  $E_T^{\text{miss}}$ , as CST  $E_T^{\text{miss}}$  contains additional particles from pileup, while soft neutral particles<sup>4</sup> are ignored by TST  $E_T^{\text{miss}}$ . To determine this in data, we again use  $Z \rightarrow \mu\mu$  events, where the  $Z \rightarrow \mu\mu$  system is treated as a well-measured reference object. The component of  $E_T^{\text{miss}}$  which is in the same direction as the reconstructed  $Z \rightarrow \mu\mu$  system is sensitive to potential biases in the detector response. The unit vector  $\mathbf{A}_Z$  of the  $Z$  system is defined as

$$\mathbf{A}_Z = \frac{\vec{p}_T^{\ell^+} + \vec{p}_T^{\ell^-}}{|\vec{p}_T^{\ell^+} + \vec{p}_T^{\ell^-}|}, \quad (6.8)$$

1342 where  $\vec{p}_T^{\ell^+}$  and  $\vec{p}_T^{\ell^-}$  are the transverse momenta of the leptons from the  $Z$  boson  
 1343 decay. The relevant scale metric is the mean value of the  $\vec{E}_T^{\text{miss}}$  projected onto  $\mathbf{A}_Z$  :  
 1344  $\langle \vec{E}_T^{\text{miss}} \cdot \mathbf{A}_Z \rangle$ . In Fig. 6.12, the scale is shown for the early 2015 dataset. The negative  
 1345 bias, which is maximized at about 5 GeV, is a reflection of two separate effects. The  
 1346 soft neutral particles are missed by the tracking system, and thus ignored in TST  
 1347  $E_T^{\text{miss}}$ . Missed particles due to the limited ID acceptance can also affect the scale.

For events with real  $E_T^{\text{miss}}$ , one can also look at the *linearity* in simulation. This

---

<sup>4</sup>“Soft” here means those particles which are not hard enough to be reconstructed as their own particle, using the reconstruction algorithms above.

is defined as

$$\text{linearity} = \langle \frac{E_T^{\text{miss}} - E_T^{\text{miss,Truth}}}{E_T^{\text{miss,Truth}}} \rangle. \quad (6.9)$$

1348  $E_T^{\text{miss,Truth}}$  refers to “truth” particles as defined before, or the magnitude of the vector  
1349 sum of all noninteracting particles. The linearity is expected to be zero if the  $E_T^{\text{miss}}$   
1350 is reconstructed at the correct scale.

## 1351 Particle Flow Performance

1352 As described above, the resolution, scale, and linearity are metrics to understand the  
1353 performance of the different  $E_T^{\text{miss}}$  algorithms. In this section, we present comparisons  
1354 of the different algorithms, including particle flow, in simulation and using a data  
1355 sample from 2015 of  $80 \text{ pb}^{-1}$ . In these plots, “MET\_PFlow-TST” refers to charged  
1356 PFlow  $E_T^{\text{miss}}$ , while the other algorithms are as described above.

1357 Figs. 6.14 and 6.15 show the resolution and scale in simulated  $Z \rightarrow \mu\mu$  events.  
1358 The resolution curves follow the expected behavior discussed before. Due to the high  
1359 pileup in 2015 run conditions, the CST  $E_T^{\text{miss}}$  resolution is poor, and further degrades  
1360 with increasing pileup and event activity. The “regular” PFlow  $E_T^{\text{miss}}$  shows reduces  
1361 pileup and event activity dependence as compared to the CST. PFlow  $E_T^{\text{miss}}$  can be  
1362 seen as a hybrid of TST  $E_T^{\text{miss}}$  and CST  $E_T^{\text{miss}}$ . The charged PFOs ( $\sim 2/3$ ) are pileup  
1363 suppressed, while the neutral PFOs (or topoclusters) are not. Both charged PFlow  
1364 and TST  $E_T^{\text{miss}}$  show only a small residual dependence on  $N_{\text{PV}}$  and  $\sum E_T$ , since they  
1365 have fully pileup suppressed inputs through track associations.

1366 The scale plots are shown for  $Z+\text{jets}$  events and  $Z$  events with no jets. For the  
1367 nonsuppressed CST, the scale continues to worsen with increasing  $p_T^Z$ . The standard  
1368 PFlow algorithm performs the second worst in the region of high  $p_T^Z$ , but is the best at  
1369 low  $p_T^Z$ . We note the improved scale of the charged PFlow  $E_T^{\text{miss}}$  compared to the TST  
1370  $E_T^{\text{miss}}$ . Considering the resolution is essentially identical, the PFlow algorithm is better  
1371 picking up the contributions from additional neutral particles. In events with no jets,

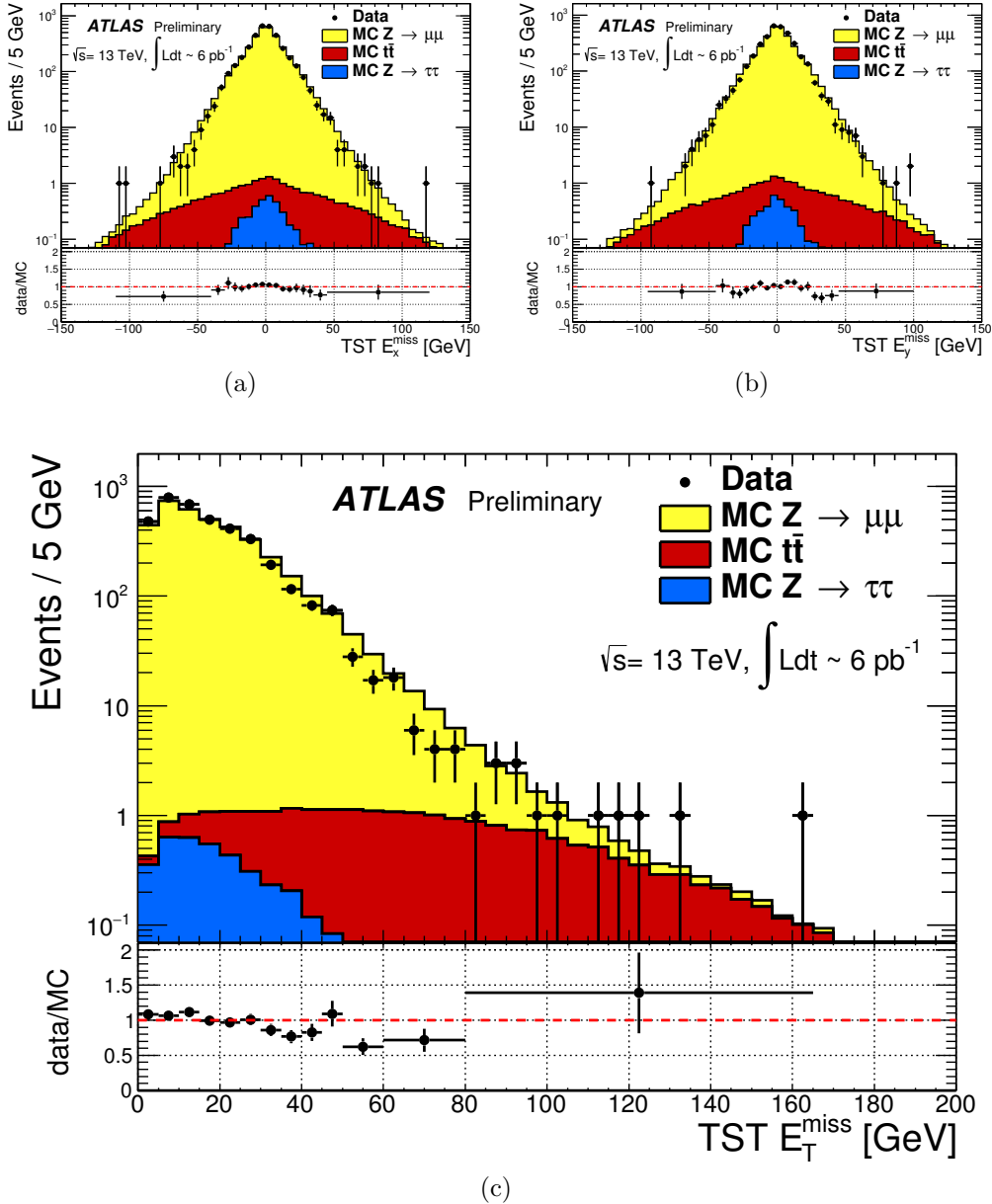


Figure 6.10: TST  $E_x^{\text{miss}}$ ,  $E_y^{\text{miss}}$ , and  $E_T^{\text{miss}}$  distributions of early  $\sqrt{s} = 13$  TeV data compared with simulation after the  $Z \rightarrow \mu\mu$  selection. The data sample consists of 6 pb $^{-1}$ .

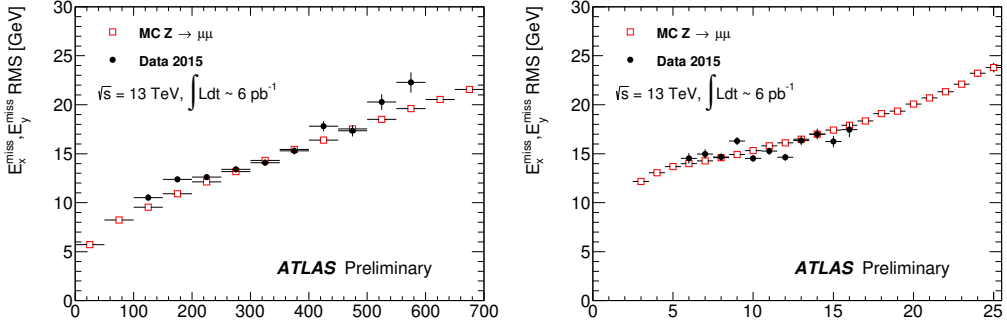


Figure 6.11: Resolution of TST  $E_T^{\text{miss}}$  of early  $\sqrt{s} = 13$  TeV data compared with simulation after the  $Z \rightarrow \mu\mu$  selection. The data sample consists of  $6 \text{ pb}^{-1}$ .

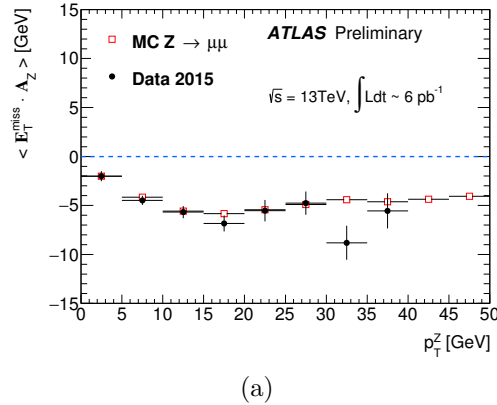


Figure 6.12: Scale of TST  $E_T^{\text{miss}}$  of early  $\sqrt{s} = 13$  TeV data compared with simulation after the  $Z \rightarrow \mu\mu$  selection. The data sample consists of  $6 \text{ pb}^{-1}$ .

1372 the soft term is essentially the only indication of the  $E_T^{\text{miss}}$  mismeasurement, since  
 1373 the muons will be well-measured. In this case, the pileup effects cancel, on average,  
 1374 due to the  $U(1)_\phi$  symmetry of the ATLAS detector, and CST performs rather well  
 1375 compared to the more complicated track-based algorithms. The full PFlow algorithm  
 1376 performs best, since it provides a small amount of pileup suppression on the neutral  
 1377 components from CST.

1378 The resolution and linearity are shown in simulated  $W \rightarrow e\nu$  events in Fig. 6.13.  
 1379 The resolution in  $W \rightarrow e\nu$  events shows a similar qualitative behavior to  $Z \rightarrow$   
 1380  $\mu\mu$  events. The CST  $E_T^{\text{miss}}$  has the worst performance, with charged PFlow  $E_T^{\text{miss}}$

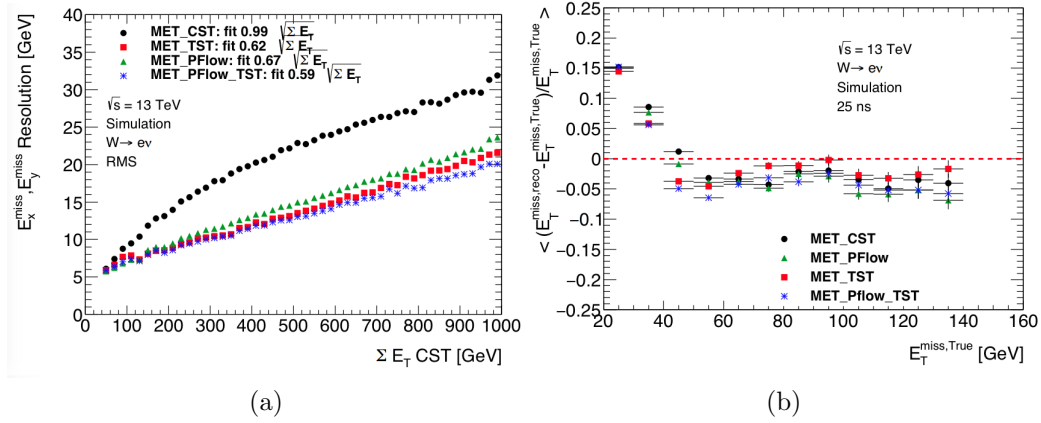


Figure 6.13: Comparison of  $E_{\text{T}}^{\text{miss}}$  resolution and linearity using different  $E_{\text{T}}^{\text{miss}}$  algorithms with simulated  $W \rightarrow e\nu$  events.

1381 performing best. The surprise here is the scale associated to TST  $E_{\text{T}}^{\text{miss}}$  has the  
 1382 strongest performance throughout the space parameterized by  $E_{\text{T}}^{\text{miss,Truth}}$ , except for  
 1383 one bin at  $40 \text{ GeV} < E_{\text{T}}^{\text{miss,Truth}} < 50 \text{ GeV}$ . The scale in these events is best measured  
 1384 using a track-based soft term.

1385 The resolution also investigated in real data passing the  $Z \rightarrow \mu\mu$  selection  
 1386 described above. A comparison of the  $E_{\text{T}}^{\text{miss}}$  between real data and simulation for  
 1387 each algorithm is presented in Fig. 6.16. The resolution as a function of  $\sum E_{\text{T}}$  and  
 1388  $N_{\text{PV}}$  is shown in Fig. 6.17 for this dataset. Overall, the real dataset shows the  
 1389 same general features as the simulation dataset in terms of algorithm performance.  
 1390 However, the performance of all algorithms seems to be significantly worse in data.  
 1391 This is likely due to simplifications made in the simulation: soft interactions which  
 1392 are not simulated have a significant effect on an event level variable such as the  $E_{\text{T}}^{\text{miss}}$   
 1393 resolution.

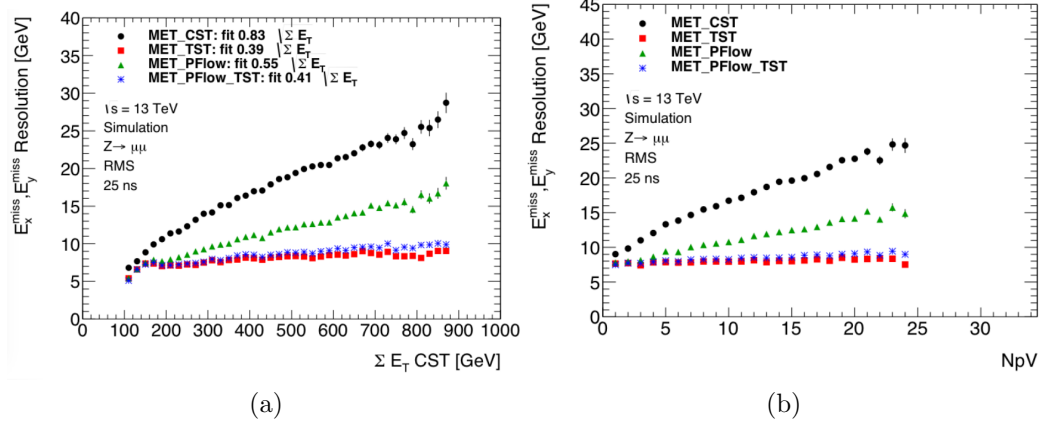


Figure 6.14: Comparison of  $E_T^{\text{miss}}$  resolution using different  $E_T^{\text{miss}}$  algorithms with simulated  $Z \rightarrow \mu\mu$  events.

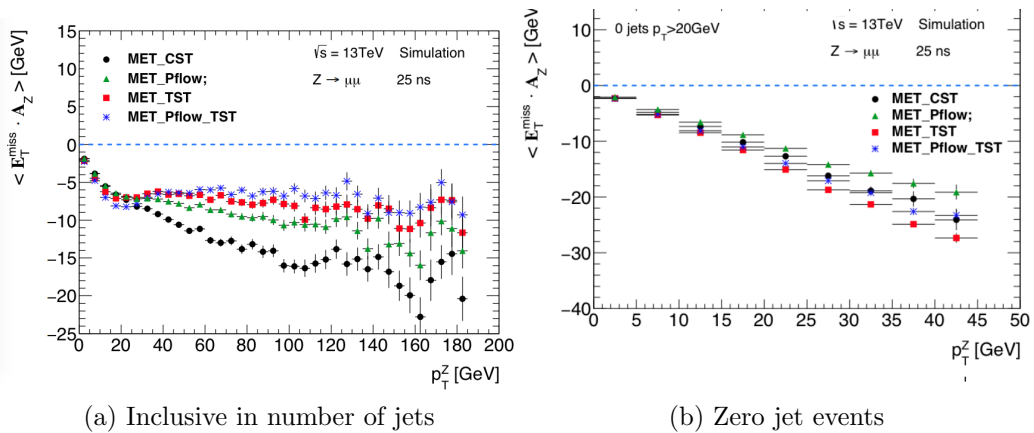


Figure 6.15: Comparison of  $E_T^{\text{miss}}$  scale using different  $E_T^{\text{miss}}$  algorithms with simulated  $Z \rightarrow \mu\mu$  events.

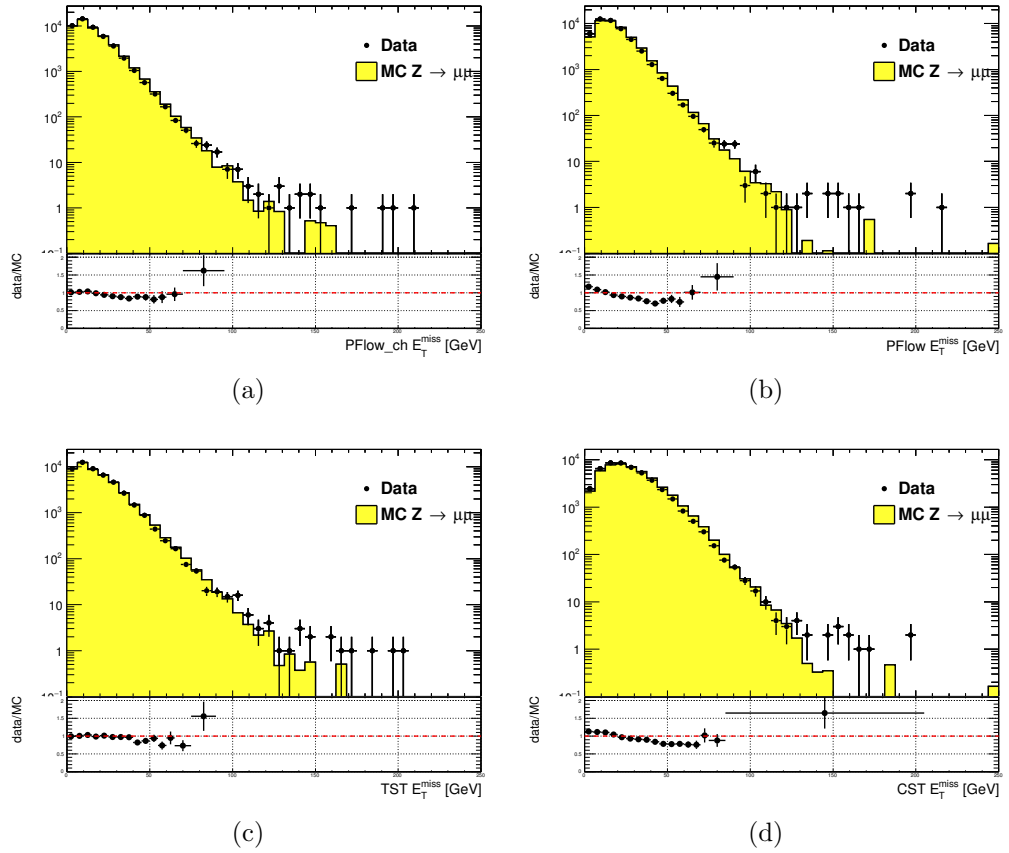


Figure 6.16: Comparison of  $E_T^{\text{miss}}$  distributions using different  $E_T^{\text{miss}}$  algorithms with a data sample of  $80 \text{ pb}^{-1}$  after the  $Z \rightarrow \mu\mu$  selection

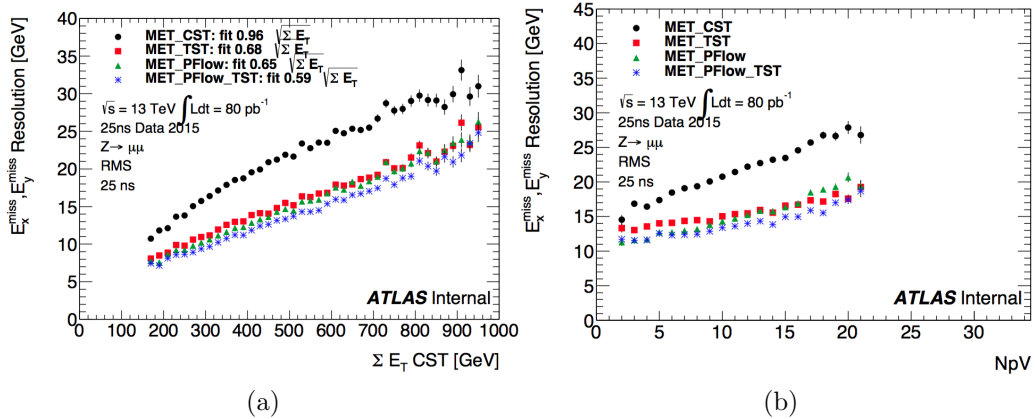


Figure 6.17: Comparison of  $E_T^{\text{miss}}$  resolution using different  $E_T^{\text{miss}}$  algorithms with a data sample of  $80 \text{ pb}^{-1}$  after the  $Z \rightarrow \mu\mu$  selection



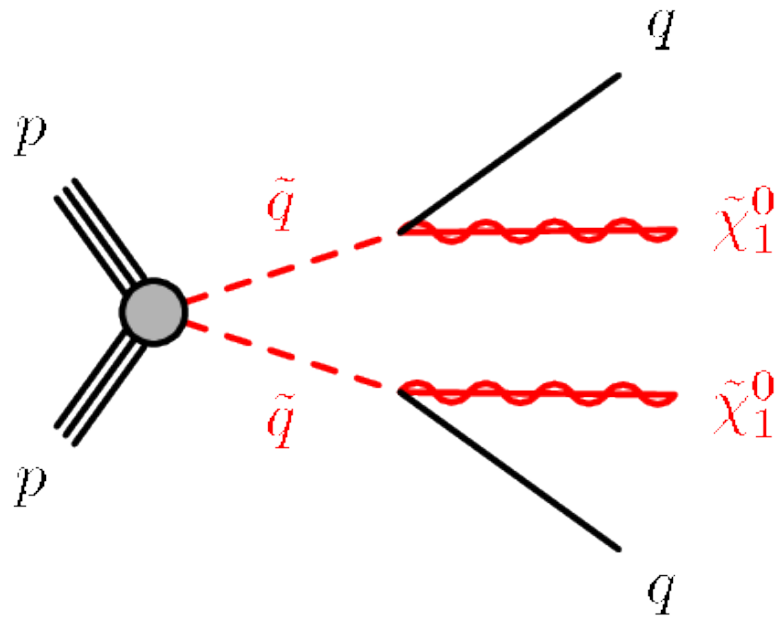
*Recursive Jigsaw Reconstruction*

1396 *Recursive Jigsaw Reconstruction* (RJR) [119, 120] is a novel algorithm used for  
 1397 the analysis presented in this thesis. RJR is the conceptual successor to the razor  
 1398 technique [121, 122], which has been used successfully in many new physics searches  
 1399 [37, 38, 40, 41, 47, 123]. In this chapter, we will first present the razor technique,  
 1400 and describe the razor variables. We will then present the RJR algorithm. After the  
 1401 description of the algorithm, we will describe the precise RJR variables used in the  
 1402 analysis.

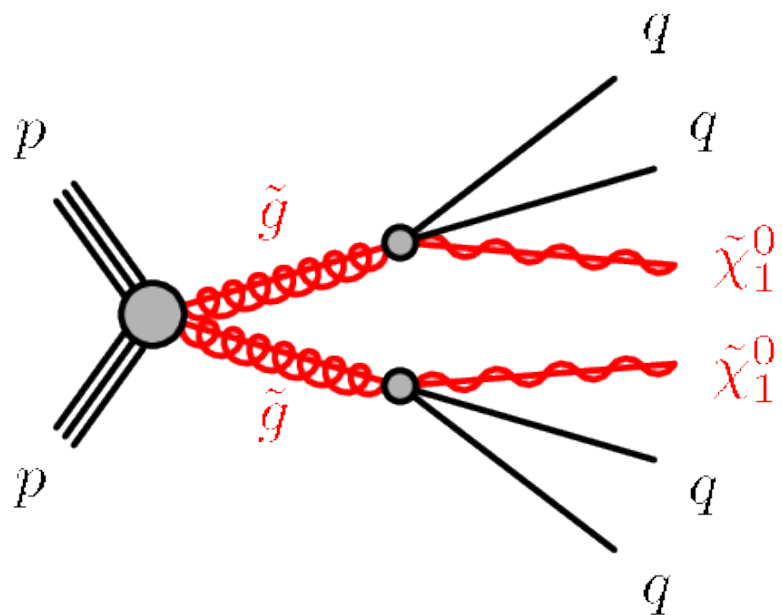
1403 **7.1 Razor variables**1404 **Motivation**

1405 We consider SUSY models where gluinos and squarks are pair-produced. Pair-  
 1406 production is a consequence of the  $R$ -parity imposed in many SUSY models.  $R$ -parity  
 1407 violation is highly constrained by limits on proton decay [15], and is often assumed  
 1408 in SUSY model building. The Feynman diagrams considered are shown in Fig. 7.1.

1409 The consequences of this  $\mathbb{Z}_2$  symmetry are drastic [15]. To understand the  
 1410 utility of the razor variables, the stability of the lightest supersymmetric particle  
 1411 is important. In many SUSY models, including the ones considered in this thesis,  
 1412 this is the lightest neutralino  $\tilde{\chi}_1^0$ . This means that on either side of a SUSY decay  
 1413 process, where we begin with sparticle pair production, we have a final state particle  
 1414 which is not detected. Generically, this leads to  $E_T^{\text{miss}}$ . Selections based on  $E_T^{\text{miss}}$  are



(a) Squark pair production



(b) Gluino pair production

Figure 7.1: Feynman diagrams for the SUSY signals considered in this thesis

1415 very good at reducing backgrounds, for example from QCD processes.

1416 However, there are limitations to searches based on  $E_T^{\text{miss}}$ . Due to jet mismeasurements, instrumental failures, finite detector acceptance, nongaussian tails in the detector response, and production of neutrinos inside of jets, there are many sources of “fake”  $E_T^{\text{miss}}$  which does not correspond to a Standard Model neutrino or new physics object such as an LSP. An additional limitation is the complete lack of longitudinal information. As events from QCD backgrounds tend to have higher boosts along the  $z$ -direction, this neglects an important discriminator for use in searches for SUSY. Finally,  $E_T^{\text{miss}}$  is only one object, which is a measurement for *two* separate LSPs. If one could factorize this information somehow, this would provide additional information to potentially discriminate against backgrounds. The *razor variables* ( $M_{\Delta}^R, R^2$ ) are more robust than  $E_T^{\text{miss}}$ -based variables against sources of fake  $E_T^{\text{miss}}$  as well as providing additional longitudinal information which can be used to discriminate against backgrounds [121, 122].

## 1429 Derivation of the razor variables

1430 To derive the razor variables ( $M_{\Delta}^R, R^2$ ), we start with a generic situation of the pair  
1431 production of heavy sparticles with mass  $m_{\text{Heavy}}$ .<sup>1</sup> Each sparticle decays to a number  
1432 of observable objects (in this thesis, jets), and an unobservable  $\tilde{\chi}_1^0$  of mass  $m_{\tilde{\chi}_1^0}$ . We  
1433 will combine all of the jets into a *megajet*; this process will be described below. We  
1434 begin by analyzing the decay in the “rough-approximation”, or in modern parlance,  
1435 *razor frame* ( $R$ -frame). This is the frame where the sparticle is at rest. Note that  
1436 by construction, there are two razor frames corresponding to each sparticle. The  
1437 complete set of frames considered in the case of the razor variables is shown in Fig. 7.2.

1438

---

<sup>1</sup>The razor variables have undergone confusing notational changes over the years. We will be self-consistent, but the notation used here may be different from references.

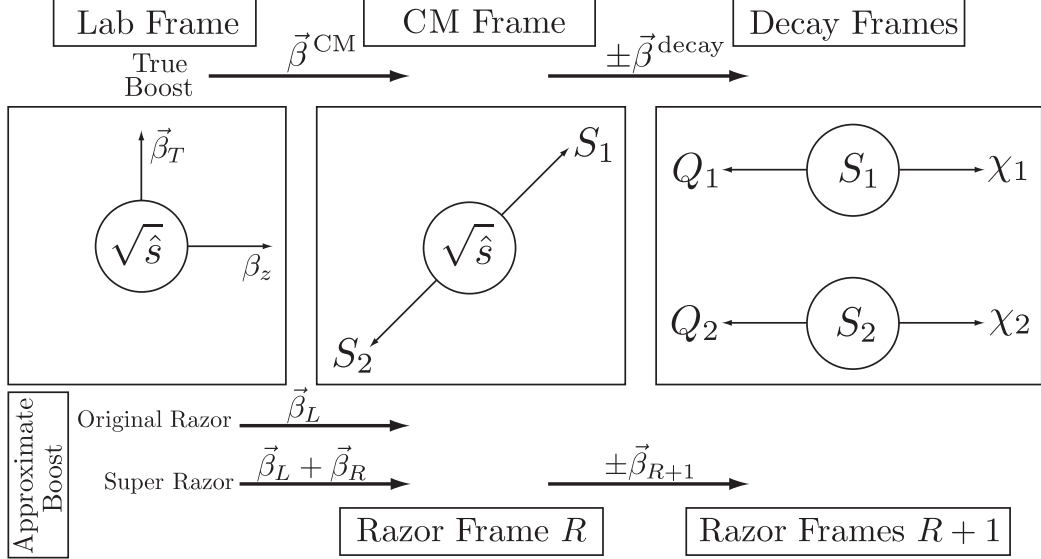


Figure 7.2: Frames considered when applying the razor technique, from [122].

In the  $R$ -frame, the decay is straightforward to analyze. Each megajet has energy  $E_1^R, E_2^R$  in the frame of its parent sparticle, and we define a characteristic mass  $M_R$ :

$$E_1^R = E_2^R = \frac{m_{\text{Heavy}}^2 - m_{\tilde{\chi}_1^0}^2}{2m_{\text{Heavy}}} \quad (7.1)$$

$$M_R = 2 \times E_1^R = 2 \times E_2^R = \frac{m_{\text{Heavy}}^2 - m_{\tilde{\chi}_1^0}^2}{m_{\text{Heavy}}} \quad (7.2)$$

For cases where  $m_{\text{Heavy}} \gg m_{\tilde{\chi}_1^0}$ ,  $M_R$  is an estimator of  $m_{\text{Heavy}}$ . This scenario happens in the SM, such as in  $t\bar{t}$  and  $WW$  events, where the  $\tilde{\chi}_1^0$  is instead a neutrino.

The question now is how to use this simple derivation in the lab frame, where we actually conduct our measurements. There are two related issues: how to combine the jets into the megajets, and how to “transform” (or *boost*) to the  $R$ -frame.

To construct the megajets, the procedure is the following. For a given set of jets  $j_i, i = 0, \dots, n_{\text{jet}}$ , we construct *all* combinations of their four-momenta such that there is at least one jet inside each megajet. Among this set of possible megajets  $\{J_{1,2}\}$ , we make the following unique choice for the megajets. We minimize the following quantity:

$$m_{J_1}^2 + m_{J_2}^2. \quad (7.3)$$

1444 In modern parlance, this is known as a *jigsaw*. This is a *choice*. It may have nice  
 1445 physical qualities or satisfy some convenient intuition about the events, but as we  
 1446 will see later, other choices are possible.

We now describe how we translate our megajet kinematics, measured in the lab frame, to the  $R$ -frame. This is a two-step procedure. We perform two *boosts*: a longitudinal boost  $\beta_L$  and a transverse boost  $\beta_T$ . Schematically,

$$J_1^R \xrightarrow{\beta_T} J_1^{CM} \xrightarrow{\beta_L} J_1^{\text{lab}} \quad (7.4)$$

$$J_2^R \xrightarrow{-\beta_T} J_2^{CM} \xrightarrow{\beta_L} J_2^{\text{lab}} \quad (7.5)$$

(7.6)

1447 The  $J_{1,2}^{\text{lab}}$  correspond directly to those in the megajet construction. We drop the  
 1448 “lab” designation for the rest of the discussion. The question is how to compute the  
 1449 magnitudes of these boosts, given the missing degrees of freedom.

For the transverse boost  $\beta_T$ , recall the two megajets have equal energies in their  $R$ -frame by construction. This constraint can be reexpressed as a constraint on the magnitude of this boost, in terms of the boost velocity  $\beta_L$  and corresponding Lorentz factor  $\gamma_L$ :

$$\beta_T = \frac{\gamma_L(E_1 - E_2) - \gamma_L\beta_L(p_{1,z} - p_{2,z})}{\hat{\beta}_T \cdot (p_{1,T} + p_{2,T})} \quad (7.7)$$

where we have denoted the lab frame four-vectors as  $p_i = (E_i, \vec{p}_{i,T}, p_z)$ . We now make the *choice* for the direction of the transverse boost  $\hat{\beta}_T$ :

$$\hat{\beta}_T = \frac{\vec{p}_{1,T} + \vec{p}_{2,T}}{|\vec{p}_{1,T} + \vec{p}_{2,T}|}. \quad (7.8)$$

1450 This choice forces the denominator of Eq. (7.7) to unity, and corresponds to aligning  
 1451 the transverse boost direction with the sum of the two megajets transverse directions.

For the longitudinal boost, we choose  $\vec{\beta}_L$  along the  $z$ -direction, with magnitude:

$$\beta_L = \frac{p_{1,z} + p_{2,z}}{E_1 + E_2}. \quad (7.9)$$

1452 Viewed in terms of the original parton-parton interactions, this is the choice which  
 1453 “on average” gives  $p_{z,\text{CM}} = 0$ , as we would expect. This well-motivated choice due to  
 1454 the total  $z$  symmetry.

We now have intuitive guesses for both boosts, which allow us write our original characteristic mass  $M_R$  in terms of the lab frame variables, by application of these two Lorentz boosts to the energies of Eq. (7.1):

$$M_R^2 \xrightarrow{\beta_T} M_{R,\text{CM}}^2 \xrightarrow{\beta_L} M_{R,\text{lab}}^2 = (E_1 + E_2)^2 - (p_{1,z} + p_{2,z})^2. \quad (7.10)$$

Finally, we define an additional mass variable, which include the missing transverse energy  $E_T^{\text{miss}}$ . Importantly, note that we did not use the  $E_T^{\text{miss}}$  in the definition of  $M_R$ , which depends only on the energies of the megajets. Backgrounds with no invisible particles (such as multijet events) must have  $J_1$  and  $J_2$  back to back. Thus, we define the transverse mass:

$$(M_R^T)^2 = \frac{1}{2} \left[ E_T^{\text{miss}}(p_{1,T} + p_{2,T}) - \vec{E}_T^{\text{miss}} \cdot (\vec{p}_{1,T} + \vec{p}_{2,T}) \right]. \quad (7.11)$$

Generally, we have  $M_R^T < M_R$ , so we define a dimensionless ratio (“the razor”):

$$R^2 = \left( \frac{M_R^T}{M_R} \right)^2. \quad (7.12)$$

1455 For signal events, we expect  $R$  to peak around  $R \sim 1/4$ , while backgrounds without  
 1456 real  $E_T^{\text{miss}}$  are expected to have  $R \sim 0$ .

## 1457 7.2 Recursive Jigsaw Reconstruction

1458 Recursive Jigsaw Reconstruction is an algorithm allowing the imposition of a decay  
 1459 tree interpretation of a particular event [119, 120]. The idea is to construct the  
 1460 underlying kinematic variables (the masses and decay angles) on an event-by-event  
 1461 level. This is done “recursively” through a decay tree which corresponds, sometimes  
 1462 approximately, to the Feynmann diagram for the signal process of interest. After

1463 each step of the recursive procedure, the objects are “placed” into one bucket (or  
1464 branch) of the decay tree, and the process is repeated on each frame we have imposed.  
1465 The imposition of these decay trees is done by a *jigsaw* rule: a procedure to resolve  
1466 combinatoric or kinematic ambiguities while traversing the decay tree. This procedure  
1467 is performed by the `RestFrames` software packages [124]

1468 In events where all objects are fully reconstructed, this is straightforward, and  
1469 of course has been used for many years in particle physics experiments. Events  
1470 which contain  $E_T^{\text{miss}}$  are more difficult, due to the loss of information: the potential  
1471 for multiple mismeasured or simply unmeasureable objects, such as neutrinos or the  
1472 LSP in SUSY searches. There can also be combinatoric ambiguities in deciding how  
1473 to group objects of the same type. Specifically here, we will be concerned with the  
1474 jigsaw rule to associate jets to a particular branch of a decay tree. The jigsaw rules  
1475 we impose will remove these ambiguities. First, we will describe the decay trees used  
1476 in this thesis, and then describe the jigsaw rules we will use. Finally, we will describe  
1477 the variables used in the all-hadronic SUSY search presented in this thesis.

## 1478 Decay Trees

1479 The decay trees imposed in this thesis are shown in Fig. 7.3. Leaving temporarily the  
1480 question of “how” we apply the jigsaw rules, let us compare these trees to the signal  
1481 processes of interest. In particular, we want to compare the Feynman diagrams of  
1482 Fig. 7.1 with the decay trees of Fig. 7.3. The decay tree in Fig. 7.4(a) corresponds  
1483 exactly to that expected from squark pair production, and matches closely with the  
1484 principles of the razor approach. We first apply a jigsaw rule, indicated by a line, to  
1485 the kinematics of the objects in the *lab* frame. This outputs the kinematics of our  
1486 event in the *parent-parent (PP)* frame, or in the razor terminology, the CM frame.  
1487 That is, the kinematics of this frame are an estimator for the kinematics in the center  
1488 of mass frame of the CM of pass of the squark pair production system. We apply

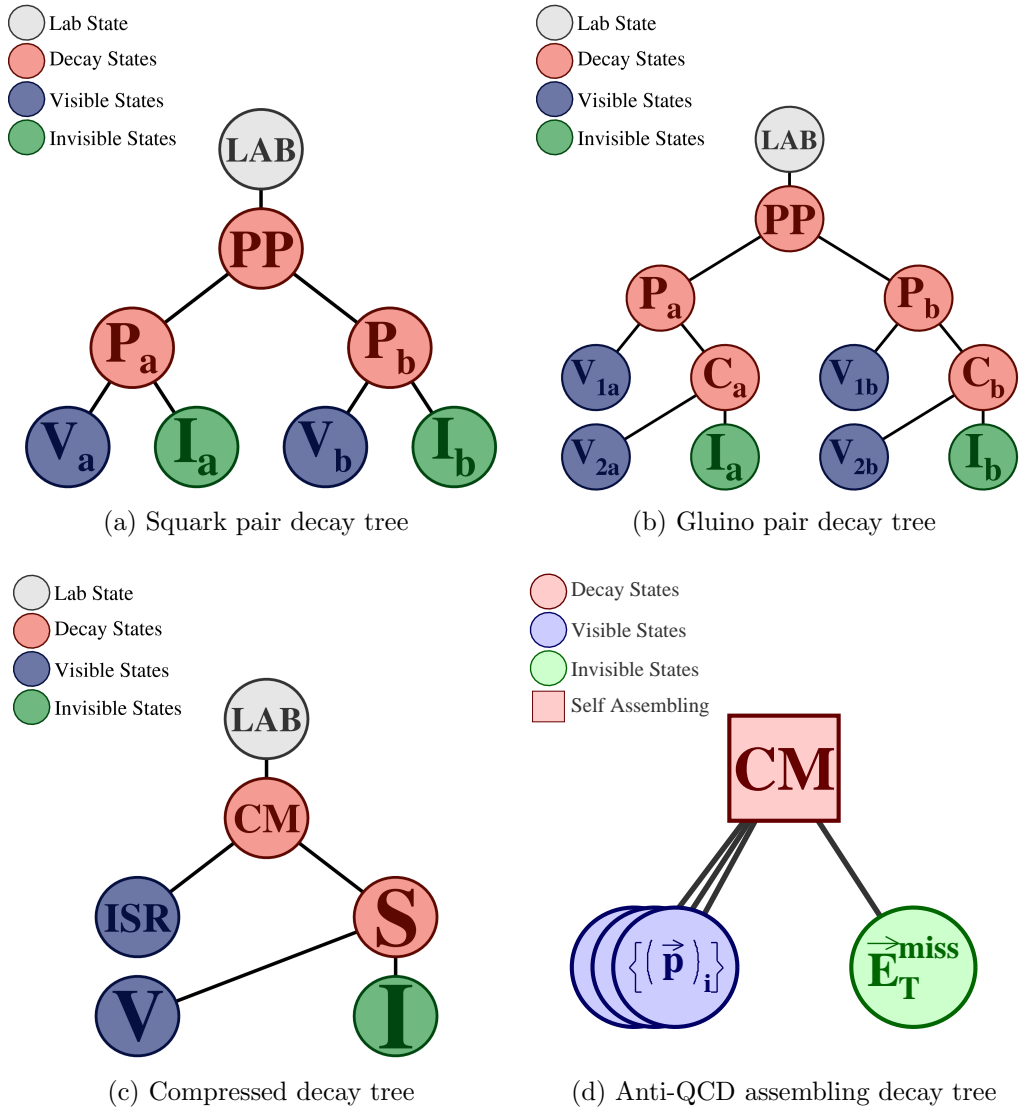


Figure 7.3: RJR decay trees

1489 another jigsaw, which splits the objects in the  $PP$  frame into two new frames, known  
 1490 as the  $P_a$  and  $P_b$  systems. These are equivalent to the razor frames, and represent  
 1491 proxy frames where each squark is at rest. In  $P_a$  ( $P_b$ ), the decay is symmetric between  
 1492 the visible  $V_a$  ( $V_b$ ) objects and the invisible system  $I_a$  ( $I_b$ ). To generate the estimator  
 1493 of the kinematics of the  $V_a$ ,  $V_b$ ,  $I_a$ , and  $I_b$  systems in the  $P_a$  and  $P_b$  systems, we apply  
 1494 another jigsaw rule to split the total  $E_T^{\text{miss}}$  between  $P_a$  and  $P_b$ . For the case of squark  
 1495 pair production, this is the expected decay tree, and we stop the recursive calculation

1496 at that level.

1497 In the case of gluino pair production, we expect two additional jets, and we can  
1498 perform an additional boost in each of  $P_a$  and  $P_b$ , to what we call the  $C_a$  and  $C_b$   
1499 frames. The decay tree is shown in Fig. 7.4(b). In this case we apply a jigsaw at the  
1500 level of  $P_a$  ( $P_b$ ) which separates a single visible object  $V_{1a}$  ( $V_{2a}$ ) from the child frame  
1501  $C_a$  ( $C_b$ ). This child frame represents the hypothesized squark after the decay  $\tilde{g} \rightarrow g\tilde{q}$ ,  
1502 which then decays as in the squark case.

The third decay tree used in this thesis is the *compressed* decay tree. Compressed refers to signal models which have a small splitting between the mass of the proposed sparticle and the  $\tilde{\chi}_1^0$ . The sparticle decay products in compressed models (i.e. the jets and  $E_T^{\text{miss}}$ ) do not generally have large scale [119]. Instead, the strategy is generally to look for a large-scale initial state radiation (ISR) jet which is recoiling off the pair-produced sparticles. In the case where the LSPs receive no momentum from the sparticle decays, the following approximation holds:

$$E_T^{\text{miss}} \sim -p_T^{\text{ISR}} \times \frac{m_{\tilde{\chi}_1^0}}{m_{\text{sparticle}}} \quad (7.13)$$

1503 where  $p_T^{\text{ISR}}$  is the transverse momentum associated to the entire ISR system.

1504 RJR offers a natural and straightforward way to exploit this feature in events  
1505 containing ISR. One imposes the simple decay tree in Fig. 7.4(c) with associated  
1506 jigsaw rules. With suitable jigsaw rules, this decay tree “picks out” the large  $p_T$  ISR  
1507 jet, recoiling off the  $E_T^{\text{miss}}$  and additional radiation from the sparticle decays. This  
1508 provides a convenient set of variables to understand compressed scenarios.

1509 There is one other decay tree, shown in Fig. 7.4(d). This is special, as it is only  
1510 used for the purpose of QCD rejection, and does not directly map to a sparticle decay  
1511 chain. Due to the large production cross-sections of QCD events, even very rare large  
1512 jet mismeasurements can lead to significant  $E_T^{\text{miss}}$  which can enter the signal region.  
1513 To reduce these backgrounds, one usually rejects events which contain jets which are

1514 “too close” by some distance metric to the  $E_T^{\text{miss}}$  in the event. Generally, in the past,  
1515 the distance metric has been defined as simply the angular distance  $\Delta R$ .

1516 The *self-assembling tree* can be seen as defining a distance metric which depends  
1517 on the magnitudes of the  $E_T^{\text{miss}}$  and jets rather than simply their distance in angular  
1518 space. Depending on the exact kinematics, the one or two closest jets are found, and  
1519 label the  $E_T^{\text{miss}}$  *siblings*.

1520 In this section, we have seen how one imposes particular decay trees on an event  
1521 to produce a basis of kinematic variables in the approximated frames relevant to  
1522 the hypothesized sparticle decay chain. This explains why we call this procedure  
1523 “recursive”: the procedure can be iterated through as many steps of a decay tree as  
1524 necessary, and each application of a jigsaw rule is dependent on the variables produced  
1525 in the last step. The question is: *what are these jigsaw rules?*.

## 1526 Jigsaw Rules

1527 Jigsaw rules are the fundamental step that allow the recursive definitions of the  
1528 variables of interest. The rules we imposed must fully define kinematic variables  
1529 at each step in a decay tree. The only possible solution to fully define the event  
1530 kinematics in terms of the frames of the hypothesized decays is the imposition of  
1531 external constraints to eliminate additional degrees of freedom. In principle, these  
1532 need not have any particular physical motivation. Instead, the jigsaw rules are a  
1533 way to resolve the mathematical ambiguities to fully reconstruct the full decay chain  
1534 kinematics. However, most practical jigsaw rules also have some reasonable physical  
1535 motivation, which we will also elucidate.

1536 In the original razor point of view, some jigsaw rules can be seen as the definitions  
1537 of the boosts which relate the different frames of interest, while other rules allow one  
1538 to combine multiple objects and place them into a particular hemisphere (previously  
1539 megajet). These are the two forms of jigsaw rules: combinatoric and kinematic. As

1540 we have stressed before, the jigsaw rules are a *choice*: as long as a particular jigsaw  
1541 rule allows the definition of variables at each step in a decay tree, it is “as valid” as  
1542 any other rule.

Practically speaking, we use only a small subset of possible jigsaw rules. The combinatoric jigsaw rule has already been introduced as megajet construction above. The minimization of

$$m_{J_1}^2 + m_{J_2}^2. \quad (7.14)$$

1543 is a jigsaw rule to deal with the combinatoric ambiguity implicit in which jets go in  
1544 which hemisphere. This is the jigsaw rule used in the decay trees when going from  
1545 one frame to two frames such as  $PP \rightarrow P_a, P_b$ .

1546 We will use three other jigsaw rules, which are all kinematic jigsaw rules. One has  
1547 already been used in the razor technique. The minimization of  $\beta_L$  will be used as the  
1548 jigsaw rule in the first step of each decay tree: the lab frame to the  $PP/\text{CM}$  frame.  
1549 This is equivalent to the imposition of longitudinal boost invariance, as we expect on  
1550 average  $p_{z,PP,\text{CM}} = 0$ . One defines a unique longitudinal boost by imposition of this  
1551 external constraint.

1552 The final two jigsaw rules used in this thesis was not used in the razor technique.  
1553 We describe them here.

The first kinematic ambiguity is the total mass of the invisible system  $M_I$ . We guess this to be:

$$M_I^2 = M_V^2 - 4M_{V_a}M_{V_b}. \quad (7.15)$$

1554 As we stated above, there is no need to “justify” the jigsaw rules, as they are in some  
1555 ways a mathematical trick to fully resolve the event kinematics. The symmetry of  
1556 the production mechanism, where we have two decay products  $V_i$  and  $I_i$  produced  
1557 from the decay of the same heavy sparticle, is explicit with this jigsaw choice.

1558     The final jigsaw rule is used to resolve the “amount” of  $E_T^{\text{miss}}$  that “belongs” to  
1559    each hemisphere, and therefore how to impose the transverse boost onto each of i.e.  
1560     $P_a$  and  $P_b$  from  $PP$ . Equivalently, it can be seen as the resolution of the kinematics of  
1561    the  $I_a$  and  $I_b$  objects in the squark and gluino pair production decay trees. Recall that  
1562    at this point, we have already approximated the boost of the  $PP$  frame. The choice we  
1563    use is to minimize the masses  $P_a$  and  $P_b$ , while simultaneously constraining  $P_a = P_b$ .  
1564    As is the case in the last step, there is a straightforward physical interpretation of this  
1565    choice. In the signal models we are considering,  $P_a$  and  $P_b$  are the estimated frames  
1566    of the squark or gluino pair-produced as a heavy resonance. We then of course expect  
1567     $M_{P_a} = M_{P_b}$ .

1568     The imposition of the decay trees, with ambiguities resolved through the jigsaw  
1569    rules, give a full set of boosts relating the frames of each decay tree. In each frame,  
1570    we have estimates for the frame mass and decay angles, which can be used in searches  
1571    for new physics. In the next section, we describe the variables that are used in this  
1572    thesis in more details.

## 1573   **7.3 Variables used in the search for zero lepton**

### 1574   **SUSY**

1575    We describe here the variables used in the RJR search described in [120]. These  
1576    were reconstructed using the RJR algorithm as just described, using the RestFrames  
1577    packages [124]. In these frames, the momenta of all objects placed into that branch  
1578    of the decay tree are available (after application of the approximated boost), and in  
1579    principle we can calculate any variable of interest such as invariant masses or the  
1580    angles between these objects. The truly useful set of variables are highly dependent  
1581    on the signal process, and we leave their discussion to the subsequent sections. It is  
1582    useful to understand the philosophy employed in the construction of these variables.

1583 In general, we can split variables useful for searches for new physics into two  
1584 categories: *scaleful* and *scaleless* variables. In this search, we will use a set of scaleful  
1585 variables called the  $H$  variables. The scaleless variables will consist of ratios and  
1586 angles. In general, we want to restrict the number of scaleful cuts we apply, for two  
1587 reasons. Different scaleful variables are often highly correlated, and this of course  
1588 limits the utility of additional cuts. Additionally, selections based on many scaleful  
1589 variables often overoptimize for particular signal model of interest, especially as  
1590 related to the mass difference chosen between the sparticle and the LSP. To avoid  
1591 this, each decay tree will only use two scale variables, one which quantifies the overall  
1592 mass scale of the event, and another which acts as a measure of the event balance.

### 1593 **Squark and gluino variables**

1594 Taking our general philosophy to a particular case, we here describe the variables  
1595 used by the squark and gluino searches. We have a suite of scale variables which we  
1596 will call the  $H$  variables, and a suite of angles and ratios.

1597 As we have described above, the RJR algorithm gives us access to the masses  
1598 of each frame of interest. It may seem natural that these variables would be the  
1599 most useful for discrimination of the signal from background processes. However, these  
1600 masses, such as the invariant mass of the  $PP$  system  $M_{PP}$ , can be significantly  
1601 affected by the additional jets in the events. In backgrounds with significant jet  
1602 activity such as  $Z + \text{jets}$  and  $W + \text{jetsevents}$ , these masses can have large values which  
1603 complicate discrimination from the signal processes. Instead, we use the  $H$  variables,  
1604 as they show resilience to this effect, and provide stronger discrimination from the SM  
1605 backgrounds. They take their name from the commonly used variable  $H_T$ , which is the  
1606 scalar sum of the visible momentum. From the RJR technique, we can evaluate these  
1607 variables in the non-lab frame and include longitudinal information. They are also  
1608 constructed with *aggregate* momenta using a similar mass minimization procedure

1609 as we have already described.

We label these variables as  $H_{n,m}^F$ . They are evaluated in the frame  $F$ , where  $F \in \{\text{lab}, \text{PP}, P_a, P_b\}$ . When the discussion applies to both  $P_a$  and  $P_b$ , we will write  $P_i$ . The subscripts  $n$  and  $m$  denote the number of visible and invisible vectors considered, respectively. When there are more vectors available than  $n$  or  $m$ , we add up vectors using the hemisphere (megajet) jigsaw rule until there are  $n$  ( $m$ ) objects<sup>2</sup>.

In the opposite case, where  $n$  or  $m$  is greater than the number of available objects, one simply considers the available objects. The  $H_{n,m}^F$  variables are then defined as

$$H_{n,m}^F = \sum_i^n |\vec{p}_{\text{vis},i}^F| + \sum_j^m |\vec{p}_{\text{inv},i}^F|. \quad (7.16)$$

It may not be clear that these variables encode independent information. Fundamentally, this is just an expression of the triangle inequality  $\sum |\vec{p}| \geq |\sum \vec{p}|$ . One can also define purely transverse of these variables, which we will denote  $H_{T,n,m}^F$ . Including this view, it is easy to see how the  $H$  variables are extensions of the normal  $H_T$  variables, as

$$H_T = H_{T,\infty,0}^{\text{lab}}. \quad (7.17)$$

1610 Although the  $H$  variables are interesting in their own right, the true power of  
1611 the RJR technique comes from the construction of scaleless variables. The scaleless  
1612 ratios and angles are in fact measured in the “right” frame, where right here means  
1613 an approximation of the correct frame. This provides a less correlated set of variables  
1614 than those measured in the lab frame, due to the corrections to the disparticle or  
1615 sparticle system boosts from the RJR technique.

1616 To search for noncompressed squark pair production, we use the following set of  
1617 RJR variables:

---

<sup>2</sup>Recall that these vectors are constructed by the imposition of the decay tree with the relevant jigsaw rules.

- 1618     •  $H_{1,1}^{PP}$  - scale variable useful for discrimination against QCD backgrounds and  
 1619        used in a similar way to  $E_T^{\text{miss}}$

- 1620     •  $H_{T,2,1}^{PP}$  - scale variable providing information on the overall mass scale of the  
 1621        event for squark pair production. We will often call this the *full* scale variable.

- 1622     •  $H_{T,1,1}^{PP}/H_{2,1}^{PP}$  - ratio used to prevent imbalanced events where the scale variable  
 1623        is dominated by one high  $p_T$  jet or high  $E_T^{\text{miss}}$

- 1624     •  $p_{PP,z}^{\text{LAB}}/(p_{PP,z}^{\text{LAB}} + H_{T,2,1}^{PP})$  - ratio which prevents significant boosts in the  $z$ -direction.  
 1625         $p_{PP,z}^{\text{LAB}}$  is a measure of the total boost of the  $PP$  system from the lab frame

- 1626     •  $p_{T,j2}^{PP}/H_{T,2,1}^{PP}$  - ratio to force the second leading jet in the  $PP$  frame to carry a  
 1627        significant portion of the total scalar sum of the total momenta in that frame.  
 1628        This requirement is another balance requirement, on the total  $p_T$  of that second  
 1629        jet in the  $PP$  frame.

1630   First, we note that there is an implicit requirement that each hemisphere has at least  
 1631   one jet (to even reconstruct the  $P_a$  and  $P_b$  frames), thus we implicitly require two  
 1632   or more jets, as we expect for squark pair production. The other important thing  
 1633   to note is that all of the ratios use the full scale variable as the denominator. This  
 1634   is sensible, as we expect all of these effects to be scaled with the full scale variable  
 1635    $H_{T,2,1}^{PP}$ . We will see a similar behavior for the gluino regions, with a new full scale  
 1636   variable.

1637   To search for noncompressed gluino pair production, we use the following set of  
 1638   RJR variables: Due to the increased complexity of the event topology with four jets,  
 1639   there are additional handles we can exploit:

- 1640     •  $H_{1,1}^{PP}$  - same as squark pair production variable

- 1641     •  $H_{T,4,1}^{PP}$  - scale variable providing information on the overall mass scale of the  
 1642        event for gluino pair production. As before, we often call this the *full* scale

1643 variable. Since this variable allows the jets to be separated in the  $PP$  frame, it  
1644 is more appropriate for gluino pair production.

1645 •  $H_{T,1,1}^{PP}/H_{4,1}^{PP}$  - ratio used to prevent imbalanced events where the scale variable  
1646 is dominated by one high  $p_T$  jet or high  $E_T^{\text{miss}}$

1647 •  $H_{T,4,1}^{PP}/H_{4,1}^{PP}$  - ratio used to measure the fraction of the total scalar sum of the  
1648 momentum in the transverse plane. Decay products from gluino pair production  
1649 are expected to be fairly central

1650 •  $p_{PP,z}^{\text{LAB}}/(p_{PP,z}^{\text{LAB}} + H_{T,4,1}^{PP})$  - ratio to used to prevent significant boosts in the  
1651  $z$ -direction

1652 •  $\min(p_{T,j2_i}^{PP}/H_{T,2,1_i}^{PP})$ - ratio to require the second leading jet in *both* squark-like  
1653 hemispheres  $C_a$  and  $C_b$  to contain a significant portion of *that frame's* momenta.  
1654 This is similar to the  $p_{T,j2}^{PP}/H_{T,2,1}^{PP}$ squark decay tree discriminator, but applied  
1655 to both hemispheres  $C_a$  and  $C_b$ .

1656 •  $\max(H_{1,0}^{P_i}/H_{2,0}^{P_i})$ - ratio requiring one jet in each of the  $P_i$  not encompass too  
1657 much of the total momentum available in that frame. This ratio is generally a  
1658 very loose cut.

## 1659 Compressed variables

1660 As we saw above, the decay tree imposed for compressed spectra is simpler. We do  
1661 not attempt to fully reconstruct the details of the system recoiling off the ISR system,  
1662 but use a straightforward set of variables in this case. One additional simplification  
1663 is that all variables are force to be transverse in this case, by simply excluding the  
1664  $\eta/z$  information of the objects as inputs to the RJR reconstruction. We still use the  
1665 philosophy of limiting our scaleful variables to just two. The compressed scenario  
1666 uses the following set of RJR variables:

- 1667 •  $p_{T,S}^{\text{ISR}}$ - scale variable that is the magnitude of the total transverse momenta of all  
 1668 jets associated to the ISR system, as evaluated in the CM frame

- 1669 •  $R_{\text{ISR}} \equiv p_I^{\hat{\text{CM}}} \cdot p_{T,S}^{\hat{\text{CM}}} / p_{T,S}^{\text{CM}}$  - this ratio is our measurement for the ratio of the LSP  
 1670 mass to the compressed sparticle mass. In compressed cases, this should be  
 1671 large, as this estimates the amount of the total  $\text{CM} \rightarrow S$  boost carried by the  
 1672 invisible system.

- 1673 •  $M_{T,S}$ - the transverse mass of the  $S$  system

- 1674 •  $N_{\text{jet}}^V$ - the number of jets associated to the visible system  $V$

- 1675 •  $\Delta\phi_{\text{ISR},I}$ - the opening angle between the ISR system and the invisible system  
 1676 measured in the lab frame. As the invisible system is expected to carry much  
 1677 of the total  $S$  system momentum, this should be large, as we expect the ISR  
 1678 system to recoil directly opposite the  $I$  system in that case.

## 1679 Anti-QCD variables

1680 For the self-assembling tree, we contruct two variables, which we combine to form a  
 1681 single variable which rejects QCD events. In this case, we use the mass minimzation  
 1682 jigsaw, with a fully transverse version of the event (i.e. we set all jet  $z/\eta$  components  
 1683 to 0). This jigsaw defines the distance metric, and provides us with one or two jets  
 1684 known as the  $E_{\text{T}}^{\text{miss}}$  siblings. We define  $\vec{p}_{\text{sib}}$ as the sum of these jets, and define the  
 1685 following quantities.

We calculate a ratio observable which examines the relative magnitude of the sibling vector  $\vec{p}_{\text{sib}}$ and  $E_{\text{T}}^{\text{miss}}$ , and an angle relating  $\vec{p}_{\text{sib}}$ and  $E_{\text{T}}^{\text{miss}}$ :

$$R(\vec{p}_{\text{sib}}, E_{\text{T}}^{\text{miss}}) \equiv \frac{\vec{p}_{\text{sib}} \cdot \hat{E}_{\text{T}}^{\text{miss}}}{\vec{p}_{\text{sib}} \cdot \hat{E}_{\text{T}}^{\text{miss}} + |\vec{E}_{\text{T}}^{\text{miss}}|} \quad (7.18)$$

$$\cos \theta(\vec{p}_{\text{sib}}, E_{\text{T}}^{\text{miss}}) \equiv \frac{(\vec{p}_{\text{sib}} + \vec{E}_{\text{T}}^{\text{miss}}) \cdot \vec{p}_{\text{sib}} + \hat{E}_{\text{T}}^{\text{miss}}}{|\vec{p}_{\text{sib}}| + E_{\text{T}}^{\text{miss}}} \quad (7.19)$$

These observables are highly correlated, but taking the following fractional difference provides strong discrimination between SUSY signal and QCD background events:

$$\Delta_{\text{QCD}} \equiv \frac{1 + \cos \theta(\vec{p}_{\text{sib}}, E_{\text{T}}^{\text{miss}}) - 2R(\vec{p}_{\text{sib}}, E_{\text{T}}^{\text{miss}})}{1 + \cos \theta(\vec{p}_{\text{sib}}, E_{\text{T}}^{\text{miss}}) + 2R(\vec{p}_{\text{sib}}, E_{\text{T}}^{\text{miss}})}. \quad (7.20)$$

1686 We will use this variable in the next chapter.

ADD CON<sub>687</sub>  
CLUSIONS



1689     *A search for supersymmetric particles in zero lepton final  
 1690                         states with the Recursive Jigsaw Technique*

1691     This section presents the details of the first search employing RJR variables as  
 1692     discriminating variables, as described in [120]. We will describe the simulation  
 1693     samples used, and then define the selections where we search for new SUSY  
 1694     phenomena, which we call the *signal regions* (SRs) Afterwards, we describe the  
 1695     background estimation techniques used in the analysis. Finally, we discuss the  
 1696     treatment of systematic uncertainties, and how we combine them using a likelihood  
 1697     method [125].

1698     **8.1 Simulation samples**

1699     We discussed the collision data sample provided by the LHC for the analysis in this  
 1700     thesis. We analyze a dataset of  $13.3 \text{ fb}^{-1}$  of collision data, at  $\sqrt{s} = 13 \text{ TeV}$ . To select  
 1701     events in data, we use the trigger system as previously discussed, and use the lowest  
 1702     unprescaled trigger which is available for a particular Standard Model background.  
 1703     We now discuss the simulation samples used for this search.

1704     Simulated data is fundamentally important to the ATLAS physics program.  
 1705     Calibrations, measurements, and searches use Monte Carlo (MC) simulations to  
 1706     compare with collision data. In this thesis, MC samples are used to optimize the  
 1707     signal region selections, assist in background estimation, and assess the sensitivity to  
 1708     specific SUSY signal models. The details of Monte Carlo production, accuracy, and

1709 utility are far beyond the scope of this thesis, but we provide a short description here.

1710 The first step is MC *generation*. A program is run which does a matrix-element  
1711 calculation which produces a set of outgoing particles from the parton interactions.  
1712 The output particles are *interfaced* [126] with the parton decays, showering, and  
1713 hadronization processes. This can be done by the same program or another tool  
1714 altogether. This produces a set of *truth* particles with their corresponding kinematics.

1715 A summary of the generators for each sample is shown in tab. 8.1.

1716 The signal samples are produced using simplified models. Simplified models  
1717 employ an effective Lagrangian which introduces the smallest possible set of new  
1718 particles, with only one production process and one decay channel with 100%  
1719 branching ratio. The squarks are generated in pairs, where each squark decays directly  
1720 to a jet and the LSP. Gluinos are also generated in pairs, where each gluino decays  
1721 directly to a squark and jet, and the squark subsequently decays to another jet and  
1722 the LSP. Signal samples are produced in a *grid* of sparticle and  $\tilde{\chi}_1^0$  mass, where each  
1723 signal sample is generated with a particular  $(m_{\text{sparticle}}, m_{\tilde{\chi}_1^0})$ . This allows us to probe  
1724 a variety of signal models with the given mass splittings. These samples are generated  
1725 with MADGRAPH [127] interfaced with PYTHIA8 [128]. The generated squark samples  
1726 cover the grid with squark masses ranging from 200 GeV to 2000 GeV and  $\tilde{\chi}_1^0$  masses  
1727 ranging from 0 GeV up to 1100 GeV. The gluino samples cover the grid as well, with  
1728 gluino masses of 200 GeV to 2600 GeV and  $\tilde{\chi}_1^0$  masses from 0 GeV up to 1600 GeV. The  
1729 grids are well-populated, with about 200 samples covering this space, and a higher  
1730 density of samples at smaller mass splittings.

1731 For each major background, we employ a baseline sample and alternative sample,  
1732 which we will use later to derive uncertainties on the theoretical cross-sections. The  
1733 choice of generators for each background is itself a quite broad topic, which we avoid  
1734 discussing here.

1735 In this thesis, we will use SHERPA [129] to generate boson events:  $Z \rightarrow \ell\ell$ ,

Physics process	Generator	Alternative generator	Cross-section normalization	PDF set	Parton shower	Tune
$\tilde{s}\tilde{s}, \tilde{s} \rightarrow q\chi_1^0$	MG5_aMC@NLO 2.2.3	-	NLO	NNPDF2.3LO	PYTHIA 8.186	A14
$\tilde{g}\tilde{g}, \tilde{g} \rightarrow q\chi_1^0$	MG5_aMC@NLO 2.2.3	-	NLO	NNPDF2.3LO	PYTHIA 8.186	A14
$W(\rightarrow \ell\nu) + \text{jets}$	SHERPA 2.2.0	MADGRAPH	NNLO	NNPDF3.0NNLO	SHERPA	SHERPA default
$Z/\gamma^*(\rightarrow \ell\ell) + \text{jets}$	SHERPA 2.2.0	MADGRAPH	NNLO	NNPDF3.0NNLO	SHERPA	SHERPA default
$\gamma + \text{jets}$	SHERPA 2.1.1	-	LO	CT10	SHERPA	SHERPA default
$t\bar{t}$	Powheg-Box v2	Mc@NLO	NNLO+NNLL	CT10	PYTHIA 6.428	PERUGIA2012
Single top ( $Wt$ -channel)	Powheg-Box v2	Mc@NLO	NNLO+NNLL	CT10	PYTHIA 6.428	PERUGIA2012
Single top ( $s$ -channel)	Powheg-Box v2	Mc@NLO	NLO	CT10	PYTHIA 6.428	PERUGIA2012
Single top ( $t$ -channel)	Powheg-Box v1	Mc@NLO	NLO	CT10f4	PYTHIA 6.428	PERUGIA2012
$t\bar{t} + W/Z/WW$	MG5_aMC@NLO 2.2.3	-	NLO	NNPDF2.3LO	PYTHIA 8.186	A14
$WW, WZ, ZZ$	SHERPA 2.1.1	-	NLO	CT10	SHERPA	SHERPA default
Multijet	PYTHIA 8.186	-	LO	NNPDF2.3LO	PYTHIA 8.186	A14

Table 8.1: The Standard Model background Monte Carlo simulation samples used in this thesis. The generators, the order in  $\alpha_s$  of cross-section calculations used for yield normalization, PDF sets, parton showers and tunes used for the underlying event are shown. Alternative generators are only used for the major backgrounds.

1736     $W \rightarrow \ell\nu$ , diboson, and photon events. These are interfaced with the SHERPA’s parton  
 1737    showering model [130]. The alternative samples for  $Z \rightarrow \ell\ell$  and  $W \rightarrow \ell\nu$  decays are  
 1738    generated with MADGRAPH [127] interfaced with PYTHIA8 [128]. Single top and  $t\bar{t}$   
 1739    events are generated with POWHEGBOX [131] interfaced with itself and the alternative  
 1740    samples are generated with Mc@NLO [132] interfaced with HERWIG++ [133] QCD  
 1741    events are generated with PYTHIA8 [128]. Events with  $t\bar{t}$  in association with a gauge  
 1742    boson are generated in MG5\_aMC@NLO [132] interfaced with PYTHIA8 [128].

1743    After generation of the truth level particles using the various generators interfaced  
 1744    with their parton showering models, we perform *simulation*. The detector response  
 1745    to the truth particles is simulated, and simulated hits are produced. This procedure  
 1746    ensures “as close as possible” treatment of simulation and collision data. In ATLAS,  
 1747    this is done using the GEANT4 toolkit [134]. This toolkit outputs simulated detector  
 1748    signals, on which we run the exact same reconstruction algorithms as described in  
 1749    the previous chapters. This allows us to produce output simulation datasets for each  
 1750    of the backgrounds in the analysis.

1751 **8.2 Event selection**

1752 This section describes the selection of the signal region events. We begin by describing  
1753 the *preselection*, which is used to remove problematic events and reduce the dataset  
1754 to a manageable size. We then describe the signal region strategy, and present the  
1755 signal regions used in the analysis.

1756 **Preselection**

1757 The preselection is used to reduce the dataset to that of interest in this thesis. The  
1758 preselection cuts are shown in Tab. 8.2. This selection is also used for the samples  
1759 used for background estimation, except for the lepton veto.

1760 The cuts [1] and [3] are a set of cleaning requirements which remove problematic  
1761 events. The *Good Runs List* is a centrally-maintained list of data runs which have  
1762 been determined to be “good for physics”. This determination is made by analysis  
1763 of the various subdetectors, and monitoring of their status. Event cleaning is used  
1764 to veto events which could be affected by noncollision background, noise bursts, or  
1765 cosmic rays.

1766 The rest of the preselection is used for the signal region and control regions used  
1767 for background estimation. These cuts on scaleful variables used by previous searches  
1768 are mostly used for the reduction of the dataset to a manageable size. Signal models  
1769 with sensitivity to lower values of these scaleful variables have been ruled out by  
1770 previous searches [135]. The final cut is on  $m_{\text{eff}}$ , which is the scalar sum of all jets  
1771 and  $E_{\text{T}}^{\text{miss}}$ . This is the final discriminating variable used in the complementary search  
1772 to this thesis, which is also presented in [120].

Cut	Description	
1	Good Runs List	Veto events with intolerable detector errors
2	Event cleaning	Veto for noncollision background, noise bursts, and cosmic rays
3	$E_T^{\text{miss}} [\text{GeV}] >$	250
4	$p_T(j_1) [\text{GeV}] >$	200
5	$p_T(j_2) [\text{GeV}] >$	50
6	$m_{\text{eff}} [\text{GeV}] >$	800

Table 8.2: Preselection for the various event topologies used in the analysis.

## Signal regions

We define a set of signal regions using the RJR variables previously described. These signal regions are split into three general categories: squark pair production SRs, gluino pair production SRs, and compressed production SRs. Within these general SRs, we have a set of signal regions targetting different mass splittings of the sparticle and LSP. To ensure complementarity with other ATLAS SUSY searches which have lepton requirements, the signal region selections veto any events with any leptons of  $p_T > 10 \text{ GeV}$ . The hadronic signal regions also require the events to have passed the lowest unprescaled  $E_T^{\text{miss}}$  trigger at the time the event was recorded. The high  $E_T^{\text{miss}}$  selection in the preselection means these triggers (`HLT_xe70`, `HLT_xe80_tclcw_L1XE50` or `HLT_xe100_mht_L1XE50`) are fully efficient in data events.

A schematic of this strategy is shown in Fig. 8.1. This type of plane is how most *R*-parity conserving SUSY searches are organized in both ATLAS and CMS. The horizontal axis is the mass of the sparticle considered. In the case of this thesis, this will be the squark or gluino mass. On the vertical axis, we place the LSP mass. These are the two free parameters of the simplified models considered here. Our search occurs in this two-parameter space. Each signal region targets some portion of this plane. As shown in the figure, a new iteration of a search will use a set of signal regions which have sensitivity just beyond those of the previous exclusions. The choice of how

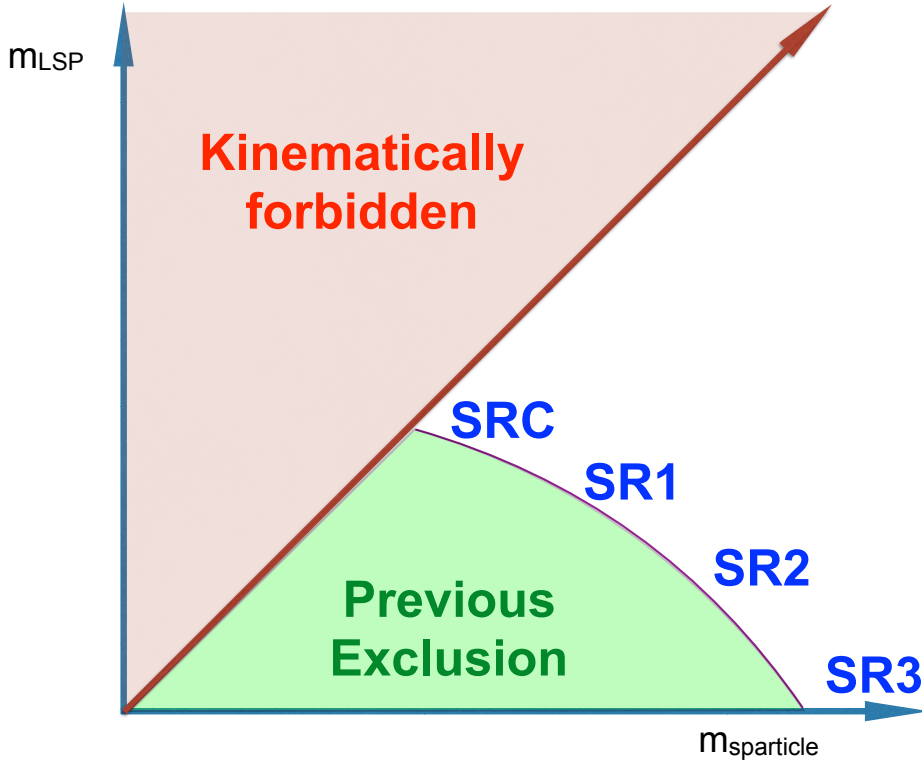


Figure 8.1: Schematic leading the development of the SUSY signal regions in this thesis. A variant of this schematic is used for most SUSY searches on ATLAS and CMS.

many signal regions to use to cover this plane is in many ways a matter of judgment, as it is important to avoid under/over-fitting to the signal models of interest. To take the extreme examples, one signal region will obscure the different phenomena in signal events with large versus small mass splittings, leading to underfitting. Binning as finely as possible<sup>1</sup> leads to overfitting due to the fluctuations present in the signal and background events passing the various selections selection. In this thesis, we use six squark signal regions, six gluino signal regions, and five compressed regions.

The full table defining all signal regions is shown in Tab. 8.3. In all cases, the signal region selections contain a combination of scaleful and scaleless cuts. Emphasis on cuts on scaleful variables provide stronger sensitivity to larger mass splittings,

---

<sup>1</sup>This can be defined as having a signal region for each simulated signal sample. There are  $\sim 100$  simulated signal samples produced in the plane.

1802 while additional sensitivity to smaller mass splittings is found using stronger cuts  
1803 on scaleless variables. One envisions walking from SR1 (with tight scaleless cuts  
1804 and loose scaleful cuts) in Fig. 8.1 towards SR3 by loosening the scaleless cuts and  
1805 tightening the scaleful cuts. We will see this strategy at work in each set of signal  
1806 regions.

1807 We have already described the useful variables in the previous chapter. The  
1808 question is how to choose the optimal cuts for a given set of signal models, which are  
1809 grouped in the mass splitting space. This was done by a brute force scan over the  
1810 cut values, using a guess of integrated luminosity with a fixed systematic uncertainty  
1811 scenario; the value of the systematic uncertainty is motivated by that from previous  
1812 analyses. We choose the lowest cut value that maximizes the  $Z_{Bi}$ , as described in  
1813 [136]. This figure of merit gives conservative estimates, as compared to i.e.  $S/\sqrt{B}$ .  
1814 A figure showing an example of this selection tuning procedure is shown in Fig. 8.2.

1815 The compressed selections are split into five regions (SRC1-5), and due to the  
1816 simplified nature of the compressed decay tree, has sensitivity in both the gluino  
1817 and squark planes. The compressed regions target mass splittings with  $m_{\text{sparticle}} -$   
1818  $m_{\text{LSP}} \tilde{<} 200$  GeV. For the compressed region,  $M_{T,S}$  is the primary scaleful variable.  
1819 We can see the general strategy of lowering increasing scale cuts while decreasing the  
1820 scaleless cuts here. SRC1 targets the most compressed scenarios, with mass splittings  
1821 of less than 25 GeV, and has the loosest  $M_{T,S}$  cut coupled with the tightest  $R_{\text{ISR}}$  and  
1822  $\Delta\phi_{\text{ISR},I}$  cuts. SRC4 and SRC5 target mass splittings of  $\sim 200$  GeV, and are coupled  
1823 with the loosest scaleless cuts on  $R_{\text{ISR}}$  and  $\Delta\phi_{\text{ISR},I}$ . We also note that SRC4 and  
1824 SRC5 have differing cuts on  $N_{\text{jet}}^V$ , since these SRs are closest to the noncompressed  
1825 regions, and can be seen as the “crossover” where the differences between squark and  
1826 gluino production begins to become manifest.

1827 The squark regions (for noncompressed spectra) are organized into six signal  
1828 regions. These are labeled by a numeral 1-3 and letter a/b. SRs sharing a common

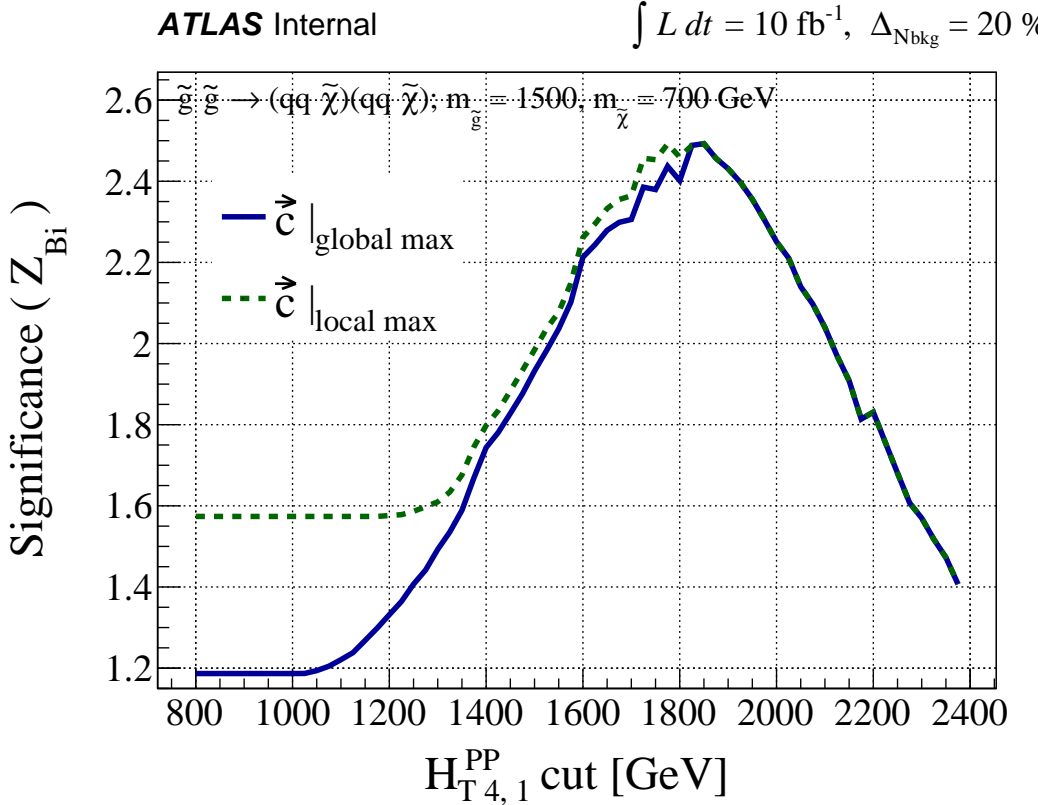


Figure 8.2: Optimization of the  $H_{T,4,1}^{PP}$  cut for a gluino signal model with  $(m_{\tilde{g}}, m_{\tilde{\chi}_1^0}) = (1500, 700)$  GeV assuming  $10 \text{ fb}^{-1}$  and an uncertainty of 20% on the background estimate.

1829 numeral i.e. SRS1a and SRS1b share a common set of scaleless cuts, while differing in  
 1830 the main scale variable  $H_{T,2,1}^{PP}$ . The two SRs for each set of scaleless cuts, only differing  
 1831 in the main scale variable, can be seen in a naïve way as providing sensitivity to a  
 1832 range of luminosity scenarios<sup>2</sup>. As before, we see that the scaleless cuts are loosened  
 1833 as we tighten the scaleful cuts, as we move across the table from SRS1a to SRS3b.  
 1834 This provides strong sensitivity to signal models with intermediate mass splittings with  
 1835 SRS1a to large mass splittings with SR3b.

1836 The gluino signal regions are organized entirely analogously to the squark signal  
 1837 regions. There are six gluino signal regions, again labeled via a numeral 1-3 and letter

---

<sup>2</sup>These SRs were defined before the entire collision dataset was produced, and thus needed to be robust in cases where the LHC provided significantly different than expected performance.

1838 a/b. Those SRs sharing a common numeral have a common set of scaleless cuts, but  
 1839 differ in their main scale variable  $H_{T,4,1}^{PP}$ . The SRs follow scaleless vs scaleful strategy,  
 1840 with SRG1 having the loosest scaleful cut cuts coupled with the strongest scaleless  
 1841 cuts, and the converse being true in SRG3. As in the squark case, this strategy  
 1842 provides strong expected sensitivity throughout the gluino-LSP plane.

### 1843 8.3 Background estimation

1844 We describe here the method of background estimation. In this thesis, we detail what  
 1845 is colloquially called a “cut-and-count” analysis. This is in contrast to a “shape fit”  
 1846 analysis, where one needs to consider the details of the variable distribution shapes.  
 1847 Instead, we must ensure the overall normalization of the Standard Model backgrounds  
 1848 are correct in the regions of phase space considered in the analysis. In order to  
 1849 do this, we define a set of *control regions* which are free of SUSY contamination  
 1850 based on the previously excluded analysis. We compare the number of events present  
 1851 in the control regions in simulation with that in data to define a *transfer factor*  
 1852 (TF). We extrapolate the number of expected events from each background using  
 1853 this transfer factor to translate from the , which provides our final estimate of the  
 1854 SM background in the corresponding signal region. To be explicit, each signal region  
 1855 SR has a corresponding set of control regions.

More precisely, for a given signal region, we are attempting to estimate the value  
 $N_{\text{SR}}^{\text{data}}$  for a given background. This value is estimated using the following equation:

$$N_{\text{SR}}^{\text{data,est}} = N_{\text{CR}}^{\text{data,obs}} \times \text{TF}_{\text{CR}} \equiv N_{\text{CR}}^{\text{data,obs}} \times \left( \frac{N_{\text{SR}}^{\text{MC}}}{N_{\text{CR}}^{\text{MC}}} \right) \quad (8.1)$$

1856 where the transfer factor TF is taken directly from MC. The two ingredients to our  
 1857 estimation of  $N_{\text{SR}}^{\text{data,obs}}$  is thus  $N_{\text{CR}}^{\text{data,obs}}$  and the transfer factor taken from MC.

The transfer factor method is potentially more straightforward written in the

Targeted signal	$\tilde{s}\tilde{s}, \tilde{s} \rightarrow q\tilde{\chi}_1^0$									
Requirement	Signal Region									
	RJR-S1		RJR-S2		RJR-S3					
$H_{1,1}^{PP}/H_{2,1}^{PP} \geq$	0.6		0.55		0.5					
$H_{1,1}^{PP}/H_{2,1}^{PP} \leq$	0.95		0.96		0.98					
$p_{PP, z}^{lab} / (p_{PP, z}^{lab} + H_{T, 2,1}^{PP}) \leq$	0.5		0.55		0.6					
$p_{j2, T}^{PP}/H_{T, 2,1}^{PP} \geq$	0.16		0.15		0.13					
$\Delta_{QCD} >$	0.001									
	RJR-S1a	RJR-S1b	RJR-S2a	RJR-S2b	RJR-S3a	RJR-S3b				
$H_{T, 2,1}^{PP}$ [GeV] >	1000	1200	1400	1600	1800	2000				
$H_{1,1}^{PP}$ [GeV] >	1000		1400		1600					
Targeted signal	$\tilde{g}\tilde{g}, \tilde{g} \rightarrow q\bar{q}\tilde{\chi}_1^0$									
Requirement	Signal Region									
	RJR-G1		RJR-G2		RJR-G3					
$H_{1,1}^{PP}/H_{4,1}^{PP} \geq$	0.35		0.25		0.2					
$H_{T, 4,1}^{PP}/H_{4,1}^{PP} \geq$	0.8		0.75		0.65					
$p_{PP, z}^{lab} / (p_{PP, z}^{lab} + H_{T, 4,1}^{PP}) \leq$	0.5		0.55		0.6					
$\min(p_{j2, T, i}^{PP}/H_{T, 2,1, i}^{PP}) \geq$	0.12		0.1		0.08					
$\max(H_{1,0}^{Pi}/H_{2,0}^{Pi}) \leq$	0.95		0.97		0.98					
$ \frac{2}{3}\Delta\phi_{V,P}^{PP} - \frac{1}{3}\cos\theta_p  \leq$	0.5		-		-					
$\Delta_{QCD} >$	0									
	RJR-G1a	RJR-G1b	RJR-G2a	RJR-G2b	RJR-G3a	RJR-G3b				
$H_{T, 4,1}^{PP}$ [GeV] >	1000	1200	1500	1900	2300	2700				
$H_{1,1}^{PP}$ [GeV] >	600		800		900					
Targeted signal	compressed spectra in $\tilde{s}\tilde{s}$ ( $\tilde{s} \rightarrow q\tilde{\chi}_1^0$ ); $\tilde{g}\tilde{g}$ ( $\tilde{g} \rightarrow q\bar{q}\tilde{\chi}_1^0$ )									
Requirement	Signal Region									
	RJR-C1	RJR-C2	RJR-C3	RJR-C4	RJR-C5					
$R_{ISR} \geq$	0.9	0.85	0.8	0.75	0.70					
$\Delta\phi_{ISR, I} \geq$	3.1	3.07	2.95	2.95	2.95					
$\Delta\phi(\text{jet}_{1,2}, \mathbf{E}_T^{\text{miss}})_{\text{min}}$	-	-	-	0.4	0.4					
$M_{TS}$ [GeV] $\geq$	100	100	200	500	500					
$p_{TS}^{CM}$ [GeV] $\geq$	800	800	600	600	600					
$N_{jet}^V \geq$	1	1	2	2	3					

Table 8.3: Selection criteria and targeted signal model used to define signal regions in the RJR-based search, indicated by the prefix ‘RJR’. Each SR is labelled with the targeted SUSY particle or the targeted region of parameter space, such that ‘S’, ‘G’ and ‘C’ denote regions searching for squark-, gluino-pair production, or compressed spectra, respectively.

following way:

$$N_{\text{SR}}^{\text{data,est}} = N_{\text{SR}}^{\text{MC}} \times \left( \frac{N_{\text{CR}}^{\text{data,obs}}}{N_{\text{CR}}^{\text{MC}}} \right) \equiv N_{\text{SR}}^{\text{MC}} \times \mu_{\text{CR}}. \quad (8.2)$$

1858 In this form, the correction to the overall normalization is explicit. The ratio  $\frac{N_{\text{CR}}^{\text{data,obs}}}{N_{\text{CR}}^{\text{MC}}}$   
1859 which we call  $\mu$  informs us how to scale  $N_{\text{SR}}^{\text{MC}}$  in order to get the right overall  
1860 normalization. The assumption made with this method is that the overall shape of  
1861 the distribution should not change “that much” as one extrapolates to the signal  
1862 region.

1863 The CR definitions are motivated and designed according to two (generally  
1864 competing) requirements:

- 1865 1. Statistical uncertainties due to low CR statistics
- 1866 2. Systematic uncertainties related to the extrapolation from the CR to the SR.  
1867 This motivates the desire to make the control regions as similar as possible  
1868 to the signal regions without risking signal contamination while ensuring high  
1869 purity in the targeted SM background.

1870 In principle, one can also apply data-driven corrections to the TF obtained for each  
1871 CR.

1872 In order to validate the transfer factors obtained from MC, we also develop a series  
1873 of *validation regions* (VRs). These regions are generally designed to be “in between”  
1874 the control region and signal region selections in phase space, and thus provide a  
1875 check on the extrapolation from the control regions into the signal regions. Despite  
1876 their closeness in phase space to the signal regions, they are also designed to have  
1877 low signal contamination.

1878 In practice, we perform this estimation procedure simultaneously across all  
1879 control regions; we describe this later. We only note this here since we can also  
1880 apply Eq. Eq. (8.1) to measure the contamination of a control region with another

CR	SM background	CR process	CR event selection
Meff/RJR-CR $\gamma$	$Z(\rightarrow \nu\bar{\nu}) + \text{jets}$	$\gamma + \text{jets}$	Isolated photon
Meff/RJR-CRQ	Multi-jet	Multi-jet	$\Delta_{\text{QCD}} < 0$ reversed requirement on $H_{1,1}^{PP}$ (RJR-S/G) or $R_{\text{ISR}} < 0.5$ (RJR-C)
Meff/RJR-CRW	$W(\rightarrow \ell\nu) + \text{jets}$	$W(\rightarrow \ell\nu) + \text{jets}$	$30 \text{ GeV} < m_T(\ell, E_T^{\text{miss}}) < 100 \text{ GeV}$ , $b$ -veto
Meff/RJR-CRT	$t\bar{t} (+\text{EW})$ and single top	$t\bar{t} \rightarrow b\bar{b}q\bar{q}'\ell\nu$	$30 \text{ GeV} < m_T(\ell, E_T^{\text{miss}}) < 100 \text{ GeV}$ , $b$ -tag

Table 8.4: Control regions used in this thesis.

1881 background as well. This procedure accounts for the correlations between regions due  
 1882 to correlated systematic uncertainties. We next describe the control region selection  
 1883 for the major SM backgrounds for the analysis.

## 1884 Control Regions

1885 The primary backgrounds of note in this analysis are  $Z + \text{jets}$ ,  $W + \text{jets}$ ,  $t\bar{t}$ , and QCD  
 1886 events. There is also a minor background from diboson events which is taken directly  
 1887 from MC with an uncertainty of 50%. We describe the strategy to estimate these  
 1888 various backgrounds here. A summary table is shown in Tab. 8.4. All distributions  
 1889 shown in this section use the scaling factors  $\mu$  from the background fits, which we  
 1890 describe later.

1891 Events with a  $Z$  boson decaying to neutrinos in association with jets are the  
 1892 primary irreducible background in the analysis. These events have true  $E_T^{\text{miss}}$  from  
 1893 the decaying neutrinos, and can have significant values of the scaleful variables of  
 1894 interest. Naively, one might expect us to use  $Z \rightarrow \ell\ell$  as the control process of interest,  
 1895 as  $Z \rightarrow \ell\ell$  events are quite well-measured. Unfortunately, the  $Z \rightarrow \ell\ell$  branching ratio  
 1896 is about half of from  $Z \rightarrow \nu\nu$ , which necessitates loosening the control region selection  
 1897 significantly. This leads to unacceptably large systematic uncertainties in the transfer  
 1898 factor.

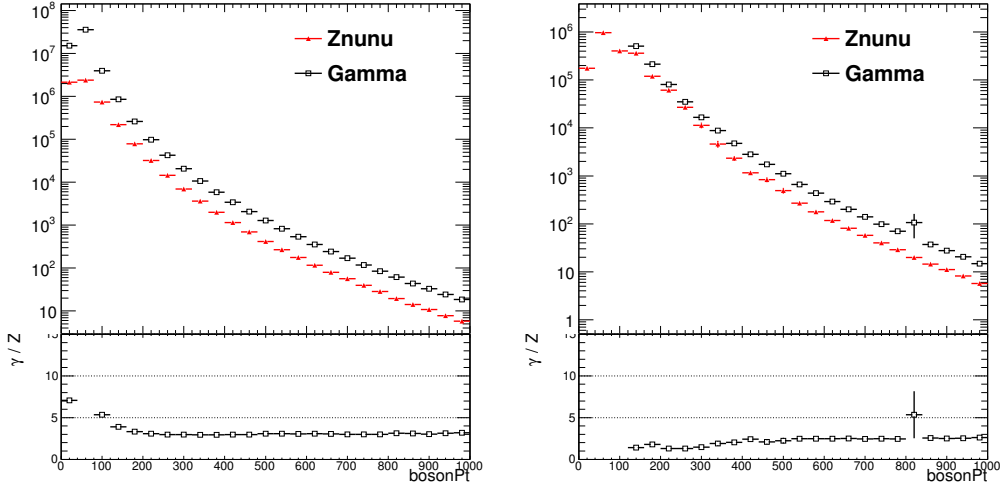
1899 Instead, photon events are used as the control region for the  $Z \rightarrow \nu\nu$  events. We

1900 label this photon control region as CRY. The photon is required to have  $p_T > 150$  GeV  
1901 to ensure the trigger is fully efficient. The kinematic properties of photon events  
1902 strongly resemble those of  $Z$  events when the boson  $p_T$  is significantly above the  
1903 mass of the  $Z$  boson. In this regime, the neutral bosons are both scaleless, and can  
1904 be treated interchangeably, up to the differences in coupling strengths. Additionally,  
1905 the cross-section for  $\gamma+\text{jets}$  events is significantly larger than  $Z+\text{jets}$  events above  
1906 the  $Z$  mass. These features are shown in Fig. 8.3 in simulated  $Z \rightarrow \nu\nu$  truth and  
1907 reconstructed events. The reconstructed  $Z \rightarrow \nu\nu$  events define the boson  $p_T$  as simply  
1908 the  $E_T^{\text{miss}}$ . In truth events, one clearly sees the effect of the  $Z$  mass below  $\sim 100$  GeV,  
1909 with a flattening of the ratio above  $\sim 300$  GeV. In reconstructed events, the effects  
1910 are less clear at low boson  $p_T$ , primarily due to cut sculpting from i.e. the trigger  
1911 requirement on photon events, which necessitates a higher  $p_T$  cut on photon events for  
1912 the trigger to remain fully efficient. Still, it is clear that the ratio flattens out at high  
1913 boson  $p_T$ , and we are justified in the use of CRY to model the  $Z+\text{jets}$  background.

1914 The CRY kinematic selection is slightly looser in the scaleful variables for the  
1915 noncompressed regions to provide sufficient control region statistics. This is chosen  
1916 to be  $H_{1,1}^{PP} > 900$  GeV ( $H_{1,1}^{PP} > 550$  GeV) for the squark (gluino) regions to minimize  
1917 the corresponding statistical and systematic uncertainties.

1918 One additional correction scale factor is applied to  $\gamma+\text{jets}$  events before calculat-  
1919 ing the transfer factors. This is known as the  $\kappa$  method, which is used to determine  
1920 the disagreement arising from the use of a LO generator for photon events vs. a NLO  
1921 generator for  $Z+\text{jets}$  events, which can reduce the theoretical uncertainties from  
1922 this disagreement. One can see this as a measurement of the k-factor for the LO  
1923  $\gamma+\text{jets}$  sample. This is effectively done with an auxiliary CRZ region, defined using  
1924 two leptons with an invariant mass close with 25 GeV of the  $Z$  mass. The correction  
1925 factor derived for this purpose is  $\kappa = 1.39 \pm 0.05$ .

1926 Distributions of CRY in squark, gluino, and compressed regions are shown in



(a) Boson  $p_T$  ratio as a function of true boson  $p_T$   
(b) Boson  $p_T$  ratio as a function of reconstructed boson  $p_T$

Figure 8.3

1927 Figs. 8.4 to 8.6. One can see the quite high purity of CRY in photon events from  
1928 these plots.

Event with a  $W$  boson decaying leptonically via  $W \rightarrow \ell\nu$  can also enter the signal region. In this case, we use leptonically to include all leptons ( $e, \mu, \tau$ ). The  $W + \text{jets}$  events passing the event selection either have a hadronically-decaying  $\tau$ , with a neutrino supplying  $E_T^{\text{miss}}$ , or the case where a muon or electron is misidentified as a jet or missed completely due to the limited detector acceptance. To model this background, we use a sample of one-lepton events with a veto on b-jets, which we label CRW. The lepton is required to have  $p_T > 27$  GeV to guarantee a fully efficient trigger. We then treat this single lepton as a jet for purposes of the RJR variable calculations. We apply a kinematic selection on the transverse mass:

$$m_T = \sqrt{2p_{T,\ell}E_T^{\text{miss}}(1 - \cos\phi_e - E_\phi^{\text{miss}})}, \quad (8.3)$$

1929 around the  $W$  mass:  $30 \text{ GeV} < m_T < 100 \text{ GeV}$ . Checks in simulation shows that  
1930 these requirements give a sample of high purity  $W \rightarrow \ell\nu$  background. Due to low  
1931 statistics using the kinematic cuts imposed in the signal regions, the control region

1932 kinematic cuts are slightly loosened with respect to the signal region cuts. We use  
1933 the loosest cut in any signal region as the control region selection for all signal  
1934 regions. More clearly, the control region selection corresponding to each signal region  
1935 is the *same*. As discussed above, this leads to a tolerable increase in the systematic  
1936 uncertainty from the extrapolation from the CR to the SR when compared to the  
1937 resulting statistical uncertainty.

1938 Distributions of CRW in squark, gluino, and compressed regions are shown in  
1939 Figs. 8.7 to 8.9. There is high purity in  $W+\text{jets}$  events in the control region  
1940 corresponding to all signal regions.

1941 Top events are also an important background, for the same reasons as the  
1942  $W+\text{jets}$  background, due to the dominant top decay channel of  $t \rightarrow Wb$ . For a  
1943 top event to be selected by the analysis criteria, as in the case of  $W+\text{jets}$ , we expect  
1944 a  $W$  to decay via a  $\tau$  lepton which decays hadronically or one a muon or electron to  
1945 be misidentified as a jet or be outside the detector acceptance. We are not so worried  
1946 about hadronic or all dileptonic tops: hadronic  $t\bar{t}$  events generally have low  $E_{\text{T}}^{\text{miss}}$   
1947 (and  $H_{1,1}^{PP}$ ) so they will not pass the kinematic cuts, while dileptonic  $t\bar{t}$  events have a  
1948 lower cross-section and good reconstruction efficiency from the two leptons. We are  
1949 thus primarily concerned with semileptonic  $t\bar{t}$  events with  $E_{\text{T}}^{\text{miss}}$  from the neutrino.  
1950 To model this background, we use the same selection as the  $W$  selection, but require  
1951 that one of the jets chosen by the analysis has at least one  $b$ -tag. This selection has  
1952 quite high purity, as we expect the  $t\bar{t}$  background to have two  $b$ -jets. Thus with  
1953 the 70%  $b$ -tagging efficiency working point used in this analysis, ignoring (small)  
1954 correlations between the two  $b$ -tags, we expect to tag one of the  $b$ -jets greater than  
1955 90% of the time. As with CRW, we need to loosen the cuts applied to CRT with  
1956 respect to the signal region in order to gain sufficient expected data statistics. We  
1957 use exactly the same scheme; the CRT corresponding to each SR is identical, due to  
1958 using the loosest set of cuts among the SRs. This comes at the cost of an increased

1959 systematic uncertainty for this extrapolation, but it was determined that this tradeoff  
1960 resulted in the lowest overall uncertainty.

1961 Distributions of CRT in squark, gluino, and compressed regions are shown  
1962 in Figs. 8.10 to 8.12. There is high purity in top events in the control region  
1963 corresponding to all signal regions.

1964 The final important background is the QCD background. As briefly discussed in  
1965 the previous chapter, QCD backgrounds are difficult, for a few reasons we describe  
1966 here. The large cross-section for QCD events means that even very rare extreme  
1967 mismeasurements can be seen in our signal regions. However, as these events are  
1968 very rare, one requires extreme confidence in the tails of the distributions to use  
1969 simulation as an input for background estimation. To avoid this, the strategy in  
1970 these cases is to apply a strong enough cut to expect *zero* QCD events in the signal  
1971 regions to avoid this issue. To produce a sample enriched in QCD, which we call CRQ,  
1972 we reverse the  $\Delta_{\text{QCD}}$  and  $H_{1,1}^{\text{PP}}$  cuts. This analysis uses the jet smearing method, as  
1973 described in [137]. This is a data-driven method which applies a resolution function  
1974 to well-measured QCD events, which also an estimate of the impact of the jet energy  
1975 mismeasurement on  $E_{\text{T}}^{\text{miss}}$  and subsequently the RJR variables.

1976 Distributions of CRQ in squark, gluino, and compressed regions are shown  
1977 in Figs. 8.13 to 8.15. There is high purity in top events in the control region  
1978 corresponding to all signal regions.

1979 The final background of note in this background is the diboson background. This  
1980 background is estimated directly from simulation. Due to the low cross-section of  
1981 electroweak processes, this background is not significant in the signal regions. We  
1982 assign a large ad-hoc 50% systematic on the cross-section, and do not attempt to  
1983 define a control region for this background.

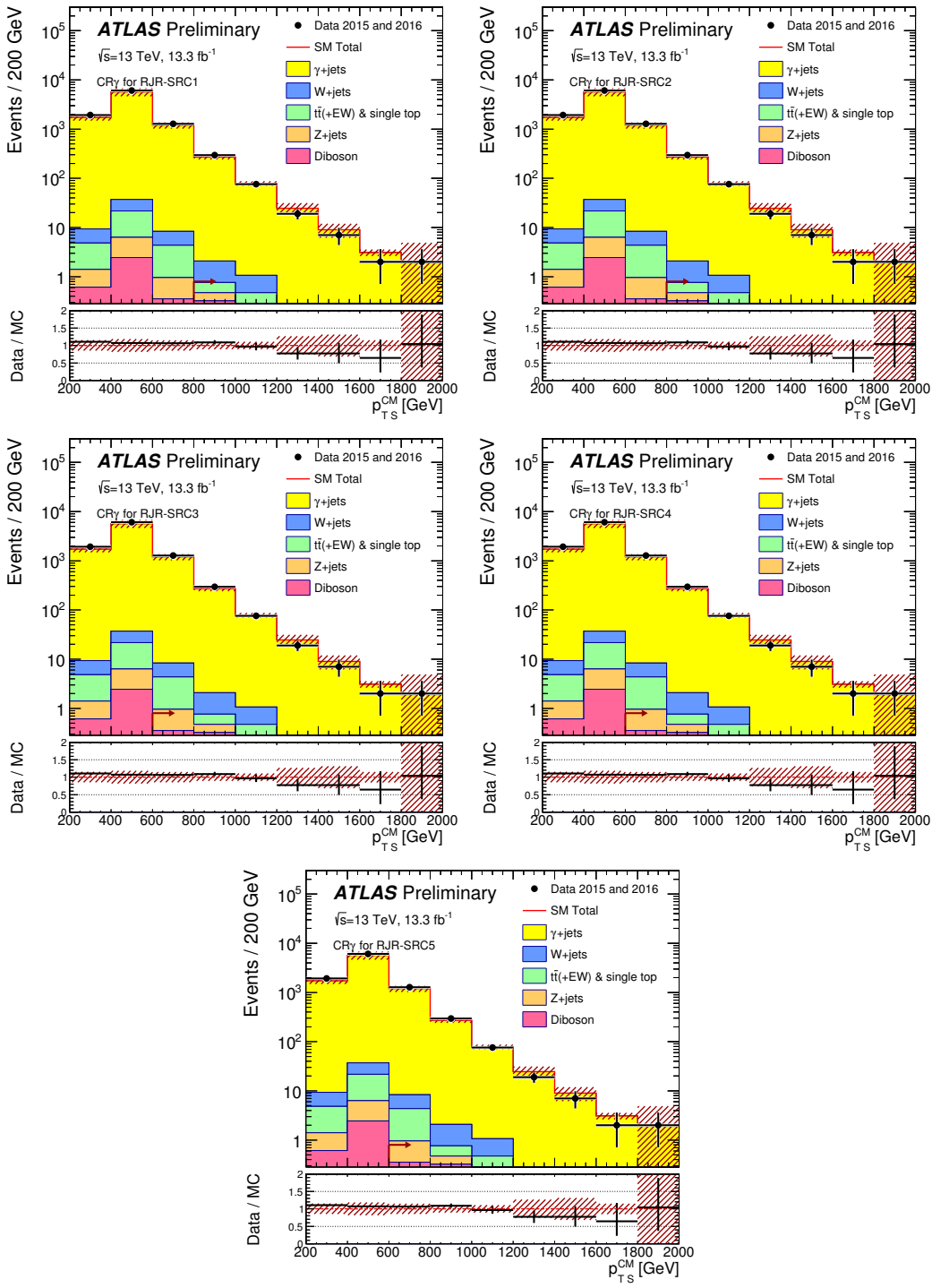


Figure 8.4: Scale variable distributions for the compressed CRY regions.

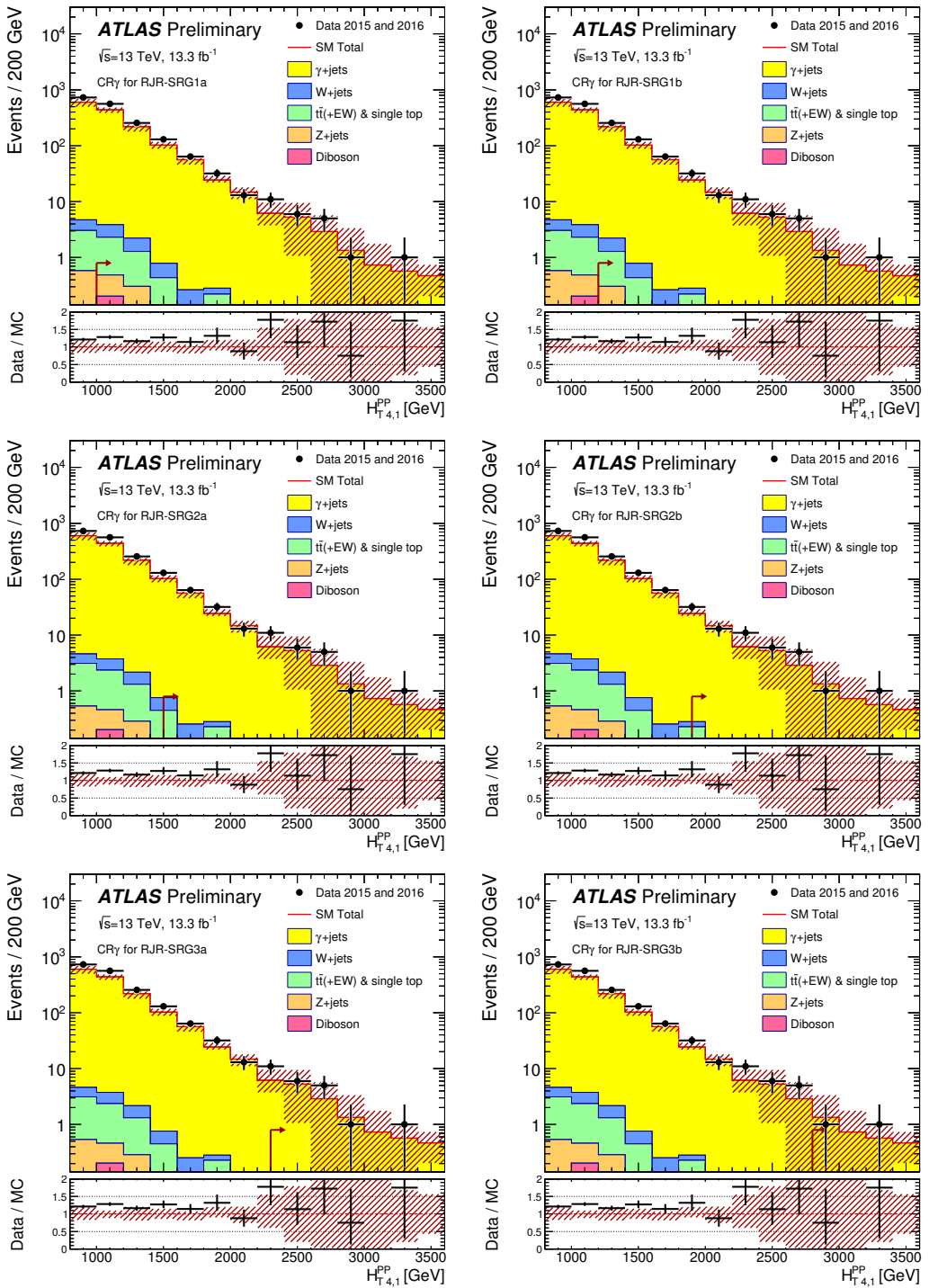


Figure 8.5: Scale variable distributions for the gluino CRY regions.

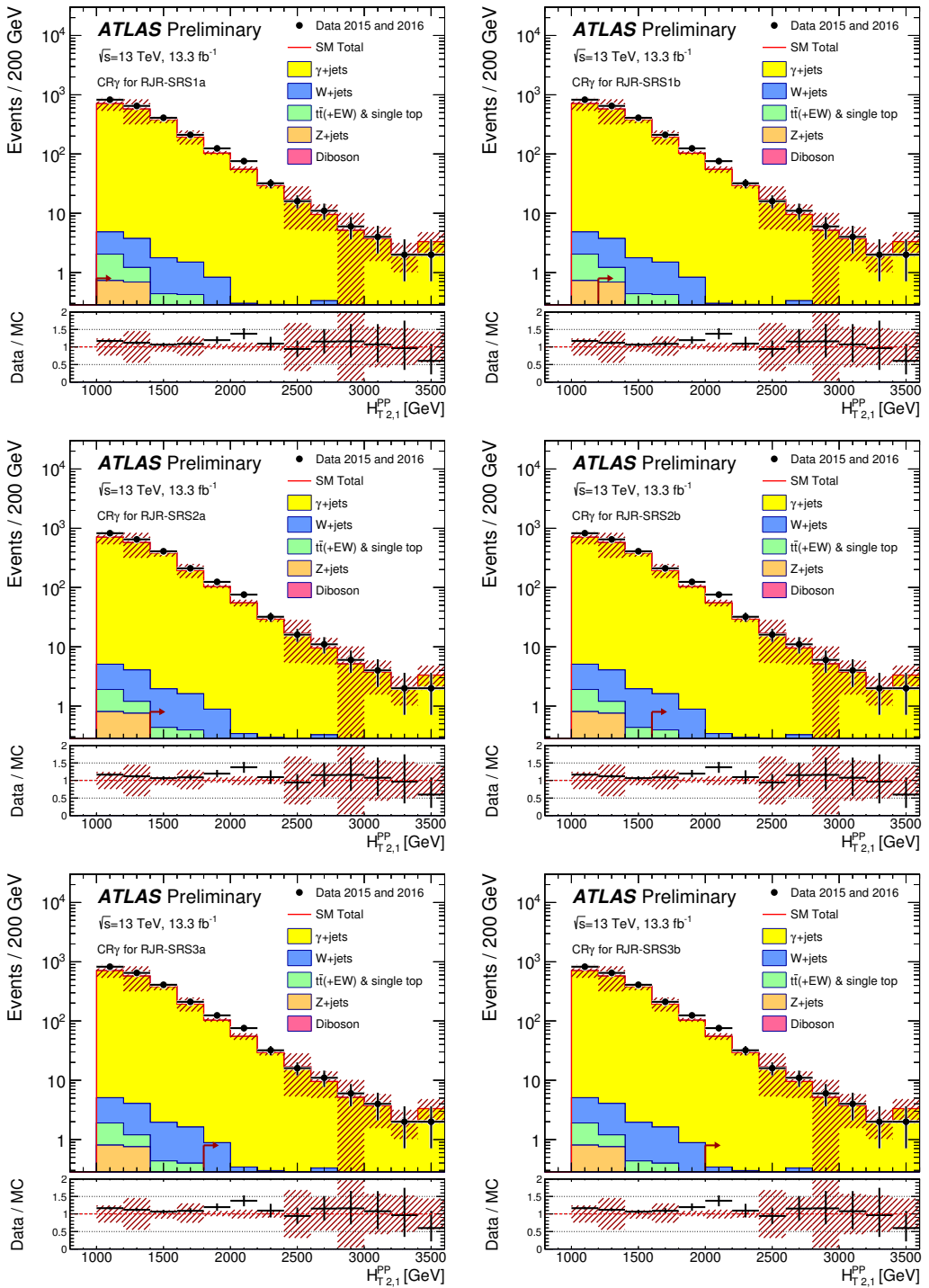


Figure 8.6: Scale variable distributions for the squark CRY regions.

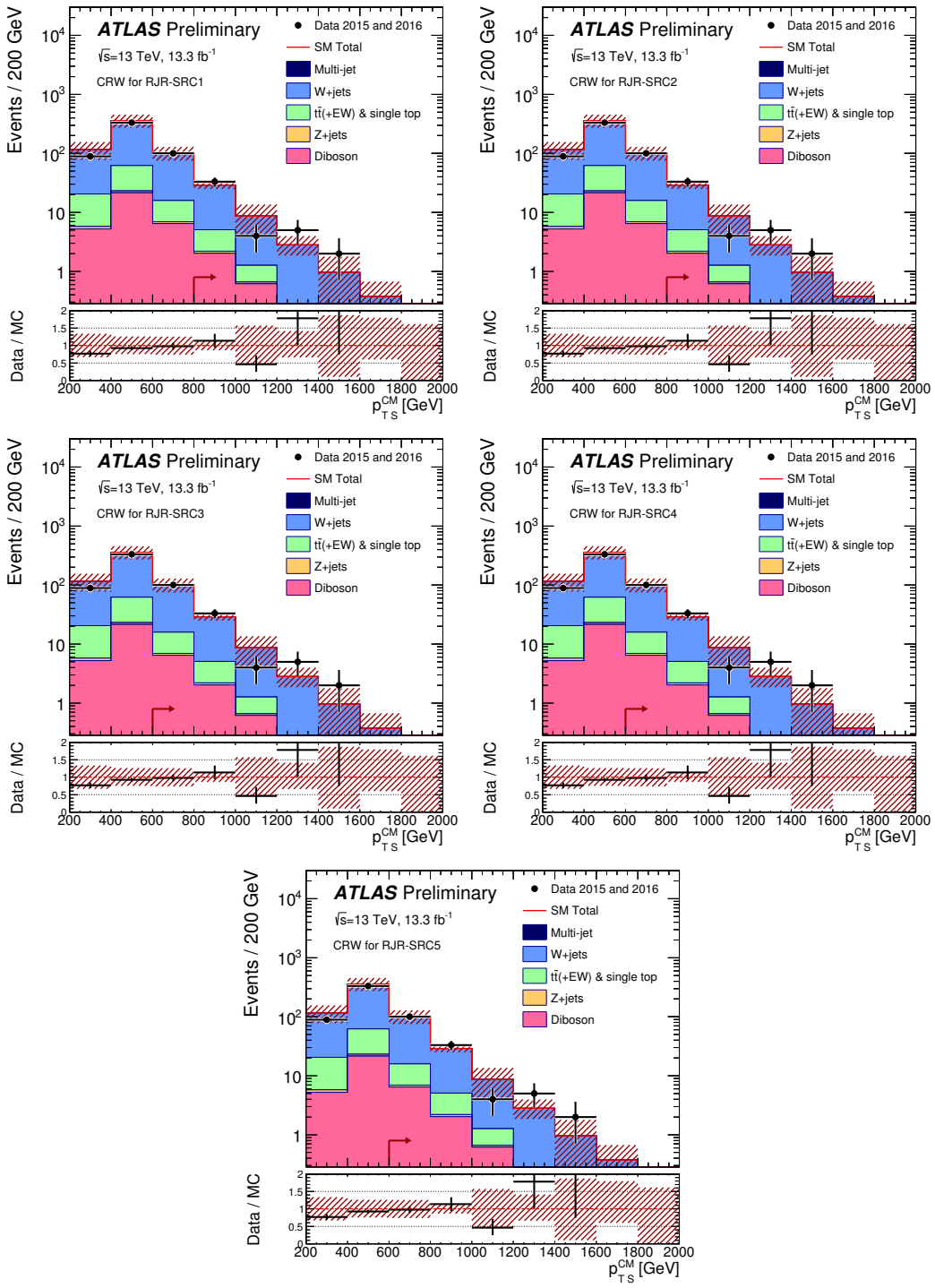


Figure 8.7: Scale variable distributions for the compressed CRW regions.

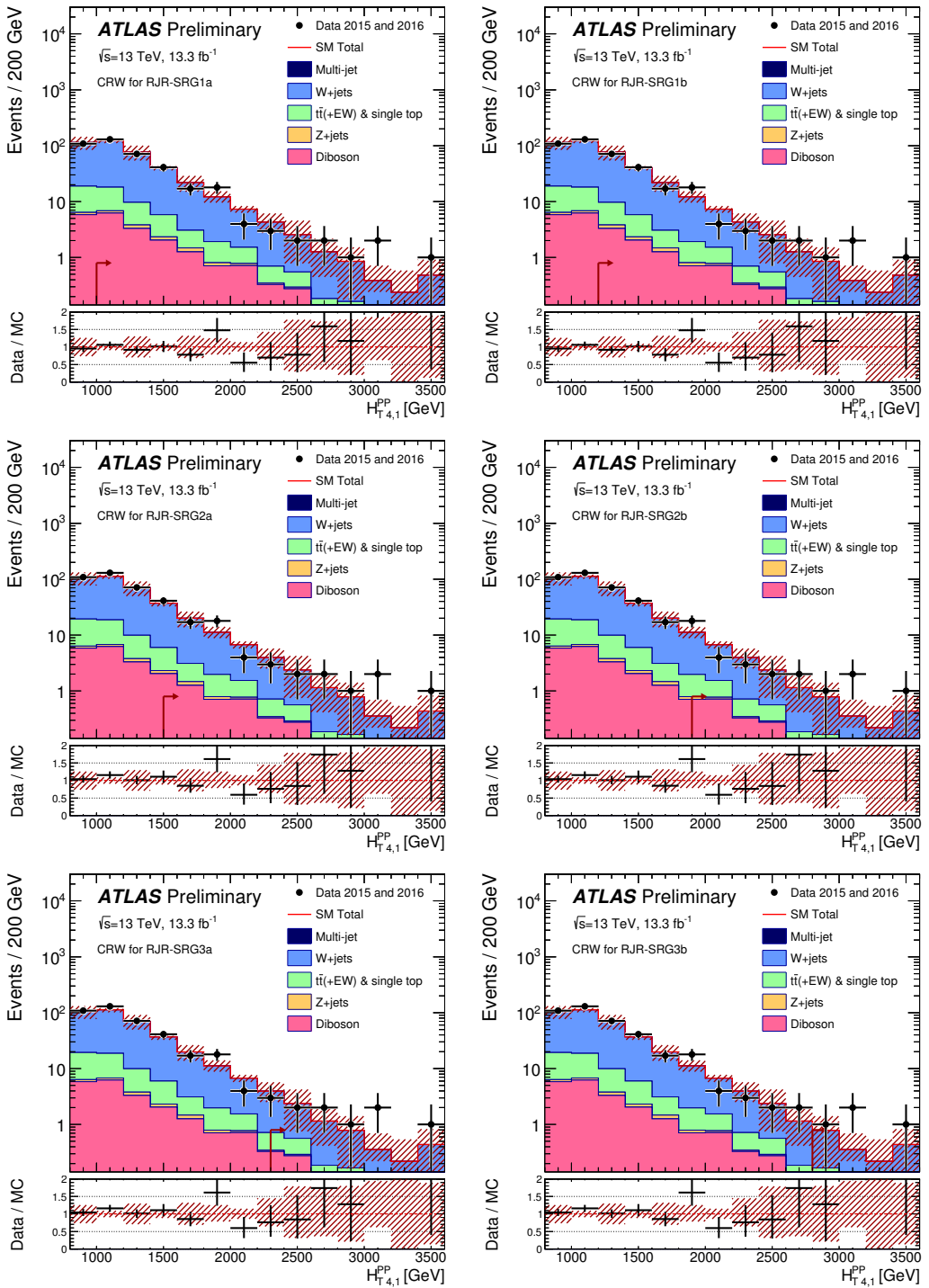


Figure 8.8: Scale variable distributions for the gluino CRW regions.

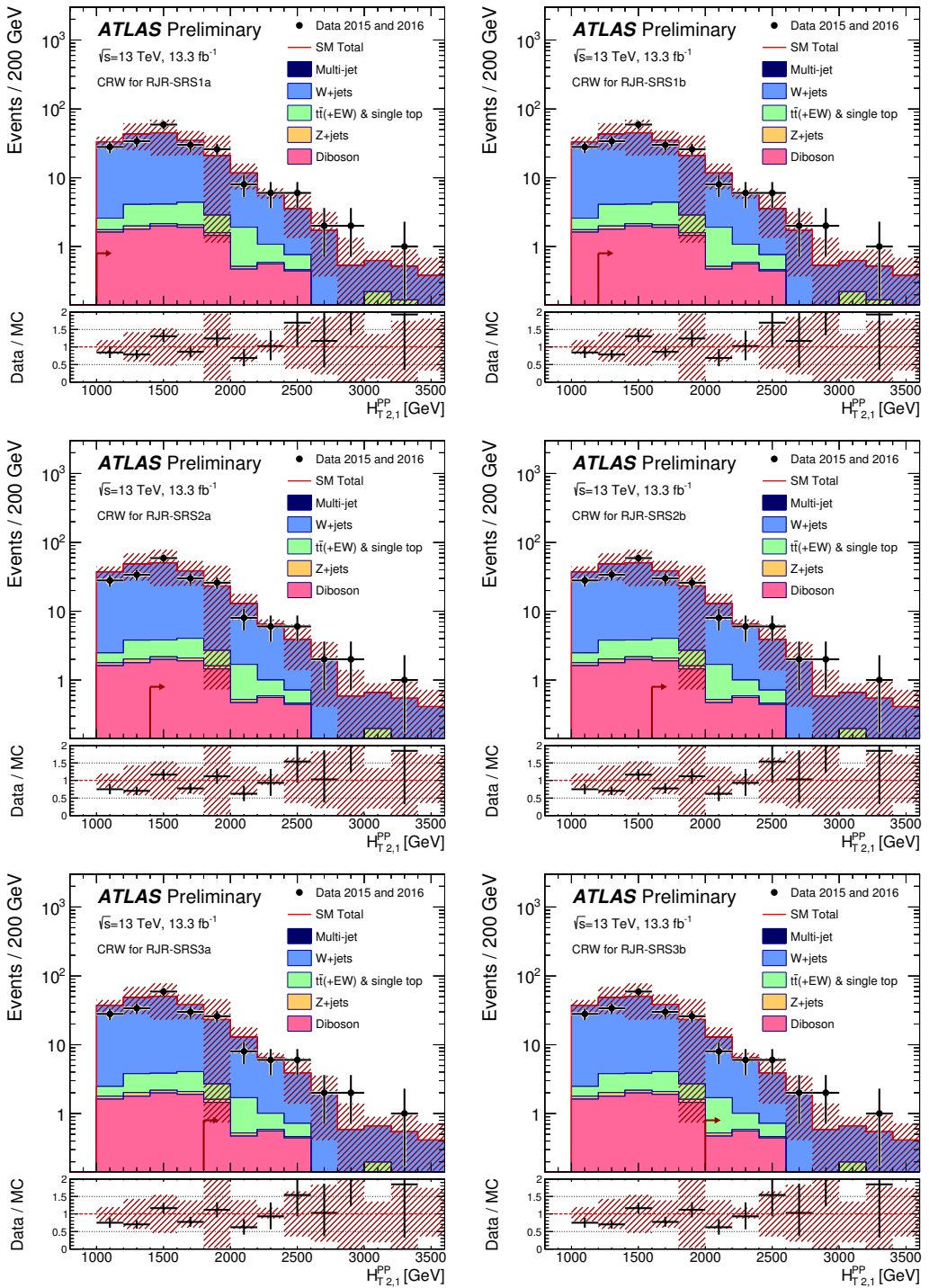


Figure 8.9: Scale variable distributions for the squark CRW regions.

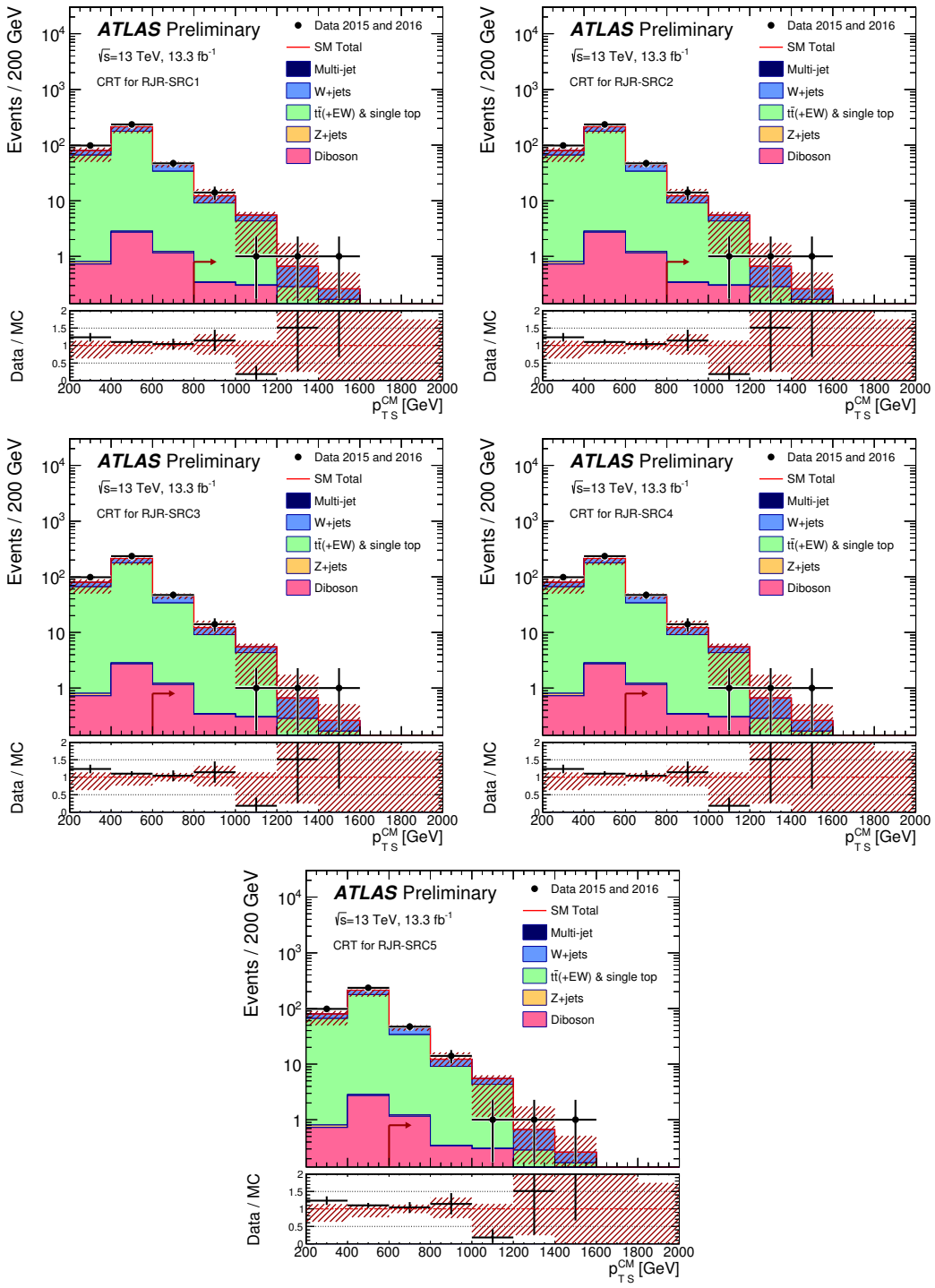


Figure 8.10: Scale variable distributions for the compressed CRT regions.

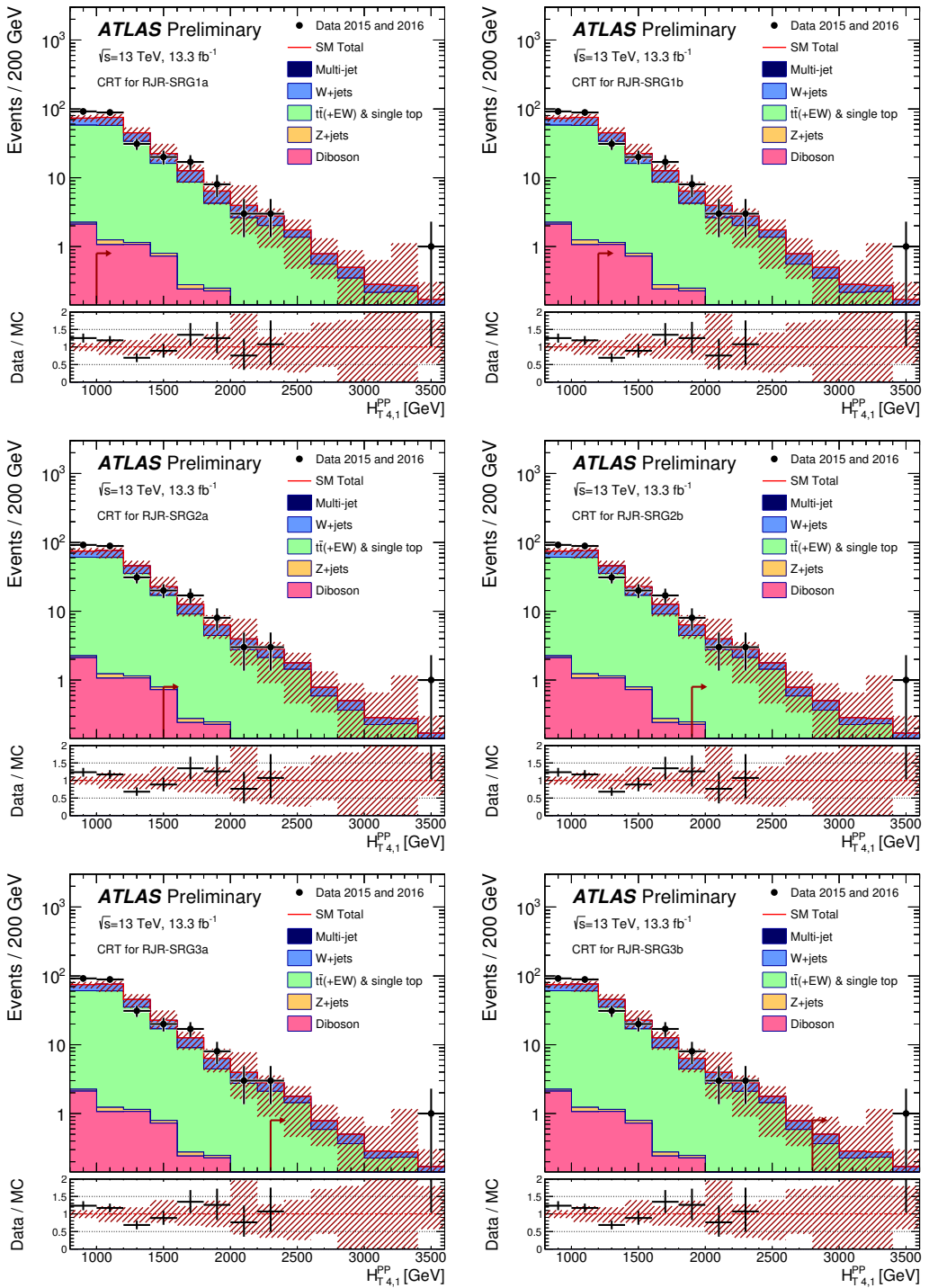


Figure 8.11: Scale variable distributions for the gluino CRT regions.

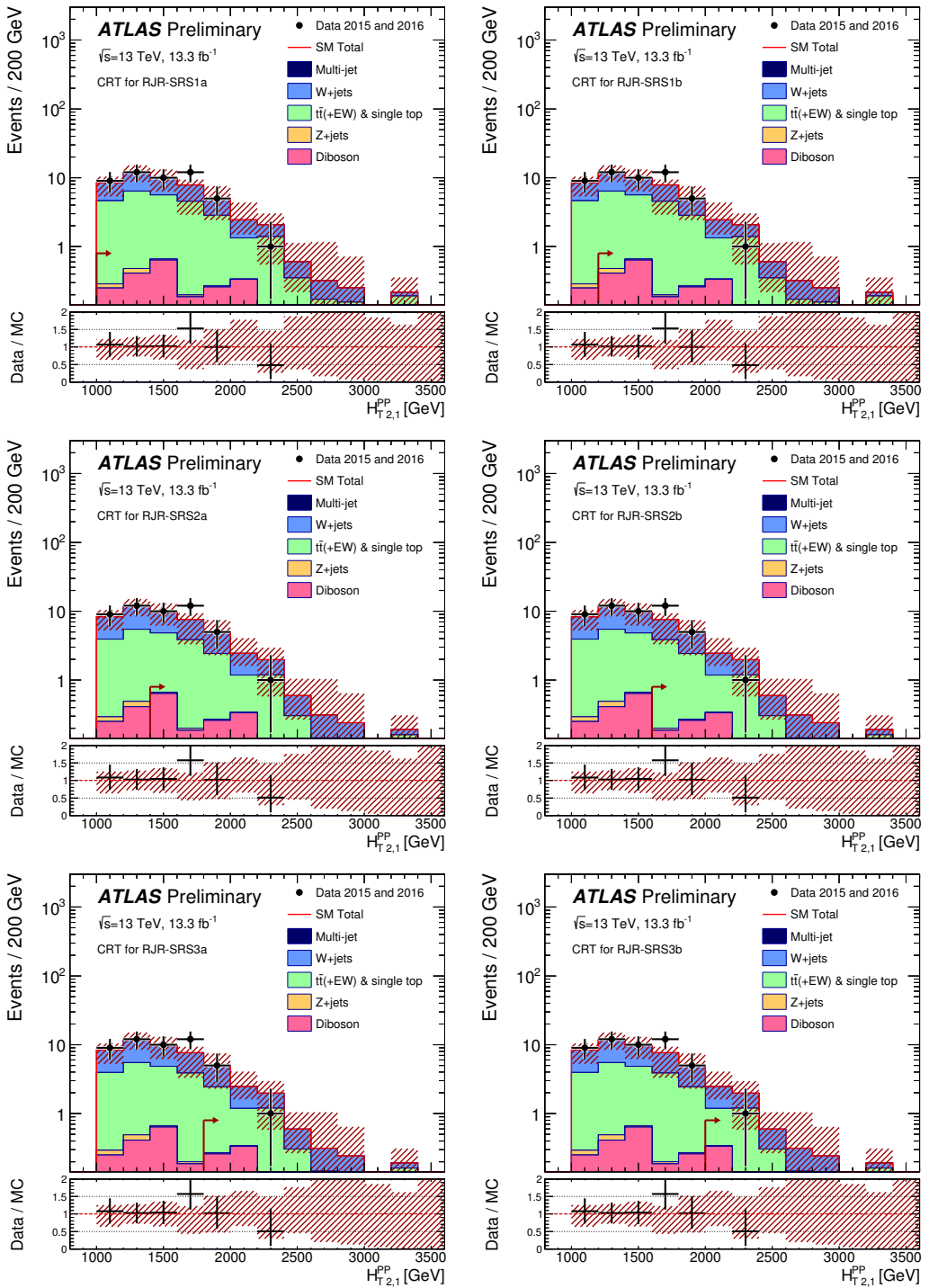


Figure 8.12: Scale variable distributions for the squark CRT regions.

1984 **Validation Regions**

1985 As discussed in general terms above, we define a set of validation regions to ensure  
1986 we can properly model the particular backgrounds as we move closer to the SRs in  
1987 phase space. We define at least one validation region for each major background.

1988 For the most important background  $Z \rightarrow \nu\nu$ , we use a series of validation regions.  
1989 The primary validation region, which we label as VRZ, is defined by selecting lepton  
1990 pairs of opposite sign and identical flavor which lie within  $\pm 25\text{ GeV}$  of the Z boson mass.  
1991 This selection has high purity for  $Z \rightarrow \ell\ell$  events as seen in simulation. We treat the  
1992 two leptons as contributions to the  $E_T^{\text{miss}}$  (as we did with the photon in CRY). This  
1993 selection uses the same kinematic cuts as the signal region. We also define two VRs  
1994 using the same event selection but looser kinematic cuts, which we label VRZa and  
1995 VRZb. VRZa has a loosened selection on  $H_{1,1}^{PP}$ , again to the loosest value among the  
1996 signal regions, as was done for CRW and CRt. VRZa has a loosened selection on  
1997 the primary scaleful variable ( $H_{T,2,1}^{PP}$  or  $H_{T,4,1}^{PP}$ ), again to the loosest value among the  
1998 signal regions, as was done for CRW and CRT. These two validation regions allow us  
1999 to test the modeling of each of these variables individually, as well as allowing more  
2000 validation region statistics in the signal regions with tighter cuts on these variables.

2001 For the compressed regions, these  $Z$  validation region were found lacking. The  
2002 leptons are highly boosted in the compressed case, and the lepton acceptance was  
2003 quite low due to lepton isolation requirements in  $\Delta R$ . Instead, two fully hadronic  
2004 validation region were developed for the compressed regions. The first, VRZc has  
2005 identical requirements to the signal regions with an inverted requirement on  $\Delta\phi_{ISR,I}$ .  
2006 From simulation, this region was found to be at least 50% pure in  $Z$  events, which  
2007 was considered enough to validate this background in this extreme portion of phase  
2008 space. For additional validation region statistics, we also developed VRZca, which  
2009 takes again uses the loosest set of cuts from each signal region. Note this means that  
2010 each compressed signal region has an identical VRZca.

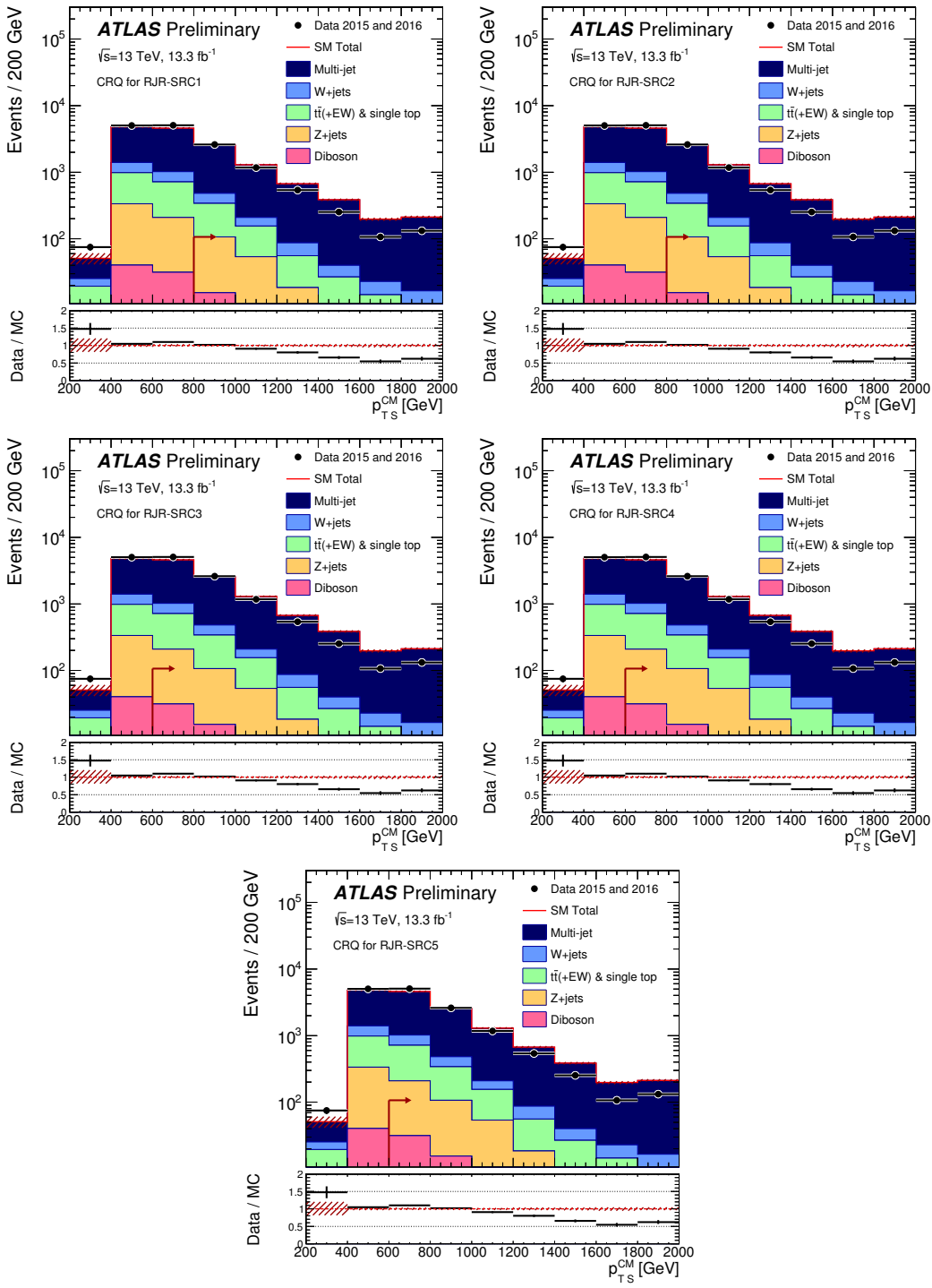


Figure 8.13: Scale variable distributions for the compressed CRQ regions.

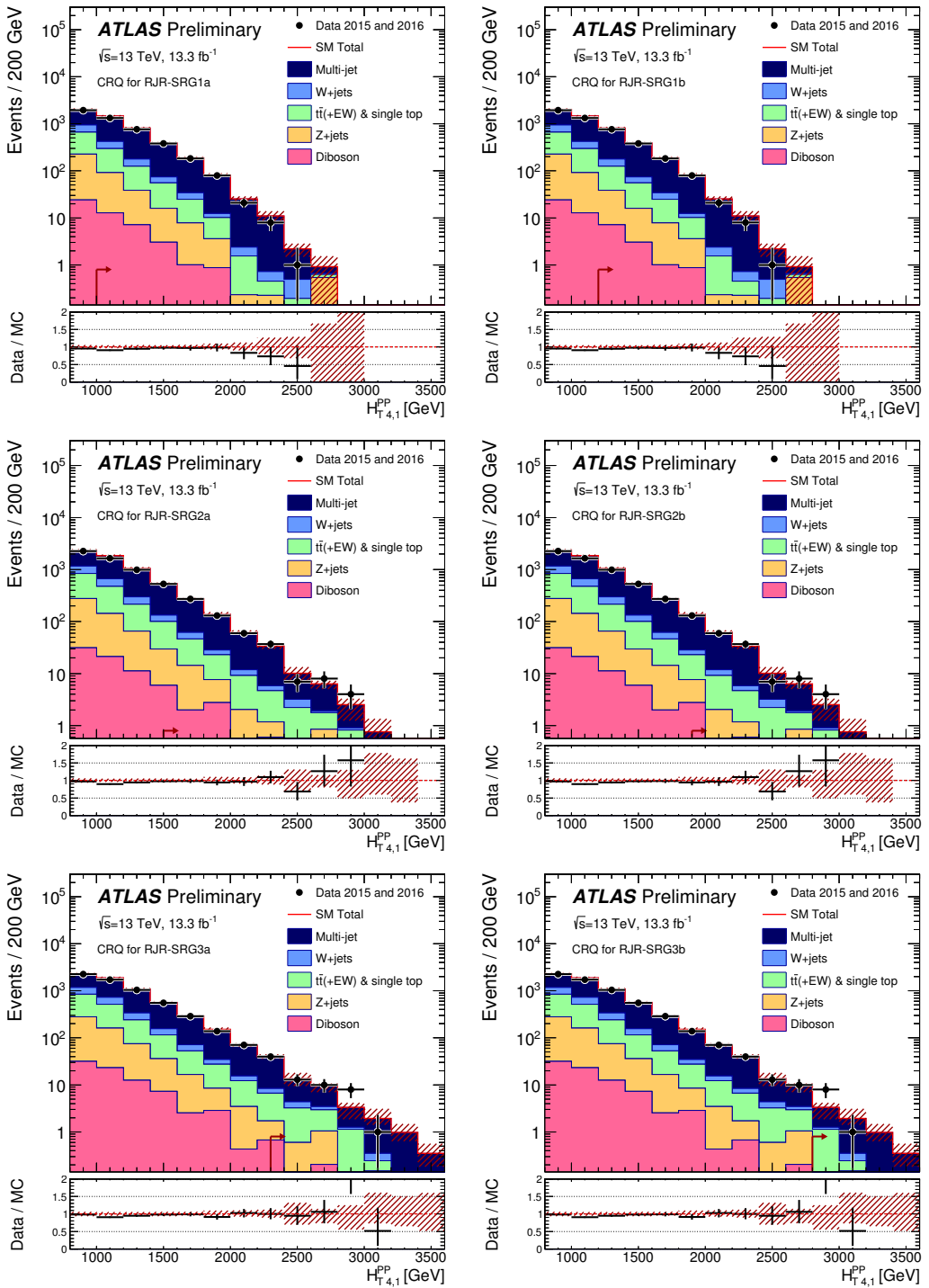


Figure 8.14: Scale variable distributions for the gluino CRQ regions.

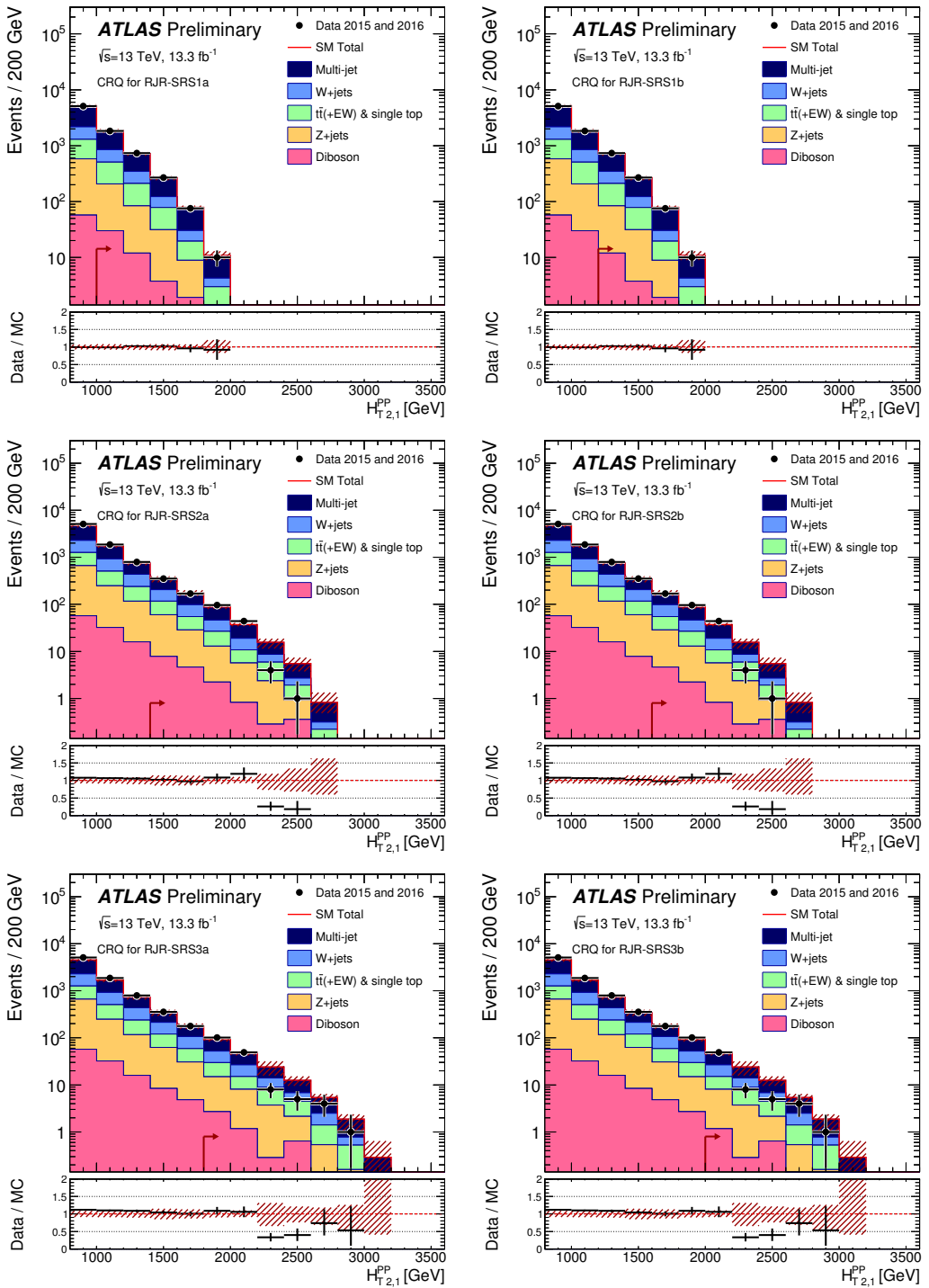


Figure 8.15: Scale variable distributions for the squark CRQ regions.

2011        The top and  $W$  validation regions use the same event selection as the correspond-  
2012        ing control regions, as described above. However, unlike the control regions, these  
2013        validation regions reimpose the SR scaleful variable selections, to be closer in phase  
2014        space to the hadronic signal regions. In the same way as we did for VRZa and  
2015        VRZb, we also define auxiliary VRs which loosen the cuts on the scale variables. We  
2016        define VRTa (VRWa) as VRT (VRW) with the same loosened cut on  $H_{1,1}^{PP}$  and VRTb  
2017        (VRWb) as VRT (VRW) with the same loosened cut on the primary scale variable.

2018        The final set of validation regions are those defined to check the estimation of  
2019        the QCD background. VRQ is defined to be identical to the corresponding CRQ,  
2020        but again we use the full SR region cuts for the scaleful variables. This selection is  
2021        then closer to the corresponding signal region to validate the CRQ estimate. We also  
2022        define the auxiliary validation regions VRQa and VRQb for the noncompressed signal  
2023        regions. In this case, we reimpose one of the two inverted cuts in CRQ with respect  
2024        to the signal regions, to make each one even closer to the SRs. In CRQa (CRQb), we  
2025        reimpose the  $H_{1,1}^{PP}$  ( $\Delta_{\text{QCD}}$ ).

2026        For the compressed case, we again define a separate validation region, due to  
2027        the special kinematics probed. We construct a validation region which is the same  
2028        as CRQ, with  $.5 < R_{\text{ISR}} < R_{\text{ISR, SR}}$ , where  $R_{\text{ISR, SR}}$  is the cut on  $R_{\text{ISR}}$  in the  
2029        corresponding SR. Again, this can be seen as probing “in between” the CR and  
2030        SR in phase space.

The results of this validation can be seen in Fig. 8.16. Each bin is *pull* of the validation region corresponding to a particular signal region. This is defined

$$\text{Pull} = \frac{N_{\text{obs}} - N_{\text{pred}}}{\sigma_{\text{tot}}} \quad (8.4)$$

2031        where  $\sigma_{\text{tot}}$  is the total uncertainty folding in all systematic uncertainties, which we  
2032        will describe later. Assuming we have well-measured our backgrounds, we expect a  
2033        Gaussian distribution of the pulls around 0, with a standard deviation of 1, as this  
2034        is measuring the number of standard deviations around the mean. We can see there

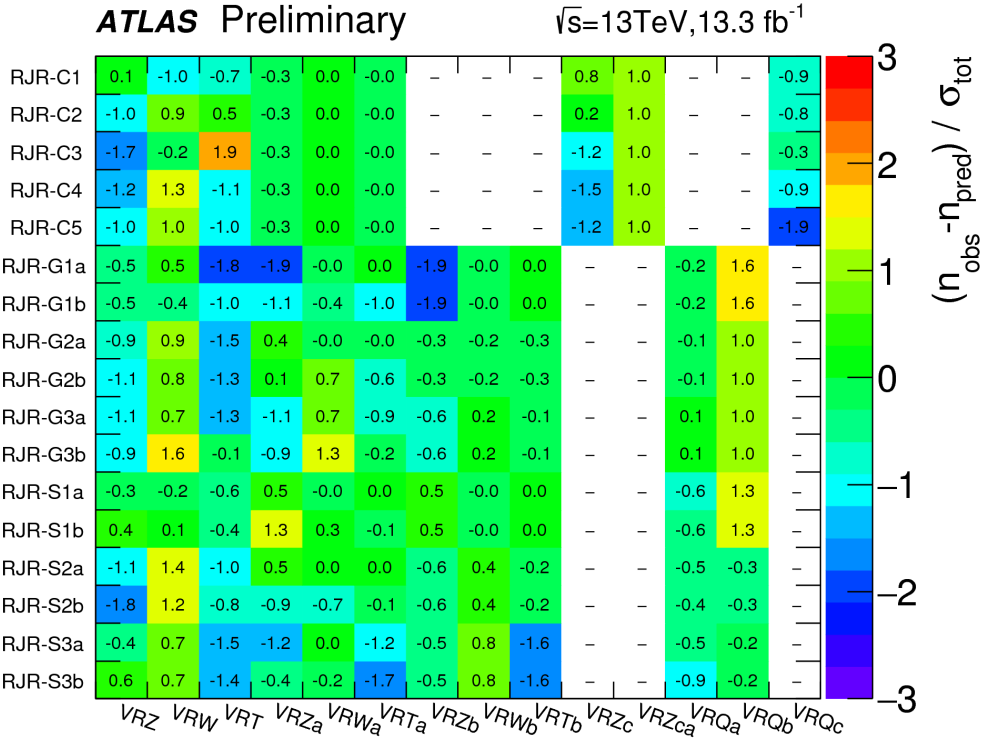


Figure 8.16: Summary of the validation region pulls

2035 are few positive pulls (indicating an underestimation of the background), indicating  
 2036 we have conservatively measured the Standard Model backgrounds with our control  
 2037 regions.

## 2038 Systematic Uncertainties

2039 In this section, we discuss the uncertainties considered. These generally fall into  
 2040 four categories: theoretical generator uncertainties, uncertainties on the CR to SR  
 2041 extrapolations, uncertainties on the data-driven transfer factor corrections, and object  
 2042 reconstruction uncertainties. We discuss each of these categories here. A table  
 2043 summarizing this section is in Tab. 8.5

2044 The theoretical generator uncertainties are evaluated by using alternative sim-  
 2045 ulation samples or varying scale uncertainties. In the case of the  $Z+jets$  and

Systematic	Uncertainty Description
alpha_GeneratorZ	Theoretical on $Z$ cross-section
alpha_generatorW	Theoretical on $W$ cross-section
alpha_generatorTop	Theoretical on $t$ cross-section
alpha_radiationTop	Theoretical on $t$ radiation tune
alpha_Pythia8Top	Theoretical on $t$ fragmentation tune
alpha_FlatDiboson	Flat on diboson cross-section
mu_Zjets	CRY extrapolation to SR
mu_Wjets	CRW extrapolation to SR
mu_Top	CRT extrapolation to SR
mu_Multijets	CRQ extrapolation to SR
alpha_Kappa	$\kappa$ factor
alpha_QCDError	Jet smearing
alpha_JET_GroupedNP_1	JES NP group 1
alpha_JET_GroupedNP_2	JES NP group 2
alpha_JET_GroupedNP_3	JES NP group 3
alpha_JER	JER
alpha_MET_SoftTrk_ResoPerp	Soft $E_T^{\text{miss}}$ resolution perpendicular to hard object system
alpha_MET_SoftTrk_ResoPara	Soft $E_T^{\text{miss}}$ resolution parallel to hard object system
alpha_MET_SoftTrk_Scale	Soft $E_T^{\text{miss}}$ scale

Table 8.5: Description of the systematic uncertainties in the analysis.

2046  $W+jets$  backgrounds, the related theoretical uncertainties are estimated by varying  
 2047 the renormalization, factorization, and resummation scales by two, and decreasing  
 2048 the nominal CKKW matching scale by 5 GeV and 10 GeV respectively. In  
 2049 the case of  $t\bar{t}$  production, we compare the nominal POWHEG-BOX generator with  
 2050 MG5\_aMC@NLO, as well as comparing different radiation and generator tunes. As  
 2051 stated above, we account for the uncertainty on the small diboson background by  
 2052 imposition of a flat 50% uncertainty.

2053 The CR to SR extrapolation uncertainties, or what could be called the transfer  
 2054 factor uncertainties, are listed in Tab. 8.5 as  $\mu_{\text{u..}}$ . There is one normalization factor  $\mu$   
 2055 for each major background, and their uncertainties, especially  $\mu_Z$ , are often dominant  
 2056 for the measurement in many signal regions. This uncertainty is generally dominated  
 2057 by the statistical uncertainty in the CR.

2058 There are two uncertainties from the data-driven corrections to the transfer  
 2059 factors. The first is the uncertainty on  $\kappa$ , which is measured using an auxiliary  $Z \rightarrow \ell\ell$   
 2060 control region. This is labeled alpha\_Kappa. The other is the uncertainty is that  
 2061 assigned to the jet smearing method, which is seen in the table as alpha\_QCDError.

2062        The final set of uncertainties are those related to object reconstruction. In the  
2063        case of the hadronic search presented, the important uncertainties are those assigned  
2064        to the jet energy and  $E_T^{\text{miss}}$ . The uncertainties on the lepton reconstruction and  
2065         $b$ -tagging uncertainties were found to be negligible in all SRs. The measurement  
2066        of the jet energy scale (JES) uncertainty is quite complicated, and described in  
2067        [138–140]. After a complicated procedure to decorrelate the various components  
2068        of the JES uncertainty, there are three components which remain, which are labeled  
2069        as alpha\_JET\_GroupedNP\_1,2,3. The jet energy resolution uncertainty is estimated  
2070        using the methods discussed in Refs. [140, 141], and is labeled alpha\_JER.

2071        The  $E_T^{\text{miss}}$  soft term uncertainties are described in [117, 118, 142]. The  
2072        uncertainty on the  $E_T^{\text{miss}}$  soft term resolution is parameterized into a component  
2073        parallel to direction of the rest of the event (the sum of the hard objects  $p_T$ )  
2074        and a component perpendicular to this direction. There is also an uncertainty  
2075        on the  $E_T^{\text{miss}}$  soft term scale. These are labeled as alpha\_MET\_SoftTrk\_ResoPara,  
2076        alpha\_MET\_SoftTrk\_ResoPerp, and alpha\_MET\_SoftTrk\_Scale.

## 2077        **Fitting procedure**

2078        This section describes the fitting procedure to properly account for the correlations  
2079        between the various uncertainties and the simultaneous fitting of the control and  
2080        signal regions.

## 2081        **Maximum likelihood fit**

2082        To properly account for the systematic uncertainties and simultaneously fit the control  
2083        regions, we employ a maximum-likelihood fit as described in [125]. The likelihood  
2084        function  $\mathcal{L}$  is the product of the Poisson distributions governing the likelihood in each  
2085        of the signal regions and the corresponding control regions: We begin by considering

2086 our event counts  $\mathbf{b}$  in a signal region with its corresponding signal regions. The  
 2087 systematic uncertainties are included as a set of nuisance parameters  $\boldsymbol{\theta}$ .

The full likelihood function can be written [125]:

$$\mathcal{L}(n|\mu, \mathbf{b}) = P_{\text{SR}} \times P_{\text{CR}} \times C_{\text{syst}} \quad (8.5)$$

$$= P(n_S|\lambda_S(\mu_S, \mathbf{b}, \boldsymbol{\theta})) \times \prod_{i \in \text{CR}} P(n_i|\lambda_i(\mu_b, \mathbf{b}, \boldsymbol{\theta})) \times C_{\text{syst}}(\boldsymbol{\theta}^0, \boldsymbol{\theta}) \quad (8.6)$$

where  $P(n_i|\lambda_i(\mu, \mathbf{b}, \boldsymbol{\theta}))$  is a Poisson distribution conditioned on the event counts  $n_i$  in the  $i$ -th CR with mean parameter  $\lambda_i(\mu, \mathbf{b}, \boldsymbol{\theta})$ . The term  $C_{\text{syst}}(\boldsymbol{\theta}^0, \boldsymbol{\theta})$  is the probability density function with central values  $\boldsymbol{\theta}^0$  which are varied with the nuisance parameters  $\boldsymbol{\theta}$ . We model these as Gaussian distributions with unit width and mean zero:

$$C_{\text{syst}}(\boldsymbol{\theta}^0, \boldsymbol{\theta}) = \prod_{s \in S} G(\mu = \theta_s, \sigma = 1), \quad (8.7)$$

2088 where  $S$  is the set of systematic uncertainties considered in the analysis.

The terms  $\lambda_j$  for any region  $j$  can be expressed as

$$\lambda_j(\mu, \mathbf{b}, \boldsymbol{\theta}) = \sum_b \mu_b b_j \prod_{s \in S} (1 + \Delta_{j,b,s} \theta_s) \quad (8.8)$$

2089 The term  $\mu_b$  is the normalization factor associated to the background  $b$  with event  
 2090 count  $b_j$  in the region  $j$ . The terms  $\Delta$  inside the product represent scale factors  
 2091 freeing the model to account for the systematic uncertainties  $\theta_s$ .

2092 The process now is to maximize this likelihood function, given the free parameters  
 2093  $\mu_b$  and the parameters  $\Delta$  associated to the systematics as nuisance parameters. This  
 2094 is done using the HISTFITTER package [125]. The normalization parameters  $\mu_b$  are  
 2095 the primary output of this maximization, and are in fact the control regions' raison  
 2096 d'être. This allows the magnitudes of each background process to be maximized *given*  
 2097 *the actual control region event counts*. We can say the normalization parameters  
 2098 are found such that the likelihood is maximized. The nuisance parameters are also  
 2099 determined by this procedure, but do not have a straightforward

The final expected background prediction in each fit by region  $r_s$  is then given by

$$N_{\text{total background}} = \sum_b \mu_b N_{b,\text{MC}} \quad (8.9)$$

## Background-only fit, model-independent fit, and model-dependent fit

The maximum likelihood fit described above can be used with a variety of event count inputs. We use three separate fit classes, which we call *background-only*, *model-independent*, and *model-dependent* fits. In terms of the likelihood function inputs, these can be seen as including a different list of event counts  $\mathbf{b}$

In this section, we describe the fitting procedure employed, which properly accounts for the correlations between the uncertainties through the use of a likelihood fit as described in [125]. We use three classes of likelihood fits: *background-only*, *model-independent*, and *model-dependent* fits. The background-only fits estimate the background yields in each signal region. These fits use only the control region event yields as inputs; they do not include the information from the signal regions besides the simulation event yield. The cross-contamination between CRs is also fit by this procedure. The systematic uncertainties described in the previous section are used as nuisance parameters. This background only fit also estimates the background event yields in the validation regions. When designing the analysis (before unblinding the signal regions), checking the validation region agreement is the primary way to validate the consistency and accuracy of the background estimation procedure.

In the case no excess is observed, we use a model-independent fit to set upper limits on the possible number of possible beyond the Standard Model events in each SR. These limits are derived using the same procedure as the background-only fit, with two additional pieces of information included in the fitting procedure. We include the SR event count, and a parameter known as the *signal strength*, defined as  $\mu =$

2123  $\sigma/\sigma_{\text{BG}}$ . Using the  $CL_s$  procedure [143] and neglecting the possible (small) signal  
2124 contamination in control regions, we derive the the observed and expected limits on  
2125 the number of events from BSM phenomena in each signal region.

2126 Model-dependent fits are used to set exclusion limits on the specific SUSY  
2127 models considered in this thesis, particular the gluino or squark pair production  
2128 with various mass splittings. This can be seen as identical to the background-only  
2129 fit with an additional simulation input from the particular model of interest, with its  
2130 corresponding systematic uncertainties from detector effects accounted for as in the  
2131 background-only fit. As noted when we introduced Fig. 8.1, the exclusion contours  
2132 from previous model-dependent fits are the primary motivating factor in the design  
2133 of our signal regions. If no excess is found, we set limits on each of the simplified  
2134 signal models with various mass splittings.

*Results*

2137 This chapter presents the results of the analysis presented in the previous chapter.  
 2138 We present the full set of signal region distributions after applying the  $\mu$  factors  
 2139 derived from the fitting procedure. We also present the systematic uncertainties in  
 2140 each signal region properly accounting for the correlations of the uncertainties. As  
 2141 no excess is observed, we show exclusion limits in the sparticle- $\tilde{\chi}_1^0$  plane based on  
 2142 the results of the model-dependent fits and present the model-independent limits.

2143 **9.1 Signal region distributions**

2144 In Figs. 9.1 to 9.3, we can see the unblinded distributions of the last scale cut used  
 2145 for each signal region. These distributions include the  $\mu$  normalization scale factors  
 2146 derived from the fitting procedure. The systematic uncertainties are also shown.  
 2147 Each plot shows the distribution from a signal model which is targetted by the given  
 2148 signal region.

2149 These distributions have all cuts applied except for the cut on this scale variable,  
 2150 which allows us to see the additional discrimination provided by the given variable.  
 2151 Since signal regions with the same numeral have identical cuts except for that on the  
 2152 main scale variable, we show (a) and (b) on the same figure. The left-most (right-  
 2153 most) arrow shown is the location of the a (b) cut applied in the analysis. We call  
 2154 these plot  $N - 1$  plots, where  $N$  refers to the number of cuts applied in the analysis.  
 2155 The full set of  $N - 1$  plots in the signal regions for the other variables used in the

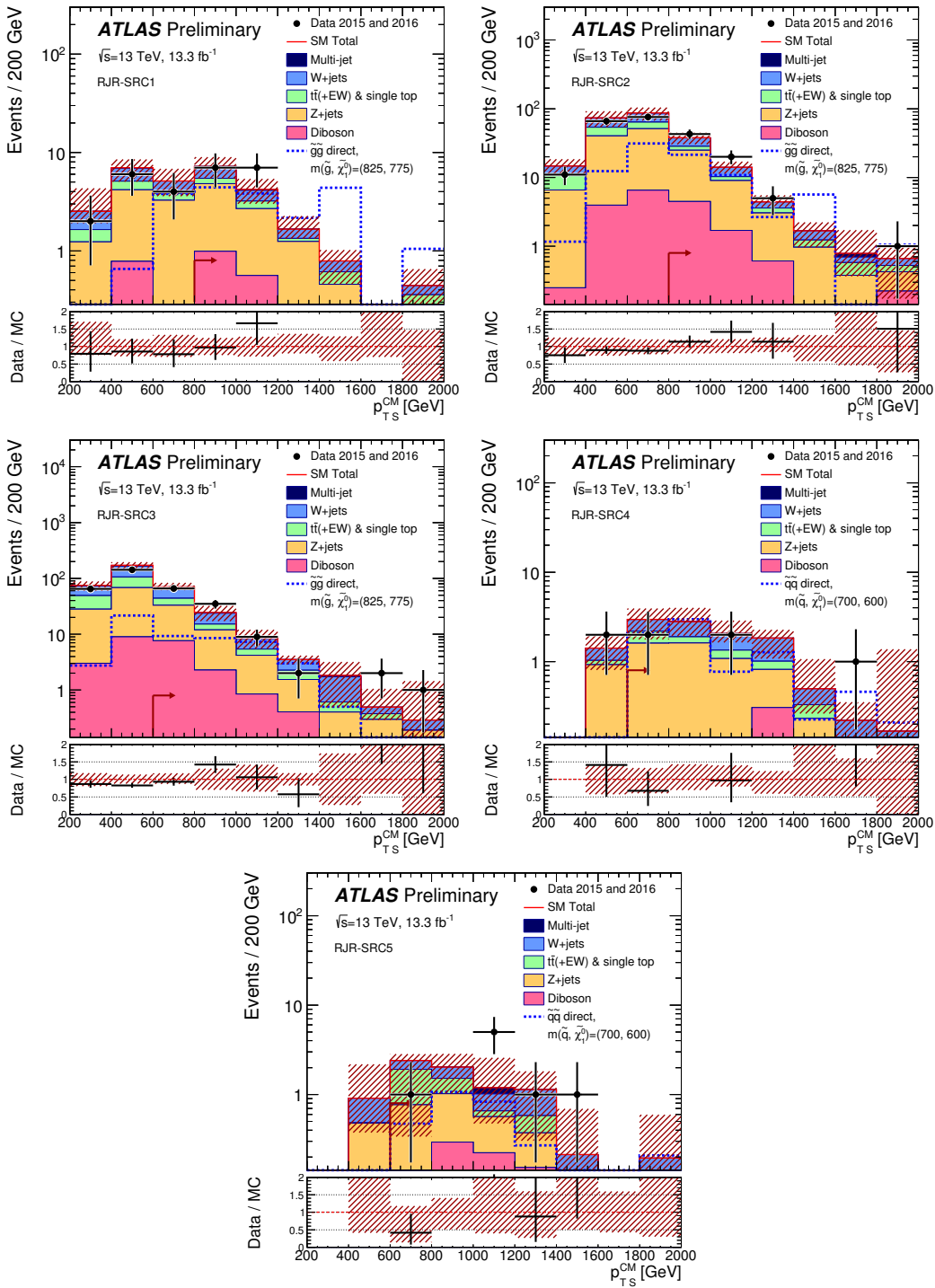


Figure 9.1: Scale variable distributions for the compressed signal regions.

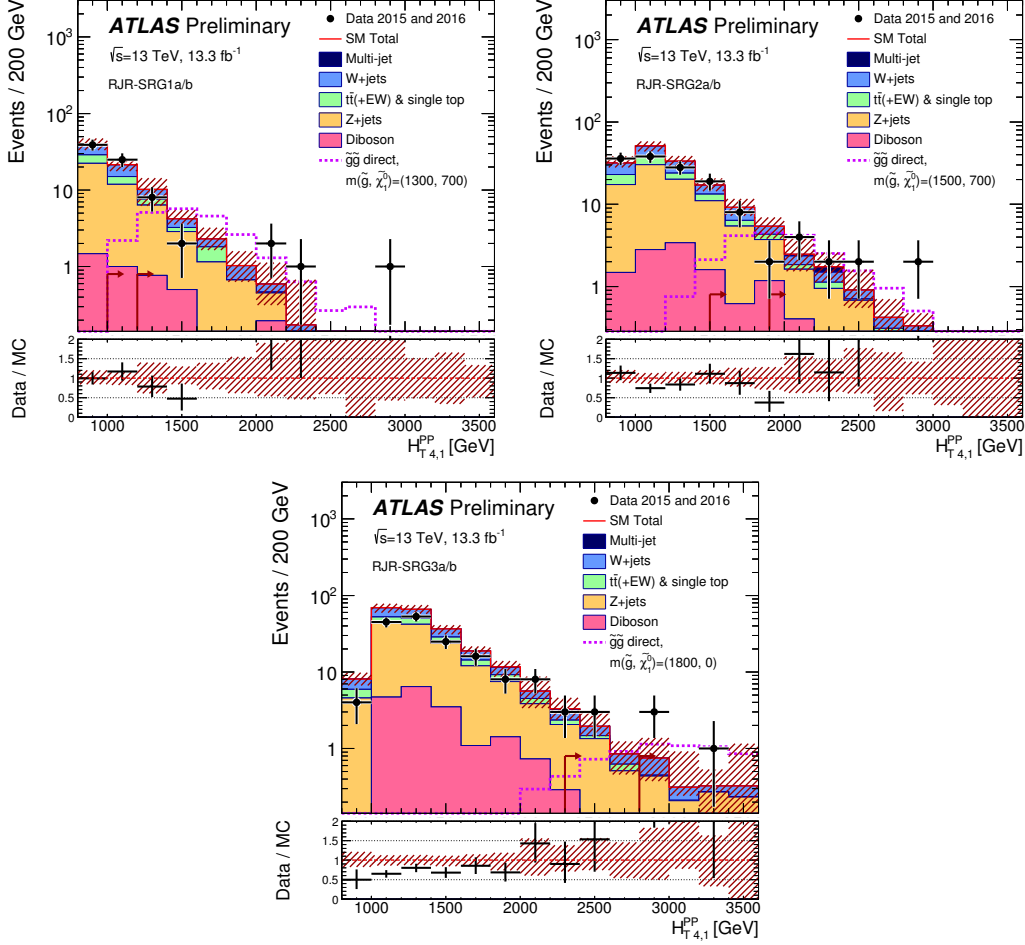


Figure 9.2: Scale variable distributions for the gluino signal regions.

analysis are shown in Sec. 9.4.

A figure showing a summary of the pulls in all of the SRs is shown in Fig. 9.4. This figure shows the integrated data and simulation values above the cut values in the N-1 plots, with the corresponding statistical and systematic uncertainties, for all signal regions simultaneously. The systematic uncertainties will be discussed in the next section. From this plot, we can see there is no significant excess of events over the Standard Model background.

This information is also presented in Tab. 9.2. The table includes the expectations from simulation before applying the  $\mu$  normalization factor, as well as the model-independent limits we will discuss later.

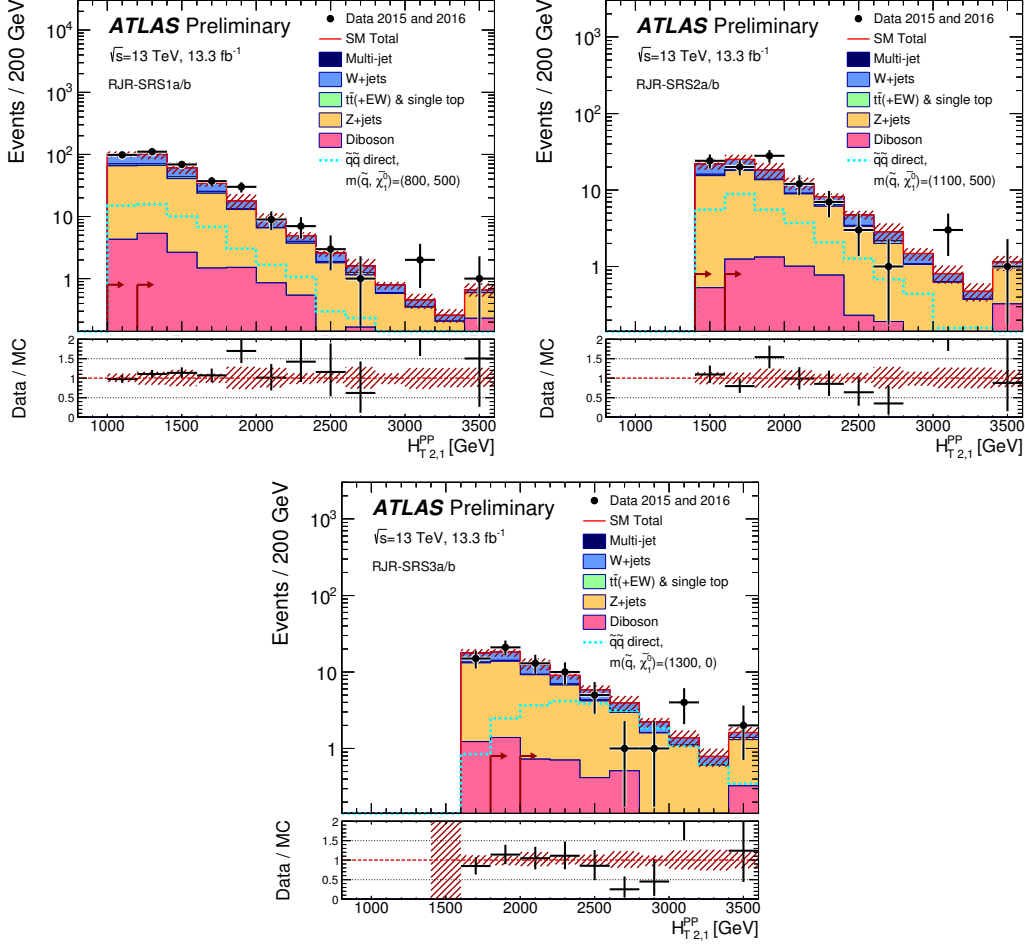


Figure 9.3: Scale variable distributions for the squark signal regions.

2166 We now consider the final values of the systematic uncertainties.

## 2167 9.2 Systematic Uncertainties

2168 This section considers the results of Tab. 9.1. This table is a summary of the resulting  
 2169 systematic uncertainties on the background estimation in each signal region, properly  
 2170 accounting for systematic uncertainties. These uncertainties are expressed both as a  
 2171 relative uncertainty and absolute uncertainty. As correlations are properly treated,  
 2172 the absolute uncertainties do not add in quadrature, although most uncertainties are  
 2173 relatively uncorrelated. We discuss the general trends in the systematic uncertainties

2174 for each type of signal region.

2175 In the squark regions, the total uncertainties range from 10% to 11%. We note  
2176 that the uncertainties on the  $Z$ , both theoretical and  $\Delta_{\mu, Z+\text{jets}}$  account for the largest  
2177 on the background estimate in each signal region. The  $\kappa$  factor uncertainty, which is  
2178 also an uncertainty on the  $Z$  estimate, is also significant at 4% in each region. The  
2179  $Z \rightarrow \nu\nu$  contribution to the squark regions is the primary irreducible background, so  
2180 even when relatively well-measured, the uncertainty on its event yield dominates the  
2181 overall uncertainty. There are also significant uncertainties from the  $W$ , top, and flat  
2182 diboson uncertainties, although these are subdominant. We note that the uncertainty  
2183 due to statistics of the MC simulation samples are very small for the squark case; this  
2184 is a reflection of the “looseness” of these regions, as the MC statistics are sufficient  
2185 for all of the major backgrounds.

2186 The gluino regions have overall larger uncertainties than the squark regions,  
2187 between 10% and 25%, due to a multitude of factors. The  $Z$  related uncertainties  
2188 all contribute significantly to the final background yield uncertainties. These  
2189 are relatively similar to the squark  $Z$  uncertainties. The  $W$ , top, and diboson  
2190 uncertainties are all significantly more important than in the squark case however. In  
2191 the gluino case, we also see that the limited simulation statistics begin to significantly  
2192 affect the measurement of the Standard Model background. These are all reflections  
2193 of the overall “tighter” quality of the gluino regions, as indicated by the event yields.  
2194 The  $\Delta_\mu$  uncertainties are affected by this due to the need to use overall looser  
2195 control regions, while the theory uncertainties are more affected by small statistical  
2196 fluctuations between different generators. The low statistics is particularly clear in  
2197 SRG3b, where the simulation statistics account for a very large 14% uncertainty.

2198 The compressed regions have systematic uncertainties ranging from 10% to 19%.  
2199 For the tighter regions, SRC1, SRC4, and SRC5, we see a large contribution from  
2200 the lack of MC statistics. SRC1 and SRC4 should a large value for the  $W$  theory

uncertainty, while all compressed regions show a large uncertainty on the  $Z$  estimate. These large uncertainties result from the fact that we are probing extreme phase space in boson  $p_T$  with the compressed regions. SRC5 shows large top and jet/ $E_T^{\text{miss}}$  uncertainties; these uncertainties are more pronounced in this region than the other compressed region due to the  $N_{\text{jet}}^V > 3$  cut, and thus the uncertainty in this region is quite affected by fluctuations in the top, jet, or  $E_T^{\text{miss}}$  uncertainties.

### 9.3 Limits and Model-dependent Exclusions

In Tab. 9.1, we show the statistical significance  $Z$  for each signal region. We calculate this using the fitted simulation mean compared with the observed event counts in each region. There is no significant excess in each region; the highest excess is in SRG3b, which is only  $Z_{\text{SRG3b}} = 1.55$ . This information is summarized in Fig. 9.4. We thus set model-independent and model-dependent limits.

As no significant excess is observed in any of the signal regions of this analysis after estimating the background using the background-only fit, we set limits on the model-independent and model-dependent cross sections.

The model-independent limits are shown in Tab. 9.1. We present the limits on the new physics cross section in each SR. The observed and expected limits  $S_{\text{obs}}^{95}$  and  $S_{\text{exp}}^{95}$  are reported for the potential contribution from new physics in each region. Including the acceptance  $\epsilon$ , the model-independent limits in most signal regions are of  $\sim 1 - 2$  fb. One should note that the (b) version of each signal region is strictly tighter in the primary scale cut, and thus provides a stronger limit when we observe no excess, as seen here.

Additionally, we derive exclusion limits for the simplified models considered in this thesis. These are the models with pair-production of squark pairs with inaccessible gluinos, and gluino pairs with inaccessible squarks. They correspond directly to the

Channel	RJR-S1a	RJR-S1b	RJR-S2a	RJR-S2b	RJR-S3a	RJR-S3b
Total bkg	334	233	96	75	56	37
Total bkg unc.	$\pm 35$ [10%]	$\pm 25$ [11%]	$\pm 10$ [10%]	$\pm 8$ [11%]	$\pm 6$ [11%]	$\pm 4$ [11%]
MC statistics	—	$\pm 2.6$ [1%]	$\pm 1.5$ [2%]	$\pm 1.3$ [2%]	$\pm 1.0$ [2%]	$\pm 0.7$ [2%]
$\Delta\mu_{Z,+jets}$	$\pm 20$ [6%]	$\pm 14$ [6%]	$\pm 4$ [4%]	$\pm 2.9$ [4%]	$\pm 2.2$ [4%]	$\pm 1.5$ [4%]
$\Delta\mu_{W,+jets}$	$\pm 10$ [3%]	$\pm 7$ [3%]	$\pm 3.1$ [3%]	$\pm 2.3$ [3%]	$\pm 1.6$ [3%]	$\pm 1.1$ [3%]
$\Delta\mu_{Top}$	$\pm 6$ [2%]	$\pm 4$ [2%]	$\pm 1.5$ [2%]	$\pm 1.1$ [1%]	$\pm 0.9$ [2%]	$\pm 0.6$ [2%]
$\Delta\mu_{Multijet}$	$\pm 0.09$ [0%]	$\pm 0.05$ [0%]	$\pm 0.02$ [0%]	—	—	—
CR $\gamma$ corr. factor	$\pm 12$ [4%]	$\pm 8$ [3%]	$\pm 4$ [4%]	$\pm 2.9$ [4%]	$\pm 2.2$ [4%]	$\pm 1.4$ [4%]
Theory Z	$\pm 23$ [7%]	$\pm 16$ [7%]	$\pm 7$ [7%]	$\pm 6$ [8%]	$\pm 4$ [7%]	$\pm 2.8$ [8%]
Theory W	$\pm 4$ [1%]	$\pm 5$ [2%]	$\pm 0.4$ [0%]	$\pm 0.11$ [0%]	$\pm 1.5$ [3%]	$\pm 1.2$ [3%]
Theory Top	$\pm 4$ [1%]	$\pm 2.7$ [1%]	$\pm 0.8$ [1%]	$\pm 0.7$ [1%]	$\pm 0.6$ [1%]	$\pm 0.4$ [1%]
Theory Diboson	$\pm 9$ [3%]	$\pm 6$ [3%]	$\pm 2.8$ [3%]	$\pm 2.6$ [3%]	$\pm 2.1$ [4%]	$\pm 1.4$ [4%]
Jet/MET	$\pm 3.3$ [1%]	$\pm 1.5$ [1%]	$\pm 0.6$ [1%]	$\pm 0.6$ [1%]	$\pm 1.2$ [2%]	$\pm 1.0$ [3%]
Multijet method	$\pm 0.7$ [0%]	$\pm 0.4$ [0%]	$\pm 0.08$ [0%]	—	—	—
Channel	RJR-G1a	RJR-G1b	RJR-G2a	RJR-G2b	RJR-G3a	RJR-G3b
Total bkg	40	18.8	27.8	8.5	5.8	1.7
Total bkg unc.	$\pm 4$ [10%]	$\pm 2.5$ [13%]	$\pm 3.4$ [12%]	$\pm 1.4$ [16%]	$\pm 1.1$ [19%]	$\pm 0.4$ [24%]
MC statistics	$\pm 1.6$ [4%]	$\pm 1.0$ [5%]	$\pm 1.2$ [4%]	$\pm 0.6$ [7%]	$\pm 0.4$ [7%]	$\pm 0.23$ [14%]
$\Delta\mu_{Z,+jets}$	$\pm 1.5$ [4%]	$\pm 0.7$ [4%]	$\pm 1.6$ [6%]	$\pm 0.5$ [6%]	$\pm 0.4$ [7%]	$\pm 0.1$ [6%]
$\Delta\mu_{W,+jets}$	$\pm 0.9$ [2%]	$\pm 0.4$ [2%]	$\pm 1.2$ [4%]	$\pm 0.31$ [4%]	$\pm 0.28$ [5%]	$\pm 0.1$ [6%]
$\Delta\mu_{Top}$	$\pm 0.8$ [2%]	$\pm 0.33$ [2%]	$\pm 0.9$ [3%]	$\pm 0.23$ [3%]	$\pm 0.07$ [1%]	$\pm 0.1$ [6%]
$\Delta\mu_{Multijet}$	$\pm 0.1$ [0%]	—	$\pm 0.03$ [0%]	$\pm 0.02$ [0%]	—	—
CR $\gamma$ corr. factor	$\pm 1.2$ [3%]	$\pm 0.6$ [3%]	$\pm 0.8$ [3%]	$\pm 0.26$ [3%]	$\pm 0.19$ [3%]	$\pm 0.05$ [3%]
Theory Z	$\pm 2.3$ [6%]	$\pm 1.1$ [6%]	$\pm 1.6$ [6%]	$\pm 0.5$ [6%]	$\pm 0.4$ [7%]	$\pm 0.1$ [6%]
Theory W	$\pm 1.1$ [3%]	$\pm 1.3$ [7%]	$\pm 0.3$ [1%]	$\pm 0.7$ [8%]	$\pm 0.6$ [10%]	$\pm 0.16$ [9%]
Theory Top	$\pm 1.2$ [3%]	$\pm 0.7$ [4%]	$\pm 1.0$ [4%]	$\pm 0.4$ [5%]	$\pm 0.4$ [7%]	$\pm 0.26$ [15%]
Theory Diboson	$\pm 1.3$ [3%]	$\pm 0.8$ [4%]	$\pm 1.5$ [5%]	$\pm 0.6$ [7%]	$\pm 0.31$ [5%]	$\pm 0.13$ [8%]
Jet/MET	$\pm 1.0$ [3%]	$\pm 0.6$ [3%]	$\pm 0.4$ [1%]	$\pm 0.17$ [2%]	$\pm 0.22$ [4%]	$\pm 0.05$ [3%]
Multijet method	$\pm 0.24$ [1%]	$\pm 0.12$ [1%]	$\pm 0.5$ [2%]	$\pm 0.4$ [5%]	—	—
Channel	RJR-C1	RJR-C2	RJR-C3	RJR-C4	RJR-C5	
Total bkg	14.5	59	110	10.5	7.3	
Total bkg unc.	$\pm 2.2$ [15%]	$\pm 6$ [10%]	$\pm 11$ [10%]	$\pm 1.5$ [14%]	$\pm 1.4$ [19%]	
MC statistics	$\pm 0.7$ [5%]	$\pm 1.7$ [3%]	$\pm 2.4$ [2%]	$\pm 0.6$ [6%]	$\pm 0.6$ [8%]	
$\Delta\mu_{Z,+jets}$	$\pm 0.5$ [3%]	$\pm 1.9$ [3%]	$\pm 2.5$ [2%]	$\pm 0.31$ [3%]	$\pm 0.13$ [2%]	
$\Delta\mu_{W,+jets}$	$\pm 0.4$ [3%]	$\pm 1.7$ [3%]	$\pm 5$ [5%]	$\pm 0.4$ [4%]	$\pm 0.25$ [3%]	
$\Delta\mu_{Top}$	$\pm 0.33$ [2%]	$\pm 1.3$ [2%]	$\pm 4$ [4%]	$\pm 0.31$ [3%]	$\pm 0.4$ [5%]	
$\Delta\mu_{Multijet}$	—	$\pm 0.1$ [0%]	$\pm 0.06$ [0%]	—	$\pm 0.1$ [1%]	
CR $\gamma$ corr. factor	$\pm 0.5$ [3%]	$\pm 1.8$ [3%]	$\pm 2.3$ [2%]	$\pm 0.29$ [3%]	$\pm 0.13$ [2%]	
Theory Z	$\pm 0.8$ [6%]	$\pm 3.5$ [6%]	$\pm 4$ [4%]	$\pm 0.6$ [6%]	$\pm 0.24$ [3%]	
Theory W	$\pm 1.3$ [9%]	$\pm 0.03$ [0%]	$\pm 2.0$ [2%]	$\pm 1.0$ [10%]	$\pm 0.13$ [2%]	
Theory Top	$\pm 0.5$ [3%]	$\pm 1.3$ [2%]	$\pm 3.2$ [3%]	$\pm 0.6$ [6%]	$\pm 0.9$ [12%]	
Theory Diboson	$\pm 1.0$ [7%]	$\pm 4$ [7%]	$\pm 6$ [5%]	$\pm 0.27$ [3%]	$\pm 0.4$ [5%]	
Jet/MET	$\pm 0.5$ [3%]	$\pm 1.5$ [3%]	$\pm 3.1$ [3%]	$\pm 0.24$ [2%]	$\pm 0.5$ [7%]	
Multijet method	$\pm 0.09$ [1%]	$\pm 0.4$ [1%]	$\pm 2.1$ [2%]	—	$\pm 0.18$ [2%]	

Table 9.1: Breakdown of the dominant systematic uncertainties in the background estimates for the RJR-based search. The individual uncertainties can be correlated, and do not necessarily add in quadrature to the total background uncertainty.  $\Delta_\mu$  uncertainties are the result of the control region statistical uncertainties and the systematic uncertainties entering a specific control region. In brackets, uncertainties are given relative to the expected total background yield, also presented in the Table. Empty cells (indicated by a ‘-’) correspond to uncertainties  $< 0.1\%$ .

Signal Region	RJR-S1a	RJR-S1b	RJR-S2a	RJR-S2b	RJR-S3a	RJR-S3b
MC expected events						
Diboson	17	13	5.6	5.1	4.2	2.8
Z/ $\gamma^*$ +jets	231	163	63	48	36	24
W+jets	97	66	22	16	11	7.8
$t\bar{t}$ (+EW) + single top	15	10	2.9	2.1	1.7	1.1
Fitted background events						
Diboson	$17 \pm 9$	$13 \pm 7$	$5.6 \pm 2.8$	$5.1 \pm 2.6$	$4.2 \pm 2.1$	$2.8 \pm 1.4$
Z/ $\gamma^*$ +jets	$207 \pm 33$	$146 \pm 23$	$65 \pm 9$	$50 \pm 7$	$37 \pm 5$	$25.0 \pm 3.5$
W+jets	$95 \pm 9$	$65 \pm 7$	$24.1 \pm 2.9$	$18.3 \pm 2.3$	$12.8 \pm 2.8$	$8.7 \pm 2.0$
$t\bar{t}$ (+EW) + single top	$14 \pm 7$	$9 \pm 5$	$2.1 \pm 1.7$	$1.6 \pm 1.3$	$1.3 \pm 1.0$	$0.8 \pm 0.7$
Multi-jet	$0.71^{+0.71}_{-0.71}$	$0.41^{+0.41}_{-0.41}$	$0.08^{+0.09}_{-0.08}$	—	—	—
Total Expected MC	362	253	93	72	53	36
Total Fitted bkg	$334 \pm 35$	$233 \pm 25$	$96 \pm 10$	$75 \pm 8$	$56 \pm 6$	$37 \pm 4$
Observed	368	270	99	75	57	36
$\langle\epsilon\sigma\rangle_{\text{obs}}^{95}$ [fb]	7.6	6.5	2.2	1.7	1.6	1.1
$S_{\text{obs}}^{95}$	101	86	29	23	22	15
$S_{\text{exp}}^{95}$	$78^{+27}_{-21}$	$61^{+22}_{-16}$	$28^{+11}_{-8}$	$23^{+9}_{-7}$	$20^{+8}_{-6}$	$16^{+7}_{-5}$
$p_0$ (Z)	0.20 (0.84)	0.12 (1.17)	0.44 (0.15)	0.50 (0.00)	0.44 (0.14)	0.50 (0.00)
Signal Region	RJR-G1a	RJR-G1b	RJR-G2a	RJR-G2b	RJR-G3a	RJR-G3b
MC expected events						
Diboson	2.6	1.6	2.9	1.1	0.62	0.26
Z/ $\gamma^*$ +jets	18	8.8	13	4.2	3.1	0.83
W+jets	11	4.7	7.7	2.0	1.9	0.63
$t\bar{t}$ (+EW) + single top	7.4	3.1	4.4	1.1	0.34	0.03
Fitted background events						
Diboson	$2.6 \pm 1.3$	$1.6 \pm 0.8$	$2.9 \pm 1.5$	$1.1 \pm 0.6$	$0.6 \pm 0.4$	$0.26 \pm 0.14$
Z/ $\gamma^*$ +jets	$21.1 \pm 3.1$	$10.2 \pm 1.6$	$14.3 \pm 2.5$	$4.5 \pm 0.8$	$3.3 \pm 0.6$	$0.88 \pm 0.19$
W+jets	$10.8 \pm 1.7$	$4.6 \pm 1.4$	$6.7 \pm 1.3$	$1.7 \pm 0.7$	$1.6 \pm 0.7$	$0.55 \pm 0.2$
$t\bar{t}$ (+EW) + single top	$5.4 \pm 1.6$	$2.3 \pm 0.9$	$3.4 \pm 1.4$	$0.8 \pm 0.5$	$0.26^{+0.45}_{-0.26}$	$0.02^{+0.26}_{-0.02}$
Multi-jet	$0.24 \pm 0.24$	$0.12 \pm 0.12$	$0.5 \pm 0.5$	$0.4 \pm 0.4$	—	—
Total Expected MC	39	18	29	8.7	5.9	1.7
Total Fitted bkg	$40 \pm 4$	$18.8 \pm 2.5$	$27.8 \pm 3.4$	$8.5 \pm 1.4$	$5.8 \pm 1.1$	$1.7 \pm 0.4$
Observed	39	14	30	10	8	4
$\langle\epsilon\sigma\rangle_{\text{obs}}^{95}$ [fb]	1.1	0.56	1.1	0.71	0.64	0.55
$S_{\text{obs}}^{95}$	15	7.5	15	9.4	8.5	7.3
$S_{\text{exp}}^{95}$	$16^{+7}_{-4}$	$10^{+5}_{-3}$	$14^{+6}_{-4}$	$7.6^{+3.5}_{-2.0}$	$7.0^{+2.5}_{-2.1}$	$4.2^{+1.9}_{-0.5}$
$p_0$ (Z)	0.50 (0.00)	0.50 (0.00)	0.36 (0.35)	0.31 (0.50)	0.21 (0.81)	0.06 (1.55)
Signal Region	RJR-C1	RJR-C2	RJR-C3	RJR-C4	RJR-C5	
MC expected events						
Diboson	1.9	7.1	11	0.54	0.75	
Z/ $\gamma^*$ +jets	8.8	36	46	5.8	2.5	
W+jets	3.5	16	43	3.8	2.3	
$t\bar{t}$ (+EW) + single top	1.9	7.2	20	1.7	2.5	
Fitted background events						
Diboson	$1.9 \pm 1.0$	$7 \pm 4$	$11 \pm 6$	$0.54 \pm 0.29$	$0.8 \pm 0.5$	
Z/ $\gamma^*$ +jets	$7.7 \pm 1.1$	$32 \pm 5$	$40 \pm 6$	$5.0 \pm 0.8$	$2.2 \pm 0.4$	
W+jets	$3.3 \pm 1.4$	$14.5 \pm 1.7$	$40 \pm 5$	$3.56 \pm 1.0$	$2.14 \pm 0.35$	
$t\bar{t}$ (+EW) + single top	$1.5 \pm 0.6$	$5.8 \pm 1.8$	$16 \pm 5$	$1.4 \pm 0.7$	$2.0 \pm 1.1$	
Multi-jet	$0.09 \pm 0.09$	$0.4 \pm 0.4$	$2.1 \pm 2.1$	—	$0.18 \pm 0.18$	
Total Expected MC	16	67	124	12	8.3	
Total Fitted bkg	$14.5 \pm 2.2$	$59 \pm 6$	$110 \pm 11$	$10.5 \pm 1.5$	$7.3 \pm 1.4$	
Observed	14	69	115	5	8	
$\langle\epsilon\sigma\rangle_{\text{obs}}^{95}$ [fb]	0.76	2.2	2.5	0.35	0.61	
$S_{\text{obs}}^{95}$	10	29	34	4.7	8.1	
$S_{\text{exp}}^{95}$	$11^{+5}_{-3}$	$21^{+9}_{-6}$	$30^{+12}_{-8}$	$8.1^{+3.0}_{-2.3}$	$7.4^{+2.9}_{-1.8}$	
$p_0$ (Z)	0.50 (0.00)	0.18 (0.92)	0.37 (0.32)	0.50 (0.00)	0.39 (0.30)	

Table 9.2: Numbers of events observed in the signal regions used in the RJR-based analysis compared with background expectations obtained from the fits described in the text. Empty cells (indicated by a ‘-’) correspond to estimates lower than 0.01. The p-values ( $p_0$ ) give the probabilities of the observations being consistent with the estimated backgrounds. For an observed number of events lower than expected, the p-value is truncated at 0.5. Between parentheses,  $p$ -values are also given as the number of equivalent Gaussian standard deviations (Z). Also shown are 95% CL upper limits on the visible cross-section ( $\langle\epsilon\sigma\rangle_{\text{obs}}^{95}$ ), the visible number of signal events ( $S_{\text{obs}}^{95}$ ) and the number of signal events ( $S_{\text{exp}}^{95}$ ) given the expected number of background events (and  $\pm 1\sigma$  excursions of the expectation).

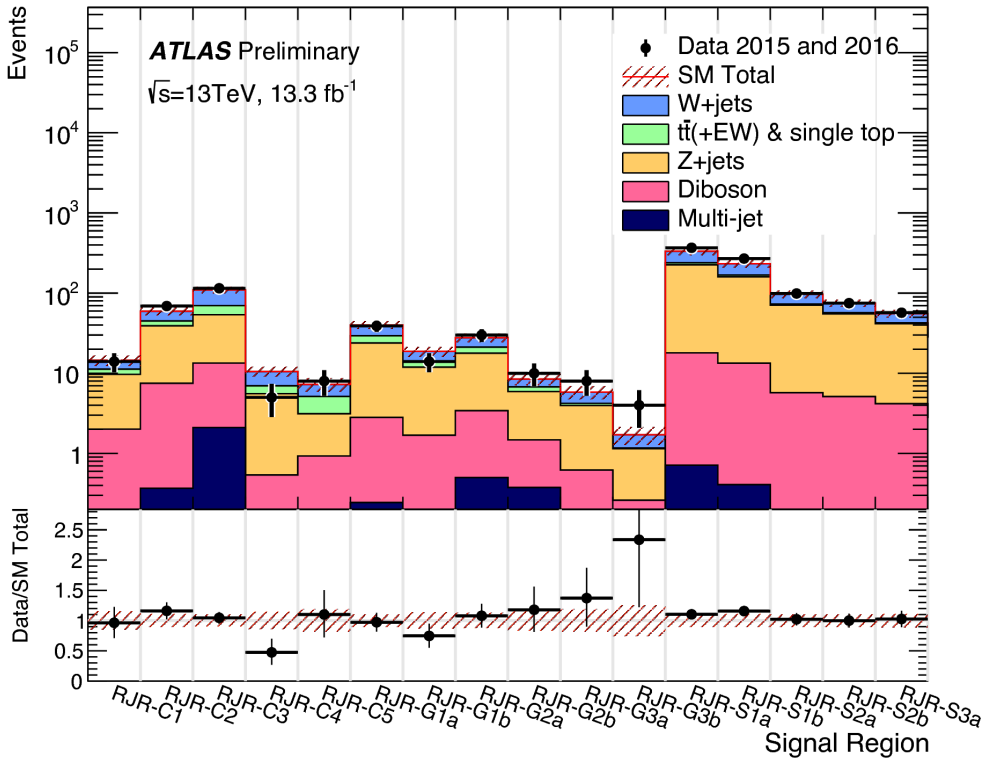


Figure 9.4: Summary of the signal region pulls

2226 Feynman diagrams shown previously. The free parameters of these simplified models  
 2227 are the relevant sparticle mass and the mass of the LSP  $\tilde{\chi}_1^0$ . We set limits in a plane  
 2228 of these free parameters.

2229 The exclusion limits are shown in Fig. 9.5. Gray text is imposed on the plane at the  
 2230 point of each simplified model with masses  $(m_{\text{sparticle}}, m_{\tilde{\chi}_1^0})$ . This gray text indicates  
 2231 the signal region which provided the best sensitivity at that point, as measured by the  
 2232 background-only fit. For each simplified signal model, we run the model-dependent fit  
 2233 described in the last chapter, where the signal model signal strength  $\mu_{\text{sig}}$  is included  
 2234 as an additional free parameter. The signal sample is also allowed to freely contribute  
 2235 to the control regions due to signal contamination. This produces a  $\text{CL}_s$   $p$ -value for  
 2236 each signal model in the plane, and we can find those with  $p = 0.05$  to set a 95%  
 2237 exclusion limit.

2238 In the squark- $\tilde{\chi}_1^0$  plane, we observe that the limits from the 2015 dataset are far  
2239 extended in all directions. The expected and observed exclusions are similar, which  
2240 is a reflection of the compatibility of the expected Standard Model event counts and  
2241 observed event counts in the squark regions. A squark with mass of 1350 GeV or less  
2242 is excluded by the analysis in direct decays to a quark and LSP. In the compressed  
2243 spectra, we have extended limits significantly over the 2015 result in the region of 600-  
2244 700 GeV in squark mass with an LSP of 450 GeV to 600 GeV. We note that directly  
2245 along the kinematically-forbidden diagonal, the shape of the exclusions is affected  
2246 by the interpolation between the signal models considered. This could be rectified  
2247 by inclusion of additional compressed signal models. The limits in the intermediate  
2248 with an LSP of  $\sim$ 450-500 GeV are not far extended beyond the previous dataset. We  
2249 also note that every signal region designed to provide sensitivity to this simplified  
2250 model (all SRS regions and SRC1-4) is chosen as the best region at least once in  
2251 the plane, indicating that each signal region provided additional sensitivity to squark  
2252 phenomena.

2253 Another curiosity is the fact that a gluino region, SRG2a is chosen as the optimal  
2254 region in the squark- $\tilde{\chi}_1^0$  plane, when the squark mass is  $\sim$ 700 GeV. Generally, the  
2255 squark regions are looser than the gluino regions, as seen in their overall event counts.  
2256 One could see this as an indication that the next iteration of the analysis should have  
2257 an additional tight squark region here. Another possibility is that this region also  
2258 benefits from the compressed region strategy of using an ISR jet. As the gluino  
2259 regions require four jets from the imposition of the gluino decay tree, these could be  
2260 capturing events where a two jet ISR system recoils off the disquark system.

2261 In the gluino- $\tilde{\chi}_1^0$  plane, the limits on gluino masses in the simplified model where  
2262 gluinos decay to two jets and an  $\tilde{\chi}_1^0$  are again far extended beyond the 2015 dataset.  
2263 We note in most of the plane, the expected limit is significantly stronger than the  
2264 observed limit; for example, the gluino mass limit is more than 50 GeV stronger in

2265 the case of a massless  $\tilde{\chi}_1^0$ . As much of the phase space is covered by SRG3a and  
2266 SRG3b, this results from the small statistical fluctuation upward in these regions.  
2267 Again, we note that every gluino signal region is the best choice at some point in this  
2268 plane. This is an indication of the utility of the signal region strategy employed in  
2269 this thesis, as each point provides additional sensitivity to new SUSY models.

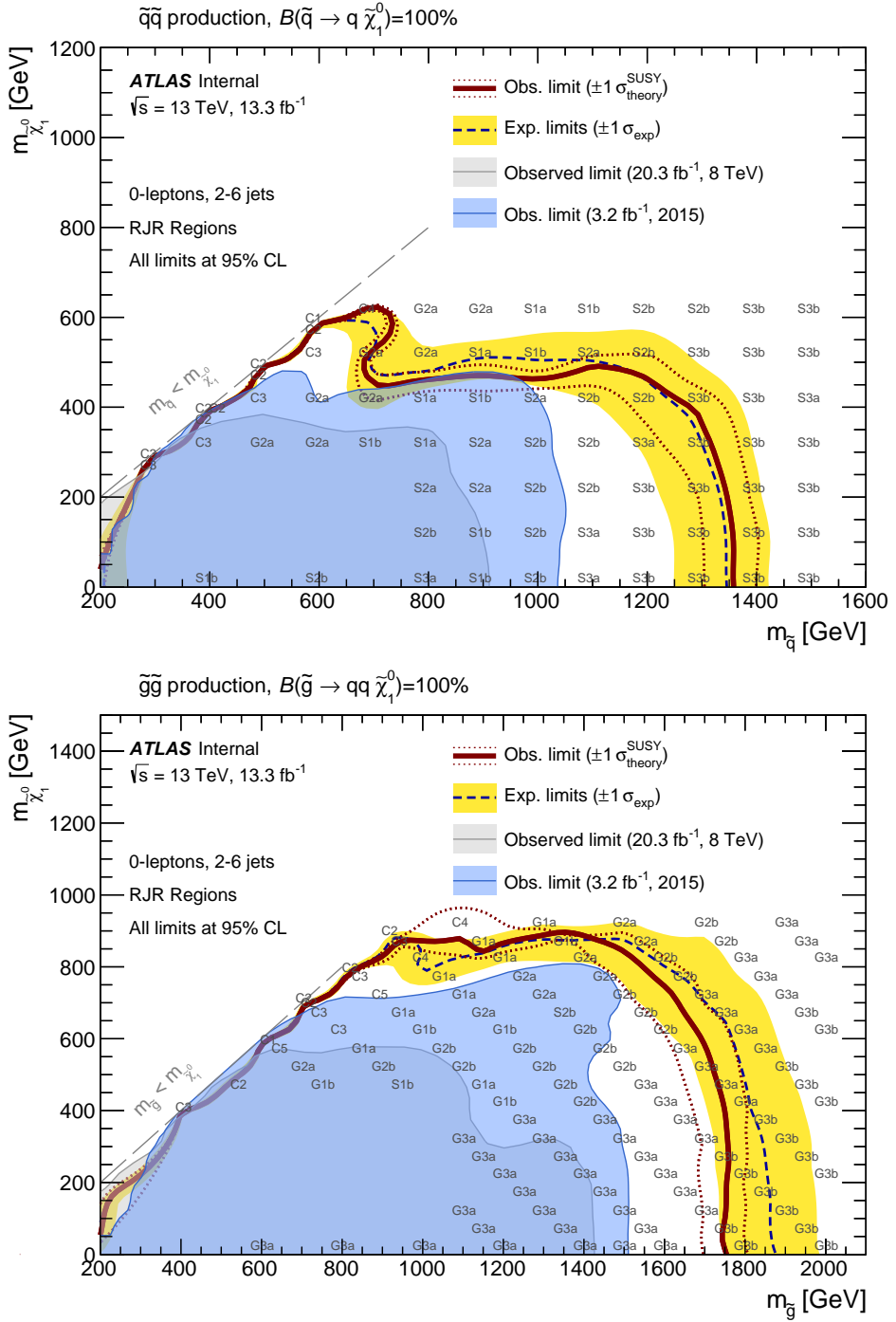


Figure 9.5: Exclusion limits for direct production of (a) light-flavour squark pairs with decoupled gluinos and (b) gluino pairs with decoupled squarks. Exclusion limits are obtained by using the signal region with the best expected sensitivity at each point. The blue dashed lines show the expected limits at 95% CL, with the yellow bands indicating the  $1\sigma$  excursions due to experimental and background-only theoretical uncertainties. Observed limits are indicated by maroon curves where the solid contour represents the nominal limit, and the dotted lines are obtained by varying the signal cross-section by the renormalization and factorization scale and PDF uncertainties. Results are compared with the observed limits obtained by the previous ATLAS searches with no leptons, jets and missing transverse momentum [135, 144].

---

2270

## *Conclusion*

2271 Here you can write some introductory remarks about your chapter. I like to give each  
2272 sentence its own line.

2273 When you need a new paragraph, just skip an extra line.

2274 **9.4 New Section**

2275 By using the asterisk to start a new section, I keep the section from appearing in the  
2276 table of contents. If you want your sections to be numbered and to appear in the  
2277 table of contents, remove the asterisk.



---

*Bibliography*

- 2279 [1] O. Perdereau, *Planck 2015 cosmological results*,  
2280 AIP Conf. Proc. **1743** (2016) p. 050014.
- 2281 [2] N. Aghanim et al.,  
2282 *Planck 2016 intermediate results. LI. Features in the cosmic microwave*  
2283 *background temperature power spectrum and shifts in cosmological parameters*  
2284 (2016), arXiv: [1608.02487 \[astro-ph.CO\]](https://arxiv.org/abs/1608.02487).
- 2285 [3] J. S. Schwinger,  
2286 *On Quantum electrodynamics and the magnetic moment of the electron*,  
2287 Phys. Rev. **73** (1948) p. 416.
- 2288 [4] S. Laporta and E. Remiddi,  
2289 *The Analytical value of the electron (g-2) at order alpha\*\*3 in QED*,  
2290 Phys. Lett. **B379** (1996) p. 283, arXiv: [hep-ph/9602417 \[hep-ph\]](https://arxiv.org/abs/hep-ph/9602417).
- 2291 [5] S. Schael et al., *Precision electroweak measurements on the Z resonance*,  
2292 Phys. Rept. **427** (2006) p. 257, arXiv: [hep-ex/0509008 \[hep-ex\]](https://arxiv.org/abs/hep-ex/0509008).
- 2293 [6] S. L. Glashow, *Partial Symmetries of Weak Interactions*,  
2294 Nucl. Phys. **22** (1961) p. 579.
- 2295 [7] S. Weinberg, *A Model of Leptons*, Phys. Rev. Lett. **19** (1967) p. 1264.
- 2296 [8] A. Salam, *Weak and Electromagnetic Interactions*,  
2297 Conf. Proc. **C680519** (1968) p. 367.
- 2298 [9] M. Gell-Mann, *A Schematic Model of Baryons and Mesons*,  
2299 Phys. Lett. **8** (1964) p. 214.
- 2300 [10] G. Zweig, “An SU(3) model for strong interaction symmetry and its  
2301 breaking. Version 2,” *DEVELOPMENTS IN THE QUARK THEORY OF*  
2302 *HADRONS. VOL. 1. 1964 - 1978*, ed. by D. Lichtenberg and S. P. Rosen,  
2303 1964 p. 22,  
2304 URL: <http://inspirehep.net/record/4674/files/cern-th-412.pdf>.

- 2305 [11] S. Weinberg, *Implications of Dynamical Symmetry Breaking*,  
 2306 Phys. Rev. **D13** (1976) p. 974.
- 2307 [12] S. Weinberg, *Implications of Dynamical Symmetry Breaking: An Addendum*,  
 2308 Phys. Rev. **D19** (1979) p. 1277.
- 2309 [13] E. Gildener, *Gauge Symmetry Hierarchies*, Phys. Rev. **D14** (1976) p. 1667.
- 2310 [14] L. Susskind, *Dynamics of Spontaneous Symmetry Breaking in the*  
 2311 *Weinberg-Salam Theory*, Phys. Rev. **D20** (1979) p. 2619.
- 2312 [15] S. P. Martin, “A Supersymmetry Primer,” 1997,  
 2313 eprint: [arXiv:hep-ph/9709356](https://arxiv.org/abs/hep-ph/9709356).
- 2314 [16] V. C. Rubin and W. K. Ford Jr., *Rotation of the Andromeda Nebula from a*  
 2315 *Spectroscopic Survey of Emission Regions*, Astrophys. J. **159** (1970) p. 379.
- 2316 [17] M. S. Roberts and R. N. Whitehurst,  
 2317 “*The rotation curve and geometry of M31 at large galactocentric distances*,  
 2318 Astrophys. J. **201** (1970) p. 327.
- 2319 [18] V. C. Rubin, N. Thonnard, and W. K. Ford Jr.,  
 2320 *Rotational properties of 21 SC galaxies with a large range of luminosities and*  
 2321 *radii, from NGC 4605 /R = 4kpc/ to UGC 2885 /R = 122 kpc/*,  
 2322 Astrophys. J. **238** (1980) p. 471.
- 2323 [19] V. C. Rubin et al., *Rotation velocities of 16 SA galaxies and a comparison of*  
 2324 *Sa, Sb, and SC rotation properties*, Astrophys. J. **289** (1985) p. 81.
- 2325 [20] A. Bosma,  
 2326 *21-cm line studies of spiral galaxies. 2. The distribution and kinematics of*  
 2327 *neutral hydrogen in spiral galaxies of various morphological types.*,  
 2328 Astron. J. **86** (1981) p. 1825.
- 2329 [21] M. Persic, P. Salucci, and F. Stel, *The Universal rotation curve of spiral*  
 2330 *galaxies: 1. The Dark matter connection*,  
 2331 Mon. Not. Roy. Astron. Soc. **281** (1996) p. 27,  
 2332 arXiv: [astro-ph/9506004](https://arxiv.org/abs/astro-ph/9506004) [astro-ph].
- 2333 [22] M. Lisanti, “Lectures on Dark Matter Physics,” 2016,  
 2334 eprint: [arXiv:1603.03797](https://arxiv.org/abs/1603.03797).
- 2335 [23] H. Miyazawa, *Baryon Number Changing Currents*,  
 2336 Prog. Theor. Phys. **36** (1966) p. 1266.

- 2337 [24] J.-L. Gervais and B. Sakita, *Generalizations of dual models*,  
 2338 *Nucl. Phys.* **B34** (1971) p. 477.
- 2339 [25] J. Gervais and B. Sakita,  
 2340 *Field theory interpretation of supergauges in dual models*,  
 2341 *Nucl. Phys. B* **34** (1971) p. 632.
- 2342 [26] Y. A. Golfand and E. P. Likhtman, *Extension of the Algebra of Poincare  
 2343 Group Generators and Violation of p Invariance*,  
 2344 *JETP Lett.* **13** (1971) p. 323, [*Pisma Zh.Eksp.Teor.Fiz.* **13**:452-455,1971].
- 2345 [27] A. Neveu and J. H. Schwarz, *Factorizable dual model of pions*,  
 2346 *Nucl. Phys. B* **31** (1971) p. 86.
- 2347 [28] A. Neveu and J. H. Schwarz, *Quark Model of Dual Pions*,  
 2348 *Phys. Rev. D* **4** (1971) p. 1109.
- 2349 [29] D. V. Volkov and V. P. Akulov, *Is the Neutrino a Goldstone Particle?*  
 2350 *Phys. Lett. B* **46** (1973) p. 109.
- 2351 [30] J. Wess and B. Zumino,  
 2352 *A Lagrangian Model Invariant Under Supergauge Transformations*,  
 2353 *Phys. Lett. B* **49** (1974) p. 52.
- 2354 [31] A. Salam and J. A. Strathdee, *Supersymmetry and Nonabelian Gauges*,  
 2355 *Phys. Lett. B* **51** (1974) p. 353.
- 2356 [32] S. Ferrara, J. Wess, and B. Zumino, *Supergauge Multiplets and Superfields*,  
 2357 *Phys. Lett. B* **51** (1974) p. 239.
- 2358 [33] J. Wess and B. Zumino, *Supergauge Transformations in Four-Dimensions*,  
 2359 *Nucl. Phys. B* **70** (1974) p. 39.
- 2360 [34] J. D. Lykken, “Introduction to supersymmetry,” *Fields, strings and duality. Proceedings, Summer School, Theoretical Advanced Study Institute in Elementary Particle Physics, TASI’96, Boulder, USA, June 2-28, 1996*, 1996  
 2361 p. 85, arXiv: [hep-th/9612114](https://arxiv.org/abs/hep-th/9612114) [hep-th],  
 2362 URL: [http://lss.fnal.gov/cgi-bin/find\\_paper.pl?pub=96-445-T](http://lss.fnal.gov/cgi-bin/find_paper.pl?pub=96-445-T).
- 2363 [35] A. Kobakhidze, “Intro to SUSY,” 2016, URL: <https://indico.cern.ch/event/443176/page/5225-pre-susy-programme>.
- 2364 [36] G. R. Farrar and P. Fayet, *Phenomenology of the Production, Decay, and Detection of New Hadronic States Associated with Supersymmetry*,  
 2365 *Phys. Lett. B* **76** (1978) p. 575.

- 2370 [37] ATLAS Collaboration,  
 2371 *Search for the electroweak production of supersymmetric particles in*  
 2372  $\sqrt{s} = 8 \text{ TeV}$  *pp collisions with the ATLAS detector,*  
 2373 *Phys. Rev. D* **93** (2016) p. 052002, arXiv: [1509.07152 \[hep-ex\]](#).
- 2374 [38] ATLAS Collaboration, *Summary of the searches for squarks and gluinos*  
 2375 *using  $\sqrt{s} = 8 \text{ TeV}$  pp collisions with the ATLAS experiment at the LHC,*  
 2376 *JHEP* **10** (2015) p. 054, arXiv: [1507.05525 \[hep-ex\]](#).
- 2377 [39] ATLAS Collaboration, *ATLAS Run 1 searches for direct pair production of*  
 2378 *third-generation squarks at the Large Hadron Collider,*  
 2379 *Eur. Phys. J. C* **75** (2015) p. 510, arXiv: [1506.08616 \[hep-ex\]](#).
- 2380 [40] CMS Collaboration, *Search for supersymmetry with razor variables in pp*  
 2381 *collisions at  $\sqrt{s} = 7 \text{ TeV}$ , Phys. Rev. D* **90** (2014) p. 112001,  
 2382 arXiv: [1405.3961 \[hep-ex\]](#).
- 2383 [41] CMS Collaboration, *Inclusive search for supersymmetry using razor variables*  
 2384 *in pp collisions at  $\sqrt{s} = 7 \text{ TeV}$ , Phys. Rev. Lett.* **111** (2013) p. 081802,  
 2385 arXiv: [1212.6961 \[hep-ex\]](#).
- 2386 [42] CMS Collaboration, *Search for Supersymmetry in pp Collisions at 7 TeV in*  
 2387 *Events with Jets and Missing Transverse Energy,*  
 2388 *Phys. Lett. B* **698** (2011) p. 196, arXiv: [1101.1628 \[hep-ex\]](#).
- 2389 [43] CMS Collaboration, *Search for Supersymmetry at the LHC in Events with*  
 2390 *Jets and Missing Transverse Energy, Phys. Rev. Lett.* **107** (2011) p. 221804,  
 2391 arXiv: [1109.2352 \[hep-ex\]](#).
- 2392 [44] CMS Collaboration, *Search for supersymmetry in hadronic final states using*  
 2393  *$M_{T2}$  in pp collisions at  $\sqrt{s} = 7 \text{ TeV}$ , JHEP* **10** (2012) p. 018,  
 2394 arXiv: [1207.1798 \[hep-ex\]](#).
- 2395 [45] CMS Collaboration, *Searches for supersymmetry using the  $M_{T2}$  variable in*  
 2396 *hadronic events produced in pp collisions at 8 TeV, JHEP* **05** (2015) p. 078,  
 2397 arXiv: [1502.04358 \[hep-ex\]](#).
- 2398 [46] CMS Collaboration, *Search for new physics with the  $M_{T2}$  variable in all-jets*  
 2399 *final states produced in pp collisions at  $\sqrt{s} = 13 \text{ TeV}$ , JHEP* (2016),  
 2400 arXiv: [1603.04053 \[hep-ex\]](#).
- 2401 [47] ATLAS Collaboration, *Multi-channel search for squarks and gluinos in*  
 2402  $\sqrt{s} = 7 \text{ TeV}$  *pp collisions with the ATLAS detector at the LHC,*  
 2403 *Eur. Phys. J. C* **73** (2013) p. 2362, arXiv: [1212.6149 \[hep-ex\]](#).

- 2404 [48] Y. Grossman, “Introduction to the SM,” 2016, URL: <https://indico.fnal.gov/sessionDisplay.py?sessionId=3&confId=11505#20160811>.
- 2405
- 2406 [49] W Buchmuller and C Ludeling, *Field Theory and Standard Model* (Sept. 2006) p. 70, URL: <https://cds.cern.ch/record/984122>.
- 2407
- 2408 [50] P. W. Higgs, *Broken Symmetries and the Masses of Gauge Bosons*, Phys. Rev. Lett. **13** (1964) p. 508.
- 2409
- 2410 [51] ATLAS Collaboration, *Observation of a new particle in the search for the Standard Model Higgs boson with the ATLAS detector at the LHC*, Phys. Lett. B **716** (2012) p. 1, arXiv: [1207.7214 \[hep-ex\]](https://arxiv.org/abs/1207.7214).
- 2411
- 2412
- 2413 [52] CMS Collaboration, *Observation of a new boson at a mass of 125 GeV with the CMS experiment at the LHC*, Phys. Lett. B **716** (2012) p. 30, arXiv: [1207.7235 \[hep-ex\]](https://arxiv.org/abs/1207.7235).
- 2414
- 2415
- 2416 [53] A. Chodos et al., *A New Extended Model of Hadrons*, Phys. Rev. **D9** (1974) p. 3471.
- 2417
- 2418 [54] A. Chodos et al., *Baryon Structure in the Bag Theory*, Phys. Rev. **D10** (1974) p. 2599.
- 2419
- 2420 [55] J. C. Collins, D. E. Soper, and G. F. Sterman, *Factorization of Hard Processes in QCD*, Adv. Ser. Direct. High Energy Phys. **5** (1989) p. 1, arXiv: [hep-ph/0409313 \[hep-ph\]](https://arxiv.org/abs/hep-ph/0409313).
- 2421
- 2422
- 2423
- 2424 [56] K. A. Olive et al., *Review of Particle Physics*, Chin. Phys. **C38** (2014) p. 090001.
- 2425
- 2426 [57] N. Cabibbo, *Unitary Symmetry and Leptonic Decays*, Phys. Rev. Lett. **10** (1963) p. 531, [[648\(1963\)](#)].
- 2427
- 2428 [58] M. Kobayashi and T. Maskawa, *CP Violation in the Renormalizable Theory of Weak Interaction*, Prog. Theor. Phys. **49** (1973) p. 652.
- 2429
- 2430
- 2431 [59] W. F. L. Hollik, *Radiative Corrections in the Standard Model and their Role for Precision Tests of the Electroweak Theory*, Fortsch. Phys. **38** (1990) p. 165.
- 2432
- 2433
- 2434 [60] D. Yu. Bardin et al., *ELECTROWEAK RADIATIVE CORRECTIONS TO DEEP INELASTIC*
- 2435

- 2436            *SCATTERING AT HERA! CHARGED CURRENT SCATTERING,*  
 2437            *Z. Phys. C***44** (1989) p. 149.
- 2438 [61] D. C. Kennedy et al.,  
 2439            *Electroweak Cross-Sections and Asymmetries at the Z0,*  
 2440            *Nucl. Phys. B***321** (1989) p. 83.
- 2441 [62] A. Sirlin, *Radiative Corrections in the SU(2)-L x U(1) Theory: A Simple*  
 2442            *Renormalization Framework*, *Phys. Rev. D***22** (1980) p. 971.
- 2443 [63] S. Fanchiotti, B. A. Kniehl, and A. Sirlin,  
 2444            *Incorporation of QCD effects in basic corrections of the electroweak theory*,  
 2445            *Phys. Rev. D***48** (1993) p. 307, arXiv: [hep-ph/9212285 \[hep-ph\]](#).
- 2446 [64] C. Quigg, “Cosmic Neutrinos,” *Proceedings, 35th SLAC Summer Institute on*  
 2447            *Particle Physics: Dark matter: From the cosmos to the Laboratory (SSI*  
 2448            *2007): Menlo Park, California, July 30- August 10, 2007*, 2008,  
 2449            arXiv: [0802.0013 \[hep-ph\]](#),  
 2450            URL: [http://lss.fnal.gov/cgi-bin/find\\_paper.pl?conf-07-417](http://lss.fnal.gov/cgi-bin/find_paper.pl?conf-07-417).
- 2451 [65] S. R. Coleman and J. Mandula, *All Possible Symmetries of the S Matrix*,  
 2452            *Phys. Rev. 159* (1967) p. 1251.
- 2453 [66] R. Haag, J. T. Lopuszanski, and M. Sohnius,  
 2454            *All Possible Generators of Supersymmetries of the s Matrix*,  
 2455            *Nucl. Phys. B***88** (1975) p. 257.
- 2456 [67] A. Salam and J. A. Strathdee, *On Superfields and Fermi-Bose Symmetry*,  
 2457            *Phys. Rev. D***11** (1975) p. 1521.
- 2458 [68] S. Dimopoulos and H. Georgi, *Softly Broken Supersymmetry and SU(5)*,  
 2459            *Nucl. Phys. B***193** (1981) p. 150.
- 2460 [69] S. Dimopoulos, S. Raby, and F. Wilczek,  
 2461            *Supersymmetry and the Scale of Unification*, *Phys. Rev. D***24** (1981) p. 1681.
- 2462 [70] L. E. Ibanez and G. G. Ross,  
 2463            *Low-Energy Predictions in Supersymmetric Grand Unified Theories*,  
 2464            *Phys. Lett. B***105** (1981) p. 439.
- 2465 [71] W. J. Marciano and G. Senjanovic,  
 2466            *Predictions of Supersymmetric Grand Unified Theories*,  
 2467            *Phys. Rev. D***25** (1982) p. 3092.

- 2468 [72] L. Girardello and M. T. Grisaru, *Soft Breaking of Supersymmetry*,  
 2469 *Nucl. Phys.* **B194** (1982) p. 65.
- 2470 [73] D. J. H. Chung et al.,  
 2471 *The Soft supersymmetry breaking Lagrangian: Theory and applications*,  
 2472 *Phys. Rept.* **407** (2005) p. 1, arXiv: [hep-ph/0312378 \[hep-ph\]](#).
- 2473 [74] J. Hisano et al., *Lepton flavor violation in the supersymmetric standard*  
 2474 *model with seesaw induced neutrino masses*, *Phys. Lett.* **B357** (1995) p. 579,  
 2475 arXiv: [hep-ph/9501407 \[hep-ph\]](#).
- 2476 [75] F. Gabbiani et al., *A Complete analysis of FCNC and CP constraints in*  
 2477 *general SUSY extensions of the standard model*,  
 2478 *Nucl. Phys.* **B477** (1996) p. 321, arXiv: [hep-ph/9604387 \[hep-ph\]](#).
- 2479 [76] F. Gabbiani and A. Masiero,  
 2480 *FCNC in Generalized Supersymmetric Theories*,  
 2481 *Nucl. Phys.* **B322** (1989) p. 235.
- 2482 [77] J. S. Hagelin, S. Kelley, and T. Tanaka, *Supersymmetric flavor changing*  
 2483 *neutral currents: Exact amplitudes and phenomenological analysis*,  
 2484 *Nucl. Phys.* **B415** (1994) p. 293.
- 2485 [78] J. S. Hagelin, S. Kelley, and V. Ziegler, *Using gauge coupling unification and*  
 2486 *proton decay to test minimal supersymmetric SU(5)*,  
 2487 *Phys. Lett.* **B342** (1995) p. 145, arXiv: [hep-ph/9406366 \[hep-ph\]](#).
- 2488 [79] D. Choudhury et al.,  
 2489 *Constraints on nonuniversal soft terms from flavor changing neutral currents*,  
 2490 *Phys. Lett.* **B342** (1995) p. 180, arXiv: [hep-ph/9408275 \[hep-ph\]](#).
- 2491 [80] R. Barbieri and L. J. Hall, *Signals for supersymmetric unification*,  
 2492 *Phys. Lett.* **B338** (1994) p. 212, arXiv: [hep-ph/9408406 \[hep-ph\]](#).
- 2493 [81] B. de Carlos, J. A. Casas, and J. M. Moreno,  
 2494 *Constraints on supersymmetric theories from mu —> e gamma*,  
 2495 *Phys. Rev.* **D53** (1996) p. 6398, arXiv: [hep-ph/9507377 \[hep-ph\]](#).
- 2496 [82] J. A. Casas and S. Dimopoulos,  
 2497 *Stability bounds on flavor violating trilinear soft terms in the MSSM*,  
 2498 *Phys. Lett.* **B387** (1996) p. 107, arXiv: [hep-ph/9606237 \[hep-ph\]](#).
- 2499 [83] C. Borschensky et al., *Squark and gluino production cross sections in pp*  
 2500 *collisions at  $\sqrt{s} = 13, 14, 33$  and 100 TeV*,  
 2501 *Eur. Phys. J.* **C74** (2014) p. 3174, arXiv: [1407.5066 \[hep-ph\]](#).

- 2502 [84] M. Klasen, M. Pohl, and G. Sigl, *Indirect and direct search for dark matter*,  
 2503 Prog. Part. Nucl. Phys. **85** (2015) p. 1, arXiv: [1507.03800](https://arxiv.org/abs/1507.03800) [hep-ph].
- 2504 [85] L. Evans and P. Bryant, *LHC Machine*, JINST **3** (2008) S08001.
- 2505 [86] Vladimir Shiltsev, “Accelerator Physics and Technology,” Aug. 2016,  
 2506 URL: [https://indico.fnal.gov/sessionDisplay.py?sessionId=3&](https://indico.fnal.gov/sessionDisplay.py?sessionId=3&confId=11505#20160811)  
 2507 [confId=11505#20160811](https://indico.fnal.gov/sessionDisplay.py?sessionId=3&confId=11505#20160811).
- 2508 [87] *LEP design report*, Copies shelved as reports in LEP, PS and SPS libraries,  
 2509 Geneva: CERN, 1984, URL: <https://cds.cern.ch/record/102083>.
- 2510 [88] ATLAS Collaboration,  
 2511 *The ATLAS Experiment at the CERN Large Hadron Collider*,  
 2512 JINST **3** (2008) S08003.
- 2513 [89] G. Aad et al., *ATLAS pixel detector electronics and sensors*,  
 2514 JINST **3** (2008) P07007.
- 2515 [90] ATLAS Collaboration, *ATLAS Insertable B-Layer Technical Design Report*,  
 2516 ATLAS-TDR-19 (2010), URL: <http://cdsweb.cern.ch/record/1291633>.
- 2517 [91] ATLAS Collaboration,  
 2518 *Operation and performance of the ATLAS semiconductor tracker*,  
 2519 JINST **9** (2014) P08009, arXiv: [1404.7473](https://arxiv.org/abs/1404.7473) [hep-ex].
- 2520 [92] ATLAS Collaboration, *2015 start-up trigger menu and initial performance*  
 2521 *assessment of the ATLAS trigger using Run-2 data*,  
 2522 ATL-DAQ-PUB-2016-001 (2016),  
 2523 URL: <https://cds.cern.ch/record/2104298>.
- 2524 [93] ATLAS Collaboration, *Performance of the ATLAS Inner Detector Track and*  
 2525 *Vertex Reconstruction in High Pile-Up LHC Environment*,  
 2526 ATLAS-CONF-2012-042, 2012,  
 2527 URL: <https://cds.cern.ch/record/1435196>.
- 2528 [94] ATLAS Collaboration, *Early Inner Detector Tracking Performance in the*  
 2529 *2015 Data at  $\sqrt{s} = 13$  TeV*, ATL-PHYS-PUB-2015-051, 2015,  
 2530 URL: <https://cds.cern.ch/record/2110140>.
- 2531 [95] K Hamano, A Morley, and A Salzburger,  
 2532 “Track Reconstruction Performance and Efficiency Estimation using different  
 2533 ID geometry samples,” tech. rep. ATL-COM-PHYS-2012-1541,  
 2534 plots for a poster at HCP: CERN, Oct. 2012,  
 2535 URL: <https://cds.cern.ch/record/1489674>.

- 2536 [96] ATLAS Collaboration,  
 2537 *Electron reconstruction and identification efficiency measurements with the*  
 2538 *ATLAS detector using the 2011 LHC proton–proton collision data,*  
 2539 *Eur. Phys. J. C* **74** (2014) p. 2941, arXiv: [1404.2240 \[hep-ex\]](#).
- 2540 [97] ATLAS Collaboration, *Topological cell clustering in the ATLAS calorimeters*  
 2541 *and its performance in LHC Run 1* (2016), arXiv: [1603.02934 \[hep-ex\]](#).
- 2542 [98] ATLAS Collaboration, *Jet energy resolution in proton–proton collisions at*  
 2543  $\sqrt{s} = 7 \text{ TeV}$  *recorded in 2010 with the ATLAS detector,*  
 2544 *Eur. Phys. J. C* **73** (2013) p. 2306, arXiv: [1210.6210 \[hep-ex\]](#).
- 2545 [99] ATLAS Collaboration, *Electron performance measurements with the ATLAS*  
 2546 *detector using the 2010 LHC proton–proton collision data,*  
 2547 *Eur. Phys. J. C* **72** (2012) p. 1909, arXiv: [1110.3174 \[hep-ex\]](#).
- 2548 [100] M. Aaboud et al., *Measurement of the photon identification efficiencies with*  
 2549 *the ATLAS detector using LHC Run-1 data* (2016),  
 2550 arXiv: [1606.01813 \[hep-ex\]](#).
- 2551 [101] ATLAS Collaboration, *Electron and photon energy calibration with the*  
 2552 *ATLAS detector using LHC Run 1 data*, *Eur. Phys. J. C* **74** (2014) p. 3071,  
 2553 arXiv: [1407.5063 \[hep-ex\]](#).
- 2554 [102] “Electron and photon energy calibration with the ATLAS detector using  
 2555 data collected in 2015 at  $\sqrt{s} = 13 \text{ TeV}$ ,”  
 2556 tech. rep. ATL-PHYS-PUB-2016-015, CERN, Aug. 2016,  
 2557 URL: <https://cds.cern.ch/record/2203514>.
- 2558 [103] ATLAS Collaboration, *Muon reconstruction performance of the ATLAS*  
 2559 *detector in proton–proton collision data at  $\sqrt{s} = 13 \text{ TeV}$ ,*  
 2560 *Eur. Phys. J. C* **76** (2016) p. 292, arXiv: [1603.05598 \[hep-ex\]](#).
- 2561 [104] ATLAS Collaboration, *Jet energy measurement with the ATLAS detector in*  
 2562 *proton–proton collisions at  $\sqrt{s} = 7 \text{ TeV}$* , *Eur. Phys. J. C* **73** (2013) p. 2304,  
 2563 arXiv: [1112.6426 \[hep-ex\]](#).
- 2564 [105] ATLAS Collaboration,  
 2565 *Jet energy measurement and its systematic uncertainty in proton–proton*  
 2566 *collisions at  $\sqrt{s} = 7 \text{ TeV}$  with the ATLAS detector,*  
 2567 *Eur. Phys. J. C* **75** (2015) p. 17, arXiv: [1406.0076 \[hep-ex\]](#).
- 2568 [106] S. D. Ellis and D. E. Soper,  
 2569 *Successive combination jet algorithm for hadron collisions,*  
 2570 *Phys. Rev. D* **48** (1993) p. 3160, arXiv: [hep-ph/9305266 \[hep-ph\]](#).

- 2571 [107] M. Cacciari and G. P. Salam, *Dispelling the  $N^3$  myth for the  $k_t$  jet-finder*,  
2572 Phys. Lett. B **641** (2006) p. 57, arXiv: [hep-ph/0512210](#).
- 2573 [108] M. Cacciari, G. P. Salam, and G. Soyez, *The anti- $k_t$  jet clustering algorithm*,  
2574 JHEP **04** (2008) p. 063, arXiv: [0802.1189 \[hep-ph\]](#).
- 2575 [109] *Particle-Flow Event Reconstruction in CMS and Performance for Jets, Taus,  
2576 and MET* (2009).
- 2577 [110] ATLAS Collaboration,  
2578 *Tagging and suppression of pileup jets with the ATLAS detector*,  
2579 ATLAS-CONF-2014-018, 2014,  
2580 URL: <https://cds.cern.ch/record/1700870>.
- 2581 [111] M. Cacciari, G. P. Salam, and G. Soyez, *The Catchment Area of Jets*,  
2582 JHEP **04** (2008) p. 005, arXiv: [0802.1188 \[hep-ph\]](#).
- 2583 [112] G. Aad et al., *Performance of b-Jet Identification in the ATLAS Experiment*,  
2584 JINST **11** (2016) P04008, arXiv: [1512.01094 \[hep-ex\]](#).
- 2585 [113] ATLAS Collaboration,  
2586 *Optimisation of the ATLAS b-tagging performance for the 2016 LHC Run*,  
2587 ATL-PHYS-PUB-2016-012 (2016),  
2588 URL: <https://cds.cern.ch/record/2160731>.
- 2589 [114] G. Aad et al., *Performance of algorithms that reconstruct missing transverse  
2590 momentum in  $\sqrt{s} = 8$  TeV proton-proton collisions in the ATLAS detector*  
2591 (2016), arXiv: [1609.09324 \[hep-ex\]](#).
- 2592 [115] ATLAS Collaboration,  
2593 *Prospects for Supersymmetry discovery based on inclusive searches at a*  
2594 *7 TeV centre-of-mass energy with the ATLAS detector*,  
2595 ATL-PHYS-PUB-2010-010, 2010,  
2596 URL: <https://cds.cern.ch/record/1278474>.
- 2597 [116] ATLAS Collaboration,  
2598 *Expected sensitivity studies for gluino and squark searches using the early*  
2599 *LHC 13 TeV Run-2 dataset with the ATLAS experiment*,  
2600 ATL-PHYS-PUB-2015-005, 2015, URL:  
2601 <https://atlas.web.cern.ch/Atlas/GROUPS/PHYSICS/PUBNOTES/ATL-PHYS-PUB-2015-005>.
- 2603 [117] ATLAS Collaboration, *Expected performance of missing transverse  
2604 momentum reconstruction for the ATLAS detector at  $\sqrt{s} = 13$  TeV*,

- 2605           ATL-PHYS-PUB-2015-023, 2015,  
 2606           URL: <https://cds.cern.ch/record/2037700>.
- 2607 [118] ATLAS Collaboration,  
 2608           *Performance of missing transverse momentum reconstruction with the*  
 2609           *ATLAS detector in the first proton–proton collisions at  $\sqrt{s} = 13$  TeV,*  
 2610           ATL-PHYS-PUB-2015-027, 2015,  
 2611           URL: <https://cds.cern.ch/record/2037904>.
- 2612 [119] P. Jackson, C. Rogan and M. Santoni, *Sparticles in Motion - getting to the*  
 2613           *line in compressed scenarios with the Recursive Jigsaw Reconstruction*  
 2614           (2016), arXiv: [1607.08307 \[hep-ph\]](https://arxiv.org/abs/1607.08307).
- 2615 [120] ATLAS Collaboration,  
 2616           *Further searches for squarks and gluinos in final states with jets and missing*  
 2617           *transverse momentum at  $\sqrt{s} = 13$  TeV with the ATLAS detector,*  
 2618           ATLAS-CONF-2016-078, 2016,  
 2619           URL: <https://cds.cern.ch/record/2206252>.
- 2620 [121] C. Rogan, *Kinematical variables towards new dynamics at the LHC* (2010),  
 2621           arXiv: [1006.2727 \[hep-ph\]](https://arxiv.org/abs/1006.2727).
- 2622 [122] M. R. Buckley et al.,  
 2623           *Super-Razor and Searches for Sleptons and Charginos at the LHC*,  
 2624           Phys. Rev. **D89** (2014) p. 055020, arXiv: [1310.4827 \[hep-ph\]](https://arxiv.org/abs/1310.4827).
- 2625 [123] CMS Collaboration, *Search for supersymmetry using razor variables in*  
 2626           *events with b-tagged jets in pp collisions at  $\sqrt{s} = 8$  TeV,*  
 2627           Phys. Rev. D **91** (2015) p. 052018, arXiv: [1502.00300 \[hep-ex\]](https://arxiv.org/abs/1502.00300).
- 2628 [124] Chris Rogan, “RestFrames,” URL: <http://restframes.com>.
- 2629 [125] M. Baak et al., *HistFitter software framework for statistical data analysis*,  
 2630           Eur. Phys. J. **C75** (2015) p. 153, arXiv: [1410.1280 \[hep-ex\]](https://arxiv.org/abs/1410.1280).
- 2631 [126] M. L. Mangano et al., *Matching matrix elements and shower evolution for*  
 2632           *top-quark production in hadronic collisions*, JHEP **01** (2007) p. 013,  
 2633           arXiv: [hep-ph/0611129 \[hep-ph\]](https://arxiv.org/abs/hep-ph/0611129).
- 2634 [127] F. Maltoni and T. Stelzer,  
 2635           *MadEvent: Automatic event generation with MadGraph*,  
 2636           JHEP **02** (2003) p. 027, arXiv: [hep-ph/0208156 \[hep-ph\]](https://arxiv.org/abs/hep-ph/0208156).
- 2637 [128] T. Sjöstrand et al., *An Introduction to PYTHIA 8.2*,  
 2638           Comput. Phys. Commun. **191** (2015) p. 159, arXiv: [1410.3012 \[hep-ph\]](https://arxiv.org/abs/1410.3012).

- 2639 [129] T. Gleisberg et al., *Event generation with SHERPA 1.1*,  
 2640 JHEP **02** (2009) p. 007, arXiv: [0811.4622 \[hep-ph\]](#).
- 2641 [130] S. Schumann and F. Krauss,  
 2642 *A Parton shower algorithm based on Catani-Seymour dipole factorisation*,  
 2643 JHEP **03** (2008) p. 038, arXiv: [0709.1027 \[hep-ph\]](#).
- 2644 [131] S. Alioli et al., *A general framework for implementing NLO calculations in*  
 2645 *shower Monte Carlo programs: the POWHEG BOX*, JHEP **06** (2010) p. 043,  
 2646 arXiv: [1002.2581 \[hep-ph\]](#).
- 2647 [132] J. Alwall, R. Frederix, S. Frixione, V. Hirschi, F. Maltoni, O. Mattelaer, H.  
 2648 -S. Shao, T. Stelzer, P. Torrielli, M. Zaro,  
 2649 *The automated computation of tree-level and next-to-leading order differential*  
 2650 *cross sections, and their matching to parton shower simulations*,  
 2651 JHEP **07** (2014) p. 079, arXiv: [1405.0301 \[hep-ph\]](#).
- 2652 [133] S. Frixione et al., *NLO QCD corrections in Herwig++ with MC@NLO*,  
 2653 JHEP **01** (2011) p. 053, arXiv: [1010.0568 \[hep-ph\]](#).
- 2654 [134] S. Agostinelli et al., *GEANT4: A simulation toolkit*,  
 2655 Nucl. Instrum. Meth. A **506** (2003) p. 250.
- 2656 [135] ATLAS Collaboration,  
 2657 *Search for squarks and gluinos in final states with jets and missing transverse*  
 2658 *momentum at  $\sqrt{s} = 13$  TeV with the ATLAS detector*,  
 2659 Eur. Phys. J. C **76** (2016) p. 392, arXiv: [1605.03814 \[hep-ex\]](#).
- 2660 [136] R. D. Cousins, J. T. Linnemann, and J. Tucker,  
 2661 *Evaluation of three methods for calculating statistical significance when*  
 2662 *incorporating a systematic uncertainty into a test of the background-only*  
 2663 *hypothesis for a Poisson process*, Nucl. Instrum. Meth. A **595** (2008) p. 480.
- 2664 [137] ATLAS Collaboration, *Search for squarks and gluinos with the ATLAS*  
 2665 *detector in final states with jets and missing transverse momentum using*  
 2666  *$4.7 \text{ fb}^{-1}$  of  $\sqrt{s} = 7$  TeV proton-proton collision data*,  
 2667 Phys. Rev. D **87** (2013) p. 012008, arXiv: [1208.0949 \[hep-ex\]](#).
- 2668 [138] ATLAS Collaboration, *Jet energy measurement with the ATLAS detector in*  
 2669 *proton-proton collisions at  $\sqrt{s} = 7$  TeV*, Eur. Phys. J. C **73** (2013) p. 2304,  
 2670 arXiv: [1112.6426 \[hep-ex\]](#).
- 2671 [139] ATLAS Collaboration, *Single hadron response measurement and calorimeter*  
 2672 *jet energy scale uncertainty with the ATLAS detector at the LHC*,  
 2673 Eur. Phys. J. C **73** (2013) p. 2305, arXiv: [1203.1302 \[hep-ex\]](#).

- 2674 [140] ATLAS Collaboration, *Jet Calibration and Systematic Uncertainties for Jets*  
2675 *Reconstructed in the ATLAS Detector at  $\sqrt{s} = 13 \text{ TeV}$ ,*  
2676 ATL-PHYS-PUB-2015-015, 2015,  
2677 URL: <https://cds.cern.ch/record/2037613>.
- 2678 [141] ATLAS Collaboration, *Jet energy resolution in proton-proton collisions at*  
2679  *$\sqrt{s} = 7 \text{ TeV}$  recorded in 2010 with the ATLAS detector,*  
2680 *Eur. Phys. J. C* **73** (2013) p. 2306, arXiv: [1210.6210 \[hep-ex\]](https://arxiv.org/abs/1210.6210).
- 2681 [142] ATLAS Collaboration,  
2682 *Performance of algorithms that reconstruct missing transverse momentum in*  
2683  *$\sqrt{s} = 8 \text{ TeV}$  proton–proton collisions in the ATLAS detector* (2016),  
2684 arXiv: [1609.09324 \[hep-ex\]](https://arxiv.org/abs/1609.09324).
- 2685 [143] G. J. Feldman and R. D. Cousins,  
2686 *A Unified approach to the classical statistical analysis of small signals*,  
2687 *Phys. Rev. D* **57** (1998) p. 3873,  
2688 arXiv: [physics/9711021 \[physics.data-an\]](https://arxiv.org/abs/physics/9711021).
- 2689 [144] ATLAS Collaboration, *Search for squarks and gluinos with the ATLAS*  
2690 *detector in final states with jets and missing transverse momentum using*  
2691  *$\sqrt{s} = 8 \text{ TeV}$  proton–proton collision data*, *JHEP* **09** (2014) p. 176,  
2692 arXiv: [1405.7875 \[hep-ex\]](https://arxiv.org/abs/1405.7875).



---

2693

## *The Standard Model*

2694

2695 **Compressed region N-1 plots**

add some  
text or cut  
this

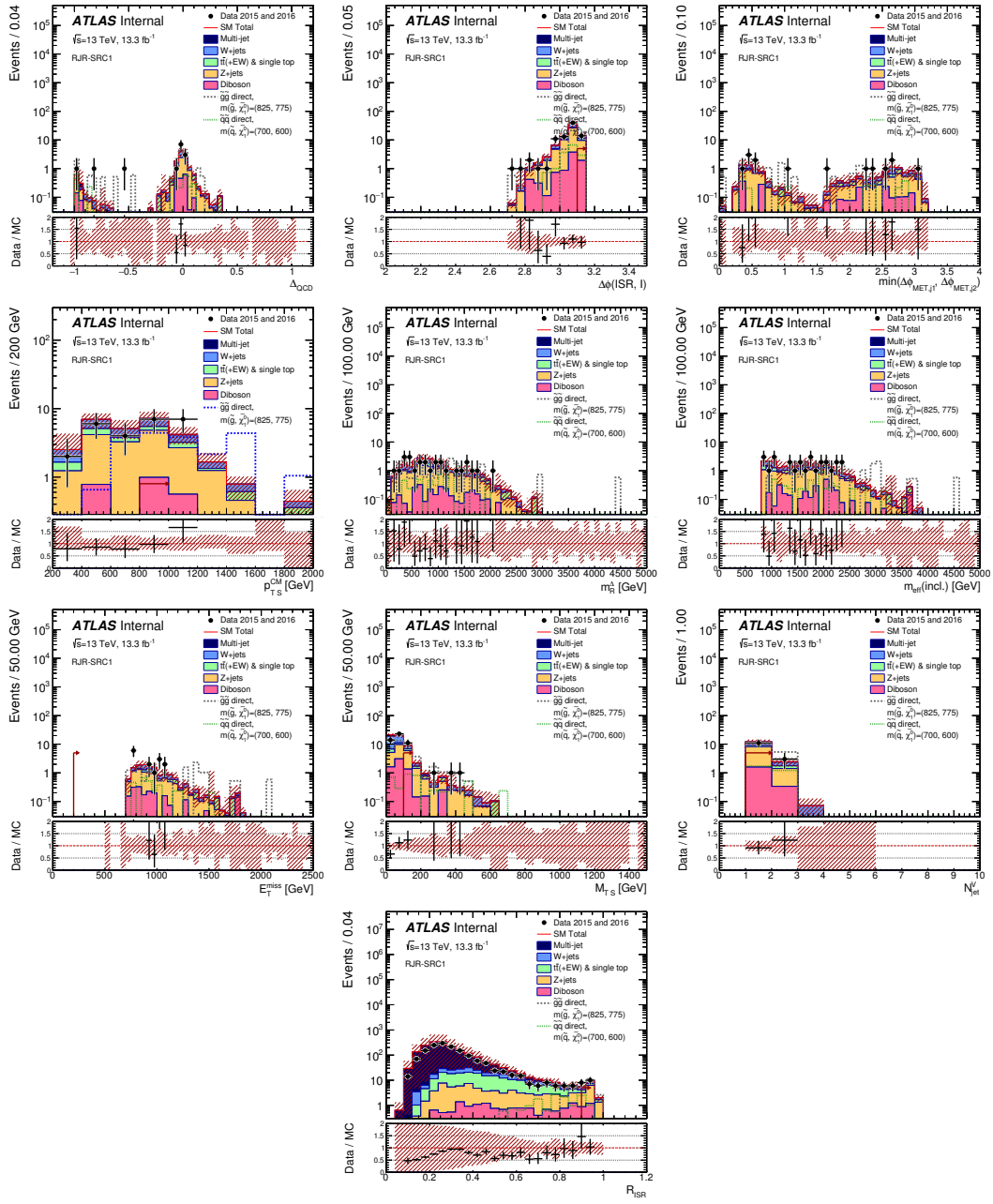


Figure 1

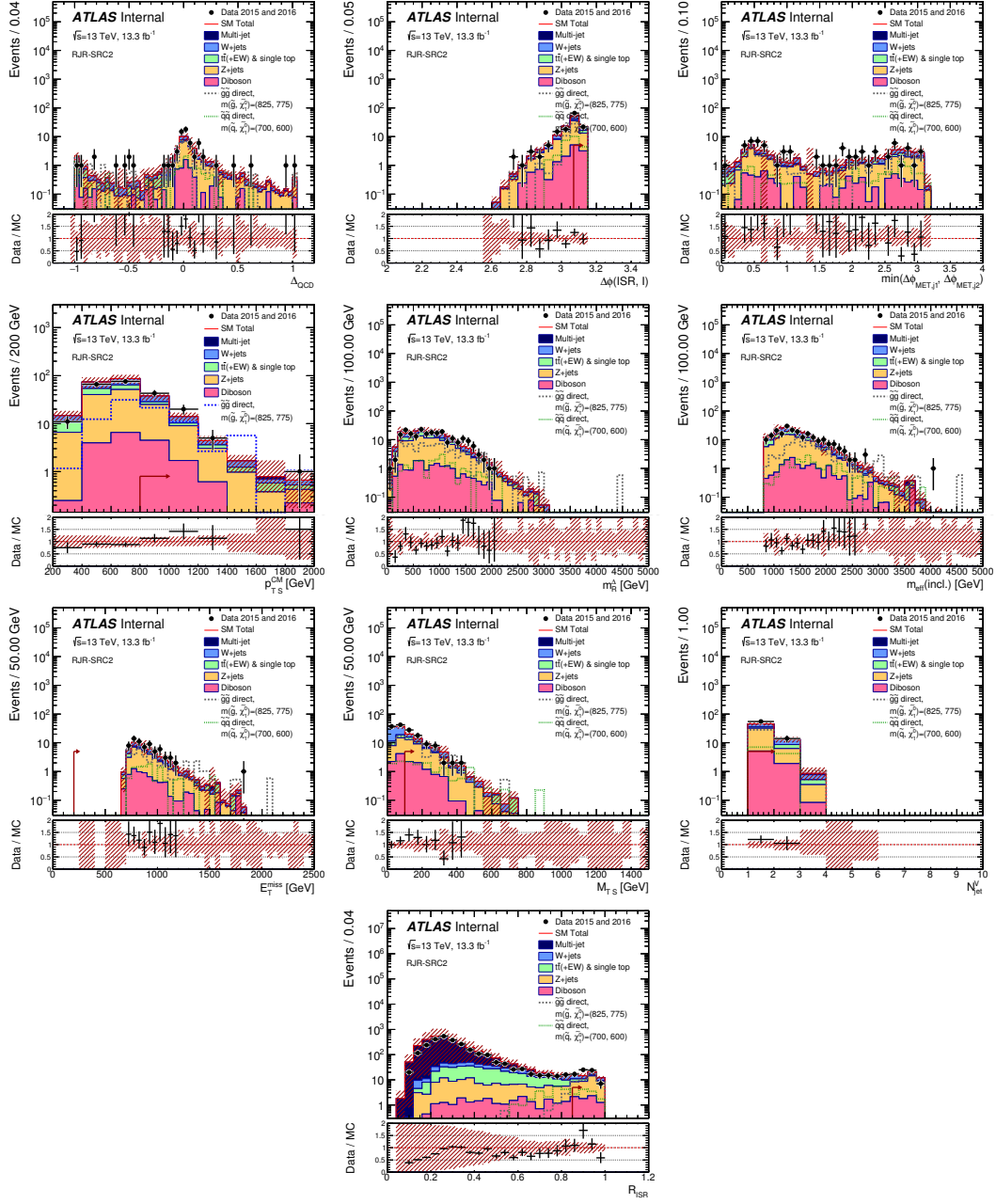


Figure 2

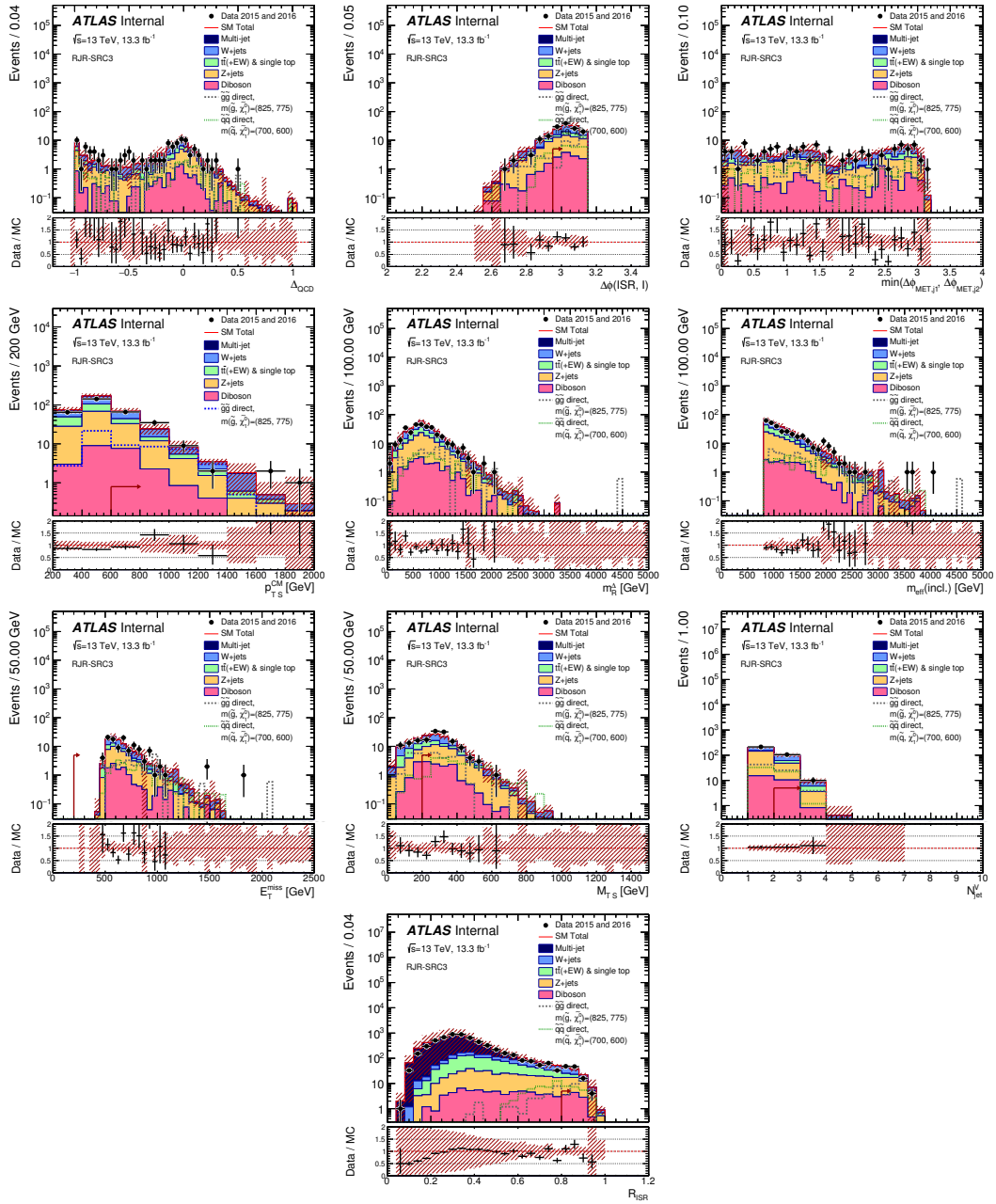


Figure 3

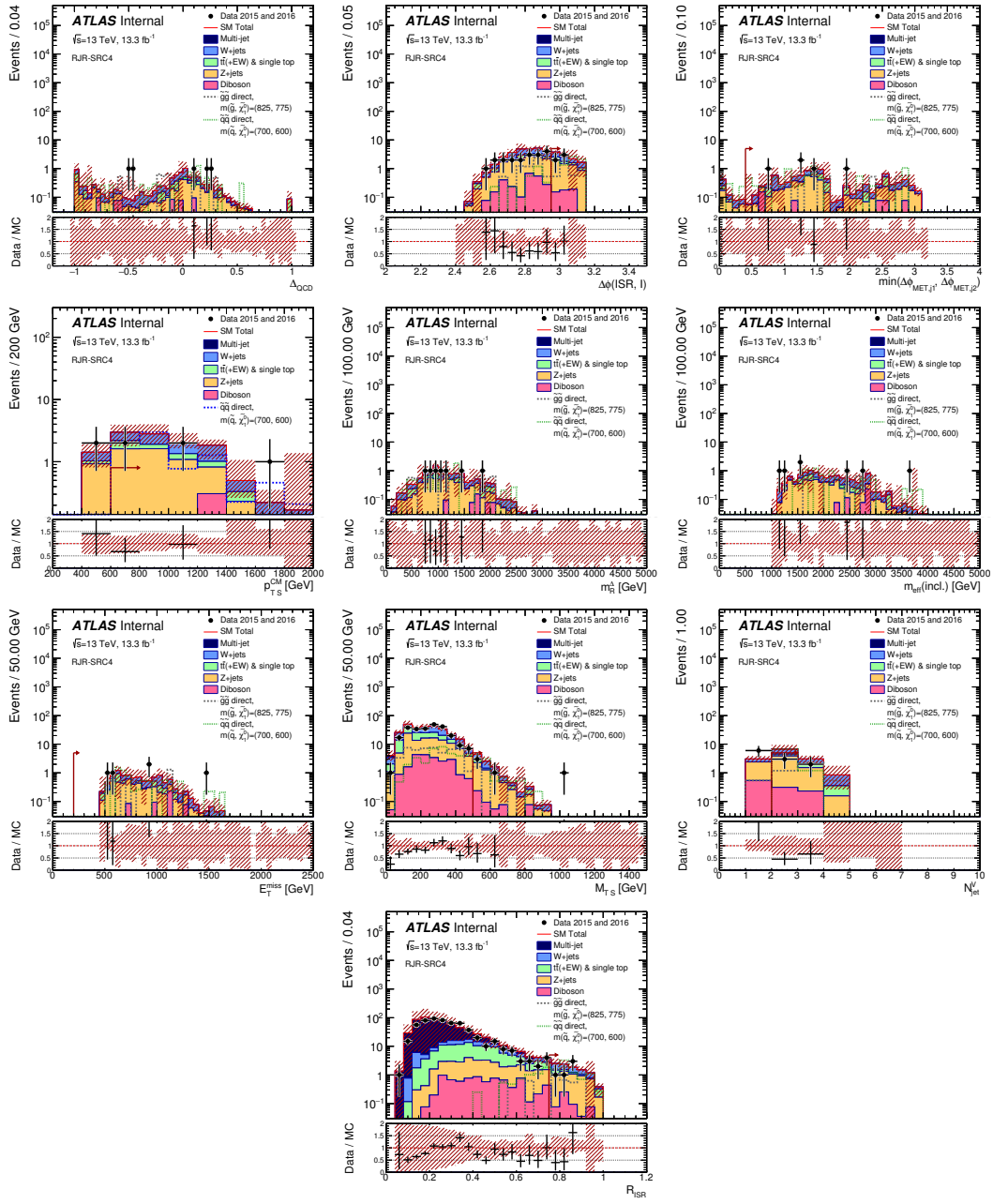


Figure 4

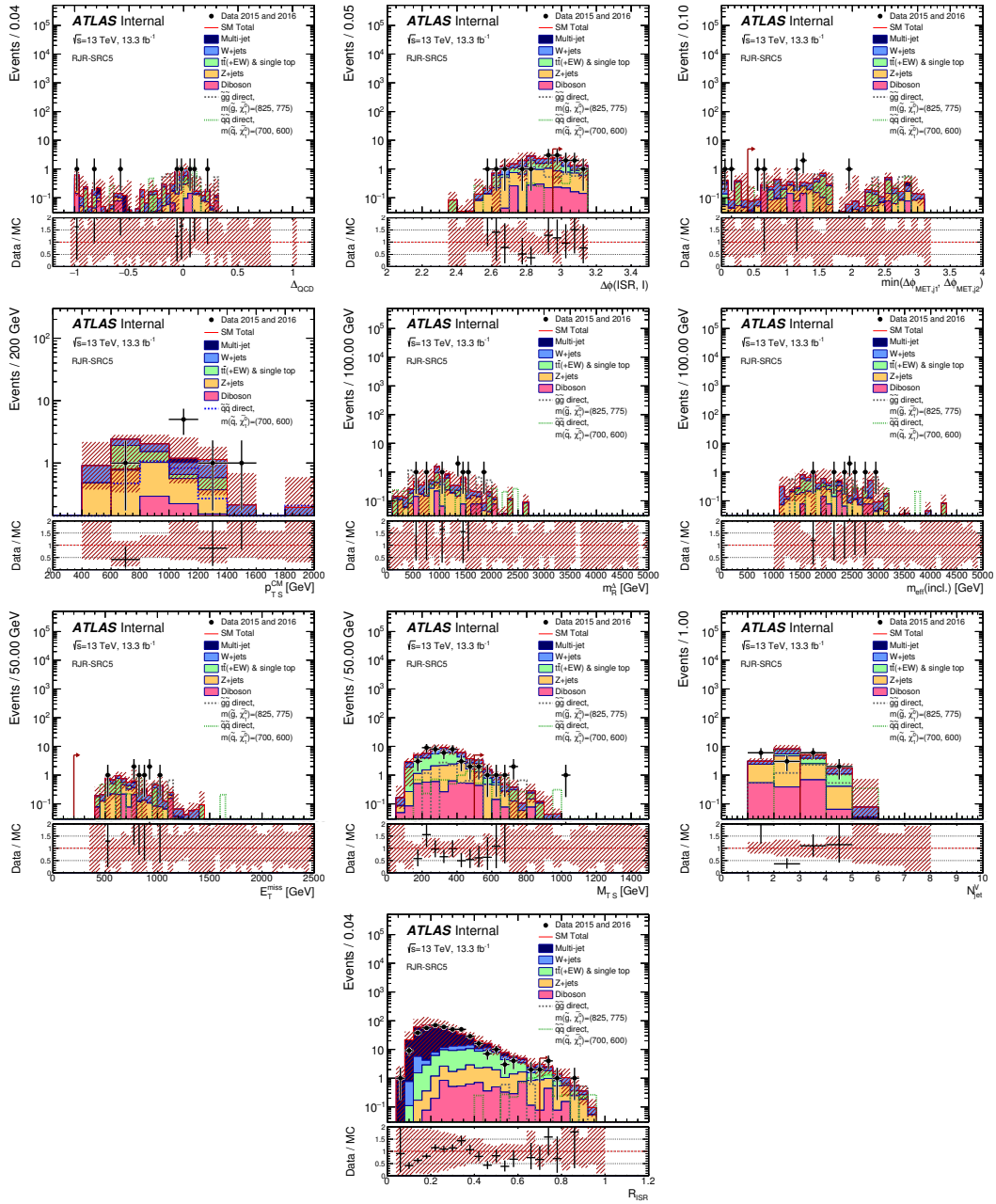


Figure 5

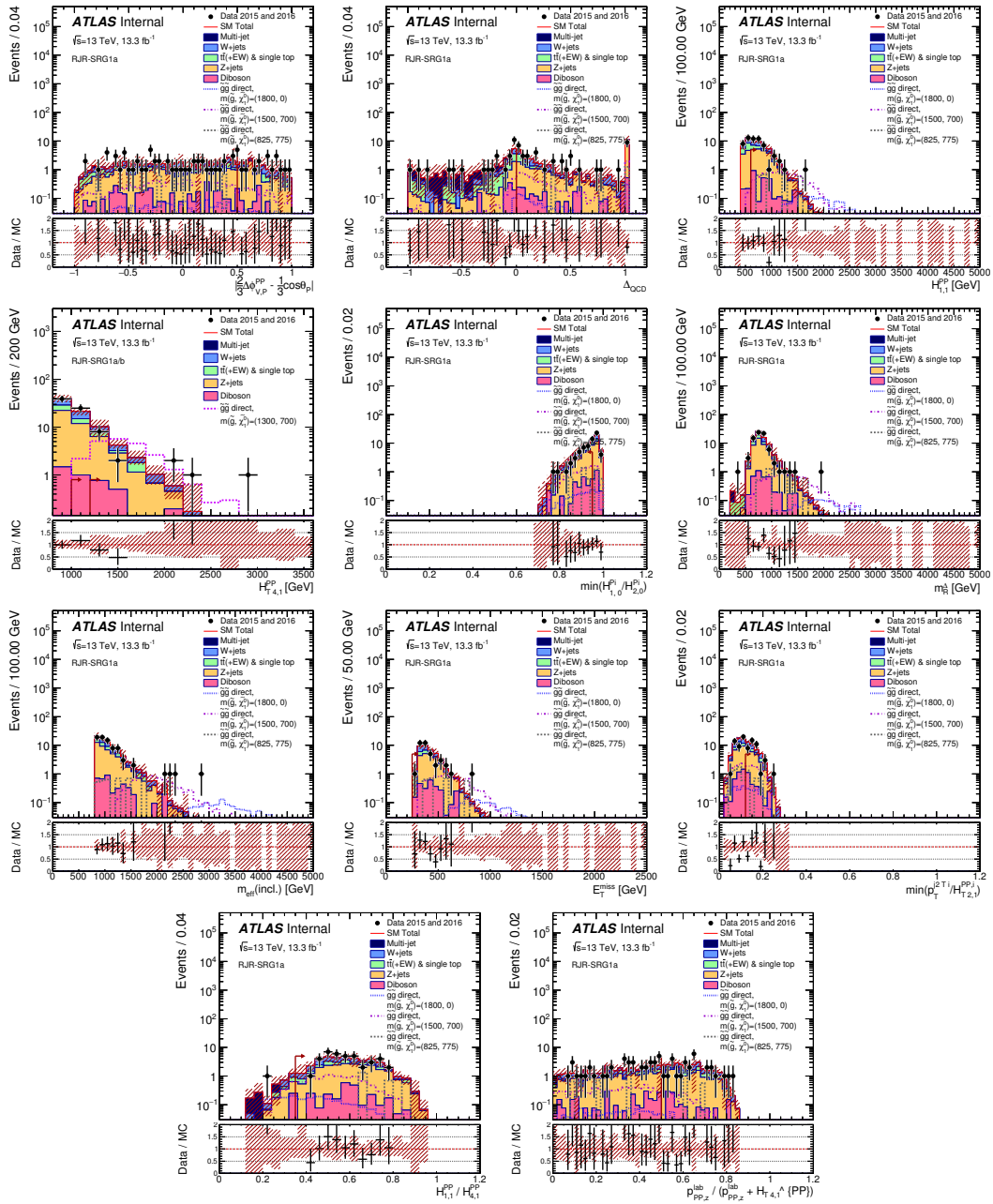


Figure 6

Figure 7

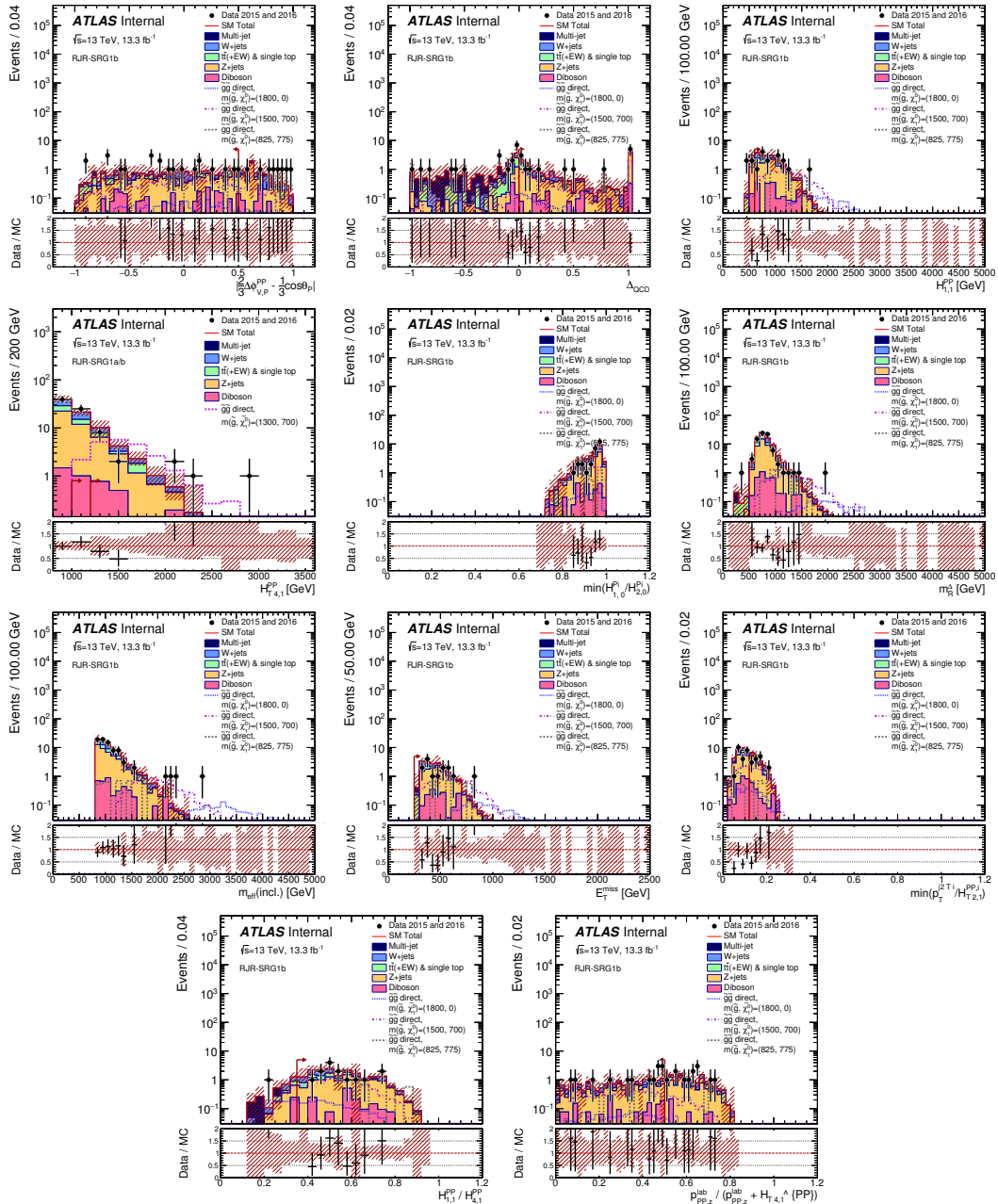


Figure 8

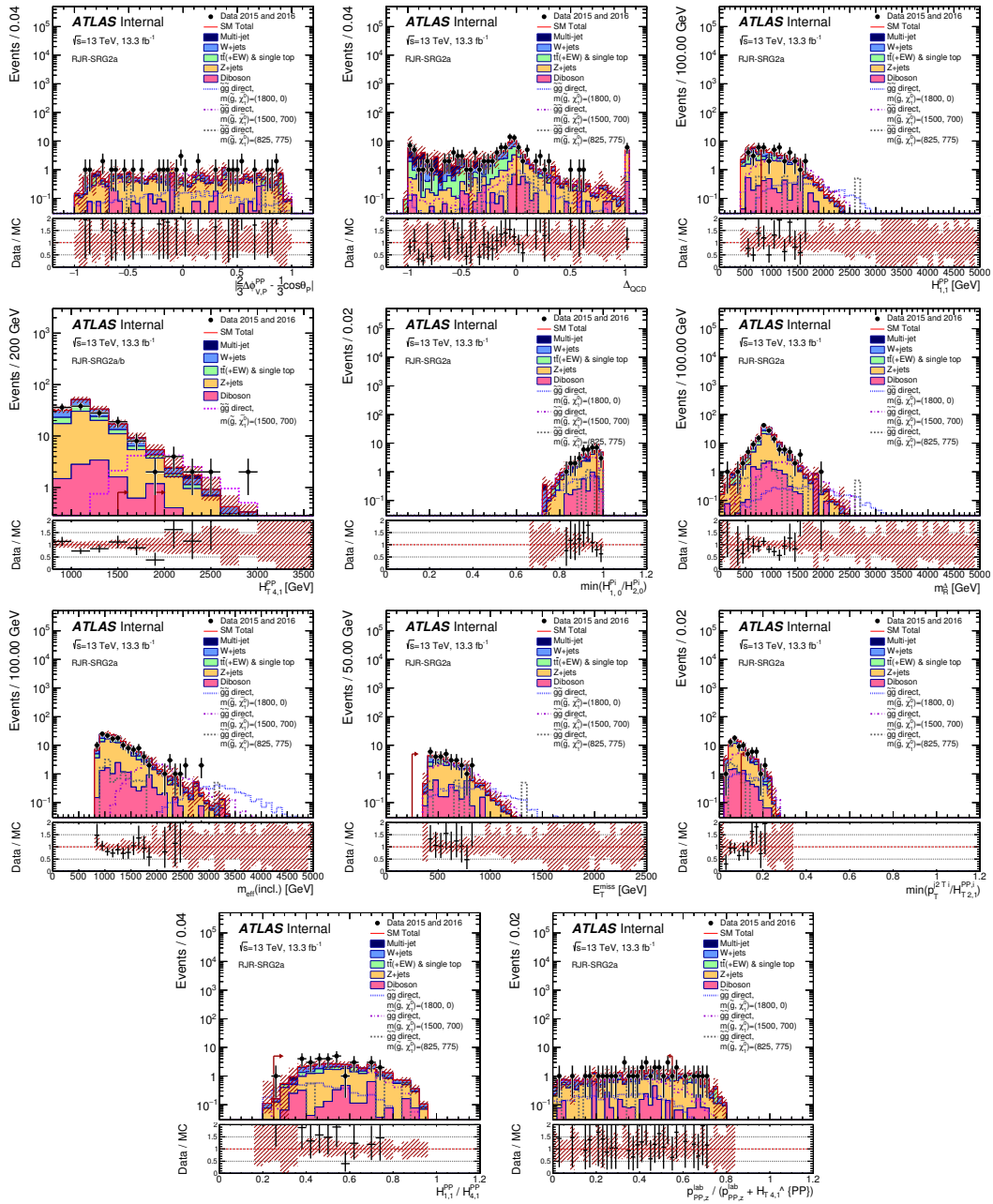


Figure 9

Figure 10

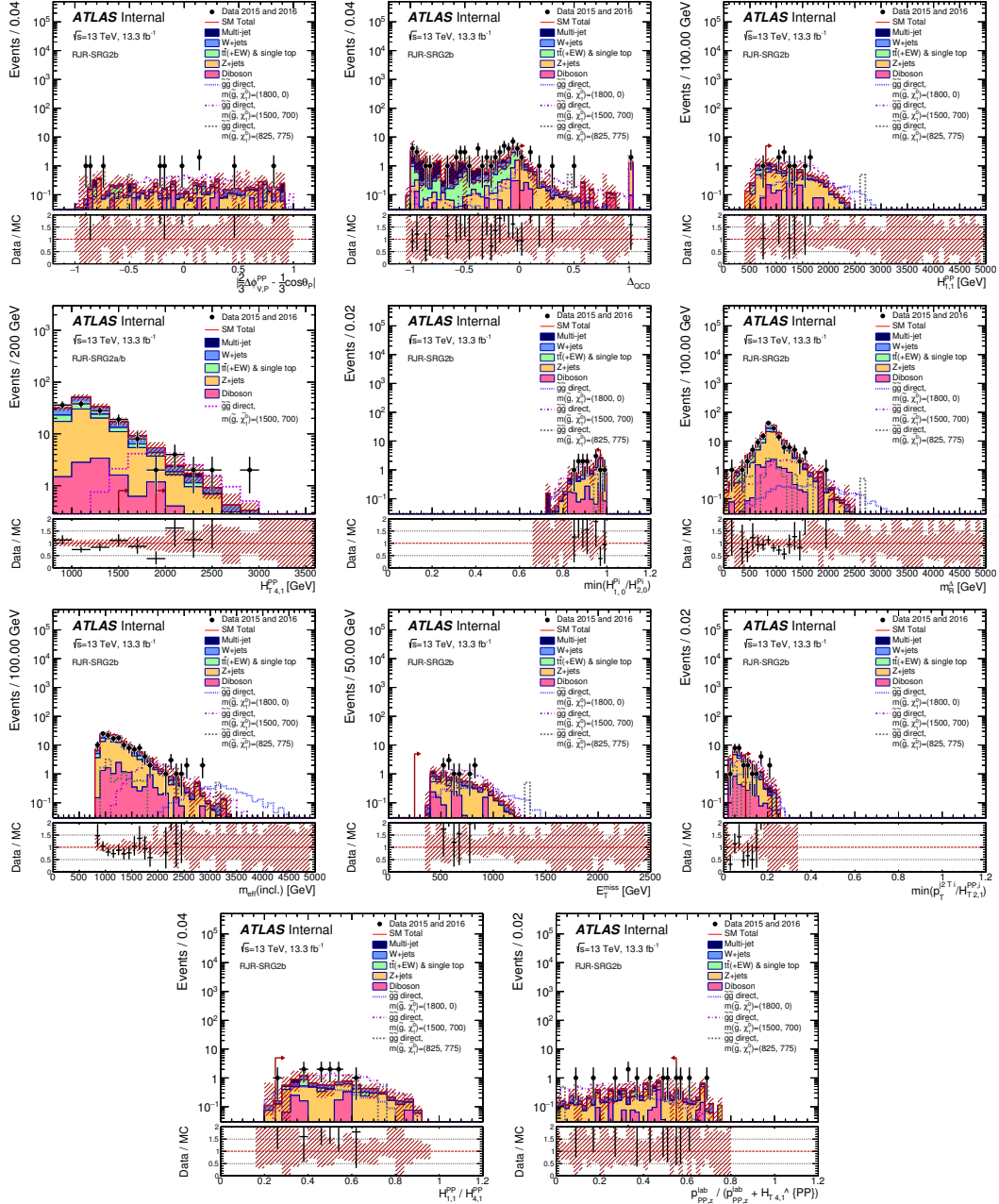


Figure 11

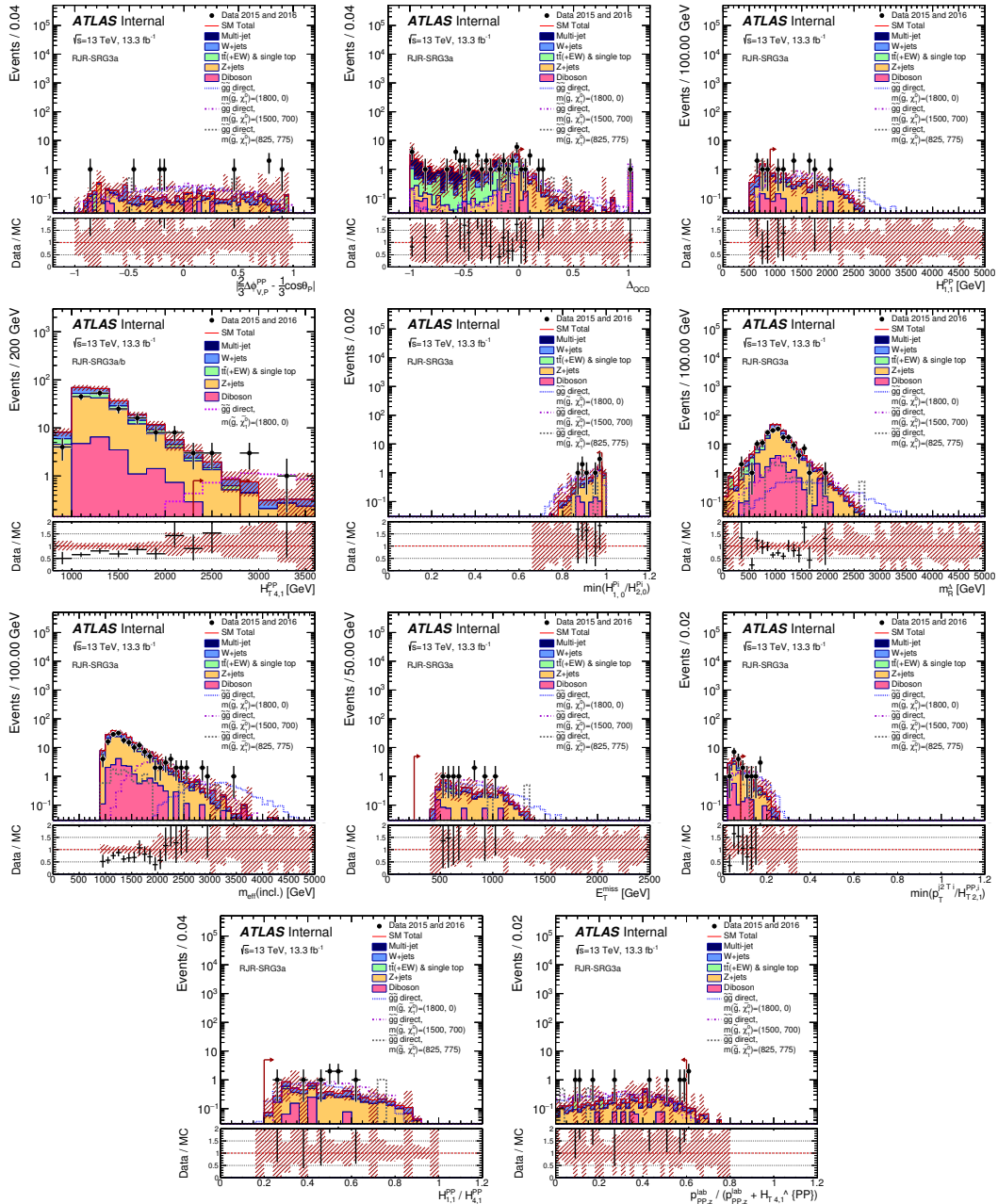


Figure 12

Figure 13

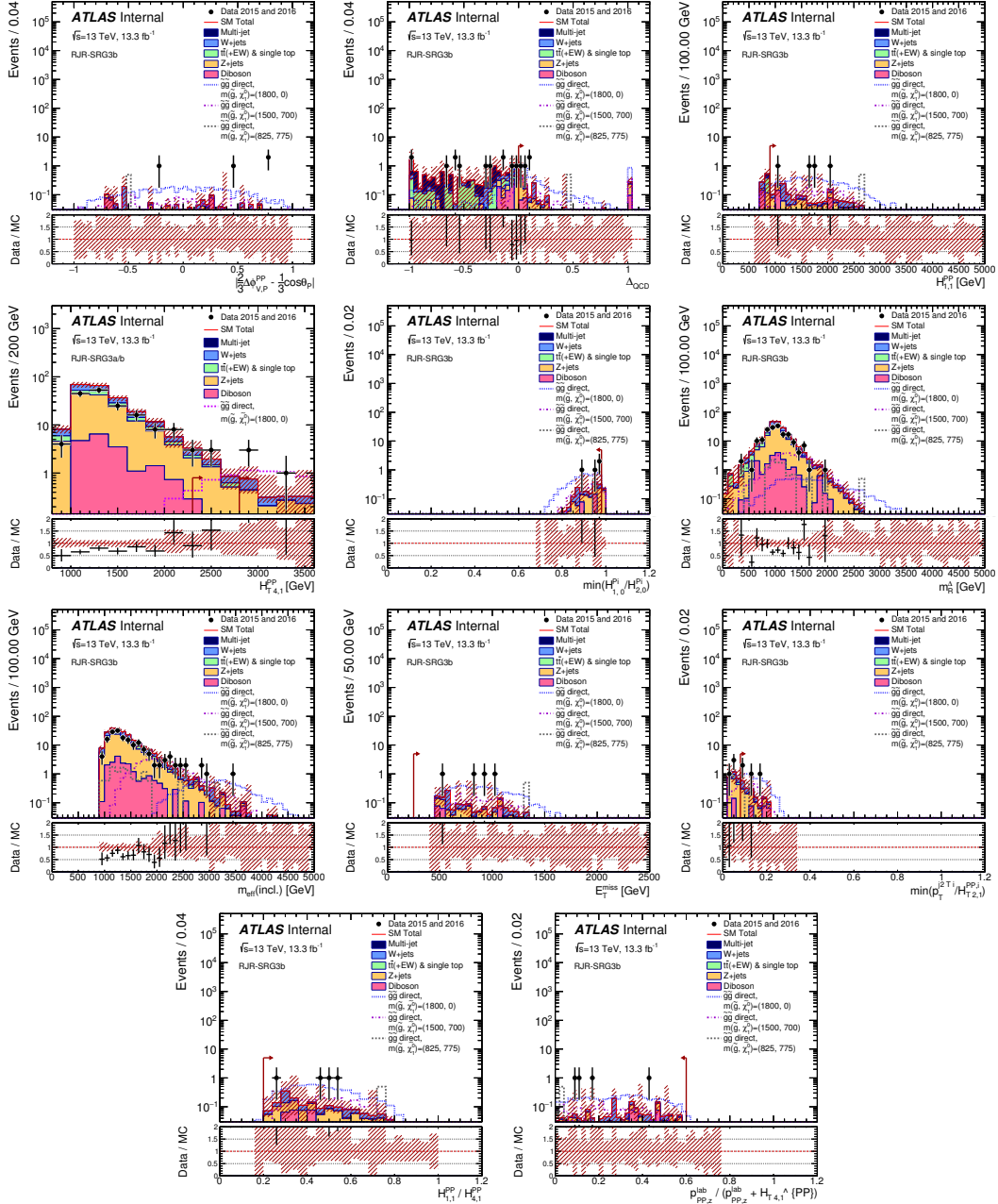


Figure 14

Figure 15

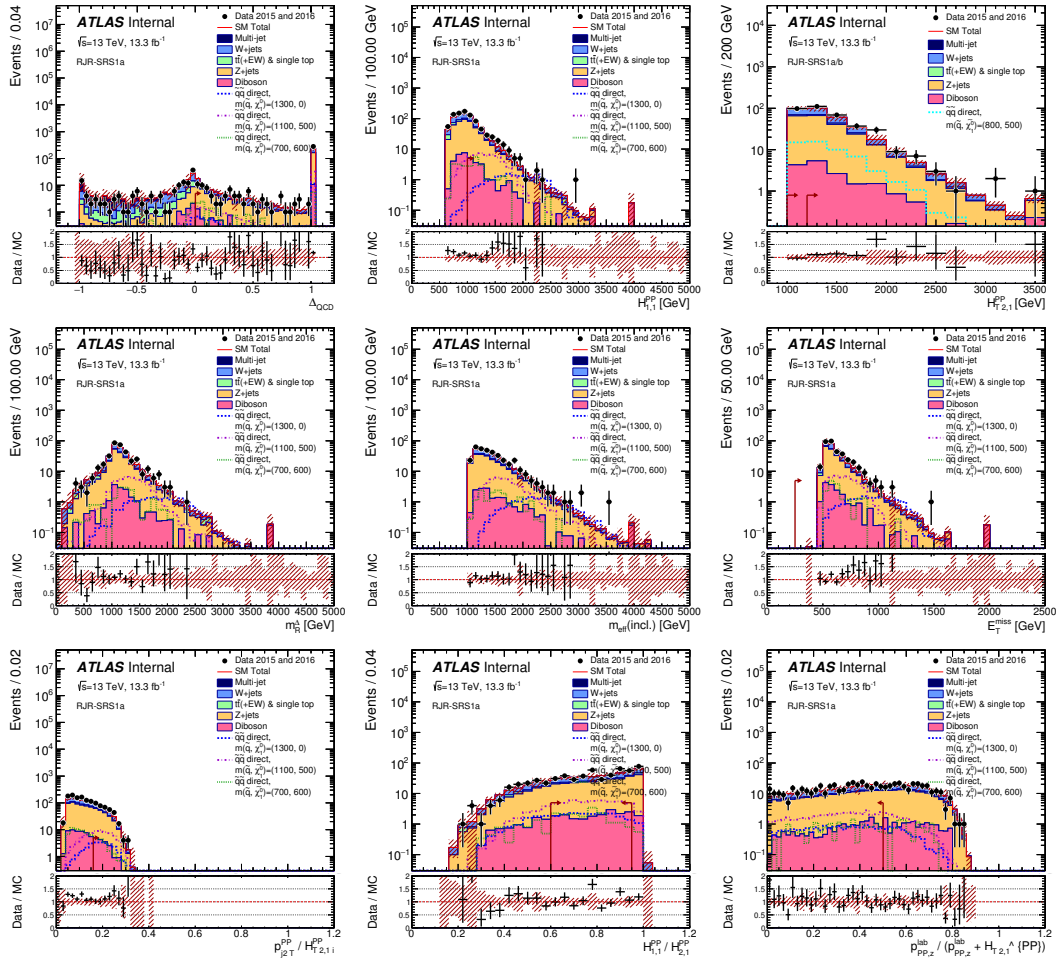


Figure 16

Figure 17

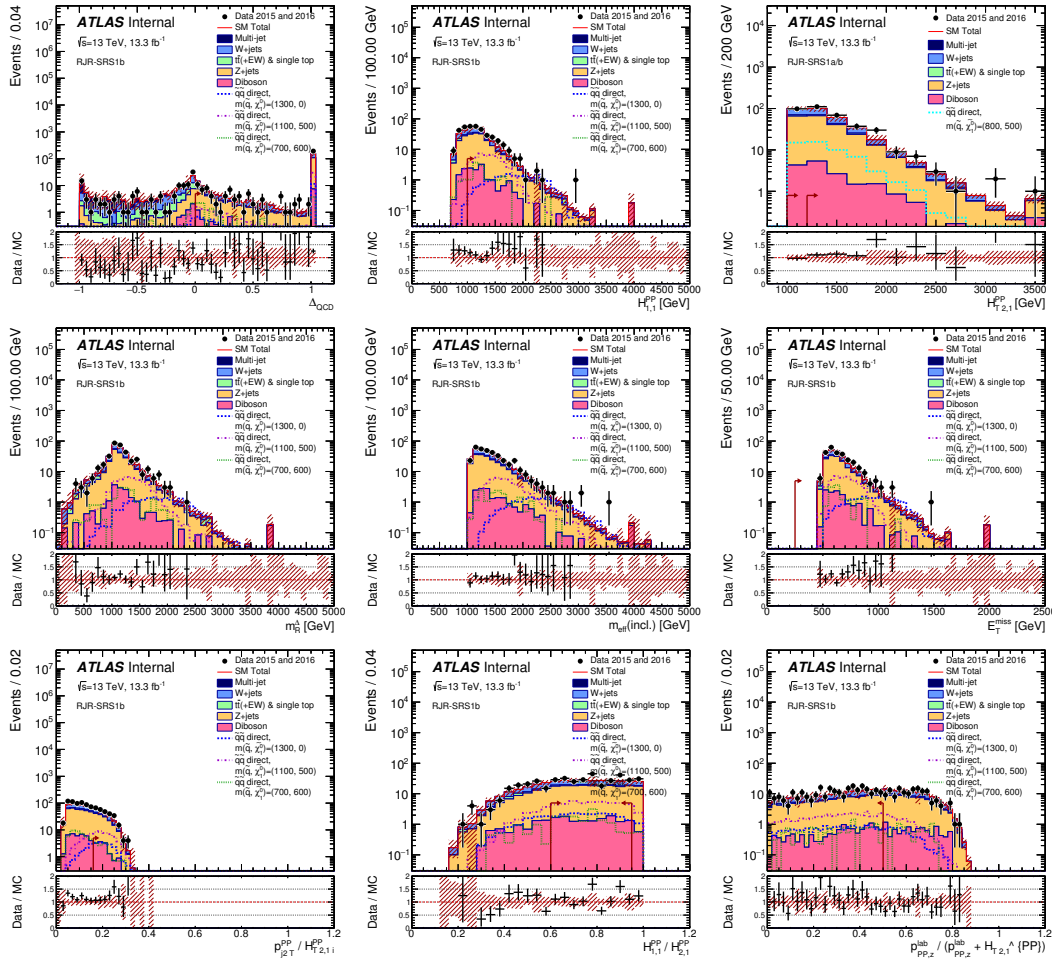


Figure 18

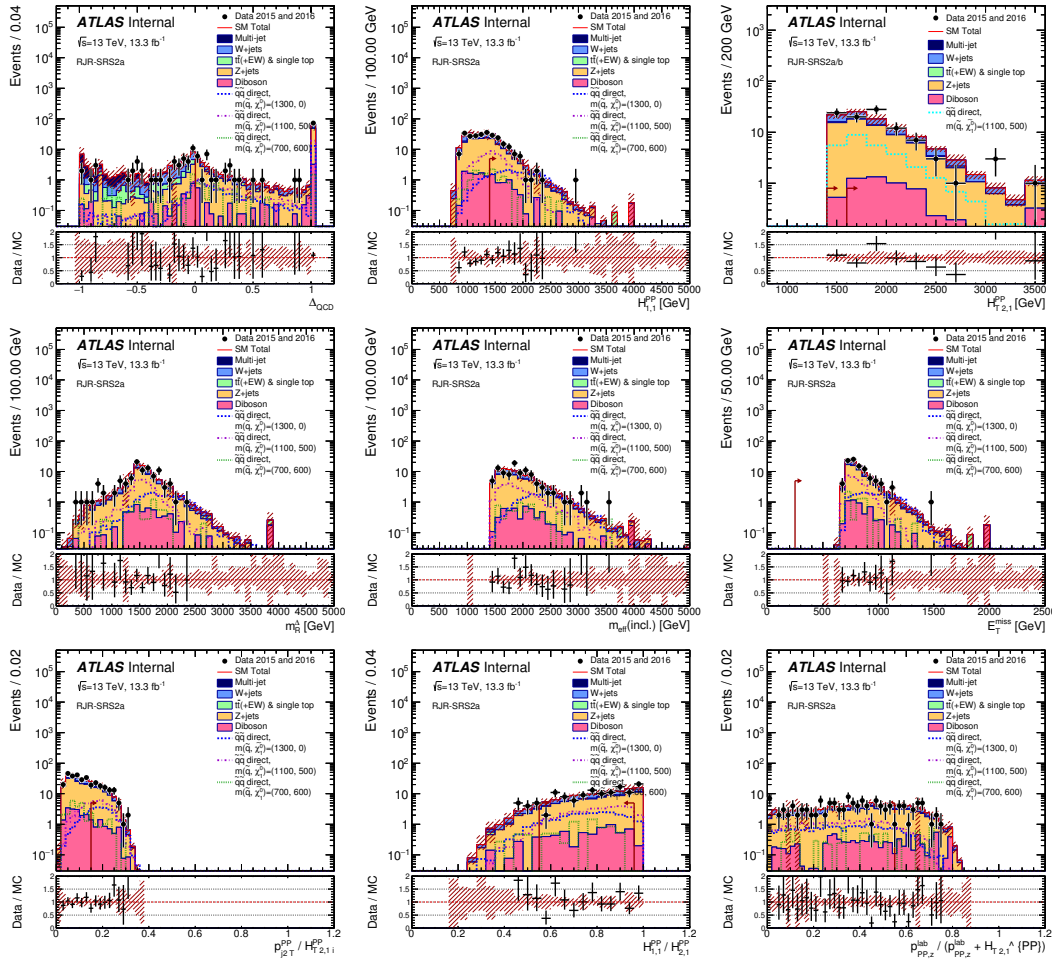


Figure 19

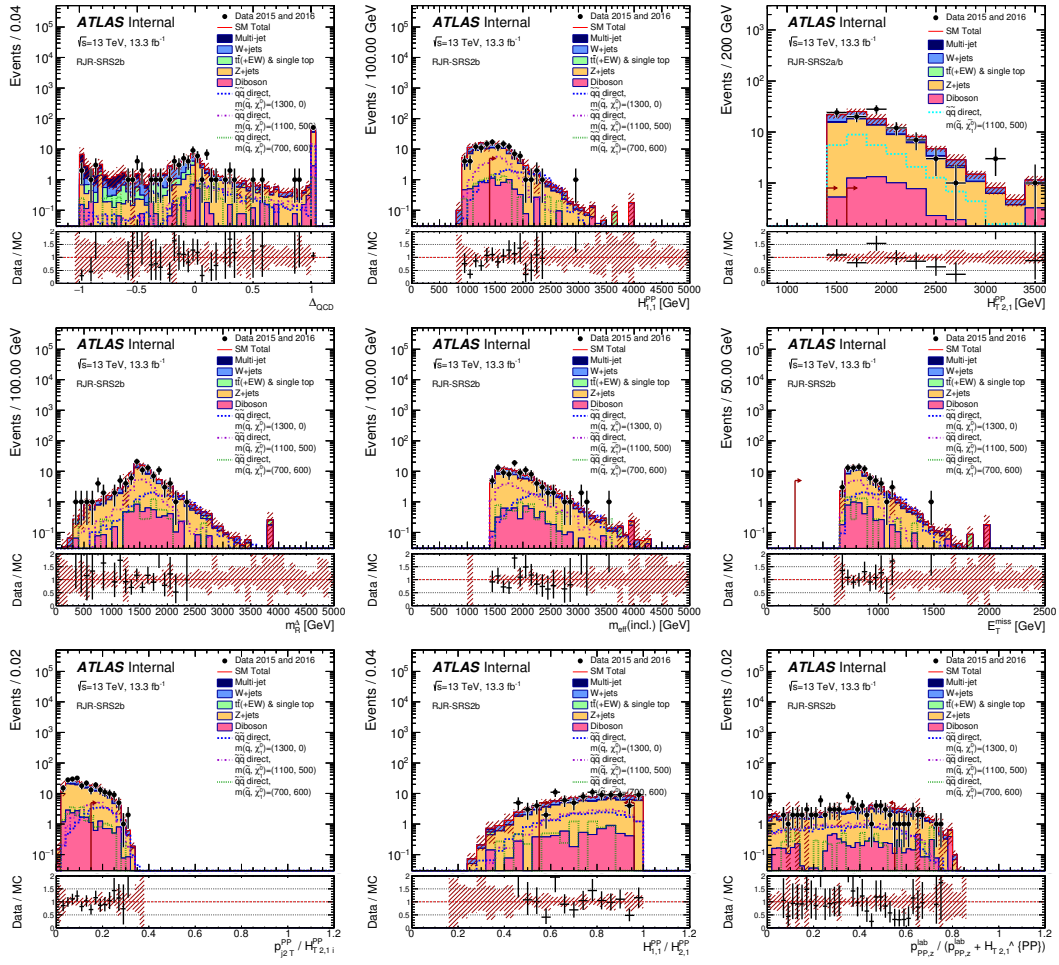


Figure 20

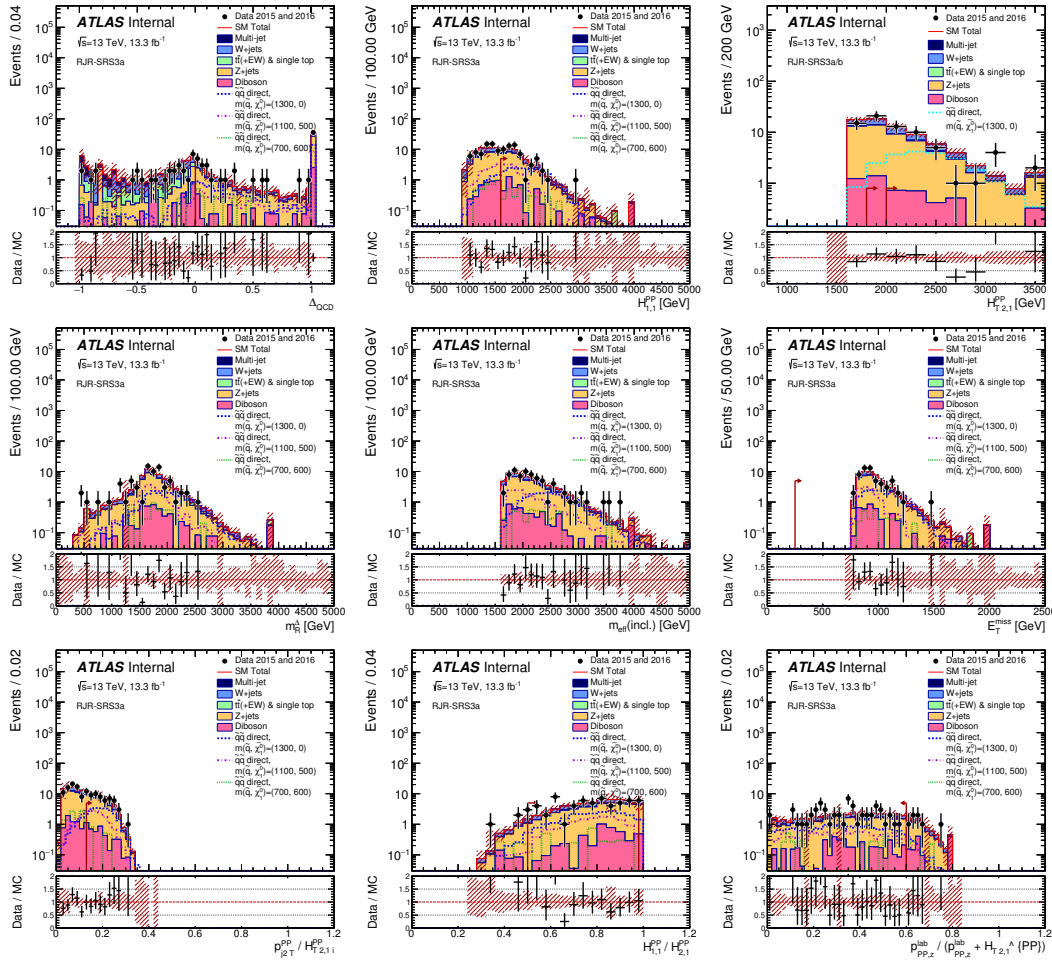


Figure 21

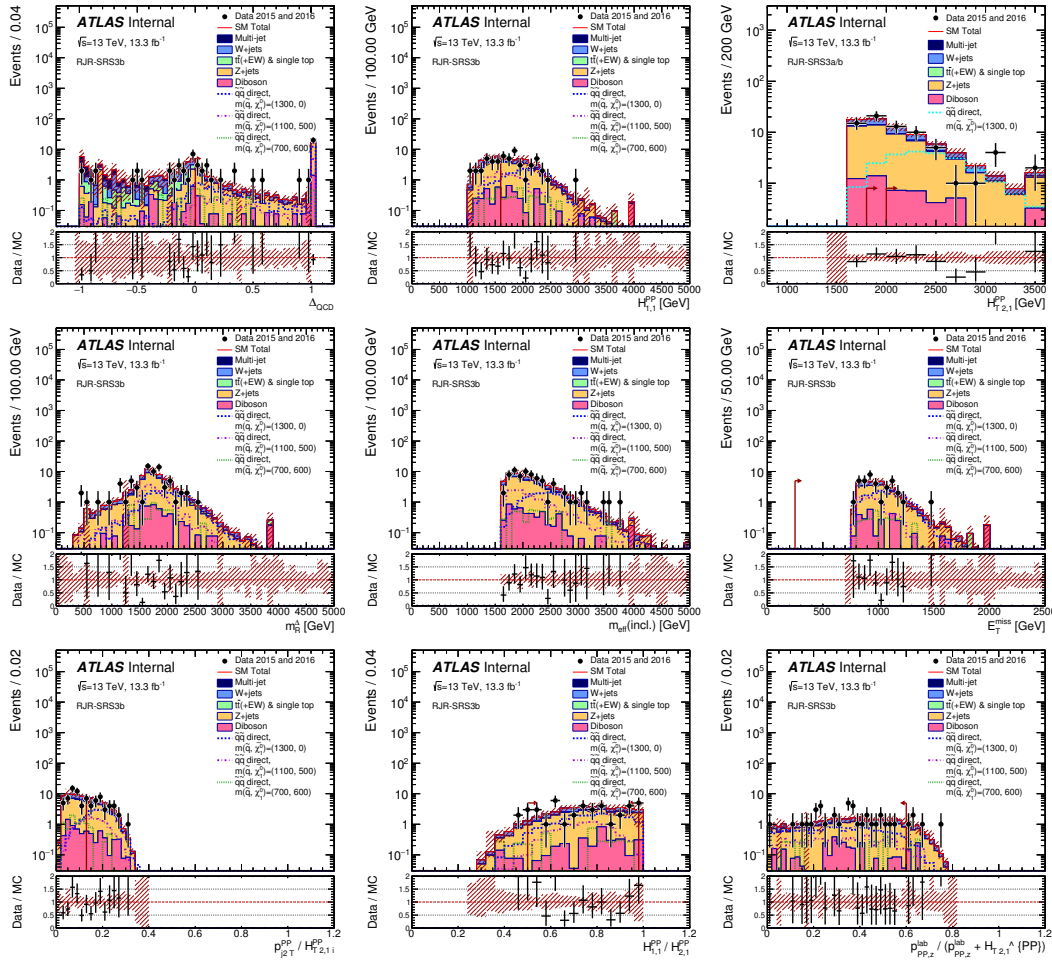


Figure 22